Semiconductors, Vol. 38, No. 7, 2004, pp. 737–741. Translated from Fizika i Tekhnika Poluprovodnikov, Vol. 38, No. 7, 2004, pp. 769–774.
Original Russian Text Copyright © 2004 by Boltovets, Ivanov, Konakova, Kudrik, O. Litvin, P. Litvin, Milenin.

ATOMIC STRUCTURE AND NONELECTRONIC PROPERTIES OF SEMICONDUCTORS

Interphase Interactions and Features of Structural Relaxation in TiB_x–*n*-GaAs (InP, GaP, 6*H*-SiC) Contacts Subjected to Active Treatment

N. S. Boltovets*, V. N. Ivanov*, R. V. Konakova^, Ya. Ya. Kudrik**,**
O. S. Litvin, P. M. Litvin**, and V. V. Milenin****
**State Enterprise Research Institute Orion, Kiev, 03057 Ukraine*
***Lashkarev Institute of Semiconductor Physics, National Academy of Sciences of Ukraine, Kiev, 03028 Ukraine*
^e-mail: konakova@isp.kiev.ua

Submitted November 18, 2003; accepted for publication November 26, 2003

Abstract—The results of experimental studies of interphase interactions in TiB_x–*n*-GaAs (GaP, InP, 6*H*-SiC) contacts stimulated by external effects are described. These effects are rapid thermal annealing at temperatures as high as 1000°C, microwave treatment at $f = 2.5$ GHz, and ^{60}Co γ radiation in the range of doses 10^5–10^7 rad. Possible thermal and athermal relaxation mechanisms of internal stresses are considered. It is shown that thermally stable TiB_x–*n*-GaAs (GaP, InP, 6*H*-SiC) interfaces can be formed. © *2004 MAIK “Nauka/Interperiodica”.*

1. INTRODUCTION

Interest in the problem of obtaining contacts with parameters that are tolerant to high-temperature treatment considerably increased when the sizes of solid-state devices became submicronic. Recent studies [1, 2] that used silicides and nitrides of refractory metals in contact-metallization systems yielded encouraging results for the improvement of their thermal stability. No less attractive for solving the above problem are films based on compounds of refractory metals with boron. Owing to specific features of the chemical bonds in these materials, they combine high thermal stability, hardness, and melting temperature with the properties inherent in materials with metal bonds [3].

The methods of fabrication of borides now developed allow one not only to vary the composition of films within a wide range, which changes the structure from amorphous to crystalline; they also combine well with microelectronic technologies [3, 4]. One of the most promising methods of production of metal borides is magnetron sputtering deposition, which makes it possible to control modification of the morphology and the electronic and atomic structure of the deposited layers [3, 5].

Despite great progress in the technology of production of TiB_x layers, the physical mechanisms of their interaction with a semiconductor substrate and the closely related features of the initiation and relaxation of stress–strain states in these spatially inhomogeneous structures have not yet been studied.

In this study, we continue the research begun in [6]. We focus our attention on the relation between the nature of the interphase interactions and the structural relaxation in TiB_x–semiconductor contacts.

2. EXPERIMENTAL

We studied TiB_x–*n*-GaAs (GaP, InP, 6*H*-SiC) structures. We used wafers of *n*-type GaAs, GaP, InP, and 6*H*-SiC single crystals with an area of 10×10 mm^2 as substrates. The GaAs, GaP, and InP substrates had a free-electron concentration of $(1–2) \times 10^{16}$ cm^{-3}; GaAs and GaP were doped with tellurium, and InP was nominally undoped. The 6*H*-SiC substrates were obtained by the Lely method and doped with nitrogen to $(1–2) \times 10^{18}$ cm^{-3}. The thickness of GaAs, GaP, and InP wafers amounts to ~350 μm, and that of 6*H*-SiC was ~420 μm.

We deposited metal contacts 70–80 nm thick on semiconductor surfaces cleaned by pulsed photon irradiation using dc magnetron sputtering of pressed TiB_2-powder targets in an Ar + N_2 atmosphere. The TiB_2-sputtering mode was chosen so that the structure of the deposited layer was close to amorphous. The contacts were exposed to rapid thermal annealing (RTA) at $T =$ 400, 600, 800, and 1000°C in a hydrogen atmosphere for 60 s; to microwave electromagnetic radiation in vacuum at $f = 2.5$ GHz and $P = 1.5$ W/cm^2; and to ^{60}Co γ-ray radiation ($E = 1.25$ MeV) with doses of 10^5–10^7 rad.

In order to study the interphase interactions and the features of the relaxation of stress–strain states in the contact-forming pairs, we used a complex of methods including Auger spectroscopy in combination with ion etching (Ar^+, $E_i = 1$ keV), X-ray phase analysis, and atomic-force microscopy (AFM). The residual stresses were measured by the X-ray method [7].

3. RESULTS AND DISCUSSION

Thin films deposited on semiconductor substrates are usually in a stressed state. This is induced by differences in the physical and mechanical characteristics of the films and substrates and by the thermal treatment to which they are subjected in technological processes [8].

Strains ε calculated from the experimentally measured radii of curvature of contact structures in the contact area of the substrate for contacts of TiB_x with various semiconductor substrates are listed in the table [7]. It can be seen that, in an initial state, the elastic strains in the contacts increase in the sequence (TiB_x–6*H*-SiC)–(TiB_x–InP)–(TiB_x–*n*-GaAs)–(TiB_x–*n*-GaP) and do not correlate with the thermal and crystallochemical properties of the semiconductor substrates [9]. This is an indication of a general feature in the mechanisms of initiation of stress–strain states in the objects under study. This feature is apparently related to the characteristics of the structural phase transitions in titanium-boride films and to the nature of their interactions with various semiconductor substrates [10].

In this case, the internal stresses in the contact structures should depend on the nature and intensity of the external factors that affect the structure of the TiB_x layers and the processes at the phase interfaces. In this study, we used thermal and athermal treatment as examples of such effects. First, we will consider the features of interphase interactions on the metal–semiconductor interface and their relation to the relaxation processes in the contacts subjected to thermal treatment.

In the table, we list data on the effect of RTA in the range 400–1000°C on the internal stresses that exist in the structures at room temperature. As follows from the table, irrespective of the relation between the linear-expansion coefficients of a TiB_x film and various semiconductor substrates and their structural parameters, the internal-stress values decrease with increasing annealing temperature. Furthermore, the relaxation processes in III–V compounds are most pronounced when annealing is conducted at about 600°C, whereas for SiC, this temperature threshold shifts to higher temperatures (≤1000°C); i.e., the dominant factors determining the internal-stress relaxation in TiB_x–III–V and TiB_x–SiC contacts are different.

Figure 1 shows AFM images of the GaAs surface after removal of a TiB_x layer. It can be seen that the interface starts to transform significantly at an RTA temperature of 600°C. The observed structural changes in the local areas of the TiB_x–GaAs interface are apparently associated with the centers of fluctuation nucleation or crystal growth in a quasi-amorphous TiB_x film (Figs. 2, 3).

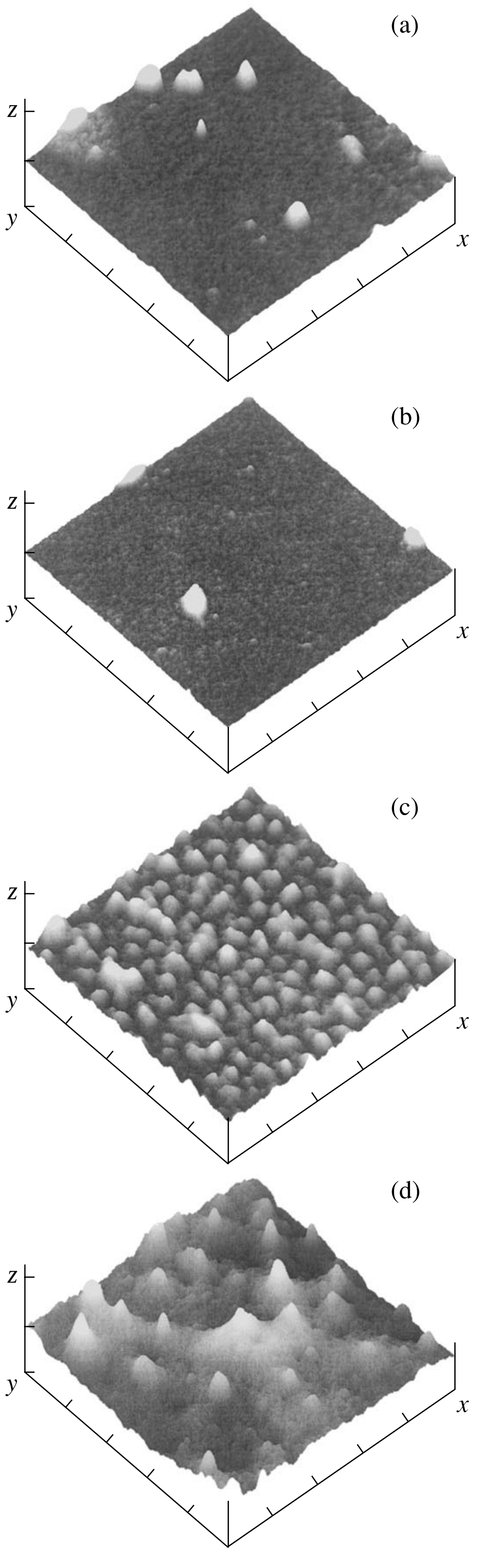

Fig. 1. Morphology of the GaAs surface on the TiB_x–*n*-GaAs interface: (a) initial sample; (b), (c), and (d) after RTA at T = 400, 600, and 800°C, respectively. The scale is 0.2 μm/division along the x and y axes and 20 nm/division along the z axis.

At crystallite-growth sites, the stresses relax and the arising stress gradient stimulates a flux of film atoms to the crystallization centers with their subsequent diffusion into the substrate over the inclusion–semiconductor phase interface.

This mechanism of relaxation of internal stresses is also confirmed by the data of the layer-by-layer Auger analysis performed for the TiB_x–InP contacts. Figure 4 shows the atomic distributions of contact-pair compo-

Strains in the TiB_x–*n*-GaAs (InP, GaP, 6H-SiC) contacts before and after exposure to external effects

Structure		ε TiB_x–GaAs	ε TiB_x–InP	ε TiB_x–GaP	ε TiB_x–SiC
RTA, 60 s	Initial	4×10^{-5}	2×10^{-5}	8×10^{-4}	7×10^{-6}
	400°C	3.8×10^{-5}	1.5×10^{-5}	7×10^{-4}	7×10^{-6}
	600°C	0.6×10^{-5}	0.7×10^{-5}	5×10^{-4}	7×10^{-6}
	800°C	0.8×10^{-5}	0.2×10^{-5}		6×10^{-6}
	1000°C				10^{-5}
Microwave	Initial	4×10^{-5}	2×10^{-5}	8×10^{-4}	6×10^{-6}
$f = 2.5$ GHz	1 s	2×10^{-5}	10^{-5}	8×10^{-4}	6×10^{-6}
$P = 1.5$ W/cm^2	10 s	0.7×10^{-5}	0.7×10^{-5}	7×10^{-4}	6×10^{-6}
γ-^{60}Co rad	Initial	3.5×10^{-5}		7×10^{-4}	7×10^{-6}
	10^5	3.5×10^{-5}		7×10^{-4}	7×10^{-6}
	10^6	10^{-5}		6×10^{-4}	5×10^{-6}
	10^7	0.5×10^{-5}		6×10^{-4}	4×10^{-6}

nents for various RTA modes. Indeed, an enhancement in diffusion begins at the same temperature (600°C).

In contrast to the TiB_x–III–V group of contacts, we observed no changes in the distributions of components at the phase interfaces for the TiB_x–*n*-6*H*-SiC contacts up to 1000°C (Figs. 5b, 5d). At the same time, the morphology of the film coating undergoes a radical transformation: a weak ordering appears in the TiB_x-film grain structure, and the dome-shaped-island fraction (Fig. 5a, 5c) increases. As was shown in [11], such modifications in the structural state of a film coating are conducive to a reduction in the average level of internal stress in the structure, although this level may possibly increase in certain local interface areas. The structural transitions into the TiB_x layers play a leading role in the relaxation of stresses in systems subjected to athermal treatment, specifically, microwave irradiation. As Fig. 6 shows, the relaxation of the stress state in a heterojunction occurs due to the formation of islands of a certain shape. The microwave radiation interacting with a thin metallized layer heats the latter and promotes these structural rearrangements. The further relaxation of stresses is associated with the coagulation of these islands and the formation of an ordered striped structure (Fig. 6c). The mechanism of decrease in intrinsic stresses for this case was thoroughly analyzed in [12].

In addition, we found that the relaxation effects were most pronounced in the TiB_x–*n*-GaAs and TiB_x–

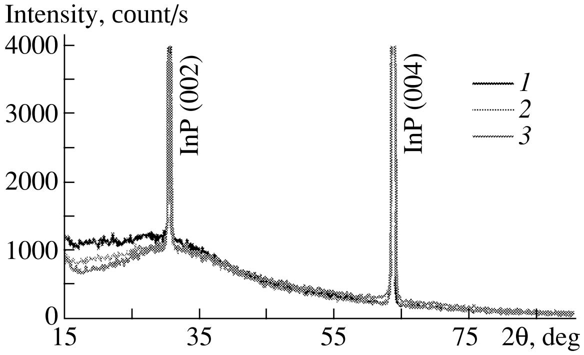

Fig. 2. X-ray diffraction patterns of the TiB_x–*n*-InP structure: (*1*) initial sample; (*2*, *3*) after RTA at T = 400 and 800°C, respectively.

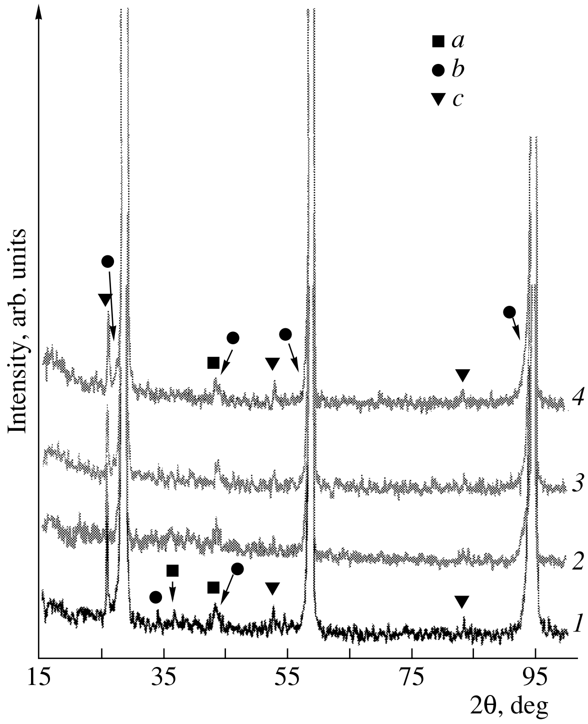

Fig. 3. X-ray diffraction patterns of the TiB_x–*n*-GaP structure: (*1*) initial sample; (*2*, *3*, and *4*) after RTA at T = 400, 600, and 800°C, respectively; (*a*) TiB ($F43m$), (*b*) TiB_2 ($P6/mmm$), and (*c*) TiO_2 ($I4_1/a$).

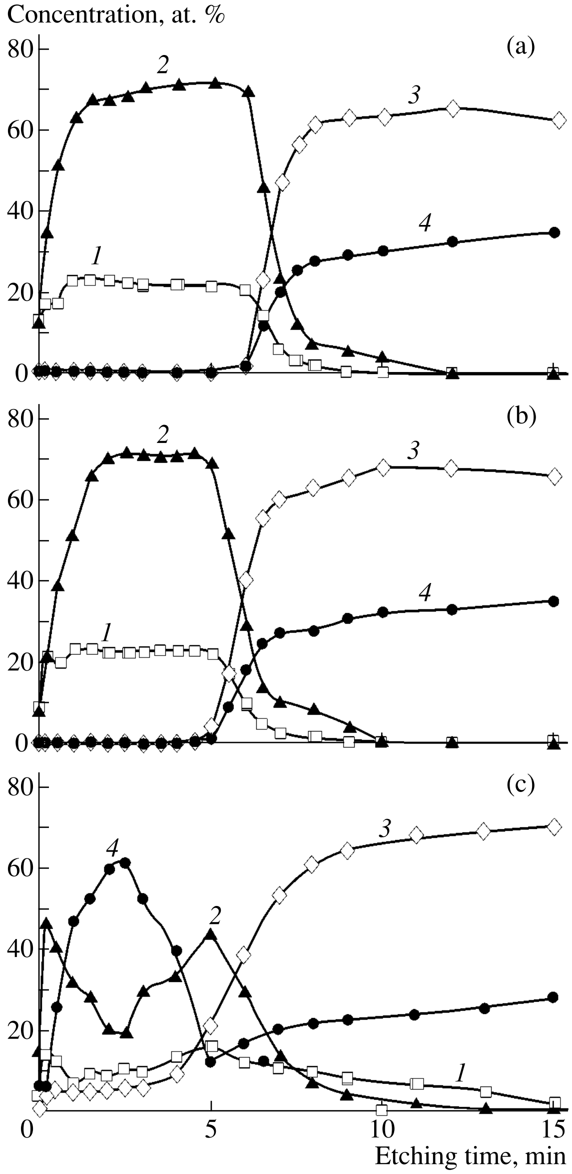

Fig. 4. Distribution of components in the TiB_x–*n*-InP contacts: (a) the initial sample; (b, c) after RTA at $T = 600$ and 800°C, respectively. (*1*) Ti, (*2*) B, (*3*) P, and (*4*) In.

n-InP structures. At the same time, the level of strains remained virtually unchanged when the TiB_x–*n*-GaP and TiB_x–*n*-6*H*-SiC contacts were subjected to microwave radiation. However, in this case we deposited thinner boride layers on the semiconductor surfaces.

In research on the contact structures formed by elemental metals and semiconductors [10, 13–15], another possibility for implementing the athermal activation of relaxation of internal stresses was realized. The results of studying the effect of γ-ray irradiation from a ^{60}Co source on the internal stresses in the TiB_x–*n*-semiconductor structures (see table) confirm the previous conclusions according to which the causes of the relaxation of stresses are radiation-stimulated mass transport at the metal–semiconductor phase interfaces [14].

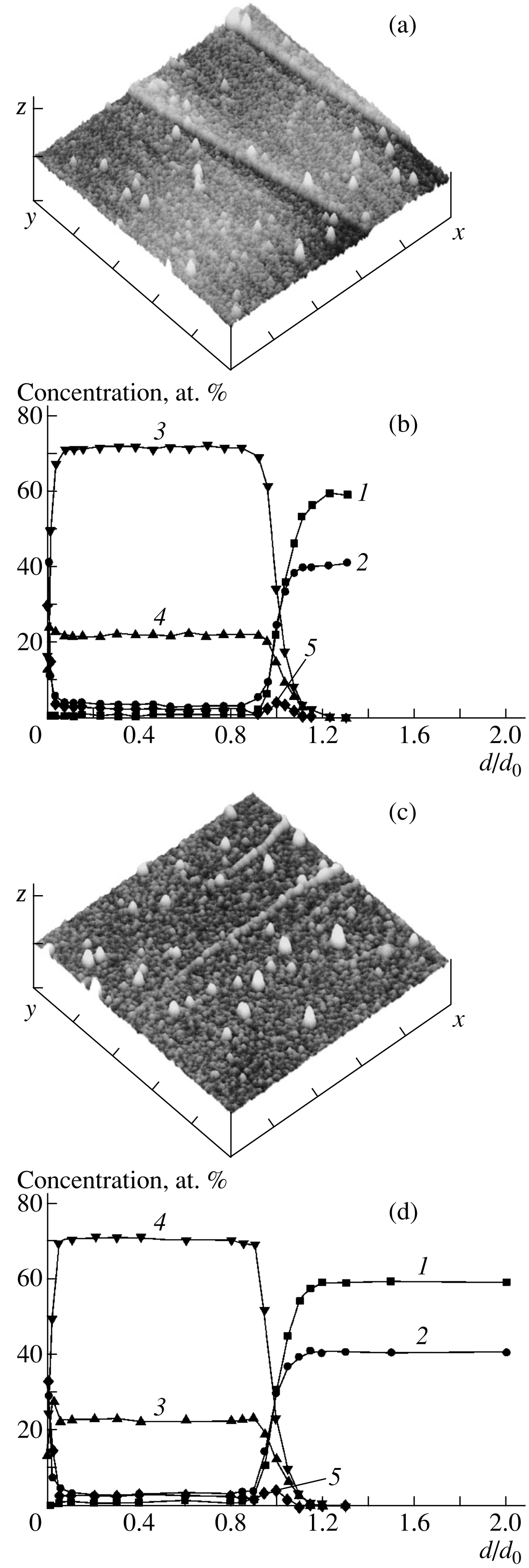

Fig. 5. Morphology of the surface of a TiB_x film on *n*-SiC-6*H* and the distribution of components in the TiB_x–*n*-SiC-6*H* contacts (a, b) before and (c, d) after RTA at $T = 1000$°C. The scale is 0.2 μm/division along the *x* and *y* axes and 20 nm/division along the *z* axis. (*1*) Si, (*2*) C, (*3*) Ti, (*4*) B, and (*5*) O.

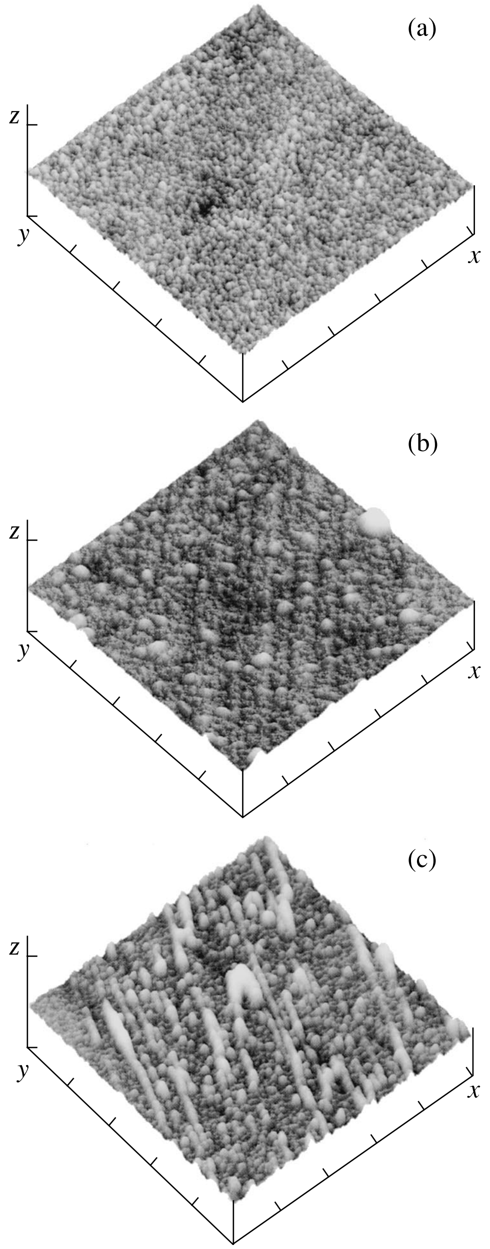

Fig. 6. Morphology of the TiB$_x$ surface on n-SiC-6H: (a) the initial sample; (b, c) after microwave treatment for 10 and 60 s, respectively. The scale is 0.2 μm/division along the x and y axes and 20 nm/division along the z axis.

Minor changes in the stress–strain state of the contacts based on GaP and SiC may be a consequence of their greater structural imperfection in the contact layers of semiconductors; higher levels of radiation are required to eliminate this phenomenon.

Thus, our complex study of the contact structures formed by TiB$_x$ with III–V compounds and SiC under thermal and athermal treatment enabled us to reveal the causes of the initiation of internal stresses in these structures and the factors affecting the relaxation of these stresses.

REFERENCES

1. L. M. Porter and R. F. Davis, Mater. Sci. Eng. B **34**, 83 (1995).
2. A. G. Baca, F. Ren, and J. C. Zolper, Thin Solid Films **308–309**, 599 (1997).
3. R. A. Andrievskiĭ, Usp. Khim. **66**, 57 (1997).
4. R. A. Andrievskiĭ, Usp. Khim. **63**, 431 (1994).
5. R. A. Andrievskiĭ, G. V. Kalinnikov, N. P. Kobelev, *et al.*, Fiz. Tverd. Tela (St. Petersburg) **39**, 1859 (1997) [Phys. Solid State **39**, 1661 (1997)].
6. E. F. Venger, V. V. Milenin, I. B. Ermolovich, *et al.*, Fiz. Tekh. Poluprovodn. (St. Petersburg) **33**, 948 (1999) [Semiconductors **33**, 865 (1999)].
7. J. K. Codwod, A. T. Nagy, and Z. Rek, Phys. Status Solidi A **34**, 705 (1976).
8. E. F. Venger, M. Grendel, V. Danishka, *et al.*, in *Structural Relaxation in Semiconductor Crystals and Device Structures*, Ed. by Yu. A. Tkhorik (Feniks, Kiev, 1994).
9. *Physical Quantities. Handbook*, Ed. by I. S. Grigor’ev and E. Z. Meĭlikhov (Énergoatomizdat, Moscow, 1991).
10. S. A. Grusha, R. V. Konakova, V. V. Milenin, *et al.*, Élektron. Tekh., Ser. 2: Poluprovodn. Prib., No. 5 (208), 68 (1990).
11. N. S. Boltovets, A. B. Kamalov, E. Yu. Kolyadina, *et al.*, Pis’ma Zh. Tekh. Fiz. **28** (4), 57 (2002) [Tech. Phys. Lett. **28**, 154 (2002)].
12. E. F. Venger, R. V. Konakova, G. S. Korotchenkov, *et al.*, in *Interphase Interactions and Degradation Mechanisms in the Metal–InP and Metal–GaAs Structures* (Nauchnaya Kniga, Kiev, 1999).
13. E. F. Venger, I. B. Ermolovich, V. V. Milenin, *et al.*, Vopr. At. Nauki Tekh., Ser.: Fiz. Radiats. Povrezhdenii Radiats. Materialoved. **B3** (75), 60 (1999).
14. J. Breza, M. Kadlecikova, R. V. Konakova, *et al.*, Appl. Phys. Lett. **67**, 1462 (1995).
15. S. A. Grusha, L. S. Khazan, R. V. Konakova, *et al.*, Thin Solid Films **215**, 50 (1992).

Translated by V. Bukhanov

Semiconductors, Vol. 38, No. 7, 2004, pp. 742–744. Translated from Fizika i Tekhnika Poluprovodnikov, Vol. 38, No. 7, 2004, pp. 775–777.

ATOMIC STRUCTURE AND NONELECTRONIC PROPERTIES OF SEMICONDUCTORS

Local Symmetry of the $Pb_{1-x}Sn_xSe$ Lattice near the Zero-Gap State

E. S. Khuzhakulov

State Pedagogical Institute of the Tashkent Region, Angren, 702500 Republic of Uzbekistan

e-mail: khuzhakulove@mail.ru

Submitted December 18, 2003; accepted for publication December 24, 2003

Abstract—By applying Mössbauer spectroscopy with isotopes ^{83}Kr and ^{119}Sn to $Pb_{1-x}Sn_xSe$ solid solutions, it is shown that the local symmetry and electronic structure of anionic and cationic lattice sites remain unchanged during the transition to the zero-gap state. *© 2004 MAIK “Nauka/Interperiodica”.*

For the $Pb_{1-x}Sn_xSe$ system in the range of compositions $0 \le x \le 0.4$, there are solid solutions with a NaCl-type lattice; for x equal to 0.30, 0.25, and 1.19 and at temperatures 300, 195, and 78 K, respectively, the inversion of the valence and conduction bands leads to the formation of the zero-gap state [1]. It is assumed that the transition of a $Pb_{1-x}Sn_xSe$ solid solution to the zero-gap state is accompanied by a change in the local symmetry of regular lattice sites. Specifically, such a change was observed in [2, 3] for $Pb_{1-x}Sn_xTe$ solid solutions using Mössbauer spectroscopy with the ^{119}Sn isotope, although more detailed Mössbauer spectroscopy studies of $Pb_{1-x}Sn_xTe$ solid solutions using the ^{67}Zn and ^{129}J isotopes have not confirmed this assumption [4, 5].

The aim of this study was to detect possible changes in the local symmetry of cationic and anionic sites in $Pb_{1-x}Sn_xSe$ solid solutions near the zero-gap state using Mössbauer spectroscopy with the ^{119}Sn (absorption version of spectroscopy) and ^{83}Se (^{83}Kr) isotopes (the emission version of spectroscopy using parent ^{83}Se atoms).

The $Pb_{1-x}Sn_xSe$ solid solutions (x = 0.02, 0.10, 0.19, 0.25, 0.30, and 0.40) were synthesized by alloying the initial components of semiconductor-grade purity in evacuated graphitized quartz cells with subsequent annealing of the samples at 500°C for 240 h. The furnace charge was prepared with an excess of selenium so that the samples had p-type conductivity (at room temperature the hole concentration was $\sim 10^{17}$ cm^{-3}). All the investigated samples were single-phase, had an NaCl-type structure, and the composition dependence of the lattice parameter a for $Pb_{1-x}Sn_xSe$ solid solutions was linear,

$$a = (6.13 - 0.12x)\ \text{Å},$$

which is consistent with the data of [6].

The samples were synthesized using metallic tin enriched with the ^{119}Sn isotope to 98% and selenium enriched with the ^{82}Se isotope to 96%. To obtain Mössbauer $Pb_{1-x}Sn_x{}^{83}Se$ sources, the corresponding samples were irradiated with a thermal neutron flux of $\sim 9 \times 10^{17}$ cm^{-2} in the water-cooled channel of a nuclear reactor.

The ^{119}Sn and ^{83}Se (^{83}Kr) Mössbauer spectra were measured using an SM-2201 spectrometer. When the ^{119}Sn absorption spectra were measured, $Ca^{119mm}SnO_3$ served as the source of gamma-ray photons (the width of the emission line at the half-height was 0.402(4) mm/s). When the ^{83}Se (^{83}Kr) emission spectra were measured, clathrate of krypton with a krypton surface density of 3 mg/cm^2 served as an absorber. The spectra were recorded at 80, 200, and 295 K, and the temperatures of the source and the absorber were equal to each other. When the ^{119}Sn spectra were measured, a set of absorbers was used with the ^{119}Sn isotope (surface densities in the range 0.02–2.0 mg/cm^2). By extrapolating the dependence [7]

$$G_{\text{exp}} = G_{\text{a}} + G_{\text{s}} + 0.27G_{\text{nat}}t$$

to $t = 0$, we determined the width G_0 of the experimental spectrum within the limits of an infinitely thin absorber. Here, $t = ns_0f$; n is the surface density of ^{119}Sn isotope absorbers; $s_0 = 1.4 \times 10^{-18}$ cm^2 is the maximum absorption cross section at resonance; G_{exp} is the width of the experimental spectrum; G_{a} and G_{s} are the widths of spectral lines of the absorber and the source, respectively; and $G_{\text{nat}} = 0.3235$ mm/s is the intrinsic ^{119}Sn line width.

Typical spectra are shown in Fig. 1 and the results of their processing are shown in Fig. 2.

The ^{119}Sn Mössbauer spectra (Fig. 1a) for all the $Pb_{1-x}Sn_xSe$ samples under study consisted of single lines whose width at half-height G_0 was about double that of the intrinsic width, $2G_{\text{nat}}$ (Fig. 2a). No anomalous changes in the magnitude of G_0 were detected in the region of the zero-gap state of the solid solution at any temperatures of the spectral measurements. We may therefore conclude that the local symmetry of cationic sites in the lattices of $Pb_{1-x}Sn_xSe$ solid solutions

1063-7826/04/3807-0742$26.00 © 2004 MAIK “Nauka/Interperiodica”

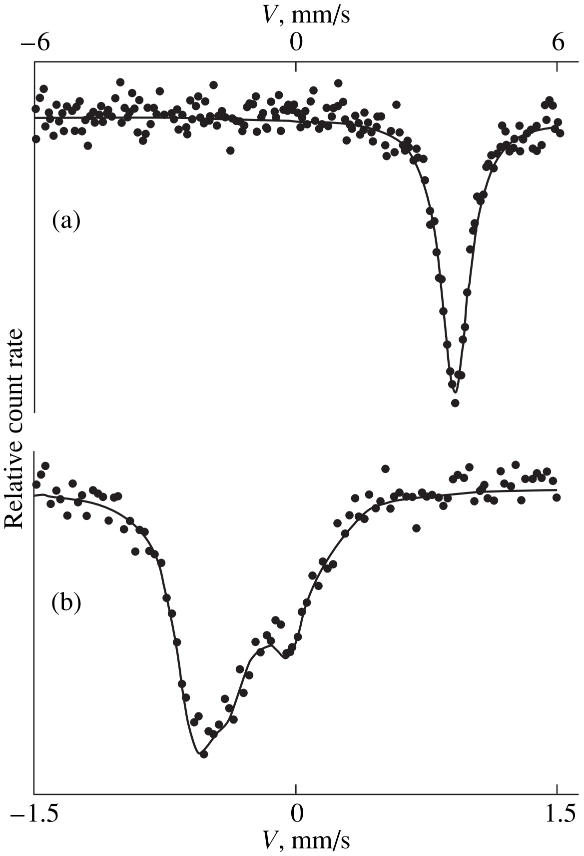

Fig. 1. Typical (a) ^{119}Sn and (b) ^{83}Se(^{83}Kr) Mössbauer spectra for the $Pb_{0.75}Sn_{0.25}Se$ solid solution at 300 K.

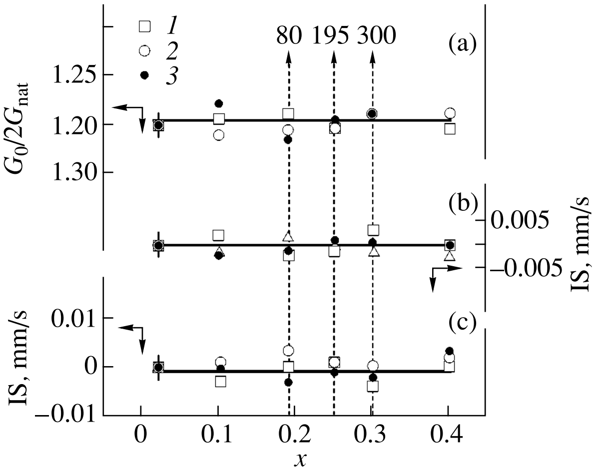

Fig. 2. (a) The line width G_0 (measured in units of double the intrinsic width $2G_{nat}$) in the experimental ^{119}Sn spectra as a function of the composition of the solid solution; (b) the isomer shift (IS) of the experimental ^{83}Se(^{83}Kr) spectra (relative to the $Pb_{0.98}Sn_{0.02}{}^{83}Se$ spectrum at the corresponding temperature) as a function of the composition of the solid solution; and (c) the isomer shift (IS) of the experimental ^{119}Sn spectra (relative to the $Pb_{0.98}{}^{119}Sn_{0.02}Se$ spectrum at the corresponding temperature) as a function of the composition of the solid solution. The measurement temperatures T are (*1*) 300, (*2*) 195, and (*3*) 80 K. Dashed straight lines indicate the compositions corresponding to the zero-gap state at 80, 195, and 300 K.

does not change in the entire range of existence of solid solutions with NaCl-type structures.

A modification of the composition of $Pb_{1-x}Sn_xSe$ solid solutions does not produce any change in the local environment of tin atoms (they have six selenium atoms in the vertices of a regular octahedron as nearest neighbors). The constancy of the isomer shift of the ^{119}Sn Mössbauer spectra of the solid solutions (Fig. 2c) is therefore not unexpected. It is important that no change in the magnitude of the isomer shift and in the range of existence of the zero-gap state was observed (see the dashed straight lines in Fig. 2), which indicates that the electronic structure of the tin atoms remains unchanged.

It can be seen in Fig. 1b that the ^{83}Se (^{83}Kr) Mössbauer spectra of $Pb_{1-x}Sn_xSe$ solid solutions are poorly resolved multiplets. The spectra should be related to isolated krypton impurity centers at selenium sites, and the appearance of the fine structure in the spectra is due to the difference between the local symmetry of krypton atoms in the absorber and the cubic symmetry: the interaction of quadrupole moments of ^{83}Kr nuclei in the ground and excited states with the electric field gradient gives rise to 11 lines whose intensities are determined by the Clebsch–Gordon coefficients. The experimental spectra can be described using the following parameters: the quadrupole interaction constant $C = eQU_{zz} = 1.252(4)$ mm/s, the asymmetry parameter of the tensor of the electric field gradient $\eta \leq 0.1$, and the width of the components of the quadrupole multiplet $G_{exp} = 0.260(4)$ mm/s. Here, Q is the quadrupole moment of the ^{83}Kr nucleus in the ground state and U_{zz} is the principal component of the tensor of the electric field gradient. These parameters are practically independent of both the composition of the solid solution and the measurement temperature. In Fig. 2b we show as an example the dependence of the isomer shift of the $Pb_{1-x}Sn_x{}^{83}Se$ spectra on the composition of the solid solution at three temperatures. It can be seen that the isomer shift of the Mössbauer ^{83}Kr probe at anionic lattice sites does not noticeably change during the transition through the zero-gap state. Note that the nuclear parameters of the ^{83}Kr probe are especially favorable for experimentally determining the changes in electron density [7].

Thus, we conclude that Mössbauer spectroscopy using ^{119}Sn and ^{83}Se (^{83}Kr) isotopes does not detect any changes either in the local site symmetry or in the electronic structure of atoms in $Pb_{1-x}Sn_xSe$ solid solutions in the domain of existence of the zero-gap state.

REFERENCES

1. L. E. Shelimova, V. N. Tomashik, and V. I. Grytsiv, *Phase Diagrams in Semiconducting Materials Science (Systems Based on Si, Ge, Sn, and Pb Chalcogenides)* (Nauka, Moscow, 1991).
2. I. N. Nikolaev, A. P. Shotov, A. F. Volkov, and V. P. Mar'in, Pis'ma Zh. Éksp. Teor. Fiz. **21**, 144 (1975) [JETP Lett. **21**, 65 (1975)].
3. I. N. Nikolaev, V. P. Potapov, A. P. Shotov, and E. E. Yurchakevich, Pis'ma Zh. Éksp. Teor. Fiz. **25**, 185 (1977) [JETP Lett. **25**, 168 (1977)].
4. V. F. Masterov, F. S. Nasredinov, S. A. Nemov, and P. P. Seregin, Fiz. Tverd. Tela (St. Petersburg) **38**, 2973 (1996) [Phys. Solid State **38**, 1625 (1996)].
5. S. A. Nemov and N. P. Seregin, Fiz. Tekh. Poluprovodn. (St. Petersburg) **36**, 914 (2002) [Semiconductors **36**, 852 (2002)].
6. N. Kh. Abrikosov and L. E. Shelimova, *Semiconducting Materials Based on IV–VI Compounds* (Nauka, Moscow, 1975).
7. S. Bukshpan, C. Goldstein, and T. Sonnino, Phys. Lett. A **27A**, 372 (1968).

Translated by I. Zvyagin

Semiconductors, Vol. 38, No. 7, 2004, pp. 745–750. Translated from Fizika i Tekhnika Poluprovodnikov, Vol. 38, No. 7, 2004, pp. 778–783.
Original Russian Text Copyright © 2004 by Kozlovskiĭ, Ivanov, Rumyantsev, Lomasov, Samsonova.

ATOMIC STRUCTURE AND NONELECTRONIC PROPERTIES OF SEMICONDUCTORS

Promotion of Metallurgical Reactions at the Ni–SiC Interface by Irradiation with Protons

V. V. Kozlovskiĭ*^, P. A. Ivanov, D. S. Rumyantsev*, V. N. Lomasov*, and T. P. Samsonova****
**St. Petersburg State Polytechnical University, Politekhnicheskaya ul. 29, St. Petersburg, 195251 Russia*
^e-mail: kozlovski@tuexph.stu.neva.ru
***Ioffe Physicotechnical Institute, Russian Academy of Sciences, Politekhnicheskaya ul. 26, St. Petersburg, 194021 Russia*

Submitted December 17, 2003; accepted for publication December 25, 2003

Abstract—It is shown that irradiation of Ni–SiC structures with protons at elevated temperatures promotes metallurgical reactions at the Ni–SiC interface owing to a diffusion mechanism stimulated by the generation of radiation defects. The most pronounced effect of mixing at the metal–semiconductor interface is observed if the thickness of the metal film is equal to the projected range of protons. © *2004 MAIK “Nauka/Interperiodica”*.

1. INTRODUCTION

As is well known, electrical properties of metal–semiconductor contacts are largely governed by the metallic and physical structure of the corresponding interfaces. For example, in order to form a nonrectifying contact of a semiconductor with a metal deposited on the semiconductor surface, thermal annealing of the metal–semiconductor structures at fairly high temperatures is typically used. During this annealing, various metallurgical reactions may take place: eutectic melting and recrystallization (solid-phase epitaxy), interdiffusion of the metal and semiconductor atoms, heterogeneous chemical reactions, and so on [1]. As for ohmic contacts to silicon carbide, the Ni–SiC contact has been most extensively studied so far [2–4]. The chemical reaction between Ni and SiC with the formation of a solid-phase product (nickel silicide) is most important in the formation of the contacts under consideration. As a rule, the contacts have an island morphology as a result of the completion of the above heterogeneous (topochemical) reaction. It is well known that topochemical reactions begin in the region of extended crystal-lattice defects (dislocations, grain boundaries, and such like) where the energy losses for the deformation of bonds are minimal and a certain free volume that facilitates the reorientation of the reacting particles exists. As a result, these reactions are very sensitive to all structural imperfections that facilitate the formation of new-phase nuclei. The reactions under consideration can be activated using thermal, mechanical, and other effects that increase the concentration of defects. Radiation effects can play an important role here.

Until recently, the main factor affecting the redistribution of metal and semiconductor atoms when metal–semiconductor structures are irradiated was thought to be the implantation of recoil atoms [5, 6]. Therefore, high-energy ions with medium or heavy masses ($M > 20$) were used in experiments; the projected path lengths (ranges) of these ions exceeded the thickness of the deposited metal layer [5–8]. In addition, the structures were irradiated only at room temperature [7–11]. However, the aforementioned ions can cause unwanted radiation damage to the semiconductor. We previously suggested and implemented another procedure for the ion-beam treatment of a metal–semiconductor interface that uses the diffusion-related, rather than implantation-related, effect [12–14]. The lightest ions (protons), for which recoil-atom implantation is insignificant, were used in the aforementioned experiments. Protons generate mainly the simplest radiation defects (vacancies and interstitial atoms), which play the role not only of structural imperfections but also of species that are conducive to the migration of the metal and semiconductor atoms. Interdiffusion of the semiconductor and metal atoms under the effect of irradiation (so-called ion-beam mixing) was made possible by the elevated temperature of the material under irradiation.

In this paper, we report the results of studying the proton-stimulated mixing of a Ni–SiC interface taking into account the effect of the spatial distribution of primary radiation defects on the mixing. To this end, we studied the effect of the proton energy and the temperature of the structure on the efficiency of the ion-beam mixing.

2. EXPERIMENTAL

In our experiments, we used commercial 6*H*-SiC crystals that were grown by the Lely method. They had *n*-type conductivity, and the concentration of uncompensated donors was $(5–7) \times 10^{18}$ cm^{-3}. Before the metal was deposited, the SiC samples were subjected to the standard chemical cleaning and were oxidized in a flow-through quartz reactor in order to reveal the polar faces. The samples were rinsed in deionized water after removal of the oxide in a 5% HF solution. Nickel films

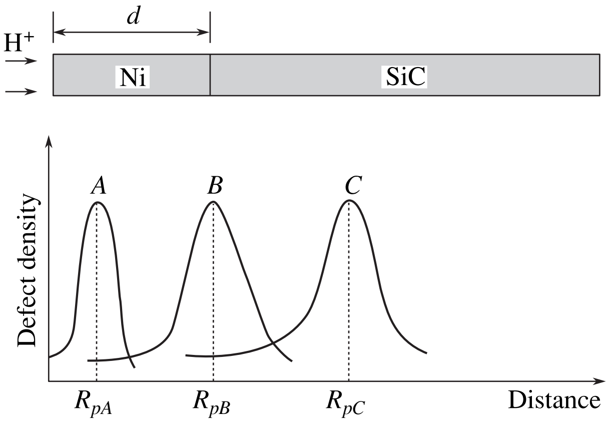

Fig. 1. Schematic representation of the irradiation of Ni–SiC structures with protons (see text for details).

were deposited on the (0001)Si face of the SiC crystals by ion-beam sputtering of a nickel target in vacuum. In order to determine the mass thickness of the deposited Ni films, we weighed the crystals before and after deposition of the film. The geometric thickness of the films was measured using a Sloan DEKTAK profilometer.

The samples were irradiated using an NG-200U accelerator. The proton energy in the beam could be varied in the range 10–100 keV, and the dose of protons could be varied from 10^{16}–5×10^{17} cm^{-2} (the current density in the beam was 5 mA/cm^2). We used protons with three energies for which the proton mean projected range (R_p) was smaller, equal to, or larger than the film thickness d. The temperature of the sample during irradiation was in the range 650–750°C. These temperatures are 250–300°C lower than those typically used for the thermal fusion of Ni into SiC (900–1000°C) in the formation of an ohmic contact to SiC [15, 16].

If we compare the degree of localization of the effect of different ions on solids (the degree of localization of ion distribution is typically identified as the ratio between the ion range and the ion-range straggling), we realize that protons have an advantage over ions of light mass (such as boron, neon, etc.) by approximately a factor of 2 and over ions of medium mass (phosphorus, argon, etc.) by a factor of 3 (for the same ion energy) [17]. These potentials of proton-beam irradiation are unique compared to other ions and make it possible to carry out experiments even with thin-layer structures in which the generation of the main amount of radiation defects is located in three different regions of the metal–semiconductor structure (Fig. 1): in the metal film (scheme *A*), at the metal–semiconductor interface (scheme *B*), and in the semiconductor bulk (scheme *C*). Radiation-induced semiconductor damage is not observed in region *A*. As a result, the effect of radiation defects on the electrical characteristics of the contacts is ruled out in this region (it is well known that radiation defects can considerably reduce the electrical conductivity of n-SiC [14]). Measurements of the current–voltage characteristics of irradiated samples showed that the Ni films deposited almost completely screen SiC from protons under the condition that the mass thickness of the film is $3\sigma_p$ greater than the projected proton range R_p, where σ_p is the straggling of the range distribution described by the type-IV Pearson function [18]. We used nickel films with a thickness of 167 ± 5 nm (a mass thickness of about 134 nm) in our experiments. Using the standard TRIM software package [19], we calculated the proton energy for which R_p is equal to about 1/3 of the film thickness. This energy was found to be equal to 10 keV. The localization of the energy deposition at such low energies deteriorates to a such an extent (even in the case of protons) that it becomes difficult to satisfy the condition that the proton range be smaller than the film thickness by at least $3\sigma_p$. Therefore, in the experiments carried out according to scheme *A* we chose a proton energy of 40 keV; the projected range of protons and, accordingly, the range-distribution straggling were reduced by using an oblique incidence of the proton beam onto the sample at an angle of 15° (the projected range of protons in nickel in this case was 50 nm, and the range-distribution straggling was 13 nm). For the experiments according to scheme *B*, we chose the same proton energy (40 keV), and the irradiation was performed at the normal incidence of the beam on the sample, so that the projected range of protons was 160 nm and the straggling, 45 nm. Irradiation according to scheme *C* was carried out with 100-keV protons at the normal angle of incidence. In this case, the proton range far exceeded the thickness of the metal film and was estimated to be 500 nm (the straggling was about 150 nm).

Redistribution of the metal and semiconductor atoms as a result of proton irradiation was studied using Auger spectroscopy with layer-by-layer sputtering of the material by the argon beam. We measured the concentration profiles of silicon, carbon, and nickel. The amplitude of the silicon signal was determined from the 92-eV energy line; that of the carbon signal, from the 272-eV line; and that of the nickel signal, from the 848-eV line.

3. RESULTS AND DISCUSSION

In Figs. 2a–2c, we show the Auger profiles for the distribution of Si, C, and Ni in the samples irradiated with protons for 30 min at a temperature of 750°C according to schemes *A*, *B*, and *C*, respectively. The concentration profiles for the same elements in the control part of the samples that was protected against the penetration of protons are shown in Fig. 2d. As can be seen, the metallurgical reactions proceeded at relatively low rates in the unirradiated part of the samples. In contrast, interdiffusion and chemical reactions proceeded with a much greater rate in irradiated crystals. It is noteworthy that two clearly pronounced regions appear in the contact structure according to the Auger profiles:

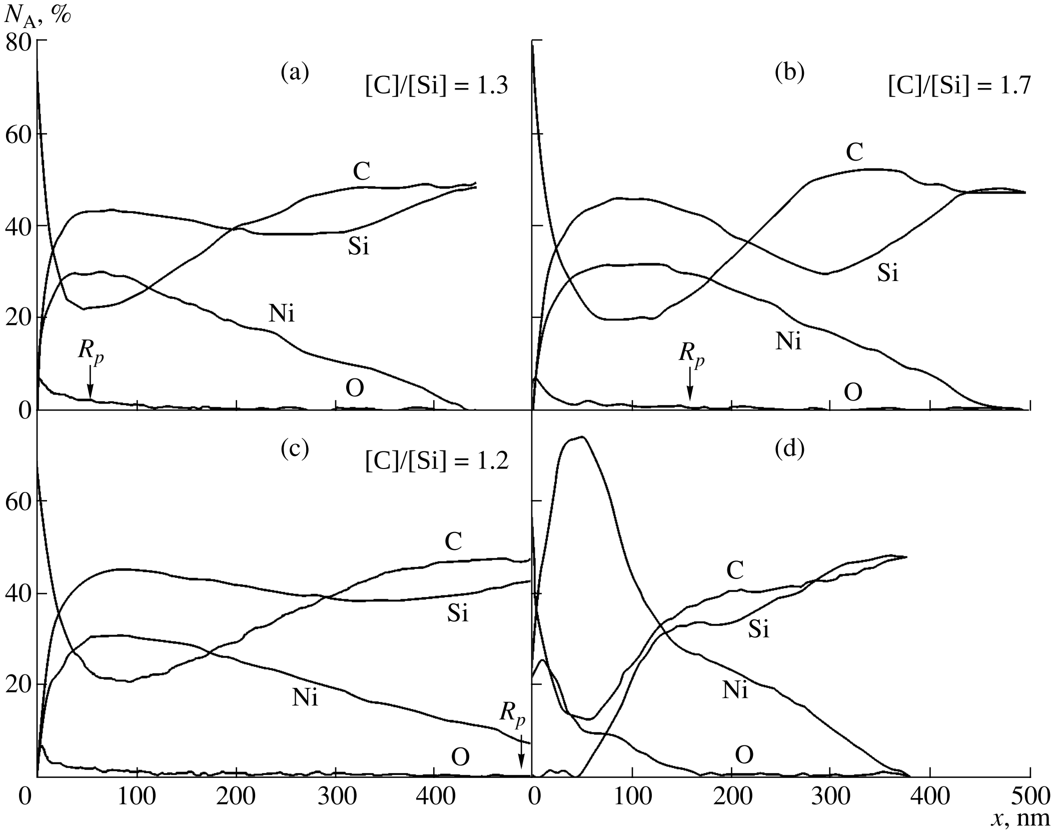

Fig. 2. Auger concentration profiles for Si, C, Ni, and O in (a–c) irradiated and (d) unirradiated structures. The relative content of a particular component N_A is plotted on the vertical axis, while the depth of etching with an argon beam is plotted on the horizontal axis. The values of the [C]/[Si] ratio in the disordered region are given in panels a–c; arrows indicate the projected ranges R_p of protons. The samples were irradiated with protons according to schemes (a) *A*, (b) *B*, and (c) *C* (see Fig. 1).

the first region corresponds to a layer of disordered SiC that is highly enriched with carbon and has a high concentration of nickel (this layer is on top of stoichiometric SiC); the second region corresponds to a layer that constitutes a mixture of nickel silicides (NiSi and $NiSi_2$) with a substantial content of carbon. It is noteworthy that a very thin carbon layer (with a surface concentration of ~10^{16} cm^{-2}) can appear even at the metal surface. Most likely, the origination of this layer is related either to the deposition of carbon on the surface of the material in the course of annealing in vacuum [20] or to the effect of outdiffusion [1], i.e., anomalous diffusion of carbon to the outer surface of the nickel layer. The largest ratio between the concentrations of carbon and silicon ([C]/[Si]) in the damaged layer can be used as the criterion for mixing the metal and semiconductor atoms at the interface. As can be seen from a comparison of the profiles shown in Fig. 2, irradiation enhances the processes of the metal–semiconductor interdiffusion. The degree of mixing depends on the section of the structure in which protons are stopped down: the ratio [C]/[Si] = 1.3 if the structure is irradiated according to scheme *A*; this ratio increases to 1.7 if scheme *B* is used; and the ratio is reduced to 1.2 if the irradiation is carried out according to scheme *C*. Thus, it is clear that irradiation with protons stimulates ion-beam mixing. The contribution of this mixing to interdiffusion is largest when the mean projected range of protons coincides with the thickness of the nickel film, i.e., when the region where the most intense generation of primary defects occurs coincides exactly with the metal–semiconductor interface. Note that here we are referring to the mass thickness of the films, which was about 15–20% smaller than the linear thickness of the films because of their porosity.

In Table 1, we list data on the relative contribution of ion-beam mixing to interdiffusion in relation to the temperature and duration of irradiation. On the one hand, an increase in the sample temperature during irradiation from 700 to 750°C (with the irradiation duration retained at 30 min) led to an increase in the contribution of ion-beam mixing to interdiffusion by a factor of 2. On the other hand, an increase in the duration of irradiation from 10 to 30 min (at the same sample temperature of 750°C) led to an increase in the relative contribution of ion-beam mixing to interdiffusion by more than a factor of 10.

The temperature dependence of the contribution of ion-beam mixing to interdiffusion is more indicative of

Table 1. Comparison of the relative contribution of ion-beam mixing to interdiffusion at the Ni–SiC interface under various conditions of irradiation

Sample no.	Conditions of treatment	Relative magnitude of ion-beam mixing, %
1	750°C, 10 min	4
2	700°C, 30 min	22
3	750°C, 30 min	54

migration-related mechanisms (proton-enhanced diffusion [6]) than a mechanism related to the implantation of recoil atoms. Moreover, silicon diffuses more rapidly into nickel than nickel does into silicon carbide during irradiation, as can be seen from a comparison of the Auger profiles in Fig. 2. This may be explained by the fact that the mechanism of diffusion is apparently ascending and is described by the equation [21, 22]

$$\frac{1}{F}\frac{\partial C}{\partial t} = V(x)\frac{\partial^2 C}{\partial x^2} - C(x)\frac{\partial^2 V}{\partial x^2}, \qquad (1)$$

where $F = \lambda^2\psi$ (here, λ is the diffusion-hop length and ψ is the probability of migration) and C and V are the concentrations of the diffusing atoms and vacancies, respectively. Equation (1) differs from the conventional Fick equation in that it has an additional second term: a nonuniform distribution of vacancies leads not only to a coordinate dependence of the impurity-diffusion coefficient but also to a change in the diffusion equation itself. The physical meaning of the second term in the diffusion equation for conditions of nonuniform generation of radiation defects consists in the following. If diffusion occurs via the vacancy mechanism, each hop of an atom is accompanied by a hop of the vacancy in the opposite direction. The resulting vacancy flux is in the opposite direction to that of the migration of atoms. Therefore, the formation of a depth-dependent vacancy concentration is similar to the appearance of a driving force and, consequently, to the appearance of a drift flow of atoms that is proportional to the gradient of the vacancy concentration. The vacancy concentration is required in order to solve Eq. (1) and can be determined from the following continuity equation for vacancies:

$$\frac{\partial V}{\partial t} = D_V\frac{\partial^2 V}{\partial x^2} + G(x) - kV. \qquad (2)$$

Here, the first term on the right-hand side of Eq. (2) describes the vacancy diffusion with the diffusion coefficient D_V, the second term describes the vacancy generation, and the third term describes the vacancy recombination ($k = 1/\tau_V$ is the recombination coefficient for vacancies and τ_V is the lifetime of vacancies). If the diffusion of radiation defects is taken into account, the distribution of these defects at a depth $x \gg R_p$ becomes exponential [14]:

$$V = V_0 \exp\left(-\frac{|x - R_p|}{L_V}\right), \qquad (3)$$

where

$$L_V = (D_V\tau_V)^{1/2}$$

is the diffusion length of a radiation defect. It can be seen from Eqs. (1) and (2) and formula (3) that the quantity L_V controls to a great extent the intensity of diffusion processes at the interface. Since the highest concentration of radiation defects (vacancies) is generated in the nickel film (schemes *A* and *B*), it is reasonable to assume that the flux of silicon atoms into the zone with increased concentration of defects exceeds the flux of nickel atoms from this zone. The diffusion of nickel is enhanced somewhat only at high proton energies (scheme *C*), in which case the defects are mainly produced in the semiconductor. The coefficients of nickel diffusion into silicon carbide were estimated from the concentration profiles shown in Fig. 2; the estimates are 7.6×10^{-14} cm^2 s^{-1} (scheme *A*), 15.6×10^{-14} cm^2 s^{-1} (scheme *B*), and 28.4×10^{-14} cm^2 s^{-1} (scheme *C*). The diffusion length of defects L_V plays an important role in a situation where impurities migrate via the lattice sites (according to the vacancy mechanism). Specifically, it follows from Eq. (1) that the distance between the zone of the most intense generation of radiation defects (R_p) and the metal–semiconductor interface (d) should not exceed (1–2)L_V for efficient ascending diffusion at $d < R_p$. In the case under consideration, the quantity L_V is about 50 nm (which corresponds closely to the known values of L_V in silicon [23]). Furthermore, the value of L_V also imposes a restriction on the lowest allowable energies of incident protons: the projected range R_p should exceed L_V. If this condition is not satisfied, the generated defects drain to the outer surface of the metal film and recombine at this surface. In that case, the radiation-related factor no longer plays an important role in the processes of migration. We can use the data obtained to make certain assumptions about the mechanism of ion-beam mixing. In the first stage of the process, the incident particle causes a displacement of the metal and/or semiconductor atoms from the sites of the corresponding lattices. The displaced atoms then migrate over vacancies or interstices, possibly with a smaller (relative to conventional thermal diffusion) value of the activation energy.

In conclusion, we will discuss certain aspects related to the mechanism of formation of the nonrectifying characteristic of ohmic Ni–SiC contacts and the possible effect of ion-beam mixing on this mechanism. In Table 2, we list certain data on the characteristics of the contacts obtained.

First, a necessary condition for attaining a nonrectifying characteristic is the formation of a disordered

Table 2. Comparison of electrical characteristics of Ni–SiC contacts after irradiation under different conditions

Sample no.	Metallization	Conditions of treatment	[C]/[Si]	Contact resistance, Ω cm^2
1	Ni: 170 nm	750°C, 10 min	2	6.6×10^{-4}
2	Ni + Si: (90 + 200) nm	750°C, 10 min	<1	Rectifying
3	Ni: 170 nm	700°C, 30 min	1.7	Rectifying
4	Ni: 170 nm	750°C, 30 min	2.6	1.7×10^{-3}

region in silicon carbide, which occurs owing to the exit of silicon from SiC. In order to verify this assumption, we specially fabricated Ni–Si–SiC structures in which the silicon film efficiently prevented silicon from leaving the SiC. Measurements showed that the Ni–SiC contacts (sample 1), in which a heavily damaged region was formed ([C]/[Si] ≈ 2), had a nonrectifying characteristic. In contrast, the Ni–Si–SiC contacts (sample 2), in which there is no such damaged layer ([C]/[Si] < 1 in the transition region), had a rectifying characteristic under the same conditions of treatment.

Second, although disordering of the SiC surface layer is a necessary condition, it is not enough for the contact to be nonrectifying. This conclusion follows from a comparison of Ni–SiC contacts irradiated at 700°C (sample 3) and 750°C (sample 1). The Auger profiles of Si, C, and Ni in these samples differ from each other only slightly; however, contact 3 was found to be rectifying, whereas contact 1 was ohmic.

Third, it should be emphasized that a heavy disordering also detrimentally affects the characteristics of the contacts. Indeed, contacts 4 ([C]/[Si] ≈ 2.6) have a higher interfacial resistance than that of contact 1, in which the degree of disordering is lower ([C]/[Si] ≈ 2). It is noteworthy that a similar pattern is also observed in the case of conventional thermal annealing: a minimum in the dependence of the contact resistance on the annealing temperature is observed at a temperature of about 1000°C [24]. Furthermore, the contacts fused at temperatures higher than 1000°C have weak adhesion due to an excess concentration of carbon at the interface.

The most plausible explanation for the above trends in the formation of nonrectifying Ni–SiC contacts is based on the assumption that a thermally activated structural modification of the defects occurs at a temperature of 750°C or above. This modification gives rise to electrically active donor centers of the vacancy type. In this case, the mechanism of charge transport is either macrofield tunneling emission of charge carriers or space-charge-limited currents in an insulator with trapping donor centers. The assumption that it is the donor centers that are formed during the fusing of nickel is confirmed by the fact that, in contrast to *n*-SiC, nickel does not form an ohmic contact to *p*-SiC (even at high temperatures of fusing). This observation is consistent with the fact that the Auger profiles of the Si, C, and Ni concentrations in these contacts are indicative of the formation of both nickel silicide and a disordered region [25]. The idea that there are thermally activated donor centers in SiC can also be used to explain the fact that the contact resistance increases as a result of heavy disorder: the structural modification of defects may be less efficient in this case.

4. CONCLUSION

Irradiation of Ni–SiC structures with protons at elevated temperatures (700–750°C) enhances the diffusion of silicon from SiC into a nickel film owing to the mechanism of ascending diffusion stimulated by the production of radiation defects in the nickel film. The most intense mixing is attained when the thickness of the metal film is equal to the projected range of protons, i.e., when the maximum of the depth distribution of radiations defects is located at the interface. In that case, the relative contribution of ion-beam mixing to the migration processes at the Ni–SiC interface can exceed 50%. Apparently, a nonrectifying characteristic of Ni–SiC contacts can be obtained only because of the combined effect of two factors: the disordering of silicon carbide (due to an exit of silicon from SiC) and a thermally activated structural modification of the disordered region. As a result of this modification, electrically active donor centers are formed.

REFERENCES

1. *Thin Films—Interdiffusion and Reactions*, Ed. by J. M. Poate, K. N. Tu, and J. W. Mayer (Wiley, New York, 1978; Mir, Moscow, 1982).
2. K. Robbie, S. T. Jemander, N. Lin, *et al.*, in *Proceedings of the ICSCRM-1999* (Research Triangle Park, North Carolina, USA, 1999); Mater. Sci. Forum **338–342**, 981 (2000).
3. T. Nakamura, H. Shimada, and M. Satoh, in *Proceedings of the ICSCRM-1999* (Research Triangle Park, North Carolina, USA, 1999); Mater. Sci. Forum **338–342**, 985 (2000).
4. T. Toda, Y. Ueda, and M. Sawada, in *Proceedings of the ICSCRM-1999* (Research Triangle Park, North Carolina, USA, 1999); Mater. Sci. Forum **338–342**, 989 (2000).
5. R. Kelly and J. B. Sanders, Surf. Sci. **57**, 143 (1976).
6. K. B. Winterborn, Radiat. Eff. **49**, 97 (1980).
7. J. W. Mayer, B. Y. Tsaur, S. S. Lau, and L. S. Hung, Nucl. Instrum. Methods **182–183**, 1 (1981).
8. D. B. Poker and B. R. Appleton, J. Appl. Phys. **57**, 1414 (1985).
9. D. K. Sarkar, S. Dhara, K. G. M. Nair, and S. Chaudhury, Nucl. Instrum. Methods Phys. Res. B **161**, 992 (2002).
10. *Surface Modification and Alloying by Laser, Ion, and Electron Beams*, Ed. by J. M. Poate, G. Foti, and D. C. Jacobson (Plenum, New York, 1983).
11. *Ion Beam Modification of Materials*, Ed. by J. S. Williams, R. G. Elliman, and M. C. Ridgway (North-Holland, Amsterdam, 1996).

12. V. V. Kozlovskiĭ and V. N. Lomasov, Poverkhnost **3**, 146 (1987).
13. V. V. Kozlovskiĭ, V. A. Kozlov, and V. N. Lomasov, Fiz. Tekh. Poluprovodn. (St. Petersburg) **34**, 129 (2000) [Semiconductors **34**, 123 (2000)].
14. V. V. Kozlovskiĭ, *Modification of Semiconductors by Proton Beams* (Nauka, St. Petersburg, 2003).
15. L. Calcagno, E. Zanetti, F. La Via, *et al.*, Mater. Sci. Forum **433–436**, 721 (2003).
16. J. J. Bellina and M. V. Zeller, in *Novel Refractory Semiconductors*, Ed. by D. Emin, T. L. Aselage, and C. Wood (Mater. Res. Soc., Pittsburg, PA, 1987), p. 265.
17. H. H. Andersen and J. F. Ziegler, *Hydrogen Stopping Powers and Ranges in All Elements* (Pergamon, New York, 1977).
18. A. F. Burenkov, F. F. Komarov, M. A. Kumakhov, and M. M. Temkin, *Spatial Distribution of Energy Released in a Collision Cascade in Solids* (Énergoatomizdat, Moscow, 1985).
19. J. P. Biersack and L. G. Haggmark, Nucl. Instrum. Methods **174**, 257 (1980).
20. M. J. Morschbacher and M. Behar, J. Appl. Phys. **91**, 6481 (2002).
21. Y. Morikawa, K. Yamamoto, and K. Nagami, Appl. Phys. Lett. **36**, 997 (1980).
22. R. Sh. Malkovich, *Mathematics of Diffusion in Semiconductors* (Nauka, St. Petersburg, 1999).
23. E. W. Maby, J. Appl. Phys. **47**, 830 (1976).
24. M. G. Rastegaeva, A. N. Andreev, and A. I. Babanin, in *Abstracts of 2nd International Seminar on Semiconductor SiC and Related Materials* (Novgorod, Russia, 1977), p. 38.
25. A. N. Andreev, M. G. Rastegaeva, A. I. Babanin, and N. S. Savkina, in *Abstracts of 2nd International Seminar on Semiconductor SiC and Related Materials* (Novgorod, Russia, 1977), p. 36.

Translated by A. Spitsyn

Semiconductors, Vol. 38, No. 7, 2004, pp. 751–757. Translated from Fizika i Tekhnika Poluprovodnikov, Vol. 38, No. 7, 2004, pp. 784–790.
Original Russian Text Copyright © 2004 by Biryulin, Kosheleva, Turinov.

Study of the Electrical Properties of $Cd_xHg_{1-x}Te$

P. V. Biryulin*, V. I. Kosheleva, and V. I. Turinov
State Research and Production Corporation Istok, Fryazino, Moscow oblast, 141190 Russia
**e-mail: birulin@sl.ru*

Submitted August 27, 2003; accepted for publication October 17, 2003

Abstract—On the basis of the temperature and field dependences of the Hall coefficient R_H, it was found that samples with a low electron density are, as a rule, compensated, and the degree of compensation changes upon thermal conversion of the conductivity of the sample to *p* type. For *n*-$Cd_xHg_{1-x}Te$, the ionization energy of the donor level was found from the temperature dependences of resistivity $\rho(T)$: E_d = 24–32 meV. For the same samples, after their thermal conversion to *p* type, the ionization energies of acceptors, which are related to doubly charged vacancies V_{Hg}^{++}, were determined: E_a = 32 and 48 meV. In addition, a deep level E_t, related to an unknown amphoteric impurity, was found ($E_t - E_V \approx 0.7E_g$). *© 2004 MAIK “Nauka/Interperiodica”.*

The ternary solid solution $Cd_xHg_{1-x}Te$ with *p*-type conductivity is more appropriate for fabricating high-speed IR photodiodes operating in the frequency region above 100 MHz with a maximum sensitivity at wavelength $\lambda = 10.6$ μm than the same material with *n*-type conductivity [1–4], since the former is characterized by a high mobility of minority carriers (electrons) in the *p*-type base of n^+–*p* junctions. Because we used *n*-$Cd_xHg_{1-x}Te$ samples specially intended for photoresistors as starting samples, we subjected them to thermal treatment in order to convert their conductivity and then, using ion implantation, form n^+–*p* junctions in the *p*-type samples obtained. The aim of this study was to track changes in the initial electrical properties of *n*-$Cd_xHg_{1-x}Te$ samples subjected to thermal treatment and determine the effect of these changes on the parameters of the n^+–*p* junctions formed in these samples.

The initial wafers had an irregular shape; therefore, the Hall constant R_H and resistivity ρ were measured using the van der Pauw method. The temperature dependences $R_H(T)$ and $\rho(T)$ and the magnetic field dependences $R_H(B)$ and $\rho(B)$ were measured at a constant current in a constant magnetic field on a system with automatic reading and processing of signals [5]. The lifetime of charge carriers τ was determined from the pulsed characteristics of the photoresponse from samples illuminated by ultrashort ($\sim 8 \times 10^{-9}$ s) pulses of a CO_2 laser at wavelength $\lambda = 10.6$ μm. The peak power ($\sim 3 \times 10^3$ W) was attenuated by scatterers. The characteristics measured were recorded on a C8-12 universal storage oscilloscope.

The starting *n*-CdHgTe wafers were $d \approx 800$ μm thick and up to 20 mm in size (with irregular shape). The wafers were cut into several samples, on which electric and photoelectric characteristics were measured before and after the conversion annealing. The annealing conditions were the same for all the samples: temperature $T_a = (300 \pm 5)$°C and duration $t = (30 \pm 1)$ min; the annealing was performed in mercury vapor in glass cells evacuated by a backing pump. It is known [6] that, after isothermal annealing at temperatures above 300°C, $Cd_xHg_{1-x}Te$ solid solutions with $x \approx 0.2$ have *p*-type conductivity. It is also known [7] that the conversion from *n*- to *p*-type conductivity occurs in these compounds when they are heated for a short period at temperatures above 300°C with subsequent quenching. It is believed that under such conditions mercury vacancies V_{Hg}, which are acceptors, are responsible for the *p*-type conductivity [8, 9].

Table 1 lists the parameters of the starting *n*-type samples and the *p*-type samples obtained by conversion annealing: the electron and hole densities *n* and *p*, mobilities μ_n and μ_p, and lifetimes τ_n and τ_p.

Samples cut from the same *n*-type starting wafer showed similar dependences $R_H = f(B)$. However, after annealing under the same conditions, a significant spread in the values of R_H was observed for the *p*-type samples (typical dependences are shown in Fig. 1). Thus, we may conclude that the starting *n*-type wafers had a high degree of compensation of donor and acceptor point defects (including residual impurities). This conclusion is confirmed by the concentration dependence of the electron Hall mobility $\mu_n = f(n)$ (Fig. 2). According to this dependence, the decrease in *n* is due to the compensation of impurities, which enhances the scattering of charge carriers by ionized impurities and intrinsic point defects [10, 11]. The compensation is highly inhomogeneous over the starting wafer and changes upon annealing. The spread in R_H, as well as the spread in the hole Hall mobility $\mu_p = f(p)$ (Fig. 3), decreases in *p*-type samples only at $p > 1 \times 10^{16}$ cm^{-3}, when intrinsic point defects of acceptor type (vacancies V_{Hg} and V_{Cd} [13]) in high concentrations were formed by annealing.

Table 1. Electrical parameters of $Cd_xHg_{1-x}Te$ samples with *n*- and *p*-type conductivity (before and after conversion annealing, respectively)

Sample	*n* type				*p* type				*d*, μm	$b \times l$, cm^2
	n, cm^{-3}	μ_n, 10^5 cm^2 V^{-1} s^{-1}	τ_n, 10^{-7} s	λ_{co}, μm	*p*, cm^{-3}	μ_p, 10^5 cm^2 V^{-1} s^{-1}	τ_p, 10^{-8} s	λ_{co}, μm		
A1	9.5×10^{13}	1.83	3.0	10.4	1.1×10^{15}	447	7	10.2	813/580	1×1
A2	1.19×10^{14}	1.84	–	–	5.3×10^{14}	647	–	10.27	825/660	0.7×1.1
A3	1.04×10^{14}	1.77	–	10.2	9.6×10^{15}	401	1	9.9	834/675	0.5×0.8
A4	1.3×10^{14}	2.15	–	–	1.7×10^{16}	452	–	–	811/558	0.9×1.1
B3	6.1×10^{13}	1.6	2	10.29	1.5×10^{16}	523	10	–	854/619	0.8×2.0
B4	6.2×10^{13}	1.6	–	10.4	6.6×10^{14}	520	–	10.87	817/–	0.6×1.2
C1	1.1×10^{14}	1.9	1.5	10.1	1.0×10^{16}	463	3	10.2	743/636	0.8×1.1
C2	1.1×10^{14}	2.0	–	9.9	1.8×10^{16}	410	–	–	844/719	0.6×1.7
C3	1.2×10^{14}	1.83	2.5	–	7.2×10^{16}	400	–	–	835/605	0.7×1.7
C4	8.5×10^{13}	1.8	–	–	5.5×10^{14}	632	–	9.8	840/676	0.7×1.1
D1	5.5×10^{14}	1.87	–	11.7	1.8×10^{16}	491	4	–	830/504	0.7×1.1
D2	5.0×10^{14}	1.9	2.5	11.3	9×10^{14}	471	–	10.96	–	–
					1.8×10^{15}	320	–	12.42	–	–
					1.7×10^{16}	436	6	12.29	829/494	0.6×1.2
G1	1.59×10^{14}	2.5	5	12.01	2.8×10^{16}	492	8	12.6	807/505	0.8×1.0
G2	1.73×10^{14}	2.43	–	12.26	1.0×10^{15}	631	–	12.4	671/–	0.6×0.9
G3	1.73×10^{14}	2.57	–	12.75	1.05×10^{15}	621	–	12.49	806/687	0.6×0.9
H1	1.5×10^{14}	2.6	1.6	13.88	1.8×10^{15}	658	–	–	674/–	0.7×1.2
K1	1.78×10^{14}	2.3	–	12.75	1.68×10^{15}	565	–	12.45	765/386	0.6×1.2
K2	1.78×10^{14}	2.27	–	12.85	1.46×10^{15}	601	–	–	777/392	0.7×0.9

Note: λ_{co} is the boundary wavelength in the photoconductivity spectrum; *b* and *l* are the sample width and length, respectively. The *d* column contains the thicknesses of samples in the initial (*n*-type) state and (after a slash) after conversion annealing (to the *p*-type) with subsequent removal of the surface layer by etching.

The dependence $\rho = f(T)$ (Fig. 4) was used to determine the ionization energies of donor levels (E_d) in *n*-CdHgTe before annealing and acceptor levels (E_a) in *p*-CdHgTe after the conversion annealing (Table 2). For one of the samples (C1), the following relation was obtained: $E_d + E_a = E_g$ (E_g is the band gap width); i.e., the same level manifests itself in both the *n*-type material before annealing and the *p*-type material obtained after annealing. Intrinsic point defects in the sublattices of either the metal or chalcogen behave as either donors or acceptors. Therefore, the level found is related to an impurity that is amphoteric in CdHgTe. There are no data in the literature on such behavior of impurities in CdHgTe (which is a narrow-gap semiconductor).

Table 2. Composition and parameters of the energy-band structure of samples

Sample	*n* type				*p* type
	E_g (78 K), eV	E_d, eV	*n* (78 K), 10^{14} cm^{-3}	composition, *x*	E_a, eV
A1	0.119	0.024	0.95	0.216	0.048
A2	0.121	0.024	1.0	0.217	0.032
B3	0.120	0.032	0.61	0.216	–
B4	0.120	–	0.62	0.217	–
C1	0.120	0.027	1.5	0.216	0.094
C2	0.125	0.023	1.1	0.220	–

The values of E_g at 78 K listed in Table 2 were found from the spectral characteristics of photoconductivity measured for *n*-type samples: $E_g(78\text{ K}) = 1.24/\lambda_{co}$, where λ_{co} is the boundary wavelength (in μm) in the photoconductivity spectrum at a level of 0.5 of the maximum photosensitivity (Table 1). Using the expression $E_g = -0.302 + 1.93x + 5.35 \times 10^{-4}(1 - 2x)T - 0.810x^2 + 0.832x^3$ [14] (*T* and E_g are measured in K and eV, respectively), we find the atomic fraction *x* for $Cd_xHg_{1-x}Te$ samples; these data are also listed in Table 2.

The strong magnetic field dependence of the transverse magnetoresistance $\rho_\perp(B)$ (Fig. 5), which is sensitive to inhomogeneities, and, at the same time, the weak dependence $R_H(B)$ at $T = 78$ K (Fig. 1) are indicative of

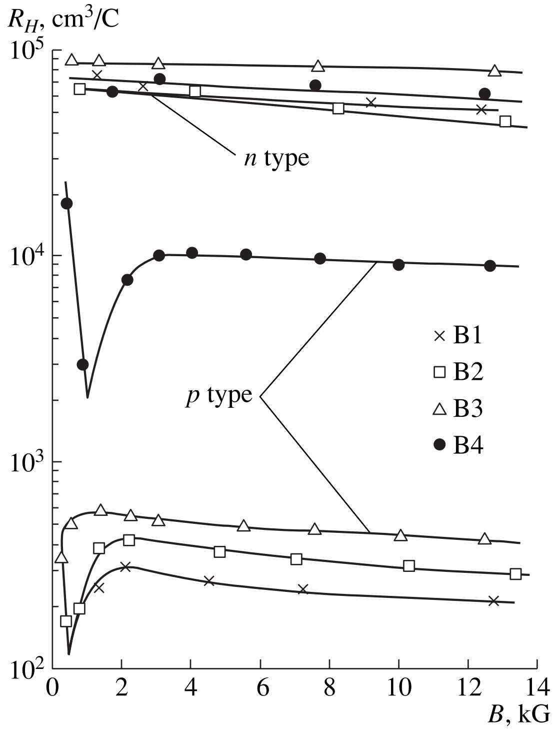

Fig. 1. Magnetic field dependence of the Hall constant for CdHgTe samples with n-type conductivity (before annealing) and p-type conductivity (after conversion annealing) at $T = 78$ K.

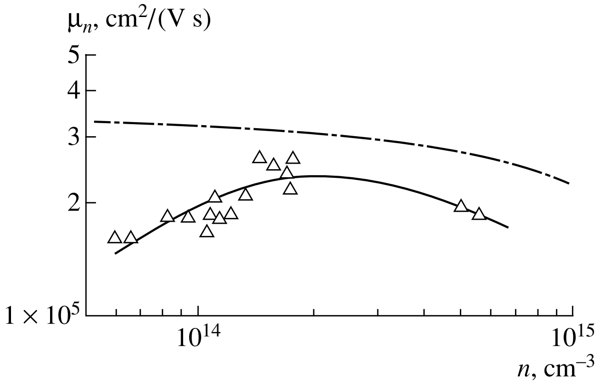

Fig. 2. Dependence of the electron Hall mobility of n-CdHgTe samples on the electron density at $T = 78$ K (Table 1) (triangles and solid line). The dot-dashed line is the theoretical curve from [11] for the scattering of charge carriers by polar optical phonons [11] and by ionized impurities and intrinsic point defects [10] in pure and lightly doped n-CdHgTe samples with $x \approx 0.2$ and the concentration of uncompensated acceptors $|N_a - N_d| \le 10^{17}$ cm^{-3}.

the inhomogeneity of the samples under study. The sizes of the n-type samples before annealing and after etching in a Br–methanol mixture (to remove the surface layer where mercury could diffuse from the vapor phase upon annealing), at a length-to-thickness ratio of $l/d > 10$ (Table 1), make it possible to disregard the geometric effect in measuring $\rho_\perp$.

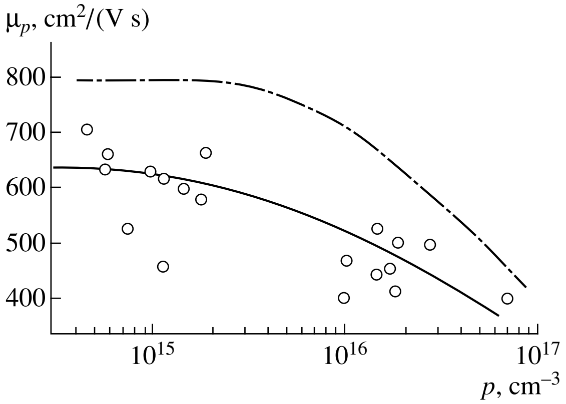

Fig. 3. Dependence of the hole Hall mobility for p-CdHgTe samples on the hole density at $T = 78$ K (Table 1). The dot-dashed line is the theoretical curve from [12] for the scattering of charge carriers by phonons and ionized impurities in p-CdHgTe with $x \approx 0.2$.

The strong dependence $\rho_\perp(B)$ (Fig. 5) we observed at $T = 78$ K was also noted in [15–17]. The anomalous behavior of galvanomagnetic effects in CdHgTe at $T \approx 78$ K is attributed in [18] to the fundamental properties of this material (the presence of an acceptor impurity band overlapping with the conduction band E_c). Others consider that these anomalies result from microinhomogeneities of technical origin that are always present in CdHgTe crystals because of the specific features of synthesis and crystal growth in the CdTe–HgTe system [19]. These features are the local graded-gap structure of the material [20], the significant nonstoichiometry of the crystals, second-phase precipitation [21], the uncorrelated distribution of impurities and the high level of impurity background due to the narrow band gap of the material [22], and some others. All these factors may lead to the formation of coupled clusters [19]. These microinhomogeneities cause fluctuations of the potential; electrons are localized in potential wells, and the values of the conductivity of crystals (even those grown in the same process) differ because of the random distribution of microinhomogeneities [19].

Based on the assumption [19] that the crystals under study are inhomogeneous, with large-scale (200–400 μm) potential fluctuations that result in the strong dependence $\rho_\perp(B)$, we used this parameter as a relative measure of the inhomogeneity of the sample and tried to relate the magnetoresistance amplitude $\Delta\rho/\rho(B)$ (Fig. 6) to the spread in the specific differential resistance of a photodiode (which is a parameter of the n^+–p junction) within a wafer with a zero shift of R_0A. The data of Fig. 6 and Table 3 suggest, for example, that the largest values of R_0A were obtained for sample B3 with the maximum value of $\Delta\rho/\rho(B)$, i.e., with a maximally inhomogeneous composition. The averaged value $\langle R_0A \rangle$ (averaging over the photodiodes fabricated on the same CdHgTe sample) also shows a tendency to drop with a decrease in $\Delta\rho/\rho(B)$. All these facts indicate that

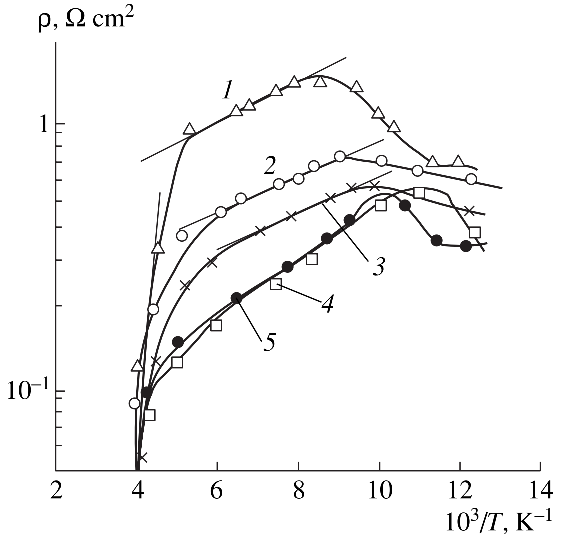

Fig. 4. Temperature dependence of the resistivity of *n*-CdHgTe samples: (*1*) B3, (*2*) A1, (*3*) C1,(*4*) C2, and (*5*) B4.

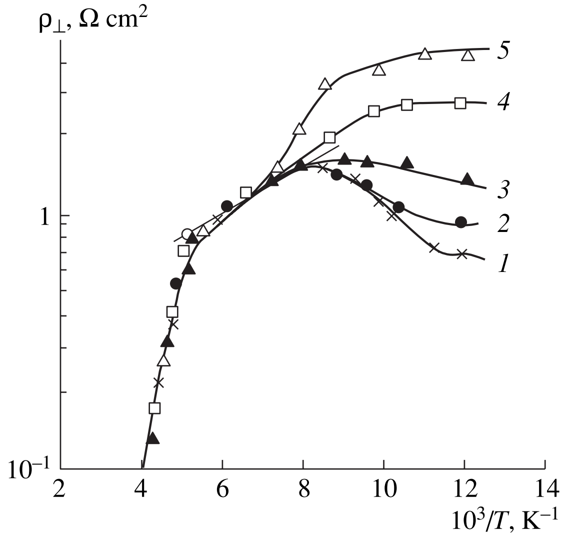

Fig. 5. Temperature dependence of the transverse magnetoresistance of *n*-CdHgTe sample B3 (before annealing) in magnetic fields with induction B = (*1*) 505, (*2*) 1280, (*3*) 3170, (*4*) 7490, and (*5*) 12680 G.

the inhomogeneity changes gradually rather than in steps. In the opposite case (in the presence of clusters or, for example, Te precipitates and a high dislocation density caused by their decomposition upon conversion annealing), we would obtain high dark currents [23], i.e., small values of R_0A. Therefore, the inhomogeneity manifests itself in a smooth change in the concentration of acceptors over the thickness of the sample due to nonuniform compensation or a variation in the composition (Δx). As the results of our long-term research show, such inhomogeneities are always present in CdH-gTe samples. The curves in Fig. 1 for *n*-type samples B3 and B4, which radically differ in R_H after annealing, as well as the magnetic field dependence of ρ for the same samples after annealing (which was not observed in other *p*-type samples), also support this conclusion. In addition, we believe that second phase inclusions, clusters, and other similar defects are unlikely to be found in the initial samples.

Measurements of the spectral characteristics of the photoconductivity signal U_S (Fig. 7) on the samples before (*n* type) and after (*p* type) annealing showed that, as a rule, the change from *n*- to *p*-type conductivity

Table 3. Parameters of photodiodes based on $Cd_xHg_{1-x}Te$ samples

Sample	Photodiode number	λ_{co}, μm	R_0A, Ω cm^{-2}	p_p, 10^{16} cm^{-3}	$\Delta\rho/\rho(B)$ (B = 12 770 G)	$\langle R_0A\rangle$, Ω cm^{-2}
A1 A2	2	10.0	0.68	1.3	4.3–5.4	0.68
	4	9.9	0.71	0.8		
	5	9.8	0.72	0.6		
	7	–	0.61	0.25		
B3 B4	9	–	0.89	0.3	2.1–5.9	0.66
	11	9.8	0.32	0.22		
	12	10.1	0.81	1.2		
	14	9.9	0.63	0.11		
C1	3	10.1	0.54	0.4	4.5	0.34
	18	10.8	0.17	1.5		
	21	9.94	0.32	3.5		

Note: The diameter of the n^+–p junctions (by photomask) is 300 μm. The $\Delta\rho/\rho(B)$ column shows the spread in the values (according to Fig. 6), obtained at T = 78 K for the initial samples used to fabricate the corresponding sets of photodiodes. Averaged values of $\langle R_0A\rangle$ were obtained for all photodiodes in each set. The majority-carrier concentrations in the *p*-type region of the n^+–p junction, p_p, were obtained by measuring the capacitance–voltage characteristics of the photodiodes.

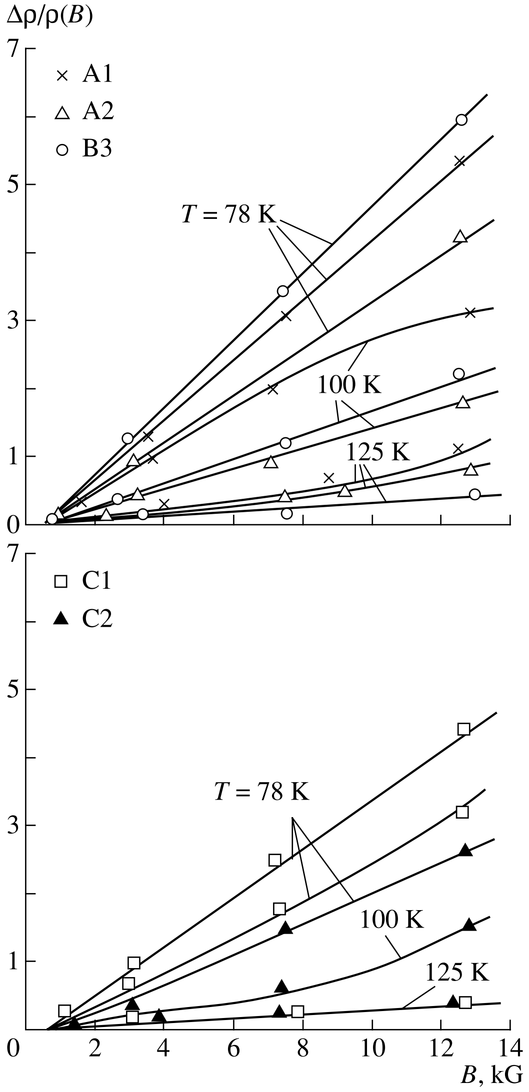

Fig. 6. Magnetic field dependences of the relative transverse magnetoresistance of *n*-CdHgTe samples (before annealing) at three temperatures.

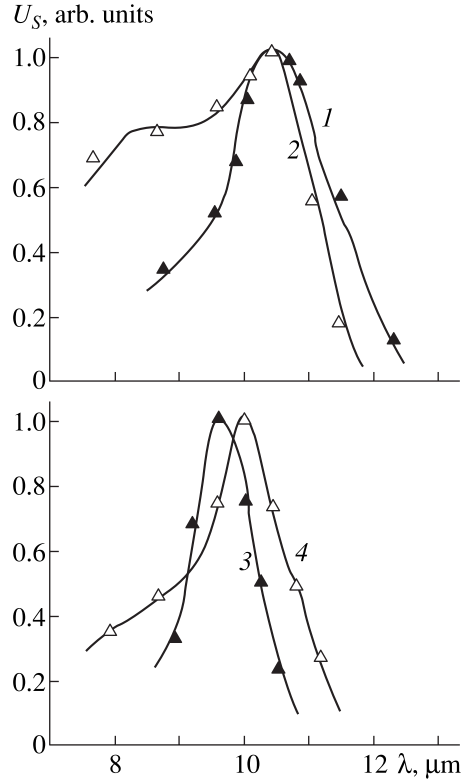

Fig. 7. Spectral characteristics of photoconductivity of CdHgTe samples with *n*-type (before annealing) and *p*-type (after conversion annealing) conductivity at T = 78 K. (a) Sample A1 with (*1*) *n*-type and (*2*) *p*-type conductivity; (b) sample B3 with (*3*) *n*-type and (*4*) *p*-type conductivity.

results in a shift of λ_{co} to either shorter or longer waves. Since layers about 100 μm thick were etched away from both sides of each sample after annealing, these data indicate an inhomogeneous composition in the bulk of the sample. For example, estimation for sample A1 gave the value of shift $\Delta\lambda_{co}$ = 0.5 μm, which corresponds to a change in the band gap width $\Delta E_g \approx 6$ meV and, therefore, $\Delta x \approx 0.003$. Taking into account that the thickness of the layer removed by etching was about a quarter of the total sample thickness and assuming that the inhomogeneity is linear in thickness, we obtain the total change in Cd content over the thickness of the initial sample: $\Delta x \approx \pm 0.006$. For comparison, note that the value of $\Delta x \approx \pm 0.003$ is considered to indicate high sample homogeneity [24]. The spread in λ_{co} over the total surface area of a starting wafer about 20 mm in size, for example, sample A, was approximately the same: $\Delta\lambda_{co} \approx 0.5$ μm (Fig. 7). With this value of $\Delta\lambda_{co}$ for the same plate, the value of R_0A may change (under conditions of limitation by a diffusion current) about threefold from one photodiode to another only because of the spread in Δx.

The lifetime of charge carriers τ_n in the *n*-type samples was, as rule, an order of magnitude longer than τ_p for the *p*-type samples (Table 1). For sample B3, in which (as an exception) τ changed only twofold as a result of the thermal conversion, two relaxation time constants of photoresponse were found (Fig. 8). However, they appeared only at high levels of optical excitation ($P \gtrsim 10^3$ W/cm^2). To make the data on τ more complete, Fig. 8 also shows the results for photodiode 12 fabricated on sample B3. For CdHgTe samples, τ is the value measured when the sample is scanned with a wide laser beam and averaged over a large area. For photodiodes, τ is controlled by the properties of the *p*-type region near the n^+–p junction in the layer ~(20–50) μm thick. Values of τ for photodiodes may differ severalfold from those for the CdHgTe samples; thus, in order to calculate, for example, the quantum efficiency of a photodiode, one should use the value of τ measured for the same photodiode. It may be assumed that the two time constants observed, τ_1 and τ_2, are

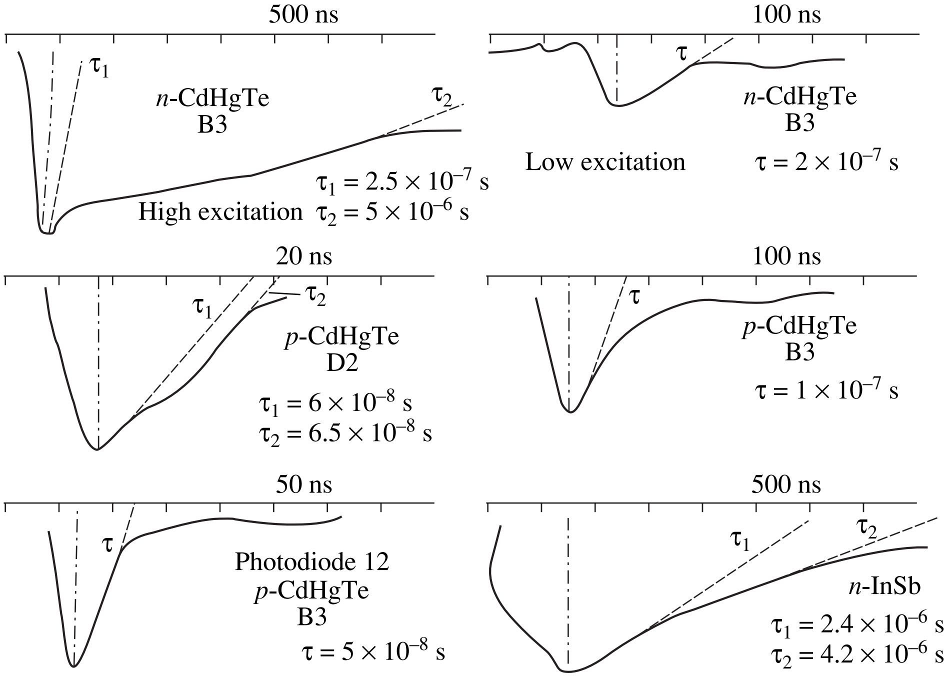

Fig. 8. Time characteristics of photoresponse measured for CdHgTe samples B3 (n and p types), D2 (p type), photodiode 12 fabricated from sample B3, and (for comparison) a sample of impurity InSb. Measurements were performed using a C8-12 storage oscilloscope after photoresponse excitation by ultrashort laser pulses at 10.6 μm.

related to recombination via two deep levels since the measurement of the tunnel current in photodiodes fabricated on this sample also revealed two levels: with $E_t - E_v = 72$ meV and with an energy of about 36 meV. This conclusion is confirmed indirectly by the measurements of τ in a compensated impurity n-InSb sample (Fig. 8), which was used as a reference with a known energy level (in this sample, along with the interband recombination with $\tau_1 = 2.4 \times 10^{-6}$ s, a slower recombination with τ_2 via impurity levels occurs). For sample D2 with $p(78\text{ K}) = 1.7 \times 10^{16}$ cm^{-3}, two time constants, τ_1 and τ_2, were also noted; they differed insignificantly from each other, although they were well resolved (Fig. 8). Prior to annealing, the photoconductivity spectra of this sample (with n-type conductivity) showed an extended long-wavelength edge, characteristic of photoconductivity that involves an impurity band. In addition, the conductivity type of this sample was not converted under conventional annealing conditions, and the sample was additionally annealed twice (the parameters of the n-type sample after such annealing are listed in Table 1). Estimation of the impurity-band location based on the photoconductivity spectra yields energy $E_c - E_t \approx 24$ meV, which is consistent with the data of Table 2, obtained for other samples.

The data reported suggest that the initial low electron density in n-type sample D2 is due to the high degree of compensation as a result of the introduction of a large number of acceptors: mercury vacancies forming singly charged shallow acceptor levels with $E_t - E_v \approx 8$ meV and deep doubly charged levels with $E_t - E_v \approx 36$ meV in CdHgTe [25, 26].

Thus, analysis of the temperature and field dependences of R_H revealed that n-Cd$_x$Hg$_{1-x}$Te samples with low electron density are, as a rule, compensated, and the degree of compensation changes upon thermal conversion of the conductivity of the sample to p type. For n-Cd$_x$Hg$_{1-x}$Te samples, the activation energy of the donor level was determined from the dependences $\rho(T)$: $E_c - E_t = 24$–32 meV. For the same samples, after their thermal conversion to p type, the activation energy of the acceptors related to doubly charged vacancies V_{Hg}^{++} was determined: E_t exceeds E_v by either 32 or 48 meV. In addition, a deep level with $E_t - E_v \approx 0.7E_g$, related to an unknown amphoteric impurity, was found for the first time.

REFERENCES

1. D. L. Spears, Proc. SPIE **227**, 108 (1980).
2. J. E. Shanley, C. T. Flanagan, and M. B. Reine, Proc. SPIE **227**, 117 (1980).
3. J. E. Shanley and C. T. Flanagan, Proc. SPIE **227**, 123 (1980).
4. D. L. Spears, Proc. SPIE **300**, 174 (1981).
5. V. I. Turinov, Élektron. Tekh., Ser. 1: Élektron. SVCh **1**, 30 (1991).
6. A. J. Syllaios and M. J. Williams, J. Vac. Sci. Technol. **21**, 201 (1982).

7. R. A. Reinolds, M. J. Brau, H. Kraus, and R. T. Bate, J. Phys. Chem. Solids **32** (Suppl. 1), 1511 (1971).
8. H. R. Vydyanath, J. Electrochem. Soc. **128**, 2609 (1981).
9. H. F. Schaake, J. H. Tregilgas, J. D. Beck, *et al.*, J. Vac. Sci. Technol. A **3**, 143 (1985).
10. W. Scott, J. Appl. Phys. **43**, 1055 (1972).
11. J. J. Dubowski, T. Dietl, W. Szymanska, and R. R. Galazka, J. Phys. Chem. Solids **42**, 351 (1981).
12. D. A. Nelson, W. W. Higgins, R. A. Lancaster, *et al.*, in *Extended Abstracts of U.S. Workshop on the Physics and Chemistry of Mercury Cadmium Telluride* (Minneapolis, 1981), p. 175.
13. R. F. Brebrick and J. P. Schwartz, J. Electron. Mater. **9**, 485 (1980).
14. G. L. Hansen, J. L. Schmidt, and T. N. Casselman, J. Appl. Phys. **53**, 7099 (1982).
15. L. A. Bovina, Yu. N. Savchenko, and V. I. Stafeev, Fiz. Tekh. Poluprovodn. (Leningrad) **9**, 2084 (1975) [Sov. Phys. Semicond. **9**, 1362 (1975)].
16. D. V. Sobolev, V. P. Ponomarenko, L. A. Bovina, *et al.*, Fiz. Tekh. Poluprovodn. (Leningrad) **15**, 1293 (1981) [Sov. Phys. Semicond. **15**, 747 (1981)].
17. L. A. Karachevtseva, A. V. Lyubchenko, and É. A. Malovichko, Fiz. Tekh. Poluprovodn. (St. Petersburg) **26**, 535 (1992) [Sov. Phys. Semicond. **26**, 302 (1992)].
18. L. A. Bovina, Yu. N. Savchenko, and V. I. Stafeev, Fiz. Tekh. Poluprovodn. (Leningrad) **9**, 26 (1975) [Sov. Phys. Semicond. **9**, 15 (1975)].
19. A. I. Elizarov, V. I. Ivanov-Omskiĭ, A. A. Korniyash, and V. A. Petryakov, Fiz. Tekh. Poluprovodn. (Leningrad) **18**, 201 (1984) [Sov. Phys. Semicond. **18**, 125 (1984)].
20. A. I. Vlasenko, Yu. N. Gavrilyuk, A. V. Lyubchenko, and E. A. Sal’kov, Fiz. Tekh. Poluprovodn. (Leningrad) **13**, 2180 (1979) [Sov. Phys. Semicond. **13**, 1274 (1979)].
21. J. Steininger, J. Cryst. Growth **37**, 107 (1977).
22. Yu. S. Gal’perin and A. L. Éfros, Fiz. Tekh. Poluprovodn. (Leningrad) **6**, 1081 (1972) [Sov. Phys. Semicond. **6**, 941 (1972)].
23. H. F. Schaake, J. H. Tregilgas, A. J. Lewis, and P. M. Everett, J. Vac. Sci. Technol. A **1**, 1625 (1983).
24. K.-P. Mollmann, H. Bittner, H. Heukenkamp, and B. Schubert, Infrared Phys. **31**, 493 (1991).
25. M. A. Kinch, M. J. Brau, and A. Simmons, J. Appl. Phys. **44**, 1649 (1973).
26. M. A. Kinch, J. Vac. Sci. Technol. **21**, 215 (1982).

Translated by Yu. Sin’kov

Semiconductors, Vol. 38, No. 7, 2004, pp. 758–762. Translated from Fizika i Tekhnika Poluprovodnikov, Vol. 38, No. 7, 2004, pp. 791–795.
Original Russian Text Copyright © 2004 by Neustroev, Smagulova, Antonova, Safronov.

ELECTRONIC AND OPTICAL PROPERTIES OF SEMICONDUCTORS

Formation of Electrically Active Centers in Silicon Irradiated with Electrons and Then Annealed at Temperatures of 400–700°C

E. P. Neustroev*, S. A. Smagulova*, I. V. Antonova, and L. N. Safronov****
**Yakutian State University, pr. Lenina 41, Yakutsk, 677891 Russia*
***Institute of Semiconductor Physics, Siberian Division, Russian Academy of Sciences,*
pr. Akademika Lavrent'eva 13, Novosibirsk, 630090 Russia

Submitted November 18, 2003; accepted for publication November 26, 2003

Abstract—The effect of irradiation with electrons on the formation of quenched-in donors in silicon is studied. It is found that *n*- and *p*-type regions are formed in the bulk of single-crystal silicon as a result of irradiation with electrons and subsequent annealing at a temperature of 450°C. The concentration of charge carriers in the regions of both types increases as the radiation dose and the annealing duration increase, which indicates that not only quenched-in donors but also quenched-in acceptors are formed. Nonuniformity in the distribution of the acceptor and donor centers correlates with fluctuations of the oxygen concentration in silicon. *© 2004 MAIK "Nauka/Interperiodica".*

1. INTRODUCTION

The transition to the nanometer scale in modern electronics led to a decrease in the temperatures used in all stages of fabricating device structures (to 700–800°C) [1]. At the same time, annealing silicon crystals at relatively low temperatures (400–700°C) gives rise to electrically active centers of both donor type (quenched-in donors) [2] and acceptor type (quenched-in acceptors) [3, 4]. Despite the fact that quenched-in donors have been studied for many years, there is still no generally accepted model for these centers. Recently, the models that have been most widely accepted are those according to which the formation of quenched-in donors occurs as a result of consecutive attachment of oxygen atoms to a charged nucleus [5]. This effect gives rise to a series of closely spaced energy levels in the vicinity of the bottom of the conduction band. At the same time, it is evident that processes of oxygen precipitation from a supersaturated oxygen solution are affected by the defect structure of the crystal; this structure is primarily governed by the growth defects and the defects formed as a result of treatment during the fabrication of the device (thermal annealing, ion implantation, oxidation, and so on). Specifically, a promoted formation of quenched-in donors was observed in silicon crystals implanted with medium- and high-energy ions [6, 7]. When the charge-carrier concentration in silicon crystals is measured, it is usually difficult to separate the effect of quenched-in acceptors from that of quenched-in donors formed at 450°C. The introduction of quenched-in acceptors in the temperature range 350–600°C manifests itself most clearly in oxygen-free silicon crystals irradiated with high doses of electrons and neutrons [4] and in oxygen-containing silicon after high-energy ion implantation and the subsequent initial stages of annealing at a temperature of 450°C [8]. One would expect quenched-in acceptors to be introduced into oxygen-containing silicon when other types of radiation are used, e.g., when silicon is irradiated with electrons. The resulting type of conductivity and the charge-carrier concentration are controlled by the relation between the number of quenched-in donors and that of quenched-in acceptors in irradiated silicon.

The aim of this study was to gain insight into the effect of electron irradiation on the formation of electrically active centers (quenched-in donors and acceptors) in oxygen-containing silicon in the temperature range 400–700°C.

2. EXPERIMENTAL

We studied silicon single crystals that were grown by the Czochralski method and had a doping impurity (boron) concentration of 8×10^{14} cm^{-3}. The oxygen concentration in the samples was 8×10^{17} cm^{-3} (in order to determine the oxygen concentration, we used the absorption peak at 1107 cm^{-1} with a calibration coefficient of 3.14×10^{17} cm^{-2}). We irradiated the samples with pulses of 2.0-MeV electrons; the duration of the pulses was 400 μs, and the current density was 0.1–0.3 A/cm^2. The radiation dose was varied from 10^{14} to 10^{17} cm^{-2} (the radiation dose was 10^{14} cm^{-2} for the sample denoted as E1, 10^{15} cm^{-2} for sample E2, 10^{16} cm^{-2} for sample E3, and 10^{17} cm^{-2} for sample E3; the unirradiated sample was designated as E0). The temperature of the samples was no higher than 50°C during irradiation. The irradiated samples were subjected to heat treatment for 1–10 h in the temperature range T = 400–700°C. In our study, we used the capacitance–voltage

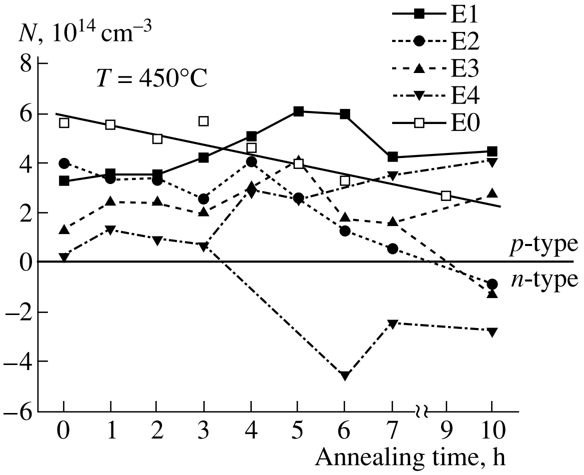

Fig. 1. Annealing-time dependence of the charge-carrier concentration in silicon samples irradiated with different doses of electrons and then subjected to heat treatment at $T = 450°C$. The values of the electron concentration (in contrast to the hole concentration) are plotted on the negative axis of N for clarity.

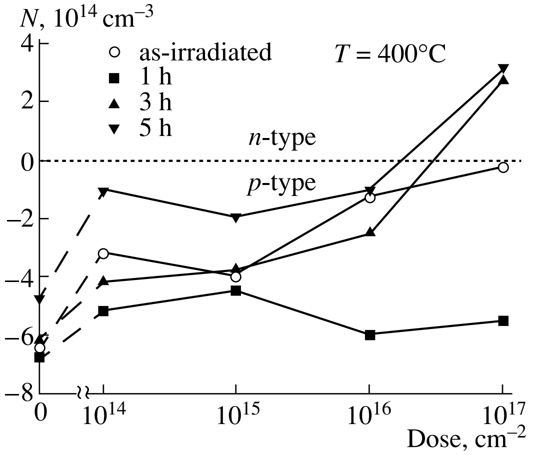

Fig. 3. Dependences of the charge-carrier concentration on the radiation dose for samples subjected to postirradiation annealing for $t = 0–5$ h at $T = 400°C$. The values of the electron concentration are plotted on the positive axis of N, while those of the hole concentration are plotted on the negative axis.

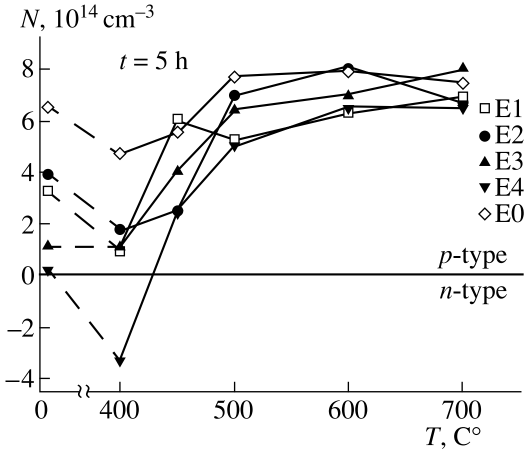

Fig. 2. Dependences of the charge-carrier concentration on annealing temperature in the range $T = 400–700°C$ for annealing time $t = 5$h. The values of the electron concentration (in contrast to the hole concentration) are plotted on the negative axis of N for clarity.

(*C*–*V*) characteristics, Hall effect, and Fourier transform infrared (FTIR) spectroscopy.

3. RESULTS

In Fig. 1 we show the charge-carrier concentration in silicon samples irradiated with electrons and then annealed at a temperature $T = 450°C$ as a function of the annealing temperature. The data were obtained using an analysis of *C*–*V* characteristics. For samples E3 and E4 (irradiated with electron doses of 10^{16} and 10^{17} cm^{-2}, respectively), different values of the charge-carrier concentration were determined at different points of the surface after annealing for more than 5–7 h. In addition, as can be seen from Fig. 1, different areas of the surface had both *p*- and *n*-type conductivity (the largest values of charge-carrier concentration are shown in the regions with *p*- and *n*-type conductivity). The size of these regions ranged from 0.5 to 1–2 cm^2. If a strip is cut along the wafer radius from the center to the periphery, these *p*- and *n*-type regions appear in the form of alternating bands. When the surface layers are removed layer by layer, the nonuniformity of the distribution of electrically active centers is retained; only the configuration of these regions may change slightly. The concentration of electrically active centers in the unirradiated (reference) sample E0 decreased almost steadily, which indicated that the concentration of donor centers increased with increasing duration of annealing (this dependence is represented by the thin solid line in Fig. 1) owing to the formation of quenched-in donors in oxygen-containing silicon.

The dependence of the charge-carrier concentration in irradiated samples and starting crystals on the annealing temperature is shown in Fig. 2. The duration of annealing was $t = 5$ h. Annealing at $T = 400°C$ leads to the conversion of *p*-type to *n*-type conductivity for sample E4 and to the smallest values of hole concentration for all other samples.

In Fig. 3, we show the dependence of charge-carrier concentration in irradiated silicon crystals annealed at $T = 400°C$ on the radiation dose. The concentration of acceptors in the samples annealed for 1h increases compared to that in the starting crystal for all the radiation doses used. As the duration of annealing increases, the concentration of acceptors decreases. The most pronounced effect is observed at a high radiation dose (10^{17} cm^{-2}). As the annealing temperature is increased to 500–700°C (the range corresponding to the forma-

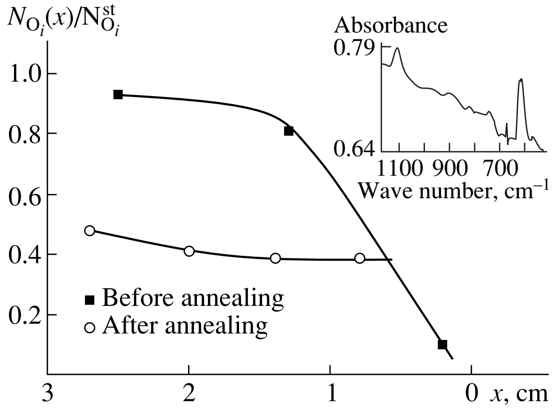

Fig. 4. Variation in relative concentration of interstitial oxygen along the radius of the silicon wafer (from the wafer's center to its edge) before and after annealing for t = 10 h at T = 425°C. A typical spectrum of optical absorption is shown in the inset.

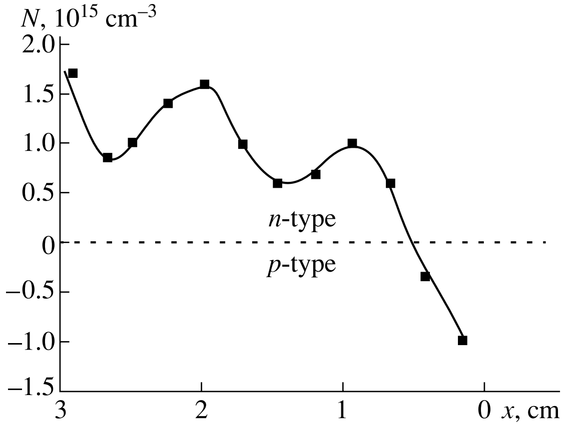

Fig. 5. Distribution of electrically active centers along the radius of a silicon wafer irradiated with electrons and then annealed for t = 10 h at T = 425°C. The values of the electron concentration are plotted on the positive axis of N; those of the hole concentration, on the negative axis.

tion of new quenched-in donors), the formation of electrically active centers (the quenched-in donors and acceptors) is not observed, since the charge-carrier concentration in all the samples studied tends to the level of the initial values. It is noteworthy that the temperature range of the existence of donor centers introduced as a result of heat treatment coincides with that of the existence of oxygen-containing quenched-in donors.

The measurements performed using IR spectroscopy showed that the concentration of optically active oxygen immediately after irradiation was (4–5) × 10^{17} cm^{-3}, which was considerably lower than the oxygen concentration in the starting material, i.e., (7–8) × 10^{17} cm^{-3}. The variation in the relative concentration of interstitial oxygen $N_{O_i}(x)/N^{st}_{O_i}$ along the radius of the silicon wafer is shown in Fig. 4 ($N^{st}_{O_i}(x)$ is the oxygen concentration in the starting crystal before annealing and x is the distance from the edge of the wafer). As can be seen from Fig. 4, the oxygen concentration after annealing at 425°C decreases to a value lower than that immediately after irradiation. A typical absorption spectrum of the samples under study is shown in the inset in Fig. 4. The variation in the concentration of electrically active centers along the radius of the wafer for the same sample is shown in Fig. 5. It can be seen that, as the oxygen content decreases, the concentration of donor centers also decreases (the distance was measured from the center of the samples) and conversion of the conductivity type occurs in the region with the lowest oxygen concentration (at the edge of the sample). Annealing at 450°C leads to an increase in the concentration of optically active oxygen to almost the initial value. In addition, it became clear that the formation of the regions with different types of conductivity was caused by the nonuniform distribution of oxygen in silicon crystals: the location of the regions with a higher oxygen concentration coincides with that of the regions with n-type conductivity. The difference between the oxygen concentrations in the regions with p- and n-type conductivity was no larger than 6 × 10^{16} cm^{-3} in the crystal annealed for 10 h at 450°C. No significant variation in the carbon content in these regions was observed.

4. DISCUSSION

It follows from the data shown in Fig. 1 that an increase in the radiation dose and duration of annealing at T = 450°C leads to the dominant generation of quenched-in donors in some regions of the crystal (initially p-type material changes to n-type conductivity); in other regions, the generation of quenched-in acceptors is dominant (the hole concentration increases). Quenched-in acceptors can be clearly observed in the situation where the generation of quenched-in donors is suppressed, i.e., in oxygen-free silicon or in oxygen-containing silicon irradiated with high-energy ions; in the latter case, the defects of different types are spatially separated [2, 7]. In the case under consideration, the change in conductivity from p type to n type is observed after irradiation with high electron doses (10^{17} cm^{-2}) and after subsequent long (more than 3 h) annealing at a temperature of 400°C (Fig. 3). As the temperature of annealing for times of up to 10 h is increased to 450°C, n-type regions are also formed after irradiation with lower doses (10^{15} cm^{-2}, see Fig. 1). Irradiation with 2-MeV electrons leads to a nearly uniform spatial distribution of the radiation defects produced. Therefore, either the growth defects formed during growth of the crystals or the nonuniformities in the distribution of background impurities (for example, oxygen) can alone be responsible for the nonuniform distribution of electrically active centers. An increase in the concentration of quenched-in donors in some regions may be caused by an increase in the number of nucleation centers formed by radiation defects (with the possible involvement of impurities). When comparing the distribution of oxygen concentration along the radius of the silicon wafer with that of free electrons (Figs. 4, 5), we must be aware that the IR-absorption measurements yield an averaged pattern of interstitial oxygen distribution over the wafer thickness, whereas electrical measurements yield the distribution of electrically active centers in the relatively thin surface layer. Therefore, the nonuniformities in the electron distribution shown in Fig. 5 (after annealing at 425°C) cannot be recognized in the results of IR measurements shown in Fig. 4. Nevertheless, the nonuniformity in the distribution of electrically active centers in the crystals annealed at 450°C begins to correlate with the nonuniform distribution of interstitial oxygen in the samples under study (apparently owing to the intensification of fluctuations in the oxygen distribution).

Apparently, the decrease in the concentration of interstitial oxygen after irradiation is related to the formation of complexes that consist of vacancies and oxygen atoms VO_n, where $n \geq 1$ [9]; as is well known, the VO center is dominant. The transformation $VO \longrightarrow VO_2$ occurs at an annealing temperature of 425°C [10]. An increase in the temperature of heat treatment to 450°C is accompanied by annealing of the VO and VO_2 complexes and, accordingly, by an increase in the concentration of interstitial oxygen.

It follows from the data shown in Fig. 1 for a dose of 10^{14} cm^{-2} (sample E1) that, when the sample is heat-treated, the concentration of holes (acceptor centers) increases somewhat compared to the starting material. As the annealing temperature is decreased to 400°C (Fig. 3), some increase in the hole concentration is observed for all radiation doses even after short-duration (1 h) annealing. Apparently, acceptor centers are formed simultaneously with quenched-in donors as a result of annealing at $T = 450$°C. However, the formation of acceptor centers is noticeable only in the regions with a relatively low concentration of quenched-in donors, for example, due to a low oxygen concentration or retardation of the formation of the quenched-in donors in the initial stages of this process. In other cases, quenched-in donors do not appear or their formation is suppressed by the formation of quenched-in acceptors.

The possibility that acceptor-type centers appear in oxygen-containing silicon as a result of heat treatment at temperatures that correspond to the formation of quenched-in donors has not usually even been considered. At the same time, as follows from the data reported in other publications that deal with the effect of electron radiation on the formation of quenched-in donors, the concentration of quenched-in donors in the samples under consideration was either equal to [11, 12] or lower than [13, 14] that in the starting samples. The discrepancies observed in the results can be adequately accounted for in the context of the simultaneous formation of the quenched-in donors (QIDs) and acceptors (QIAs). For example, depending on the defect and impurity composition of the starting material, the temperature of heat treatment, and the radiation dose, the total concentration of charge carriers, which equals $n_0 + N_{\mathrm{QID}} - N_{\mathrm{QIA}}$ (or $p_0 - N_{\mathrm{QID}} + N_{\mathrm{QIA}}$), could vary in a complex manner. This often appeared as invariability or retardation of the kinetics of formation of quenched-in donors (n_0 and p_0 are the initial concentrations of electrons and holes, respectively).

As the temperature of heat treatment is increased (to 500°C or higher), quenched-in donors and acceptors are practically not formed (Fig. 2). As is well known, the temperature of existence of quenched-in donors is limited to 520°C, but new quenched-in donors could be formed at temperatures of 600–700°C. However, the formation of these donors was not observed at the heat-treatment temperatures used in our experiments.

Thus, taking into account both the fact that electron irradiation gives rise to vacancy-containing centers (VO centers) in silicon crystals and the previous data [8], the experimental results obtained are most likely explained by the involvement of vacancy-containing defects in the formation of both the quenched-in acceptors and the quenched-in donors. The processes of generation of quenched-in acceptors are dominant in the initial stage of annealing, whereas the formation of quenched-in donors (or the transformation of quenched-in acceptors into quenched-in donors) begins to dominate as the annealing time is increased. It is worth noting that the same situation takes place in the case of irradiation with high-energy ions [8]. The formation of acceptor-type centers is observed in a narrow annealing-temperature range (~450°C); these centers do not appear against the background of quenched-in donors at a heat-treatment temperature of 400°C.

5. CONCLUSION

The irradiation of silicon single crystals with electrons (the case of uniform production of radiation defects in the bulk of the material) and subsequent annealing at 450°C lead to the formation of *n*- and *p*-type regions in the bulk of single-crystal silicon. The observed effect becomes more pronounced as the radiation dose increases. The nonuniformity of the distribution of quenched-in acceptors and donors correlates with variations in the oxygen content in silicon. Quenched-in donors start to be dominant as the duration of annealing increases. The mechanism of formation of quenched-in acceptors and donors is most likely related to the involvement of vacancy-containing centers in the process of formation of these centers.

REFERENCES

1. G. Ya. Krasnikov, *Structural and Technological Features of Submicron MOS-Transistors* (Tekhnosfera, Moscow, 2002), Part 1.

2. A. Borhgesi, B. Pivac, A. Sassella, and A. Stella, J. Appl. Phys. **77**, 4169 (1995).
3. V. N. Mordkovich, Fiz. Tverd. Tela (Leningrad) **6**, 847 (1964) [Sov. Phys. Solid State **6**, 654 (1964)].
4. V. F. Stas', I. V. Antonova, E. P. Neustroev, *et al.*, Fiz. Tekh. Poluprovodn. (St. Petersburg) **34**, 162 (2000) [Semiconductors **34**, 155 (2000)].
5. P. Deak, L. C. Snyder, and J. W. Corbett, Phys. Rev. **45**, 11612 (1992).
6. E. P. Neustroev, I. V. Antonova, V. P. Popov, *et al.*, Fiz. Tekh. Poluprovodn. (St. Petersburg) **33**, 1153 (1999) [Semiconductors **33**, 1049 (1999)].
7. E. P. Neustroev, I. V. Antonova, V. P. Popov, *et al.*, Physica B (Amsterdam) **270**, 1 (1999).
8. S. A. Smagulova, I. V. Antonova, E. P. Neustroev, and V. A. Skuratov, Fiz. Tekh. Poluprovodn. (St. Petersburg) **37**, 565 (2003) [Semiconductors **37**, 546 (2003)].
9. T. Hallberg and J. L. Lingstrom, J. Appl. Phys. **72**, 5130 (1992).
10. C. A. Londos, I. V. Antonova, M. Potsidou, *et al.*, J. Appl. Phys. **91**, 1198 (2002).
11. A. Henry, K. Saminadayar, J. L. Pantrat, and N. H. Magnea, Phys. Status Solidi A **107**, 101 (1988).
12. V. V. Litvinov, G. V. Pal'chik, and V. I. Urenev, Fiz. Tekh. Poluprovodn. (Leningrad) **24**, 376 (1990) [Sov. Phys. Semicond. **24**, 233 (1990)].
13. V. P. Markevich and L. I. Murin, Fiz. Tekh. Poluprovodn. (Leningrad) **22**, 1324 (1988) [Sov. Phys. Semicond. **22**, 840 (1988)].
14. P. F. Lugakov and V. V. Luk'yanitsa, Fiz. Tekh. Poluprovodn. (Leningrad) **24**, 1721 (1990) [Sov. Phys. Semicond. **24**, 1075 (1990)].

Translated by A. Spitsyn

Semiconductors, Vol. 38, No. 7, 2004, pp. 763–768. Translated from Fizika i Tekhnika Poluprovodnikov, Vol. 38, No. 7, 2004, pp. 796–801.
Original Russian Text Copyright © 2004 by Abdullaev.

ELECTRONIC AND OPTICAL PROPERTIES OF SEMICONDUCTORS

The Role of Trapping Levels of Nonequilibrium Electrons during the Formation of Pinning Centers for Domain Walls in the Magnetic Semiconductor $CdCr_2Se_4$

A. A. Abdullaev

Institute of Physics, Dagestan Scientific Center, Russian Academy of Sciences,
ul. 26 Bakinskikh Komissarov 94, Makhachkala, 367003 Dagestan, Russia
e-mail: analit@dinet.ru

Submitted September 9, 2003; accepted for publication November 27, 2003

Abstract—A complex study of electrical conductivity and photoconductivity in constant and variable electric fields, thermally stimulated conductivity, and the photoferromagnetic effect are carried out in the temperature range 10–300 K for a $CdCr_2Se_4$ magnetic semiconductor with various concentrations of Ga impurity and Se vacancies (V_{Se}). The phenomenon of hopping photoinduced conduction is observed for the first time. It is shown that shallow donor levels that exchange photoelectrons trapped by them with Cr^{3+} magnetic ions may be responsible for the photoferromagnetic effect. As a result of this exchange, the Cr^{3+} ions acquire valence and spin instabilities, which lead to nonequilibrium pinning of the domain wall by these ions. *© 2004 MAIK “Nauka/Interperiodica”.*

Numerous studies are devoted to studying the phenomenon of variation in dynamic magnetic permeability (DMP) under the effect of light in magnetic semiconductors, which is referred to as the photoferromagnetic effect (PFE) [1]. The interest in this phenomenon is associated with prospects for developing new methods of data recording and detecting infrared (IR) radiation [2]. The recent discovery of numerous new materials that are classified as magnetic semiconductors has stimulated interest in $CdCr_2Se_4$, the compound that has been investigated in most detail. A detailed study of the mechanism of PFE emergence in this compound could promote the search for possible ways of simultaneously increasing the amplitude and response speed of this effect.

According to [3–11], which are devoted to researching the nature of PFE in $CdCr_2Se_4$, a decrease in DMP under the effect of light is related to the pinning of domain walls (DWs) at photoinduced centers Cr^{2+}, which are antiferromagnetically oriented relative to the Cr^{3+} sublattice. However, a mechanism of formation of these centers that accounts for all the characteristics of this phenomenon has not yet been discovered.

The aim of this study was to analyze specific features of PFE in $CdCr_2Se_4$ reported previously and our experimental data in order to attempt to ascertain the nature of this phenomenon. The steady-state and kinetic properties of PFE in constant, oscillatory, and pulsed magnetic fields; the residual photoferromagnetic effect (RPFE); and its infrared and thermal quenching were investigated for the same samples with various concentrations of Ga impurity and Se vacancies V_{Se}. Simultaneously, temperature dependences of conductivity and photoconductivity in constant and variable electric fields, kinetic characteristics of photoconductivity, residual conductivity, thermally stimulated conductivity, and their thermal and IR quenching were investigated.

The energy level of the Cr^{2+} ion lies deep in the band gap. If the DW pinning center Cr^{2+} is formed directly under the effect of light, only the RPFE should occur at temperatures below the Curie point (130 K). On the contrary, PFE in the temperature range 50–130 K vanishes as the illumination ceases [5]. The RFFE under different physical factors behaves similarly to thermally stimulated conductivity and residual conductivity, which are associated with carrier trapping at the impurity levels. Therefore, our goal was to investigate the contribution of donor impurities to the formation of photoinduced DW-pinning centers. Shallow donors associate into unified complexes with the Cr^{2+} ions via collectivization of nonequilibrium electrons multiply attaching to these donors. The latter could be responsible for PFE with its inherent specific features.

It was shown [3, 7] that, regardless of the technique of sample growth (from solution–melts or by liquid-phase transport) and, consequently, regardless of the concentration of growth defects, nonstoichiometry, and porosity, the amplitude of PFE in $Ga_xCd_{1-x}Cr_2Se_4$ is peaked at the same value ($x = 0.0025$). The magnitude of PFE for crystals grown from solution–melts is severalfold greater than that for crystals grown by liquid-phase transport. However, with high concentrations of Se vacancies, PFE vanishes [7], the dark DMP decreases as the Ga concentration and the degree of imperfection of the sample increases, and the dependence of the PFE amplitude on the intensity of light is sublinear [9]. At first sight, these results seem contradictory. However, the authors of [9–11] related the decrease in amplitude and relaxation time of PFE in oscillatory magnetic fields with the release of DWs from pinning centers rather than with the variation in concentration of these centers. These kinetic characteristics of PFE, as well as the impossibility of obtaining high PFE amplitudes at high frequencies, can be explained in a model of the aforementioned complex photoinduced centers of pinning of DWs.

The spatial pinning of points of arrangement of photoinduced centers at a free-oscillating DW increases its vibration frequency, i.e., increases its rigidity. As DMP increases, the frequency of a self-excited oscillator, which is tuned to a frequency of natural oscillations of the DW when detecting PFE, decreases. Therefore, the magnitude referred to by Anzina and Rudov [9] as DW rigidity is inversely proportional to DMP ($1/\mu$) and should be proportional to the electron density at donors, if the suggested structure of photoinduced centers is true. However, judging by the above experimental data, such a dependence of DW rigidity on the number of donor levels occupied by electrons n_d should be expected only with a moderate concentration of impurity centers at certain levels of intensity of light and corresponding compensation. The causes of these restrictions will be clarified below.

The analysis of the equilibrium filling of shallow donor levels with electrons considered below is not an analysis of the situation that arises in studying PFE. In the latter case, it is necessary to use an expression for the temperature dependence of the quasi-Fermi level. In a compensated semiconductor at low temperatures, electrons can occupy shallow donor levels similarly to the equilibrium case if one considers the quasi-Fermi level instead of the Fermi level. This is the case for irradiation with photons when the energy is sufficient for band-to-band transitions.

The number of electrons n_d at shallow donor impurity levels of a single type is determined by the relation

$$n_d = \frac{N_d}{1 + \exp\left(-\frac{E_1 + F}{kT}\right)}, \tag{1}$$

where N_d is the number of all donor impurities of this type, E_1 is the activation energy of the donor level capturing the electron and involved in the formation of the DW pinning center, and F is the Fermi level.

For the case defined by the condition

$$\exp\left(\frac{E_1}{kT}\right) \gg \frac{2(2\pi m_n kT)^{3/2}}{h^3 N_d}, \tag{2}$$

where m_n is the electron effective mass, i.e., for quite deep levels with a high concentration in the low-temperature region, the Fermi level in an impurity semiconductor is given by [12]

$$F = -\frac{E_1}{2} + kT\ln\left[\frac{N_d h^3}{2(2\pi m_n kT)^{3/2}}\right]^{1/2}. \tag{3}$$

Substituting expression (3) into expression (1), we obtain

$$n_d = \frac{N_d (N_d/N_c)^{1/2}}{1 + e^{-E_1/kT}}, \tag{4}$$

where the effective density of states in the conduction band

$$N_c = \frac{2(2\pi m_n kT)^{3/2}}{h^3}$$

only slightly depends on temperature.

As one can see from expression (4), under condition (2), no exponential temperature dependence of the number of donor levels occupied by electron is observed. Rather, the carrier density freezes at these centers at sufficiently low temperatures when

$$\exp\left(-\frac{E_1}{kT}\right) \ll 1,$$

n_d is not dependent on temperature at all.

In the case opposite to condition (2), i.e., for shallow levels with a low concentration and at moderately low temperatures, when the Fermi level is determined by the relationship [12]

$$F = kT\ln\frac{N_d h^3}{2(2\pi m_n kT)^{3/2}},$$

expression (1) takes the form

$$n_d = \frac{N_d^2}{N_c} e^{E_1/kT}. \tag{5}$$

Let us assume that shallow donors have captured the photoexcited electrons and are involved as bonding links in the formation of DW pinning centers. In this case, formulas (4) and (5), which characterize the filling of these donor levels with electrons at various temperatures, could be used to explain why the DW rigidity, which is defined as $1/\mu$, exponentially rises as the temperature increases at relatively high temperatures, while at relatively low temperatures, where RPFE appears, it is not dependent on temperature at all [5].

A schematic representation of the setup for photoconductivity measurements in a variable electric field is shown in Fig. 1. The sample, shaped as a rectangular parallelepiped with nonrectifying contacts placed into optical flow-through cryostat *1*, was connected in series with a ballast resistor R_l. An ac voltage with frequencies in the range from 5 kHz to 100 MHz was supplied to the sample and resistor using a G3-7A signal generator *2*. The light from source *3* (an incandescent 150-W lamp) fell onto the sample after passing through chopper *4* (at a frequency of 39 Hz) and monochromator *5* (IKS-21). To reduce mutual induction, electrical wires were lead out from the sample to the opposite sides. The resistance R_l was selected by taking a value that was 100-fold less than the smallest resistance of the sample in the entire temperature range under study. After demodulation using amplitude detector *6*, a high-frequency signal modulated by the photosensitivity of the sample with a frequency of mechanical interruption of light was supplied to the input of a U2-8 selective amplifier *7*. After synchronous detection with a V9-2 voltage transformer *8*, a photoconductivity signal, along with voltage from a thermocouple mounted close to the sample, was supplied to computer *10* through a CAMAC interface unit *9*. The monochromator was also scanned over wavelengths by the computer using the CAMAC unit, which controlled step motor *13*. For temperature monitoring, Shch300 digital voltmeter *12* was used. After the corresponding processing using the computer, the plots of the spectral and temperature dependences of ac photoconductivity were plotted using two-coordinate plotter *11* (XY-RECORDER endim 620.02).

Figure 2 shows the temperature dependences of conductivity at $h\nu = 1.2$ eV for $Ga_xGd_{1-x}Cr_2Se_4$ ($x = 0.025$) in a variable electric field. Curve *1* corresponds to a constant electric field, and curves *2–6* correspond to frequencies $f = 5 \times 10^3$, 10^4, 10^5, 10^6, and 10^8 Hz, respectively. Analysis of photoconductivity dispersion by the frequency of the field applied indicates that photoinduced hopping conduction takes place. The largest photoconductivity dispersion by frequency is observed in the immediate proximity of the Curie point (130 K). Close to 60 K, a complex dc photoconductivity peak is observed. In this region, an increase in dc photoconductivity is accompanied by a decrease in its hopping component. In the high-temperature wing of the peak, the times of rise and decay of photoconductivity are considerably shorter than in the low-temperature wing. Analysis of the kinetics of rise and decay of photoconductivity for this region shows that the kinetics has a thermally activated nature. Here, photoconductivity is associated with the thermal release of electrons from donor levels into the conduction band. At $T > 60$ K, shallow donors with large capture cross sections, which repeatedly capture nonequilibrium electrons, impede their relaxation via deeper recombination centers, thus increasing the effective lifetimes in the conduction band and the photoconductivity amplitude. However, at $T < 60$ K, the lifetimes at donor levels increases, while photoconductivity decreases. The activation energy of photoconductivity in this region is 0.068–0.088 eV. Below 40 K, where photoexcited electrons are frozen at shallow levels, the frequency dispersion of photoconductivity vanishes. According to [13], hopping conduction could not be realized via donor states that are completely occupied by electrons.

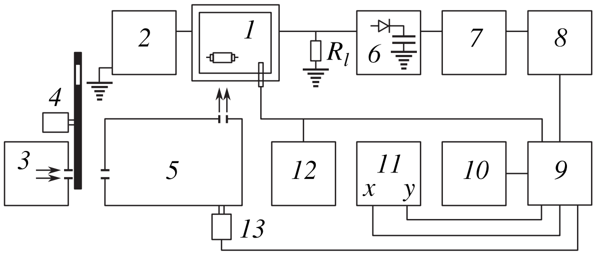

Fig. 1. Schematic representation of the setup for measuring photoconductivity in a variable electric field (see text for explanations).

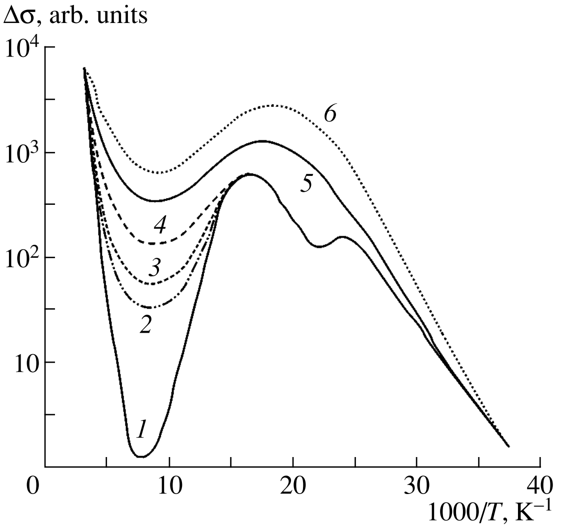

Fig. 2. Temperature dependences of photoconductivity of $Ga_xGd_{1-x}Cr_2Se_4$ ($x = 0.0025$) at various frequencies of the electric field applied and $h\nu = 1.2$ eV. Curve *1* corresponds to a constant electric field. Curves *2–6* correspond to frequencies f = (*2*) 5×10^3, (*3*) 10^4, (*4*) 10^5, (*5*) 10^6, and (*6*) 10^8 Hz.

Figure 3 shows temperature dependences of conductivity of lightly compensated $Ga_xGd_{1-x}Cr_2Se_4$ ($x = 0.01$) vacuum-annealed at 500 K for 4 h at various frequencies of the electric field applied. Curve *1* corresponds to a constant field, and curves *2–5* correspond to frequencies $f = 200$, 2×10^3, 2×10^4, and 2×10^5 Hz, respectively. These measurements were carried out using the setup shown in Fig. 1. Amplitude detector *6* and synchronous detector *8* were excluded from the setup, and the U2-8 amplifier was switched to broadband mode. To decrease the effect of the reactive conductivity of the sample with nonrectifying contacts, the latter were formed by point fusion of In. The contact areas were about 0.4 mm^2, and the sample length was about 5 mm. Curves *2–5* were obtained after subtracting the capacitor susceptance calculated for the corresponding frequencies from experimental values. To represent the results of studying conductivity in variable fields, a vacuum-annealed sample with a high impurity concentra-

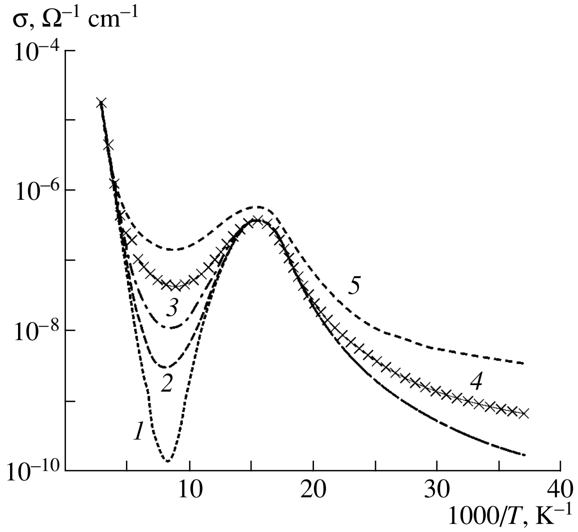

Fig. 3. Temperature dependences of conductivity of $Ga_xGd_{1-x}Cr_2Se_4$ ($x = 0.01$) at various frequencies of the electric field applied. Curve *1* corresponds to a constant electric field. Curves *2*–*5* correspond to frequencies f = (*2*) 200, (*3*) 2×10^3, (*4*) 2×10^4, and (*5*) 2×10^5 Hz.

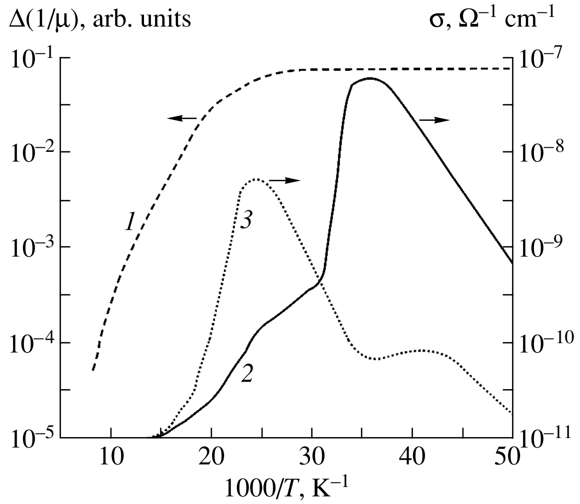

Fig. 4. Temperature dependences of (*1*) amplitude of the ferromagnetic effect $1/\mu$ for $Ga_xGd_{1-x}Cr_2Se_4$ ($x = 0.0025$) measured under continuous illumination and (*2*, *3*) thermally stimulated conductivity σ measured (*2*) after preliminary cooling the sample in the dark and (*3*) after cooling under illumination.

tion ($x = 0.01$) was chosen. As a result, for the samples with $x = 0.0025$, the temperature dependences of conductivity at all the frequencies studied decrease monotonically, similarly to undoped *p*-type samples, owing to the deeper Fermi level [14]. The temperature run of conductivity in these samples was of no interest since it was completely unrelated to the charge state of shallow donor levels. As in the case of photoconductivity (Fig. 2), the largest dispersion of conductivity of $Ga_xGd_{1-x}Cr_2Se_4$ ($x = 0.01$) in the variable field manifests itself in the vicinity of the Curie point, and a narrower peak manifests itself at 60 K. The sharp peak of dc conductivity and the decrease in its hopping component as the temperature approaches 60 K should apparently be attributed to the escape of electrons captured by shallow donors due to a decrease in the donors' activation energy during conduction-band splitting into spin-polarized subbands [15]. Conductivity falloff below 60 K is characterized by a gradual decrease in its activation energy from 0.12 to 0.04 eV.

The amplitude of PFE for $Ga_xGd_{1-x}Cr_2Se_4$ measured under modulated (39 Hz) light using the method described Vinogradova [7] is also peaked in the vicinity of 60 K. At the same measurement frequency, the peak for the samples with $x = 0.01$ is considerably sharper than for unannealed crystals with $x = 0.0025$. This peak in the selective amplification mode is largely caused by an increase in the rise time of the amplitude of PFE below 60 K. For PFE measurement under continuous light, its amplitude for $Ga_xGd_{1-x}Cr_2Se_4$ ($x = 0.0025$) rises exponentially from the Curie point to 40 K (Fig. 4, curve *1*). In this case, three portions of the increase in PFE with activation energies of 0.14, 0.088, and 0.024 eV are observed. Below 40 K, the amplitude of PFE is temperature-independent and RPFE is observed. In annealed samples with $x = 0.01$, PFE increases only to 60 K; at lower temperatures, RPFE is also observed. It would seem that in the two given cases the results should be the opposite. The larger x is, the larger should be the number of shallow donor levels per unit energy range in the band gap. In this case, if electrons are frozen at any shallow levels, even shallower levels should always exist; these can exchange electrons with the conduction band. Thus, the freezing temperature of PFE should decrease. However, the experiments carried out in this study show that an increase in the concentration of Ga impurity and V_{Se} vacancies above the values at which hopping conductivity manifests itself leads to a decrease in the amplitude and decay times of PFE and RPFE. It seems likely that the spatial delocalization of electrons captured by photoinduced centers also leads to delocalization of DWs, and, as a result, their inherent frequencies decrease. An oscillatory magnetic field with a frequency of 200 Hz can set a DW free from the pinning centers by directly affecting the DW [11]. In this case, the partial weakening of a DW under conditions of hopping conductivity is apparently associated with the emergence of a particular temperature-dependent stability of new centers of DW pinning. These centers include new donors, and photoexcited electrons hop to these donors. During such displacements of photoinduced centers, the DW acquires additional degrees of freedom, and its inherent frequency decreases. Therefore, the PFE continues to rise with decreasing temperature (down to the lowest temperatures) without the appearance of RPFE only for crystals without hopping conductivity.

Figure 4 shows temperature dependences of thermally stimulated conductivity measured for $Ga_xGd_{1-x}Cr_2Se_4$ ($x = 0.0025$) after cooling the sample in the dark (curve *2*) and under illumination (curve *3*). We can see two clearly pronounced features on these curves. If the sample is cooled in the dark, the low-temperature peak is higher than for cooling under illumination, whereas the high-temperature peak in the first case is lower than in the second case. These differences indicate that there is a competing mechanism of involvement of shallow donors in the capture of electrons. If the sample is cooled in the dark, the centers with larger capture cross sections capture the electrons first and block the capture at neighboring levels due to Coulomb interaction, despite their higher activation energies. If the samples are cooled under illumination, the centers with higher activation energy capture the electrons first, since the captures begin at higher temperatures. A similar phenomenon is observed in the temperature dependence of PFE measured in a self-excited oscillator mode. The frequency of the self-excited oscillator is higher when the sample is cooled in the dark than when it is cooled under illumination to the same temperature and at the same rate of cooling. This circumstance is indicative of the earlier (i.e., at higher temperatures) emergence of RPFE in the samples cooled under illumination. The thermally stimulated conductivity in the vicinity of the low-temperature features of the two cases depicted by curves *2* and *3* increases with activation energies of 0.06 and 0.04 eV, respectively. Analysis of the high-temperature wing of curve *3* yields a value of 0.083 eV. PFE decay with the same activation energy (0.086 eV) is observed at higher temperatures where thermally stimulated conductivity almost disappears; i.e., PFE levels off at temperatures where the thermally stimulated conductivity is clearly pronounced. The experimental results above and analysis of the published data allow us to conclude that shallow trapping levels of nonequilibrium electrons play a determining role in the formation of DW-pinning and PFE-active centers. These centers are not simply Cr^{2+} ions but complex associations or defect molecules that include these ions. The fact that PFE vanishes at high concentrations of V_{Se} vacancies indicates that acceptor centers, which disturb the saturation state of the sample relative to PFE, should also be involved in these associations. Here one should note that the amplitude of PFE for crystals grown from solution–melts is larger than that for crystals grown by liquid-phase transport. The amplitude of PFE for both types of crystals is peaked at the same Ga concentration. Therefore, it is logical to assume that there is a competitive mechanism for introducing donor centers into these formations, where Ga ions have priority over other donors. The capture cross section and activation energy of levels of Ga ions, which correspond to the operational frequency chosen, as well as the similarity of the electron states of the Ga^{3+} and Cr^{3+} ion cores, apparently determine this priority.

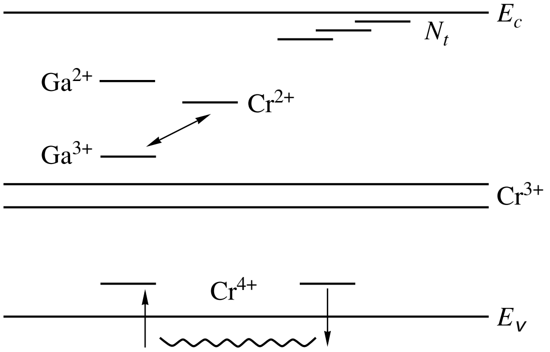

Fig. 5. Diagram of assumed electron transitions responsible for the emergence of the photoferromagnetic effect, residual ferromagnetic effect, and its infrared quenching in $Ga_xGd_{1-x}Cr_2Se_4$.

With such a priority dependence of the amplitude of PFE on the concentration of Ga donors, whose energy level lies 0.3–0.37 eV below the bottom of the conduction band [16, 17], the activation energy of this effect is in the range 0.024–0.14 eV (Fig. 4). The levels with this energy, in contrast to the rather deep Ga-related levels, can exchange electrons with the conduction band and give rise to reversible PFE in the range $40 \text{ K} < T < 130 \text{ K}$. The origin of these shallow donors, which exchange electrons with both the conduction band and Ga-related levels (and possibly with Cr ions), is apparently associated with the Coulomb interaction of the elements constituting the photoinduced centers of DW pinning. Therefore, in the range 40–130 K, the photoinduced charge drains to the conduction band even from deep levels of Cr^{2+} via the Ga ions and these shallow donors. This charge recombines when it leaves the conduction band, and the photoinduced centers are destroyed.

Figure 5 shows an approximate diagram of the energy levels responsible for PFE and RPFE and the IR quenching of these effects in $Ga_xGd_{1-x}Cr_2Se_4$. When absorbing the photon, the electron is transferred from a narrow 3*d* band of the Cr^{3+} ion to the conduction band above. From there, the electron is immediately captured by the Ga^{3+} level, thus transforming it into the Ga^{2+} state. Instead of the Cr^{3+} state, which loses an electron, a Cr^{4+} level emerges above the 3*d* band. This level, which exchanges electrons with the valence band, can migrate a little further from the Ga^{2+} ion, thus decreasing the probability of recombination. Because of the resulting difference in energy, the Ga^{2+} ion loses an electron either to the conduction band via shallow donors denoted by N_t in Fig. 5 or to the neighboring Cr^{3+} ion. In the first case, the electron from the conduction band recombines with the Cr^{4+} ion. In the second case, the Cr^{3+} ion transforms into the Cr^{2+} state, while the Ga^{2+} ion itself transforms again into the Ga^{3+} state with an energy below that of Cr^{2+}.

Thus, the Ga^{3+} and Cr^{2+} ions, as well as the N_t donors, collectivize the photoexcited electrons and form a unified photoinduced center with an unstable valence of Cr. As a result, the Cr^{2+} ion, which is antiferromagnetically oriented relative to the Cr^{3+} sublattice [3–11], has unstable spin orientation. The DW can be pinned by these spin instabilities, since its passage over the points with unstable spins is more energetically favorable. Such potential wells can give rise to higher DW rigidity and lower DMP. In this case, the local spin instability is higher and localizes DWs more rigidly compared with complexes that include other donors and intrinsic defects, for example, V_{Se}. This is apparently caused by the higher frequency of intracenter electron transitions in the Cr^{3+}–Ga^{2+} grouping (molecule) in Ga-containing crystals.

The activation energies determined from the analysis of thermally stimulated conductivity, DW rigidity (Fig. 4), and photoconductivity (Fig. 2) are in the range 0.024–14 eV and should be attributed to N_t donors. A necessary condition for reversible PFE is the multiple attachment of electrons to N_t centers with an additional charge maintained at Cr ions. At lower temperatures ($T < 40$ K), when attachment transforms into stable capture, the formation of defect molecules with stable antiferromagnetic spatial spin orientations leads to RPFE. In order to eliminate it, one should either heat the crystal or irradiate it with IR photons; as a result, electrons are transferred from photoinduced centers to the conduction band and then recombine.

Thus, our research has shown that the centers responsible for the ferromagnetic effect could be shallow donor levels that exchange electrons captured at them with Cr^{3+} ions. As a result of this exchange, the Cr ions acquire valence and spin instabilities that lead to the nonequilibrium pinning of the domain wall by them.

REFERENCES

1. W. Lems, R. J. Rijnierse, P. F. Bongers, and U. Enz, Phys. Rev. Lett. **21**, 1643 (1968).
2. V. G. Veselago and A. M. Prokhorov, in *Magnetic Semiconducting Spinels of the* $CdCr_2Se_4$ *Type* (Shtiintsa, Kishinev, 1978), p. 5.
3. T. G. Aminov, N. K. Bel'skiĭ, E. S. Vigileva, *et al.*, Neorg. Mater. **12**, 1297 (1976).
4. L. V. Anzina, V. G. Veselago, and S. G. Rudov, Pis'ma Zh. Éksp. Teor. Fiz. **23**, 520 (1976) [JETP Lett. **23**, 474 (1976)].
5. L. V. Anzina, V. G. Veselago, S. G. Rudov, *et al.*, Fiz. Tverd. Tela (Leningrad) **19**, 3001 (1977) [Sov. Phys. Solid State **19**, 1757 (1977)].
6. V. E. Makhotkin, G. I. Vinogradova, and V. G. Veselago, Pis'ma Zh. Éksp. Teor. Fiz. **28** (2), 84 (1978) [JETP Lett. **28**, 78 (1978)].
7. G. I. Vinogradova, in *Magnetic Semiconductors* (Nauka, Moscow, 1982), No. 139, p. 3.
8. G. I. Vinogradova and V. E. Makhotkin, in *Magnetic Semiconductors* (Nauka, Moscow, 1982), No. 139, p. 37.
9. L. V. Anzina and S. G. Rudov, in *Magnetic Semiconductors* (Nauka, Moscow, 1982), No. 139, p. 49.
10. V. G. Veselago and R. A. Doroshchenko, in *Magnetic Semiconductors* (Nauka, Moscow, 1982), No. 139, p. 67.
11. V. N. Kuznetsov and V. E. Makhotkin, in *Magnetic Semiconductors* (Nauka, Moscow, 1982), No. 139, p. 84.
12. L. S. Stil'bans, *Physics of Semiconductors* (Sovetskoe Radio, Moscow, 1967).
13. B. I. Shklovskiĭ and A. L. Éfros, Usp. Fiz. Nauk **117**, 401 (1975) [Sov. Phys. Usp. **18**, 845 (1975)].
14. A. A. Abdullaev and A. Z. Gadzhiev, Fiz. Tekh. Poluprovodn. (Leningrad) **25**, 30 (1991) [Sov. Phys. Semicond. **25**, 16 (1991)].
15. S. G. Stoyanov, M. N. Aliev, and S. P. Stoyanova, Solid State Commun. **18**, 1389 (1976).
16. L. N. Novikov, L. L. Golik, T. G. Aminov, and V. A. Zhegalina, Fiz. Tverd. Tela (Leningrad) **22**, 3032 (1980) [Sov. Phys. Solid State **22**, 1771 (1980)].
17. K. P. Belov, L. I. Koroleva, S. D. Batarova, *et al.*, Pis'ma Zh. Éksp. Teor. Fiz. **22**, 304 (1975) [JETP Lett. **22**, 140 (1975)].

Translated by N. Korovin

Semiconductors, Vol. 38, No. 7, 2004, pp. 769–774. Translated from Fizika i Tekhnika Poluprovodnikov, Vol. 38, No. 7, 2004, pp. 802–807.
Original Russian Text Copyright © 2004 by Brudnyĭ, Boĭko, Kamenskaya, Kolin.

ELECTRONIC AND OPTICAL PROPERTIES OF SEMICONDUCTORS

Electrical Properties and Limiting Position of the Fermi Level in InSb Irradiated with Protons

V. N. Brudnyĭ*^, V. M. Boĭko, I. V. Kamenskaya*, and N. G. Kolin**^^**
**Kuznetsov Physicotechnical Institute, pl. Revolyutsii 1, Tomsk, 634050 Russia*
^e-mail: brudnyi@ic.tsu.ru
***Karpov Institute of Physical Chemistry (Obninsk Branch), Obninsk, Kaluga oblast, 249033 Russia*
^^e-mail: ngkolin@mail.ru.com

Submitted November 11, 2003; accepted for publication November 27, 2003

Abstract—The results of experimental and simulation studies of electrical parameters and the limiting position of the Fermi level in metallurgically and transmutationally doped InSb irradiated with protons (10 MeV, 2×10^{16} cm^{-2}, 300 K) are reported. It is shown that the limiting electrical parameters of irradiated InSb correspond to a *p*-type material. Special features of the annealing of radiation defects are studied in the temperature range 20–500°C. *© 2004 MAIK "Nauka/Interperiodica".*

1. INTRODUCTION

Irradiation with protons is used to form *p*–*n* junctions, high-resistivity regions, and *n*-type regions in InSb. In addition, the use of proton radiation makes it possible to obtain material with a high density of radiation defects, which is important for studying the physics of radiation damage and for estimating the so-called limiting (steady-state) parameters of an irradiated semiconductor. Knowledge of these parameters is necessary for predictive estimates of the material's behavior under conditions of high-energy radiation. Studies of radiation defects and their thermal stability in InSb are also important for the development of methods of transmutational doping of this material.

Even early studies of InSb showed that the electrical properties of this material are very sensitive to irradiation with protons. However, the majority of researchers studied thin layers obtained using irradiation with protons with energies of 60–300 keV, in which case the damaged regions of the material were highly nonuniform over the depth and, furthermore, the surface and substrate had a significant effect on the parameters under study [1–3]. At the same time, irradiation with high-energy 17.5 [4] and 50 MeV [5] protons were carried out with relatively low integrated fluxes of protons (10^{15} and 7×10^{15} cm^{-2}).

In this paper, we report the results of studying the electrical properties of bulk InSb samples and special features of the annealing of radiation defects in these samples irradiated with high-energy protons. We studied for the first time the effect of proton radiation on the electrical parameters of InSb doped using nuclear transmutations. It is well known that transmutational doping of InSb makes it possible to obtain *n*-type material with a high uniformity of electrical properties over the volume of the material (with nonuniformity no higher than a few percent) due to the introduction of donor impurities Sn (97.9%) and Te (2.1%), which is of great practical interest [6].

2. EXPERIMENTAL

We studied the electrical properties of *n*- and *p*-InSb crystals that were grown by the Czochralski method and were doped conventionally with doping-impurity concentrations in the range from 3×10^{13} cm^{-3} (*p*-InSb) to 4×10^{14} cm^{-3} (*n*-InSb) at 77 K; samples of transmutationally doped InSb (TD-InSb) with *n*-type conductivity ($n = 1 \times 10^{15}$–2×10^{16} cm^{-3}) were also studied. As the starting material for obtaining the TD-InSb samples, we used nominally undoped InSb single crystals (grown by the Czochralski method) with electron concentrations $n = (1–2) \times 10^{14}$ cm^{-3} (sample 3), $n = (7–9) \times 10^{13}$ cm^{-3} (sample 4), and $n \leq 10^{14}$ cm^{-3} (sample 5). The TD-InSb samples were obtained by irradiating InSb with reactor neutrons in a VVR-ts water-cooled and water-moderated reactor at the Karpov Institute of Physical Chemistry, Obninsk. After the irradiated material was cooled in order to let the induced radioactivity decay, the samples were subjected to heat treatment for 1 h at 450°C.

The samples were irradiated with protons ($j = 5 \times 10^{-8}$ A/cm^2, $E = 10$ MeV, and $D = 5 \times 10^{12}$–2×10^{16} cm^{-2}) at temperatures close to 295 K using the cyclotron at the Institute of Nuclear Physics, Tomsk. We used samples with a thickness of ~200 μm, which is smaller than the mean projected range $R_p \approx 300$ μm for 10-MeV protons in InSb (the value of R_p had been previously determined from layer-by-layer measurements [7]). The parameters of InSb before and after irradiation with the highest dose (2×10^{16} cm^{-2}) of 10-MeV protons are

Table 1. Parameters of the starting InSb crystals and those irradiated with protons ($D = 2 \times 10^{16}$ cm^{-2})

Sample no.	Material	Parameters before proton irradiation			Parameters after irradiation		
		n, p	ρ	μ_H	R_H	ρ	μ_H
		cm^{-3}	Ω cm	cm^2 V^{-1} s^{-1}	cm^3/C	Ω cm	cm^2 V^{-1} s^{-1}
1	*n*-InSb–14 (Te)	1.4×10^{14}	8.0×10^{-2}	5.58×10^5	4.60×10^5	3.06×10^2	1.50×10^3
2	*n*-InSb–13 (Te)	4.3×10^{14}	3.0×10^{-2}	4.80×10^5	4.01×10^5	2.88×10^2	1.39×10^3
3	TD-InSb–3 (Sn)	1.0×10^{15}	2.0×10^{-2}	3.12×10^5	3.30×10^5	2.41×10^2	1.37×10^3
4	TD-InSb–5 (Sn)	1.2×10^{15}	1.68×10^{-2}	3.10×10^5	3.40×10^5	2.3×10^2	1.48×10^3
5	TD-InSb–4 (Sn)	$(1.0–1.8) \times 10^{16}$	5.0×10^{-3}	1.25×10^5	2.10×10^5	1.86×10^2	1.13×10^3
6	*p*-InSb–15 (Zn)	2.97×10^{13}	5.54×10^1	3.80×10^3	5.38×10^5	5.15×10^2	1.04×10^3

listed in Table 1. All the measurements were carried out at $T = 77$ K.

Isochronous annealing ($\Delta T = 20$°C, $\Delta t = 10$ min) of the starting and irradiated InSb samples was performed in a vacuum chamber in the temperature range 20–500°C; the samples were etched for 10–15 s in a tartaric acid etchant with the composition 25% $C_4H_6O_6 : H_2O_2 : HF = 18 : 14 : 1$.

The quantities R_H and ρ for InSb were calculated in the two-band approximation:

$$R_H = (1/q)(p - nb^2)/(p + nb)^2,$$

$$\rho = q(n\mu_n + p\mu_p).$$

Here, $b = \mu_n/\mu_p \approx 10^2$ is the ratio of the Hall mobilities of free electrons (μ_n) to holes (μ_p) in InSb, q is the elementary charge, R_H is the Hall coefficient, and ρ is the resistivity; the other designations are generally accepted.

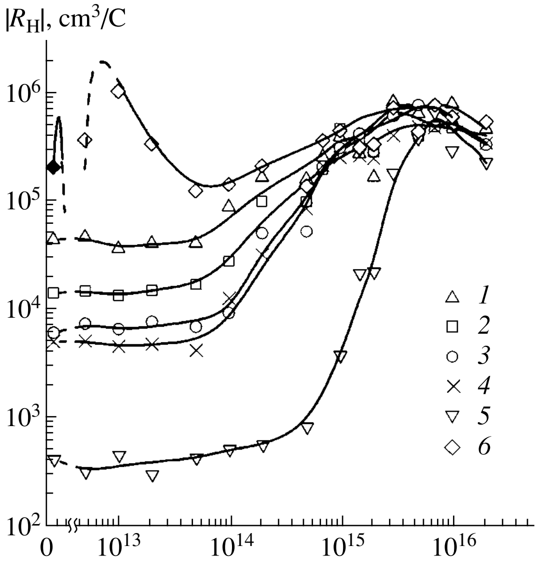

Fig. 1. Variation in the Hall coefficient $|R_H|$ for InSb samples irradiated with 10-MeV protons. The curves in Figs. 1–4 are numbered according to the numbers of the samples in Table 1.

3. RESULTS

The dose dependences of the Hall coefficient R_H are indicative of the compensation of initial electrical activity in the starting *n*-InSb samples and the *p*–*n* conversion in the starting *p*-InSb sample (Fig. 1). This behavior is generally consistent with published data on the irradiation of InSb with protons [4, 5] and with 1-MeV [8, 9] and 50-MeV [10] electrons at a temperature of about 300 K. In Fig. 1 and other figures, the open and closed symbols correspond to *n*- and *p*-InSb, respectively. In contrast to the published data, a further increase in the value of $|R_H|$ to $(6–8) \times 10^5$ cm^3/C with dose $D = 10^{16}$ cm^{-2} is observed in the dependences $R_H(D)$ after the initial portion of leveling-off. This behavior of R_H occurs not only in initial *n*-InSb but also in initial *p*-InSb that acquired *n*-type conductivity as a result of irradiation. This observation indicates that compensation of *n*-type conductivity and a shift of the Fermi level to the valence band take place in all the samples studied with proton doses that exceed 10^{14} cm^{-2}. The corresponding variations in the Hall mobility of charge carriers $\mu_H = R_H\sigma$ are shown in Fig. 2. It is worth noting that the values of $\mu_H(D)$ are nearly identical in all the studied samples after proton irradiation with $D > 10^{14}$ cm^{-2}; i.e., the kinetic parameters of the irradiated samples are completely controlled by radiation defects produced by proton radiation and do not depend on the parameters of starting crystals. These studies show that the radiation defects of both donor and acceptor type are produced in InSb as a result of irradiation with protons at 300 K. The magnitude of the effect of these defects on the electrical properties of the material depends on the doping level and the type of conductivity of the crystal under study. It is interesting that radiation-produced acceptors are more efficient in initial *n*-InSb in the entire range of proton-radiation doses. In contrast, in the case of initial *p*-InSb, radiation-produced donors are more efficient at the early stages of irradiation (up to doses of ~6×10^{14} cm^{-2}), whereas the

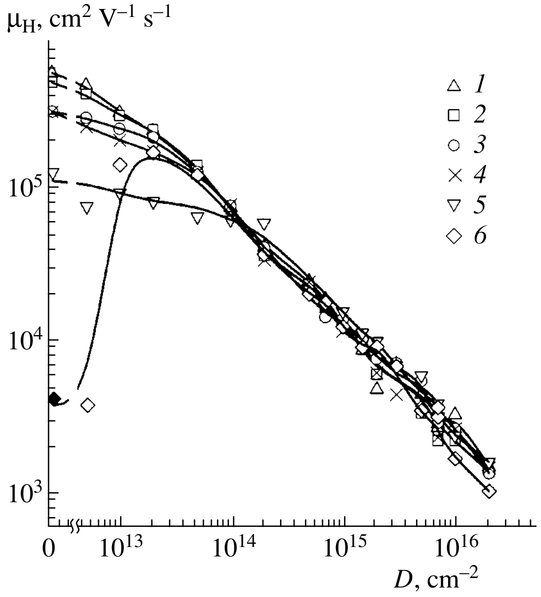

Fig. 2. Variation in the quantity $|R_H\sigma|$ in InSb samples irradiated with 10-MeV protons.

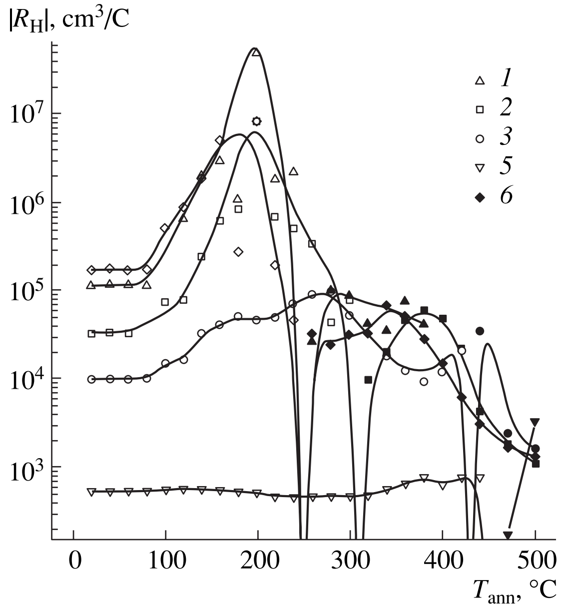

Fig. 4. Dependences of $|R_H|$ on the temperature of isochronous (10 min) annealing for InSb crystals irradiated with 10-MeV protons ($D = 1 \times 10^{14}$ cm^{-2}).

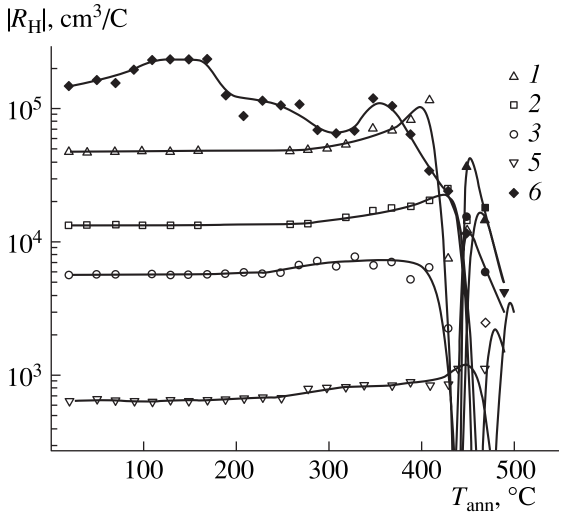

Fig. 3. Dependences of $|R_H|$ on the temperature of isochronous (10 min) annealing for InSb starting crystals.

radiation defects of acceptor type are dominant at higher doses (as in the starting samples of *n*-InSb). The donor–acceptor behavior of radiation defects in InSb is confirmed by studies of the annealing of the irradiated material.

Figures 3 and 4 illustrate the results of isochronous annealing of the starting and irradiated InSb crystals, respectively. Compensation of the initial conductivity at $T_{ann} \geq 260$–300°C and the *n*–*p* conversion at $T_{ann} =$ 420–450°C is observed in the unirradiated *n*-InSb samples. The hole concentration increases with annealing temperature when T_{ann} is higher than ~350°C. These phenomena have been reported in previous publications and are attributed to the formation of quenched-in acceptors in InSb as a result of high-temperature heat treatment [11]. We observe a consecutive change in the sign of the Hall coefficient (the n–p–p^+ conversion of the conductivity type) in the proton-irradiated samples that initially had *n*-type conductivity and are subjected to heat treatment in the temperature range 20–500°C. Specifically, radiation-produced donors are predominantly annealed out at 60–300°C, radiation-produced acceptors are annealed out at 300–400°C, and quenched-in acceptors are intensively formed at 420–460°C (Fig. 4). Similarly, we observe p–n–n^+ conversion of conductivity in InSb with initially *p*-type conductivity; i.e., an inverse *n*–*p* conversion of conductivity occurs at about 300°C, and predominant annealing of radiation-produced donors with a subsequent increase in the hole concentration to ~5×10^{15} cm^{-3} due to the formation of quenched-in acceptors occurs at heat-treatment temperatures higher than 350°C. It is noteworthy that a shift in the stages of isochronous annealing to higher temperatures is observed as the integrated flux of protons is increased or the initial doping level of InSb decreased.

4. DISCUSSION

A specific feature of previous studies of the electrical properties of irradiated InSb is the observation of a leveling-off portion in the $\rho(D)$ and $R_H(D)$ curves after irradiation with fast neutrons at 300 [12] and 77 K [13] and with 10-MeV electrons at 300 K [10] and 4.5-MeV electrons at 80 K [14]. It is especially worth noting that *n*-type samples with electron concentrations 3×10^{12}–

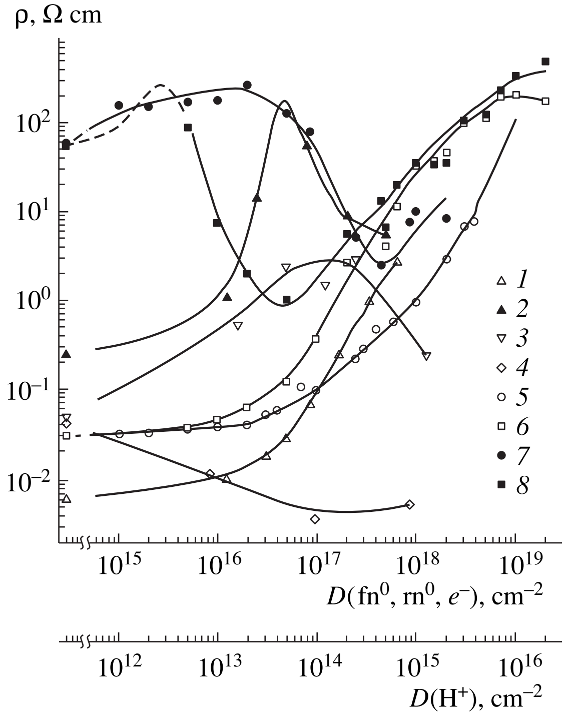

Fig. 5. Dose dependences of resistivity of InSb samples irradiated with fast neutrons: (*1*) [12], (*2*) [12], and (*3*) [19]; (*4*) [6] sample irradiated with full-spectrum reactor neutrons and then annealed for 20 min at 450°C; (*5*, *7*) samples irradiated with 1-MeV electrons; and (*6*, *8*) samples irradiated with 10-MeV protons.

6×10^{14} cm^{-3} can be obtained as a result of irradiation with fast neutrons at 77 and 300 K [12, 13] and with electrons at 300 K [8]; *p*-type samples with a free-hole concentration of 5×10^{13}–3×10^{15} cm^{-3} were obtained as a result of low-temperature (77–200 K) irradiation with γ-ray photons and electrons [14–17]. It is noteworthy that the estimated positions of the Fermi level in the region of the leveling-off of the dose dependences ρ(*D*) and $R_H(D)$ for irradiation temperatures of about 80, 200, and 300 K are approximately E_v + 0.03 eV, E_v + 0.08 eV, and E_c – 0.03 eV, respectively [9, 10, 14]. The characteristic features of the electrical parameters and *n*-type conductivity of InSb irradiated with fast neutrons or 50-MeV electrons were related to the accumulation of defects of the cluster type, although the electronic structure of such clusters in InSb is still unknown. In addition, we should note that *n*-InSb samples were also obtained by irradiation with 1-MeV electrons at 300 K [8]. According to most researchers, the governing factor that controls the type of radiation defects that accumulate in the crystal lattice and, accordingly, the properties of irradiated InSb is the temperature T_{rad} at which the irradiation is carried out. At present, data on the radiation-defect spectrum in InSb include the states with energy levels at about E_c – 0.03 eV and E_v + (0.03–0.06) eV and the states near the midgap [10, 14, 15, 18]. Furthermore, it is noted that the fraction of defects whose energy levels are in the upper half of the band gap increases as the irradiation temperature increases or if the sample irradiated at low temperatures is heated. Presumably, this is what causes the limiting Fermi level in InSb to shift to the conduction band as the irradiation temperature increases.

However, as was shown in subsequent studies of InSb irradiated with high integrated fluxes of fast ($E >$ 0.1 MeV) neutrons [19] and protons and electrons (the results of this study), the region of leveling-off on curves ρ(*D*) and $R_H(D)$ does not correspond at all to the limiting electrical parameters of irradiated InSb. Further irradiation of such material leads to changes in the dependences ρ(*D*) and $R_H(D)$. In this case, the resistivity of InSb irradiated with high integrated fluxes of fast neutrons decreases compared to its value in the leveling-off region ρ(*D*), whereas the values of both ρ and R_H increase after irradiation with 1-MeV electrons and 10-MeV protons. The results of our measurements at $T = 77$ K and those reported in previous publications (on irradiation with fast [12, 19] and reactor [6] neutrons at $T \approx 300$ K) are shown in Fig. 5.

It follows from these data that radiation defects of acceptor type are dominant in starting *n*-InSb and those of donor type are dominant in starting *p*-InSb after irradiation with low integrated fluxes of all kinds of particles ($T_{rad} \approx 300$ K). It is noteworthy that irradiation with neutrons inevitably gives rise to *n*-type material, which can be related to the effect of additional transmutational doping of InSb with Sn ($N_{Sn} \approx 0.2 D_{fn^0}$ [19], where D_{fn^0} is the integrated flux of fast neutrons). Apparently, this circumstance leads to a decrease in the resistivity of InSb as a result of irradiation with high fluxes of fast neutrons. In Fig. 5, we also show the dependence ρ(*D*) in *n*-InSb irradiated with a full-range spectrum of reactor neutrons in a VVR-ts (water-cooled and water-moderated) reactor at the Karpov Institute of Physical Chemistry (Obninsk Branch) and then annealed for 20 min at 450°C. As a result, most of the tin impurity, $N_{Sn} \approx 2.9 D_{rn^0}$, was transferred to the electrically active state [6] (here, D_{rn^0} is the total integrated flux of reactor neutrons). In contrast to irradiation with neutrons, the values of ρ and R_H increase as the dose of irradiation with electrons and protons increases in the region of high doses. This behavior indicates that acceptor-type radiation defects are predominantly effective and that the Fermi level shifts deeper into the band gap in all the materials under study.

Note that the limiting parameters of irradiated InSb were associated in previous publications with the emergence of leveling-off portions in the dose dependences ρ(*D*) and $R_H(D)$. The fact that these portions exist was in itself attributed to the establishment of equilibrium between the processes of generation and annealing of radiation defects under the given conditions of irradiation. Numerous experimental studies have shown that the limiting (steady-state) position of the Fermi level (hereinafter F_{sat}) is always attained in semiconductors irradiated with high doses of particles when the concentration of the radiation defects produced exceeds that of the initial doping impurities. The value of F_{sat} is independent of the irradiation conditions (i.e., of the spectrum of defects produced by high-energy radiation) and is, as a result, a characteristic (intrinsic) parameter of the crystal [20]. Thus, the behavior of InSb under high-energy radiation and the limiting electrical parameters (the type of conductivity type and position of the Fermi level) have not yet been adequately studied, and this is stimulating further experimental and theoretical studies of the problem under consideration.

5. SIMULATION ESTIMATES

The theoretical models developed until now for estimating F_{sat} are based on identifying F_{sat} with the position of the branching point in the complex energy structure of the crystal (i.e., with the energy where the donor–acceptor character of defect-related states in the semiconductor changes). This position of the branching point is identified in different heuristic models with the energy position of the level of charge neutrality E_{CNL} for defect-related states in the crystal [21], with the position of the neutrality level for a local defect-related amphoteric center E_{LNL} [22], and with the energy position of the most localized (deepest) defect-related state E_{DL} in the crystal in an energy range in the vicinity of the crystal's narrowest band gap [23, 24].

Calculated values of the corresponding quantities for InSb are listed in Table 2. In addition, Table 2 lists the position of the so-called midgap energy $\langle E_G \rangle/2$, where $\langle E_G \rangle$ is the average energy interval between the lower conduction band and the upper valence band within the first Brillouin zone of the crystal. Since in the case of a one-dimensional isotropic crystal with energy gap $\langle E_G \rangle$ the position of the branching point corresponds to $\langle E_G \rangle/2$ [25], this position can also be identified with F_{sat}. In general, relations between the calculated values of E_{CNL}, E_{LNL}, E_{DL}, and $\langle E_G \rangle/2$ for InSb are similar to those for other semiconductors and reveal a spread in the numerical values obtained using different models. In contrast to wide-gap semiconductors, such a spread in the calculated values is critical for InSb owing to the small value of the band gap E_g for this material. However, the results of simulations indicate in general that the limiting Fermi level is preferentially located in the vicinity of the midgap or in the lower half of the band gap of irradiated InSb. This observation is consistent with the results of experimental studies of low-temperature (77–200 K) irradiation of InSb with γ-ray photons and electrons if annealing most of the radiation defects can be avoided [14–17].

The aforementioned theoretical models relate the calculated values of E_{CNL}, E_{LNL}, E_{DL}, and $\langle E_G \rangle/2$ in an irradiated semiconductor to special features of the energy-band spectrum in a bulk crystal rather than to the characteristics of structural damage. As a result, the limiting electrical parameters of an irradiated semiconductor are insensitive to changes in the type of radiation defect and, consequently, to the conditions of irradiation and history of the material. Although the radiation-defect spectrum depends on the conditions of irradiation, a specific set of defects is always formed in the crystal. This set of defects ultimately ensures a shift of the Fermi level to the E_{sat} position when the concentration of radiation defects exceeds that of the doping impurities. This statement is confirmed, for example, by similar studies of GaAs where high-resistivity GaAs samples were obtained using irradiation with electrons at temperatures of about 300 and 570–670 K [26, 27] owing to the generation of different radiation defects (so-called *E* and *H* traps are predominantly formed at ~300 K, whereas *P* traps are mostly generated at 570–670 K) [28, 29]. Note that, in order to obtain high-resistivity GaAs under conditions of irradiation with electrons at elevated temperatures, it was only necessary to increase the integrated flux of electrons by a factor of 25.

Table 2. Calculated values of E_g, E_{CNL}, E_{LNL}, E_{DL}, and $\langle E_G \rangle/2$ (eV) for InSb at $T = 0$ K. The values of E_{CNL}, E_{LNL}, E_{DL}, and $\langle E_G \rangle/2$ are reckoned from the top of the valence band

E_g	E_{CNL}	E_{LNL}	E_{DL}	$\langle E_G \rangle/2$
0.24	0.03	0.12	0.17	0.05

Moreover, it has been shown experimentally [30] that one can also obtain *p*-InSb as a result of irradiation of *n*-InSb with (4–8)-MeV electrons at 300 K (as in the case of low-temperature irradiation) if the subsequent measurements of the parameters of the samples are performed at temperatures near 4.2 K. In this case, the point of *n*–*p* conversion shifts to higher temperatures as the integrated electron flux increases. This observation also supports the conclusion that the leveling-off portions in the $\rho(D)$ and $R_H(D)$ curves (also observed in previous studies) correspond to certain intermediate parameters of irradiated InSb rather than to the limiting parameters. As a result of the high efficiency of annealing of radiation defects in InSb at $T \approx 300$ K, higher doses of irradiation are needed to attain limiting (steady-state) values of the electrical parameters of InSb in the case of irradiation at room temperature. We may also assume that the appearance of a peak in the curves $R_H(D)$ at $D \approx 10^{16}$ cm^{-2} for InSb irradiated with protons (Fig. 1) indicates the transition of InSb to *p*-type conductivity with high integrated fluxes of H^+ ions.

Thus, the experimental and simulation studies indicate that the limiting state of irradiated InSb should correspond to a material with *p*-type conductivity (except for irradiation with neutrons) irrespective of the irradiation temperature if the corresponding concentration of radiation defects is attained.

6. CONCLUSION

Experimental studies show that *p*-type conductivity in InSb is attained rather rapidly under low-temperature (77–200 K) conditions of irradiation (except for irradiation with fast neutrons), when the majority of radiation defects in the crystal lattice are not mobile. An increase in the temperature of the sample to 300 K leads to the annealing of a large fraction of the radiation defects; however, even in this case, a concentration of radiation defects that is sufficiently high to obtain *p*-type material can be attained. *p*-InSb samples can also be obtained under conditions of high-temperature irradiation with protons or as a result of irradiating InSb at 300 K with subsequent annealing at temperatures of 230–250°C. This circumstance makes it possible to single out three groups of radiation defects in InSb. The first group is formed by radiation defects of predominantly acceptor type that are responsible for the *p*-type conductivity of InSb irradiated at low temperatures ($T \leq 200$ K). The second group is formed by donor-type radiation defects that are stable up to annealing temperatures of about 230–250°C. The third group is composed of acceptor-type radiation defects that are annealed out at temperatures of 320–370°C. These different defects are responsible for the observed special features of the electrical properties of InSb irradiated (or annealed) at various temperatures. We did not observe any differences between variations in the properties of conventionally and transmutationally doped InSb as a result of irradiation with H^+ ions (at 300 K) and subsequent annealing.

ACKNOWLEDGMENTS

This study was supported by the International Science and Technology Center as part of the “Highly Stable and Radiation-Resistant Semiconductors” program, project no. 1630.

REFERENCES

1. I. Fujisawa, Jpn. J. Appl. Phys. **19**, 2137 (1980).
2. N. Y. Chernyshova, G. A. Kachurin, and V. A. Bogatyriov, Phys. Status Solidi A **47**, K5 (1978).
3. L. V. Lezheĭko, E. V. Lyubopytova, and V. I. Obodnikov, Fiz. Tekh. Poluprovodn. (Leningrad) **16**, 1638 (1982) [Sov. Phys. Semicond. **16**, 1046 (1982)].
4. F. A. Zaitov, O. V. Gorshkova, V. N. Ovanesov, and A. Ya. Polyakov, Fiz. Tekh. Poluprovodn. (Leningrad) **14**, 398 (1980) [Sov. Phys. Semicond. **14**, 234 (1980)].
5. G. A. Vikhliĭ, A. Ya. Karpenko, I. G. Megela, and L. I. Tarabrova, Ukr. Fiz. Zh. **27**, 1104 (1982).
6. N. G. Kolin, D. I. Merkurisov, and S. P. Solov’ev, Fiz. Tekh. Poluprovodn. (St. Petersburg) **33**, 774 (1999) [Semiconductors **33**, 712 (1999)].
7. V. N. Davydov, Izv. Vyssh. Uchebn. Zaved., Fiz. **42** (9), 37 (1999).
8. V. N. Brudnyĭ and I. V. Kamenskaya, Izv. Vyssh. Uchebn. Zaved., Fiz. **34** (7), 99 (1991).
9. N. A. Vitovskiĭ, T. V. Mashovets, and O. V. Oganesyan, Fiz. Tekh. Poluprovodn. (Leningrad) **12**, 2143 (1978) [Sov. Phys. Semicond. **12**, 1277 (1978)].
10. N. A. Vitovskiĭ, T. V. Mashovets, O. V. Oganesyan, and N. Kh. Pambukhchan, Fiz. Tekh. Poluprovodn. (Leningrad) **12**, 1861 (1978) [Sov. Phys. Semicond. **12**, 1106 (1978)].
11. M. N. Kevorkov, A. N. Popkov, V. S. Uspenskiĭ, *et al.*, Izv. Akad. Nauk SSSR, Neorg. Mater. **16**, 2114 (1980).
12. H. J. W. Cleland and J. H. Crawford, Phys. Rev. **95**, 1177 (1954).
13. L. K. Vodop’yanov and N. I. Kurdiani, Fiz. Tverd. Tela (Leningrad) **7**, 2749 (1965) [Sov. Phys. Solid State **7**, 2224 (1965)].
14. L. W. Aukerman, Phys. Rev. **115**, 1125 (1959).
15. T. V. Mashovets and Z. Yu. Khansevarov, Fiz. Tverd. Tela (Leningrad) **8**, 1690 (1966) [Sov. Phys. Solid State **8**, 1350 (1966)].
16. S. Myhra, Phys. Status Solidi A **49**, 285 (1978).
17. S. Myhra, Radiat. Eff. **59**, 1 (1981).
18. S. D. Koumitz, Solid State Commun. **64**, 1171 (1987).
19. N. G. Kolin, D. I. Merkurisov, and S. P. Solov’ev, Fiz. Tekh. Poluprovodn. (St. Petersburg) **33**, 927 (1999) [Semiconductors **33**, 847 (1999)].
20. I. N. Brudnyĭ, V. G. Voevodin, O. V. Voevodina, *et al.*, Izv. Vyssh. Uchebn. Zaved., Fiz. **41** (8), 26 (1999).
21. V. N. Brudnyĭ and S. N. Grinyaev, Fiz. Tekh. Poluprovodn. (St. Petersburg) **32**, 315 (1998) [Semiconductors **32**, 284 (1998)].
22. V. N. Brudnyi, S. N. Grinyaev, and V. E. Stepanov, Physica B (Amsterdam) **212**, 429 (1995).
23. V. N. Brudnyĭ, S. N. Grinyaev, and N. G. Kolin, Fiz. Tekh. Poluprovodn. (St. Petersburg) **37**, 557 (2003) [Semiconductors **37**, 537 (2003)].
24. V. N. Brudnyĭ, S. N. Grinyaev, and N. G. Kolin, Materialovedenie **3** (72), 17 (2003).
25. J. J. Rehn and W. Kohn, Phys. Rev. B **9**, 1981 (1974).
26. V. S. Vavilov, L. F. Zakharenkov, V. V. Kozlovskiĭ, *et al.*, Izv. Vyssh. Uchebn. Zaved., Fiz. **32** (9), 110 (1989).
27. V. N. Brudnyĭ, M. D. Vilisova, and L. P. Porokhovnichenko, Izv. Vyssh. Uchebn. Zaved., Fiz. **35** (10), 57 (1992).
28. V. N. Brudnyi and V. V. Peshev, Phys. Status Solidi A **105**, K57 (1988).
29. V. V. Kozlovskiĭ, T. I. Kol’chenko, and V. M. Lomako, Fiz. Tekh. Poluprovodn. (Leningrad) **25**, 1169 (1991) [Sov. Phys. Semicond. **25**, 707 (1991)].
30. E. P. Skipetrov, V. V. Dmitriev, F. A. Zaitov, *et al.*, Fiz. Tekh. Poluprovodn. (Leningrad) **20**, 1787 (1986) [Sov. Phys. Semicond. **20**, 1120 (1986)].

Translated by A. Spitsyn

Semiconductors, Vol. 38, No. 7, 2004, pp. 775–777. Translated from Fizika i Tekhnika Poluprovodnikov, Vol. 38, No. 7, 2004, pp. 808–810.

ELECTRONIC AND OPTICAL PROPERTIES OF SEMICONDUCTORS

Anomalous Solubility of Implanted Nitrogen in Heavily Boron-Doped Silicon

D. I. Tetelbaum*, E. I. Zorin†, and N. V. Lisenkova

Nizhni Novgorod Physicotechnical Institute at Lobachevskii State University,
pr. Gagarina 23/5, Nizhni Novgorod, 603950 Russia

**e-mail: Tetelbaum@phys.unn.ru*

Submitted October 30, 2003; accepted for publication December 3, 2003

Abstract—It is established that an anomalously high electron concentration can be attained in heavily boron-doped silicon using ion implantation followed by implantation with nitrogen at an elevated temperature; the concentration of electrons can exceed that of boron. A model of this phenomenon is suggested that is based on the reaction of displacing boron atoms from the lattice sites by silicon self-interstitials with subsequent filling of the vacancies with nitrogen atoms (so that donor centers are formed). *© 2004 MAIK “Nauka/Interperiodica”.*

1. INTRODUCTION

It is well known that nitrogen (in contrast to other donor impurities of Group V elements) usually features a low solubility at the lattice sites and, when conventionally implanted into silicon, cannot give rise to a charge-carrier (electron) concentration higher than ~10^{18} cm^{-3} [1]. At the same, Kleinfelder *et al.* [2] have shown that it is possible to attain a much higher solubility and electrical activity of nitrogen. The method of staining a *p*–*n* junction was employed [2] to find that ion implantation of nitrogen into heavily boron-doped silicon can be used to form *p*–*n* junctions even at boron concentrations higher than 10^{20} cm^{-3}. This fact may indicate that the solubility of nitrogen at the lattice sites increases drastically in the presence of boron. Unfortunately, the results obtained in [2] have never been subsequently verified. It is noteworthy that the method of staining is indirect and does not provide data on the electron concentration in doped layers. A contrast in the staining can result from the neutralization of boron, for example, as a consequence of the formation of either B–N complexes or an *n*-type layer with a low concentration of electrons. It was found later [3] that anomalously high electron concentrations could be attained in the region of location of boron atoms in the case of combined implantation of both boron and nitrogen; in this case, the volume concentrations of electrons and boron atoms were on the same order of magnitude. In [3] both impurities were implanted at room temperature and the concentration profiles of boron and nitrogen immediately after implantation were quite different. The results were interpreted based on the idea that the donor properties are attributed to Si_3N_4 precipitates rather than to nitrogen atoms at the lattice sites.

We show in this study that, under certain conditions of combined boron and nitrogen implantation, the electron concentration can far exceed the boron concentration. We also suggest an explanation of this phenomenon on the basis of the Watkins mechanism [4].

The possibility of obtaining a high concentration of charge carriers as a result of ion implantation with nitrogen is of practical importance since nitrogen is obviously preferable to phosphorus or arsenic (all other factors being equal) when silicon is doped with donors using ion implantation. Efficient nitrogen implantation may be especially important in the case of doping Si nanocrystals in order, for example, to improve their luminescent properties for applications in optoelectronics [5, 6] when high impurity concentrations are required.

2. EXPERIMENTAL

Wafers of *p*-Si (ρ = 15 Ω cm) grown by the Czochralski method were first subjected to the conventional treatment. The wafers were then implanted with 40-keV boron ions at doses $\Phi = 3 \times 10^{13}$–3×10^{15} cm^{-2}. After boron implantation, the samples were heated to 650°C and implanted with nitrogen ions at doses that exceeded those for boron implantation by an order of magnitude. The samples were then annealed for 30 min at 800°C in an argon atmosphere. Average concentrations of the implanted boron atoms and of the charge carriers in the implantation layer after the dual implantation were calculated by dividing the dose and the Hall sheet concentration of charge carriers, respectively, by $R_P + \Delta R_P$,

---

[†] Deceased.

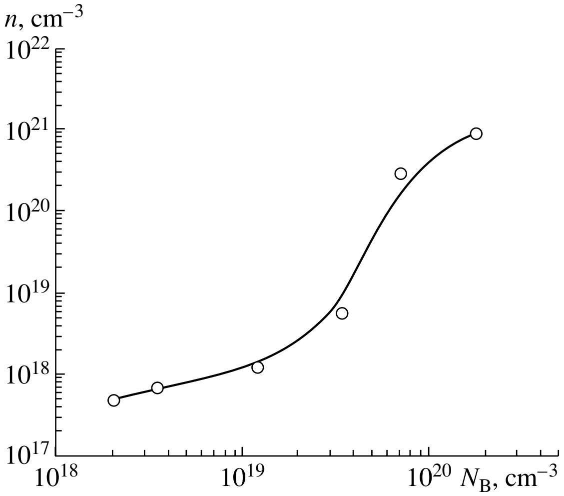

Dependence of the charge-carrier concentration (n) on the average concentration of implanted boron (N_B) in the case of dual implantation of silicon.

where R_P is the projected range of the boron or nitrogen ions and ΔR_P is the projected-range standard deviation.

3. RESULTS AND DISCUSSION

The dependence of the average charge-carrier (electron) concentration n in the sample after dual implantation on the average concentration of implanted boron N_B is shown in the figure. It follows from this dependence that the concentration of electrically active nitrogen increases as the boron concentration N_B increases and exceeds 10^{20} cm^{-3} for large values of N_B. It is notable that the values of n exceed the boron concentration for large values of N_B.

We suggest the following model of anomalous behavior of nitrogen after high-temperature implantation of nitrogen into heavily boron-doped silicon. It is well known [4] that boron atoms residing at the lattice sites of silicon can be displaced from these sites by silicon self-interstitials (the Watkins mechanism) in irradiated silicon. In particular, this mechanism manifests itself at elevated temperatures (>600°C) and gives rise to enhanced diffusion of boron in the course of annealing of ion-implanted silicon [7]. The defect complexes formed during implantation of boron act as the sources of silicon self-interstitials in the course of annealing of implanted silicon samples. Silicon self-interstitials (in addition to vacancies) are also generated during irradiation with nitrogen ions. We may suggest several scenarios for the effect of the Watkins mechanism on the concentration of nitrogen atoms at the lattice sites (i.e., on the donor concentration).

(i) Interstitial nitrogen atoms occupy vacant lattice sites. The higher the vacancy concentration (N_V), the higher the probability of finding nitrogen atoms at the lattice sites. Since a fraction of the self-interstitials that can recombine with vacancies is lost via the Watkins mechanism in the presence of a high concentration of boron, the value of N_V increases.

(ii) The Watkins mechanism involves two stages: the exit of a boron atom from a lattice site and the filling of the vacancy formed with a silicon atom. At the second stage, nitrogen atoms can compete with self-interstitials to fill the vacancies; as a result, a fraction of nitrogen atoms can be found at the lattice sites.

(iii) A direct exchange of sites between nitrogen atoms at interstices and boron atoms at the lattice sites (an analogue of the Watkins mechanism) cannot be ruled out.

(iv) The formation of neutral complex consisting of a substitutional boron atom and a substitutional nitrogen atom with the subsequent exit of the boron atom from the lattice site (according to the Watkins mechanism); as a result, a donor center (nitrogen atom at the lattice site) appears.

Since an exit to an interstice for each boron atom and its subsequent return to the interstice can be repeated many times, this atom can provide accommodation sites for several nitrogen atoms. As a result, the donor concentration can exceed the boron concentration.

The obtained supersaturated state of the solid solution of substitutional nitrogen in silicon is obviously metastable. The degree of stability of the solid solution requires further consideration. In any case, in the experimental conditions of our study, a state with a high electron concentration is retained after implantation.

4. CONCLUSION

The results obtained are notable for several reasons. First, these data indicate that the generation of defects and their interactions with impurity atoms under the conditions of dual implantation affect the resulting sites of the above atoms in the lattice and, consequently, the concentration of charge carriers. Specifically, an anomalously high concentration of substitutional impurities can be attained in this case. Second, we may conclude that the low efficiency of doping with nitrogen in the conditions of conventional ion implantation is caused by the low solubility of this element in the substitutional state rather than by specific features of the structure of the nitrogen electron shell, which differs from the corresponding structure of other elements of subgroup V and may affect the donor properties. An increase in the concentration of substitutional nitrogen makes it possible to render nitrogen as (if not more) efficient than phosphorus or arsenic. Third, the observed effect creates an interesting opportunity to use the ion implantation of nitrogen in electronics, for example, to modify luminescent properties of nanostructured systems (until now, ion implantation of nitrogen into silicon has been mainly used to synthesize Si_3N_4 layers in the fabrication of silicon-on-insulator structures).

REFERENCES

1. P. V. Pavlov, E. I. Zorin, D. I. Tetelbaum, and A. F. Khokhlov, Phys. Status Solidi **35**, 11 (1976).
2. W. J. Kleinfelder, W. S. Johnson, and J. F. Gibbons, Can. J. Phys. **46**, 597 (1968).
3. G. A. Kachurin and I. E. Tyschenko, Fiz. Tekh. Poluprovodn. (St. Petersburg) **27**, 1194 (1993) [Semiconductors **27**, 658 (1993)].
4. V. S. Vavilov, A. E. Kiv, and O. R. Niyazova, *The Mechanisms of Defect Formation and Migration in Semiconductors* (Nauka, Moscow, 1981).
5. D. I. Tetelbaum, I. A. Karpovich, M. V. Stepikhova, *et al.*, Poverkhnost **5**, 31 (1998).
6. D. I. Tetelbaum, S. A. Trushin, V. A. Burdov, *et al.*, Nucl. Instrum. Methods Phys. Res. B **174**, 123 (2001).
7. P. A. Stolk, H.-J. Gossman, D. I. Eaglesham, *et al.*, J. Appl. Phys. **81**, 603 (1997).

Translated by A. Spitsyn

Semiconductors, Vol. 38, No. 7, 2004, pp. 778–781. Translated from Fizika i Tekhnika Poluprovodnikov, Vol. 38, No. 7, 2004, pp. 811–815.

ELECTRONIC AND OPTICAL PROPERTIES OF SEMICONDUCTORS

Specific Thermoelectric Properties of Lightly Doped $Bi_2(TeSe)_3$ Solid Solutions

P. P. Konstantinov*, L. V. Prokof'eva*, Yu. I. Ravich, M. I. Fedorov*^, and V. V. Kompaniets*****

**Ioffe Physicotechnical Institute, Russian Academy of Sciences, St. Petersburg, 194021 Russia*
^e-mail: m.fedorov@mail.ioffe.ru
***St. Petersburg State Polytechnical University, St. Petersburg, 195251 Russia*
****OAO Kryotherm, St. Petersburg, 197348 Russia*

Submitted December 9, 2003; accepted for publication December 17, 2003

Abstract—Electrical and thermoelectric properties of a lightly doped n-$Bi_2Te_{2.7}Se_{0.3}$ solid solution have been studied in the temperature range 77–300 K. The results are compared with data for the compound $PbTe_{0.9}Se_{0.1}$ with a similar magnitude of the Seebeck coefficient S at 84 K. Along with lower thermal conductivity, $Bi_2Te_{2.7}Se_{0.3}$ has a higher electrical conductivity σ and a much weaker temperature dependence. As a result, the power coefficient $S^2\sigma$ in optimal samples begins to decrease only when the density of minority carriers becomes significant. In this case, $|S|$ considerably exceeds the standard value of 200 μV/K. The reduction of the electron density reduces the thermoelectric figure of merit Z at its maximum and slightly lowers the temperature of the maximum; therefore, the expected effect on the average value of Z in the range 77–300 K is absent. Similar behavior is observed in $Bi_2Te_{2.88}Se_{0.12}$, although the effect is less pronounced. The experimental results are discussed taking into account possible changes in the dominant scattering mechanisms, carrier density, and electron energy spectrum. © *2004 MAIK "Nauka/Interperiodica".*

The elaboration of high-efficiency thermoelectric materials based on ternary solid solutions $(BiSb)_2Te_3$ and $Bi_2(TeSe)_3$ has led to the development and wide use of thermoelectric coolers for the room-temperature range. Further research has begun that aims to widen the operation range down to liquid-nitrogen temperature [1–3]. According to [1, 2], in n-type materials the highest figure of merit Z in the range below room temperature was obtained in $Bi_2Te_{3-x}Se_x$ at the electron densities $(3–8) \times 10^{18}$ cm^{-3}, which corresponds to Seebeck coefficient $|S| = 100–160$ μV/K at $T \approx 84$ K.[1] The maximum value of Z in the dome-shaped $Z(T)$ curve for solid solutions with $x = 0.21–0.36$ exceeds 3×10^{-3} K^{-1} and corresponds to temperatures 220–270 K. The solid solution with $x = 0.12$ demonstrates a slightly lower figure of merit at its maximum. Studies of thermoelectric properties of lower-doped samples with $x = 0.3$ and 0.36 (in which $|S|$ is as high as ~200 μV/K at $T \approx 84$ K) [3] have demonstrated a more complex temperature dependence of the figure of merit. At temperatures below 150 K, the figure of merit increases as temperature decreases, reaching values of $(2.0–2.4) \times 10^{-3}$ K^{-1} at 84 K; the maximum in the dome-shaped portion of the $Z(T)$ curve still lies at temperatures of about 250 K, but the value of Z is significantly smaller than that for samples with higher electron density. In this study, we continue our research on the thermoelectric properties of n-type $Bi_2Te_{3-x}Se_x$ solid solutions. We aimed to reveal which specific features in the properties of the material appear at decreased electron density and find out how these features affect the value and behavior of the thermoelectric figure of merit in the temperature range 77–300 K.

To study the Seebeck coefficient and electrical and thermal conductivities (S, σ, and κ) in the temperature range 85–340 K, we fabricated samples of $Bi_2Te_{3-x}Se_x$ solid solution with an Se content of 10 at % in the chalcogenide sublattice ($x = 0.3$). The technique of vertical zone melting was used, and the doping was carried out by introducing chlorine.

To reveal the specific features in the behavior of the materials under study at low temperatures, we compared the thermoelectric properties of two lightly doped solid solutions, $Bi_2Te_{3-x}Se_x$ and $PbTe_{1-x}Se_x$, with an equal Se content (10 at %). $PbTe_{1-x}Se_x$ was chosen as a reference material, because its thermoelectric properties at low temperatures are well described in terms of a single-band model with a nonparabolic dispersion law and electron scattering on phonons and on the short-range potential of neutral impurity centers [4]. Figure 1 shows temperature dependences of electrical and thermoelectric characteristics of these solid solutions with similar values of thermoelectric power at 84 K. The

---

[1] In comparing the properties of the materials, we will use the temperatures 84 and 250 K. The latter value is chosen taking into account that, in lightly doped samples of this material, the contribution of intrinsic carriers at room temperature is considerable.

comparison of the temperature dependences of thermal conductivity κ (curves *3*, *3*') shows that the behavior of κ(*T*) is virtually the same in both alloys, not counting the very small (less than 4% at the maximum) departure from this law in $Bi_2Te_{2.7}Se_{0.3}$ at temperatures of 110–225 K. This decrease in κ does not affect the amplitude and position of the maximum figure of merit Z_{max}, and only slightly raises *Z* in this temperature range. The decrease in thermal conductivity observed in $Bi_2Te_{2.7}Se_{0.3}$ solid solution has a noticeable effect on the figure of merit. For example, the increase in Z_{max} because of the decrease in total thermal conductivity is ~20%.

The differences between the temperature dependences of the electrical conductivity σ (Fig. 1, curves *1*, *1*') and the Seebeck coefficient *S* (Fig. 1, curves *2*, *2*') in the alloys under study are of fundamental importance. The temperature variation of both parameters is much stronger in the solid solution based on PbTe. The change in electrical conductivity is especially strong: in $PbTe_{0.9}Se_{0.1}$ solid solution, it decreases by more than an order of magnitude as temperature increases from 84 to 300 K, whereas in $Bi_2Te_{2.7}Se_{0.3}$ it decreases only by a factor of 4.2. Since the Seebeck coefficient in $PbTe_{0.9}Se_{0.1}$ increases by a factor of 2.5 in this temperature range, the power coefficient $S^2\sigma$ naturally declines sharply as temperature increases. When the thermal conductivity decreases slowly, the thermoelectric figure of merit reaches its maximum at a temperature of about 100 K (Fig. 2). In this case, the magnitude of the Seebeck coefficient does not exceed its standard value of ~200 μV/K, which corresponds to scattering mechanisms with the exponent *r* in the dependence of the relaxation time on energy ($\tau \propto \varepsilon^r$) equal to –0.5 in cases of scattering on acoustic phonons and on the short-range impurity potential [5].

A completely different situation is observed for $Bi_2Te_{2.7}Se_{0.3}$ solid solution. At 84 K, the power coefficient in this material is higher because of higher σ. As temperature increases, the difference becomes much greater, because, despite the weaker increase in the thermoelectric power, $S^2\sigma$ not only does not decrease until the onset of intrinsic conduction, but even increases slightly, as can be seen in Fig. 2. Only a noticeable contribution of holes to the transport phenomena radically changes the temperature dependence $S^2\sigma = f(T)$, so that this parameter steeply decreases. Since the appearance of minority carriers also changes the behavior of κ(*T*), the thermoelectric figure of merit reaches its maximum and then starts to decrease steeply. Thus, the intrinsic conduction is the factor that limits the rise of *Z*(*T*) in $Bi_2Te_{2.7}Se_{0.3}$ solid solution. Clearly, in this material Z_{max} corresponds to higher temperatures and higher values of the Seebeck coefficient (in the case under study, $|S| \approx 290$ μV/K).

Thus, we may conclude that the rather high electrical conductivity and its slight decrease as the temperature increases in the range 85–300 K, along with low thermal conductivity, are specific features of the thermoelectric properties of the materials under study. They are responsible for the increase in the figure of merit and for the shift of its maximum to higher temperatures, where the transport properties fundamentally change under the effect of intrinsic carriers.

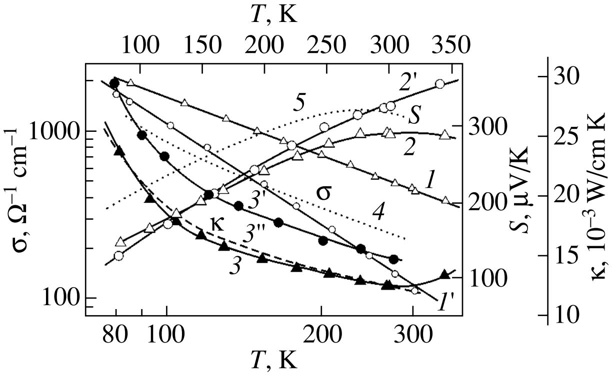

Fig. 1. Temperature dependences of (*1*, *1*') electrical conductivity σ (log–log scale), (*2*, *2*') Seebeck coefficient *S* (linear scale), and (*3*, *3*') thermal conductivity κ (linear scale) for (*1*, *2*, *3*) $Bi_2Te_{3-x}Se_x$ and (*1*', *2*', *3*') $PbTe_{1-x}Se_x$ solid solutions with equal Se content (10 at %) and similar values of *S* at 84 K. (*4*, *5*) σ and *S*, respectively, for $Bi_2Te_{2.7}Se_{0.3}$ with lower electron density [3]. (*3*'') Hypothetical thermal conductivity of solid solution based on Bi_2Te_3 calculated under the assumption that its temperature behavior is similar to that in the material based on PbTe.

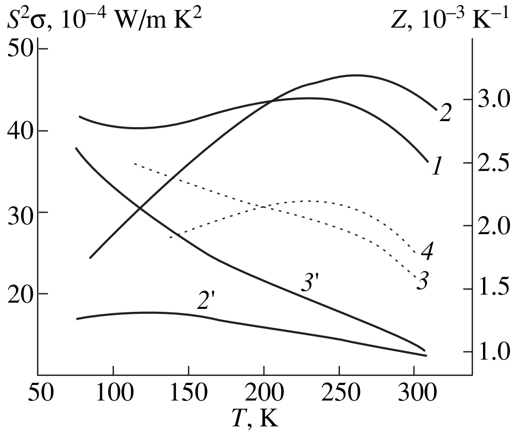

Fig. 2. Temperature dependences of (*1*, *1*') the power coefficient $S^2\sigma$ and (*2*, *2*') thermoelectric figure of merit *Z* for solid solutions based on (*1*, *2*) Bi_2Te_3 and (*1*', *2*') PbTe with 10 at % Se. Dashed lines: (*3*) $S^2\sigma$ and (*4*) *Z* for $Bi_2Te_{2.7}Se_{0.3}$ with lower electron density [3].

According to data in [3], the decrease in the electron density in $Bi_2Te_{2.7}Se_{0.3}$ solid solution depresses the temperature increase in the Seebeck coefficient to an even greater extent. However, the behavior of the electrical conductivity with temperature is not modified; it is still described by the standard power law $\sigma \propto T^\beta$, where $\beta \approx -1.2$. This is illustrated by the data of [3] obtained for a sample with $S = -200$ μV/K at 84 K (Figs. 1, 2). The steeper run of the σ(*T*) dependence at

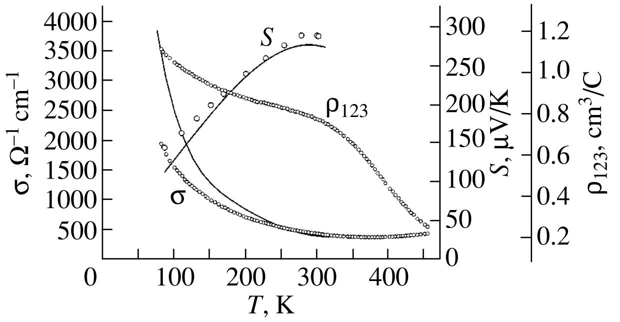

Fig. 3. Temperature dependences of electrical conductivity σ, Seebeck coefficient *S*, and Hall coefficient ρ_{123}. Solid lines: $Bi_2Te_{2.88}Se_{0.12}$ [2]; dots: $Bi_2Te_{2.7}Se_{0.3}$ (this study). The samples are characterized by similar values of *S* at 250 K.

$T < 125$ K [3], which is responsible for the anomalous behavior of *Z* at these temperatures, will be discussed below. Regarding the data on the figure of merit in the range 125–300 K, note the following: in this case, the power coefficient decreases as temperature increases, but this dependence is weaker than in $PbTe_{0.9}Se_{0.1}$ solid solution, and, therefore, the occurrence of a maximum in the $Z(T)$ dependence is still related to the onset of the intrinsic conduction, as discussed earlier. In this case, the Seebeck coefficient $|S|$ even exceeds 300 μV/K.

Based on the data presented, we may conclude that the reduction of the doping level in $Bi_2Te_{2.7}Se_{0.3}$ solid solution, which is commonly used as a method to raise the average value of *Z* by lowering the temperature of the maximum in the $Z(T)$ dependence, has its limit for this material. Beyond this limit, the figure of merit decreases in virtually the whole temperature range; in this case the temperature of Z_{max} does not decrease. Evidently, as temperature increases, the increase in the Seebeck coefficient becomes too weak to noticeably compensate the decrease in electrical conductivity. The electrical conductivity is further depressed by the decrease in mobility, which is especially sensitive to the degree of material perfection in lightly doped samples. For the range below room temperature, samples with a Seebeck coefficient of about 285–295 μV/K and Z_{max} no lower than 3.2×10^{-3} K^{-1} at $T = 250$ K are optimal.

The specific features discussed above are directly related to the introduction of Se into Bi_2Te_3. When a small amount of Se is added, the related variations in properties are also small, although they are observable and have a similar behavior. To confirm this assertion, we use the data in [2] for $Bi_2Te_{2.88}Se_{0.12}$ solid solution and find that they are similar to those presented above: the maxima of $Z(T)$ dependences lie in the same temperature range, and their relationship with the intrinsic conduction is similar; there is no gain in *Z* at temperatures $T < 300$ K in the samples with an electron density below a certain level; and the optimal value of $|S|$ noticeably exceeds 200 μV/K. We now make a quantitative comparison of the experimental data for solid solutions $Bi_2Te_{2.7}Se_{0.3}$ and $Bi_2Te_{2.88}Se_{0.12}$, which have the same value of Seebeck coefficient *S* at 250 K. As can be seen from Fig. 3, the temperature dependence of *S* in $Bi_2Te_{2.88}Se_{0.12}$ is not weakened as much as that in $Bi_2Te_{2.7}Se_{0.3}$, and, therefore, the samples of these two compositions, which have equal values of *S* and κ at 250 K, show a significant difference in these parameters at 84 K. Linear extrapolation of the Seebeck coefficient to 0 K does not yield zero *S* in either of these alloys. If we assume that two alloys with different compositions and equal values of *S* have the same electron density at 250 K (at room temperature, this result was obtained for the doping range (1×10^{18}–5×10^{19}) cm^{-3} in [1]) and this density is temperature-independent, then the low-temperature electron mobility strongly depends on the material composition; its value considerably decreases as the Se content increases. As *S* also noticeably changes (increases) in this case, it is obvious that the observed facts cannot be explained only by taking into account the scattering on the short-range potential of impurities ($r = -0.5$, the same as for scattering on acoustic phonons [5]). Our estimates of scattering on the Coulomb potential of ionized defects, which is effective for low-energy carriers and thus yields higher values of *S*, have shown that the contribution of this mechanism in the materials under study is small [6]. In this situation, it seems natural to suppose that the specific features observed in the transport phenomena in lightly doped $Bi_2Te_{3-x}Se_x$ solid solutions are related to the modification of the energy spectrum of electrons. Thus, it seemed useful to estimate how the effective mass varies with temperature at different alloy compositions, as was done for more heavily doped $Bi_2Te_{3-x}Se_x$ solid solutions with $x = 0.12$ and 0.45 [6].

In determining the temperature dependence of the effective mass, $m^* \propto T^s$, we assumed, as in [6], that the electron density *N* does not change in the range 84–250 K and mechanisms with the parameter $r = -0.5$ dominate in scattering. Figure 4 shows $\log m^* \propto \log(T^{-1}F_{3/2}^{-2/3})$ as functions of $\log T$ (here *F* are the Fermi integrals [5]) for solid solutions with 4 and 10 at % Se; their properties are shown in Fig. 3. For a lightly doped solid solution with 4 at % Se ($x = 0.12$), all the points in the range of impurity conduction are well fitted to the straight line *1* with the slope $s = 0.36$. This means that the density-of-states effective mass increases with temperature as $m^* \propto T^{0.36}$, which is indicative of the nonparabolicity of the electronic spectrum. The smaller value $s = 0.04$ for a more heavily doped sample [6] is in agreement with the result obtained, because the nonparabolicity in strongly degenerate samples does not lead to a significant increase in the averaged effective mass with increasing temperature. The behavior of the effective mass in $Bi_2Te_{2.7}Se_{0.3}$ solid solution with temperature in the range 240–120 K is qualitatively the same, only the slope of the corresponding plot, $m^* \propto T^{0.21}$ (curve *2*), is smaller. However, at $T < 120$ K the character of the dependence is reversed: the effective mass increases as temperature decreases. This may indicate that either the description of scattering by the relation $\tau \propto \varepsilon^{-0.5}$

becomes incorrect at low temperatures or the assumption of a constant carrier density in the conduction band is not well justified. In the first case, it is evident that, for a linear decrease in the effective mass to continue as T decreases to below 120 K, the negative exponent in the energy dependence of the relaxation time (see above) must decrease in magnitude, which would indicate an enhancement in the scattering of low-energy electrons. This can occur, for example, in solid solutions with an inhomogeneous distribution of components within the sample, which gives rise to a random profile of the bottom of the conduction band. In this case, localization at low temperatures is also possible. In lightly doped samples, this mechanism of carrier scattering can be dominant at low temperatures.

There is also a second possible source of the anomaly in the $m^*(T)$ dependence obtained: the increase in the electron density with temperature. In this case, the structure of the electronic spectrum in the given materials must be discussed. Valuable information can be obtained from temperature measurements of the Hall effect. Unfortunately, the determination of the temperature dependence of the electron density encounters problems related to the lack of data on how the anisotropy coefficient and the Hall factor change when the mechanism of scattering becomes operative. Nevertheless, general trends can be revealed by comparing the Hall data for samples that differ in composition and doping level. In this study, we present only the first result of projected systematic studies of this kind, and this result refers to the $Bi_2Te_{2.7}Se_{0.3}$ sample under study (Fig. 3). In the measurements of the Hall coefficient, the directions of current and Hall field were in the cleavage plane, and the magnetic field was normal to it. Assuming that the observed decrease in ρ_{123} with increasing temperature is related to the increase in electron density, we took this effect into account in our calculations and obtained curve *2*' in Fig. 4 for the dependence $m^*(T)$. In this case, all the calculated points fall with satisfactory precision on the straight line $m^* \propto T^{0.22}$. Taking into account that an even stronger decrease in ρ_{123} with increasing temperature was observed for a sample of the same composition and similar properties in [3], we may conclude that an increase in electron density with increasing temperature is quite probable in these materials. Thus, a qualitative explanation for the specific features observed is obtained.

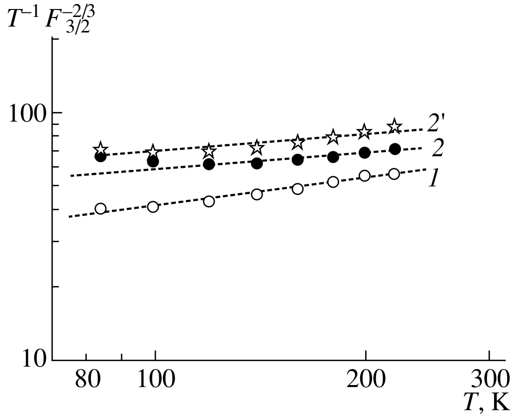

Fig. 4. Temperature dependences of the effective mass for lightly doped solid solutions, (*1*) $Bi_2Te_{2.88}Se_{0.12}$ and (*2*, *2*') $Bi_2Te_{2.7}Se_{0.3}$. (*2*) N = const(T) and (*2*') $N = f(T)$.

It remains to be understood what is the reservoir from which electrons pass to the conduction band as temperature increases. Several alternatives are possible. One is related to the inhomogeneity of the material, as discussed above. Another possibility is that a level related to structural or impurity defects is formed near the bottom of the conduction band. In terms of this model, it is possible to account for the steeper temperature dependence of the electrical conductivity at $T <$ 125 K in $Bi_2Te_{3-x}Se_x$ solid solutions with $x = 0.3$ and 0.36 and $S \approx 200$ μV/K at 84 K [3], as mentioned above. Finally, the reservoir of electrons might be the heavy conduction band, whose existence in the materials in question has been discussed in several studies [7–9]. The small separation between the heavy and light bands at 0 K and its positive temperature coefficient could stimulate the transfer of carriers to the light band with the rise of temperature; in this case, the effective density would increase. To obtain reliable information about the structure of the electronic spectrum in these materials, a more consistent experiment with a wider scope is necessary. Extending the temperature range to 4.2 K would be very helpful.

ACKNOWLEDGMENTS

This study was supported by the Russian Foundation for Basic Research (project no. 03-02-17605).

REFERENCES

1. V. A. Kutasov, L. N. Luk'yanova, and P. P. Konstantinov, Fiz. Tverd. Tela (St. Petersburg) **41**, 187 (1999) [Phys. Solid State **41**, 164 (1999)].
2. V. A. Kutasov, L. N. Luk'yanova, and P. P. Konstantinov, Fiz. Tverd. Tela (St. Petersburg) **42**, 1985 (2000) [Phys. Solid State **42**, 2039 (2000)].
3. V. A. Kutasov, L. N. Luk'yanova, P. P. Konstantinov, and G. T. Alekseeva, Fiz. Tverd. Tela (St. Petersburg) **39**, 483 (1997) [Phys. Solid State **39**, 419 (1997)].
4. E. A. Gurieva, P. P. Konstantinov, L. V. Prokof'eva, *et al.*, Fiz. Tekh. Poluprovodn. (St. Petersburg) **37**, 292 (2003) [Semiconductors **37**, 276 (2003)].
5. B. M. Askerov, *Kinetic Effects in Semiconductors* (Nauka, Leningrad, 1970).
6. B. M. Gol'tsman, G. N. Ikonnikova, V. A. Kutasov, and Yu. I. Ravich, Fiz. Tverd. Tela (Leningrad) **27**, 542 (1985) [Sov. Phys. Solid State **27**, 334 (1985)].
7. B. M. Gol'tsman, V. A. Kudinov, and I. A. Smirnov, *Semiconducting Thermoelectric Materials Based on* Bi_2Te_3 (Nauka, Moscow, 1972).
8. H. Köhler, Phys. Status Solidi B **73**, 95 (1976).
9. H. Köhler, W. Haigis, and A. von Middendorff, Phys. Status Solidi B **78**, 637 (1976).

Translated by D. Mashovets

Semiconductors, Vol. 38, No. 7, 2004, pp. 782–787. Translated from Fizika i Tekhnika Poluprovodnikov, Vol. 38, No. 7, 2004, pp. 816–821.
Original Russian Text Copyright © 2004 by Veĭnger, Zabrodskiĭ, Tisnek, Mokhov.

ELECTRONIC AND OPTICAL PROPERTIES OF SEMICONDUCTORS

Specific Features of Electron Spin Resonance in 4*H*-SiC in the Vicinity of the Insulator–Metal Phase Transition: II. Analysis of the Width and Shape of Lines

A. I. Veĭnger, A. G. Zabrodskiĭ, T. V. Tisnek, and E. N. Mokhov
Ioffe Physicotechnical Institute, Russian Academy of Sciences, Politekhnicheskaya ul. 26, St. Petersburg, 194021 Russia
e-mail: Anatoly.Veinger@mail.ioffe.ru

Submitted December 15, 2003; accepted for publication December 17, 2003

Abstract—The variation in the width and shape of the ESR line of nitrogen in 4*H*-SiC in the concentration range corresponding to the insulator–metal phase transition was investigated. It is shown that the spin relaxation in the region of hopping and metal conduction occurs at electrical multipoles (clusters) whose sizes decrease from rather large to small (characteristic of interimpurity distances) as the concentration of impurity centers increases. Analysis of the temperature dependences of the resistance made it possible to estimate the critical concentration for the insulator–metal phase transition $(N_D - N_A)_c \approx 1.5 \times 10^{19}$ cm^{-3}. The values of other characteristic concentrations that determine the effects of electron–electron interaction in the system under study were also found. *© 2004 MAIK “Nauka/Interperiodica”.*

1. INTRODUCTION

This article is the second part of a complex investigation of ESR in *n*-4*H*-SiC near the insulator–metal phase transition. The first part [1] was devoted to the effects of spin interaction in this material, which manifests itself in a rather complex set of lines observed. One of them (line I) vanishes in the vicinity of the insulator–metal transition. In contrast to this, the other two lines (III and IV) arise in the metallic phase. The experiment showed that, starting with a concentration of about 8×10^{18} cm^{-3} $\approx n_c/2$ ($n_c = 1.5 \times 10^{19}$ cm^{-3} is the critical concentration for the insulator–metal phase transition), the line becomes substantially asymmetric [1]. Specifically, the amplitude of the low-field part of the derivative of the absorption signal is significantly higher than that of the high-field part. This phenomenon can be explained in terms of the Dyson theory [2–4]. Here, we will analyze the width and shape of the lines and discuss the relationship between ESR and the insulator–metal phase transition.

2. CONCENTRATION AND TEMPERATURE VARIATIONS IN THE LINE WIDTH

The Dyson theory indicates that the half-width of a line distorted by the spin effect should by measured at the half-height of the positive wing of the derivative [2–4]. The dependence of the half-width of main resonance line I, which is measured in this way, on the concentration of impurity centers is shown in Fig. 1. One can see that, far from the critical concentration ($n_c \approx 10^{18}$ cm^{-3} in the insulator state, according to [1]), the line half-width only weakly depends on the doping level. However, when approaching the critical concentration, the line half-width starts to increase rapidly. The spread in the values increases from sample to sample. At a high doping level (the metallic phase), this line vanishes, whereas the width of ESR lines II, III, and IV [1, Fig. 2], which are observed in this concentration range, are temperature-independent.

The characteristic temperature dependences of the half-width of line I for the samples investigated are shown in Fig. 2. One can see that the line half-width is strongly dependent on the doping level. Thus, at the lowest impurity concentration (sample 2[1], curve *1*), the line half-width is temperature-independent in a wide range up to 60 K. At higher temperatures, the line rapidly broadens and vanishes. For heavily doped samples, for which a single Lorentzian or Dysonian line is observed, its half-width increases with temperature according to the law $T^{1/2}$, which is characteristic of spin relaxation at neutral centers (see below) (curves *2*–*4*). Sometimes, at low temperatures, the dependences are weaker or even absent (curve *3*). At impurity concentrations close to the concentration at which this line vanishes ($N_D - N_A \cong 10^{19}$ cm^{-3}), the temperature dependence starts to weaken (curve *5*) and even changes its sign in the low-temperature region (curve *6*, $N_D - N_A \cong 1.4 \times 10^{19}$ cm^{-3}).

3. SPIN–LATTICE RELAXATION TIME

It is known that the width of the ESR line for conducting materials is determined by the spin-lattice

---

[1] Parameters of the samples investigated are listed in Table 2 in [1].

relaxation time T_2, which is equal to the spin–spin relaxation time T_1 for such materials:

$$T_2 = h/(g\mu_B\delta H),$$

where μ_B is the Bohr magneton and δH is the line half-width.

It follows from Fig. 1 that, at an impurity concentration higher than 6×10^{18} cm^{-3}, the spin–lattice relaxation time, which is inversely proportional to the line half-width δH, starts to decrease abruptly. The large spread of values in this concentration range indicates that this parameter, as well as the concentration $N_D - N_A$ measured by the Hall effect, is affected by random technological features of the crystal growth. These are microscopic inhomogeneities in the impurity distribution, internal stresses, degree of compensation, and so on.

One can see from Fig. 1 that, at a low impurity concentration (curve *1*, sample *2*), the half-width of the ESR line is temperature-independent almost in the entire temperature range, and the corresponding relaxation time $T_2 \geq 10^{-7}$ s. As the concentration of impurity centers increases, δH increases by approximately an order of magnitude, which indicates a corresponding decrease in the spin relaxation time to 10^{-8} s. In this case, a significant temperature dependence arises. For the samples shown in Fig. 2 (curves *2*, *3*, and *4* for samples 3, 6, and 10, respectively), this dependence is mainly described by the law $T_2 \propto T^{\alpha}$. Here, $\alpha = 0.47$, 0.33, and 0.42 for samples 3, 6, and 10; i.e., for these samples, $\alpha \leq 0.5$. For heavily doped samples, when the line becomes especially broad, the temperature dependence weakens (curve *5*, sample 14): $\alpha = 0.1$. For the most heavily doped sample for which line I is still observed (curve *6*, sample 16), a portion arises in the low-temperature region in which the spin–lattice relaxation time increases with temperature, while the line half-width decreases. Let us compare these results with the previously studied spin relaxation in Ge:As [5].

When investigating ESR in compensated Ge near the insulator–metal phase transition, it was found that, when free charge carriers arise, the spin–lattice relaxation occurs at nearby charged impurities forming donor–acceptor pairs. The slowest process that governs the relaxation time is the time during which a spin approaches such a pair. In this case, the temperature dependence of T_2 allows us to determine the spatial distribution of the potential of donor–acceptor pairs.

Starting from the fact that 4*H*-SiC, like Ge:As [5], is a compensated semiconductor with relatively free spins, let us try to find out what centers are responsible for spin relaxation in this material. The potential energy of a relaxation center can be written as

$$E_P = e^2/\varepsilon r^n, \tag{1}$$

where ε is the permittivity, e is the elementary charge, and the exponent n characterizes the potential of the center.

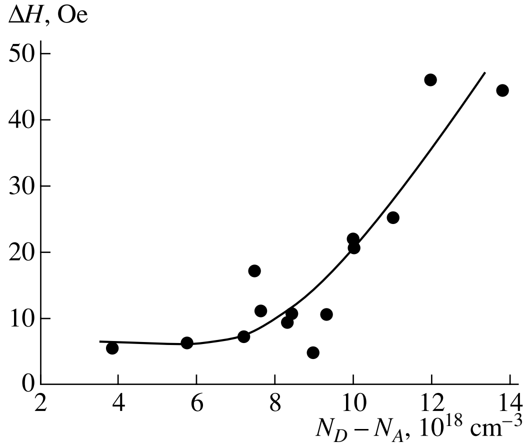

Fig. 1. Concentration dependence of the half-width of the ESR line of nitrogen in 4*H*-Si at 3.2 K.

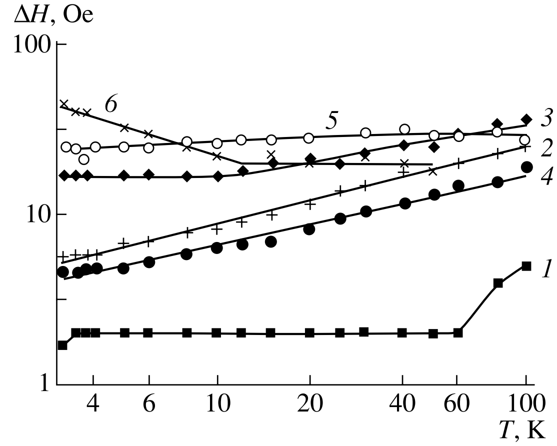

Fig. 2. Temperature dependences of the half-width of the ESR line of nitrogen in 4*H*-SiC at 3.2 K for $N_D - N_A$ = (*1*) 0.35×10^{18}, (*2*) 2.4×10^{18}, (*3*) 7.5×10^{18}, (*4*) 9×10^{18}, (*5*) 11×10^{18}, and (*6*) 13.8×10^{18} cm^{-3}.

The value of n can be determined under the assumption that the interaction cross section $\sigma = \pi r^2$ is cut at a distance r from the relaxation center, at which the potential energy E_P becomes equal to the carrier kinetic energy

$$E_K = kT. \tag{2}$$

Equating expressions (1) and (2), we obtain

$$r = (e^2/\varepsilon kT)^{1/n} \propto T^{-1/n}. \tag{3}$$

Hence,

$$\sigma = \pi r^2 \propto T^{-2/n}. \tag{4}$$

If the spin–lattice relaxation is controlled by scattering of free electrons by positively charged centers with concentration N_+, then, taking into account expression (4)

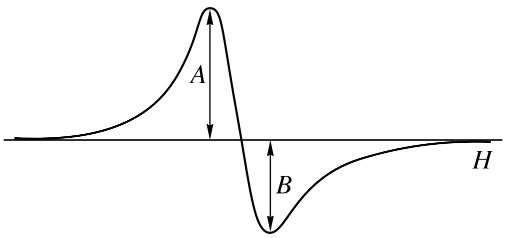

Fig. 3. Shape of the ESR line of nitrogen distorted by the skin effect (sample 11, $N_D - N_A = 9.3 \times 10^{18}$ cm^{-3}). *A* and *B* are the amplitudes of the low- and high-field wings of the derivative of the absorption line, respectively.

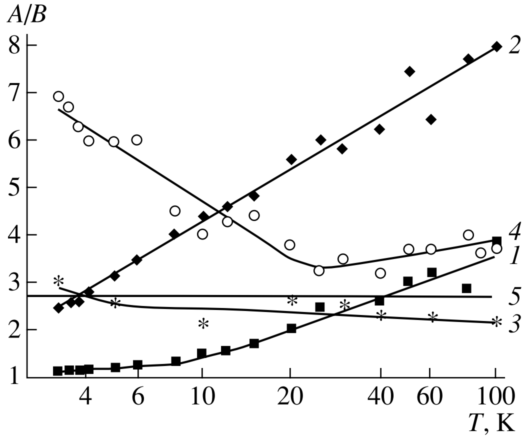

Fig. 4. Temperature dependences of the asymmetry parameter *A*/*B* of the ESR line of nitrogen in 4*H*-SiC measured for $N_D - N_A$ = (*1*) 7.2×10^{18}, (*2*) 9.3×10^{18}, (*3*) 10×10^{18}, and (*4*) 11×10^{18} cm^{-3}. (*5*) Calculation in terms of the Dyson theory for $T_2 \ll \tau_D$.

and the fact that the velocity of an electron $v = T^{1/2}$, we obtain

$$T_2 = (\sigma v N_+)^{-1} \propto T^{2/n - 1/2}. \quad (5)$$

Equating the exponent at T and the experimental value of α, we derive the relation

$$2/n - 1/2 = \alpha; \quad n = 4/(2\alpha + 1). \quad (6)$$

As can be seen from Fig. 2, for samples with free spins, the values of α differ at different temperatures and impurity concentrations. For the most heavily doped sample 16, at low temperatures $\alpha = 0.6$, and at higher temperatures $\alpha \approx 0$. The more lightly doped sample 14 is characterized by $\alpha = -0.1$, and for even more lightly doped samples $\alpha \approx -0.5$. The following exponents of the spatial distribution of the potential correspond to these values: for sample 16, $n = 1.8$ and 4 for low and high temperatures, respectively; for sample 14, $n = 5$; and for samples 3, 6, and 10, $n \longrightarrow \infty$. For all the samples, as follows from the consideration of the behavior of the ESR spectra [1], spins can move relatively freely throughout a sample.

Hence, in relatively lightly doped samples, in which moving spins already exist, spin–lattice relaxation occurs at almost neutral centers that have a short-range potential. Areas of internal stresses and dislocations, fluctuations in the distribution of neutral impurities, and some other aggregates can serve as such centers. As the concentration of impurity centers increases and the spin–lattice relaxation time decreases, relaxation starts to occur at increasingly smaller charged aggregates. In sample 14, relaxation apparently occurs at clusters consisting of nearby donors and acceptors, which yield the effective exponent $n = 5$. In the most heavily doped sample 16, high-temperature relaxation occurs at the quadrupole potential, i.e., at clusters containing two charged donors and two charged acceptors each, whereas at a lower temperature, it occurs at dipoles consisting of donor–acceptor pairs.

Such a concentration dependence of the spin–lattice relaxation time is apparently due to the fact that charged clusters are formed rather rarely at lower impurity concentrations and spins relax at almost neutral aggregates of technological origin. As the impurity concentration increases, spin relaxation at charged clusters starts to compete with the above mechanism and then becomes dominant.

Note that, according to [1], in addition to line I from free or weakly localized spins, which broadens as the impurity concentration increases, three other lines from spins in other states are observed in the ESR spectrum of a sample. The spin–lattice relaxation time for these lines is temperature-independent. For lines II, III, and IV, $T_2 \approx 10^{-7}$, 2.8×10^{-8}, and 2.1×10^{-8} s.

4. DISTORTIONS OF THE DYSONIAN LINE

The ratio of the amplitude of the low-field wing *A* to the amplitude of the high-field wing *B* is the measure of distortion (the asymmetry parameter) for a Dysonian line (Fig. 3) [2–4]. For symmetric lines, both amplitudes are equal and $A/B = 1$. This ratio increases with increasing conductivity. However, the dependence of the ratio *A*/*B* on the impurity concentration for the samples investigated is so unambiguous that it seems unreasonable to represent it as a curve. From comparison of these ratios for various impurity concentrations at a temperature of 3.2 K, one can only note that the ratio *A*/*B* increases from 1 to 3 as the concentration increases. However, for some samples, this ratio is much larger. The largest ratio observed was 7.

The temperature dependences of the ratio *A*/*B* (Fig. 4) are more informative. For the most lightly doped samples, this ratio was temperature-independent until the sample conductivity became so high that the skin layer turned out thinner than the sample width (curve *1*, sample 5). A further increase in temperature and impurity concentration led to an increase in this ratio. The higher the concentration, the greater this increase (curve *1*, sample 5; curve *2*, sample 11). However, on attaining the impurity concentration critical for the insulator–metal transition (about 10^{19} cm^{-3}), the *A*/*B* ratio became almost temperature-independent (curve *3*, sample 13). A further increase in the concentration at low temperatures led to a decrease in this ratio with increasing temperature (curve *4*, sample 14).

It is noteworthy that the Dyson theory predicts the smallest value of $A/B = 2.7$ when the time of diffusion through the skin layer is much shorter than the spin–lattice relaxation time (dependence 5).

5. EFFECT OF INTERNAL FIELDS ON THE ESR SPECTRA

The Dyson theory relates the ESR line distortion with the ratio of the time of spin diffusion through the skin layer, τ_D, to the spin–lattice relaxation time T_2. This relation is rather complex but unambiguous. In [3, 4] it is shown in the form of nomograms. This relation is justified well in the case of metals, for which these two quantities are of the same order of magnitude. However, for semiconductors containing free carriers, the skin depth is much larger because of their relatively high resistance, and the time of diffusion through the skin layer exceeds the spin–lattice relaxation time by many orders of magnitude. In this case, the ratio *A*/*B* is 2.7, and this value should not vary with either temperature or impurity concentration.

However, the experiment shows that the ratio *A*/*B* varies with both the temperature and impurity concentration (Fig. 4). Similar variations were also observed for ESR in heavily doped Ge [5]. For relatively lightly doped 4*H*-SiC samples, the ratio *A*/*B* increases with temperature. The increase is slow at low temperatures but becomes close to exponential at high temperatures (curve *1*, sample 5). As the concentration increases, a kink is observed in the curve at increasingly lower temperatures, and, for sample 11, the slope of the ratio *A*/*B* is described by a common exponential dependence in the entire temperature range. For sample 13, the dependence becomes qualitatively different. At low temperatures, a slight falloff is observed, and then the ratio *A*/*B* becomes almost independent of temperature. For the most heavily doped shown in Fig. 4, sample 14, this falloff is much more pronounced. At high temperatures, a slight rise is observed instead of the falloff.

These dependences are also quantitatively inconsistent with the Dyson theory. This theory was developed for metals, for which the Fermi level is located high in the conduction band and, thus, the potential fluctuations at the bottom of the conduction band exert no effect on spins. It was shown using compensated Ge as an example that precisely these fluctuations play the main role in the resonance-line distortion [5]. The Dyson theory is based on the assumption that a spin is capable of diffusing through the skin layer. The frequency of its emergence in the field-free part of the sample is about $1/\tau_D$. The external magnetic field affecting the spin is thereby modulated with a frequency of $1/\tau_D$, which leads to the distortion of the resonance line. The additional field that arises due to fluctuations of the bottom of the conduction band [6] also affects free spins in a semiconductor. In this case, τ_D should be the time of diffusion at a distance of the same order of magnitude as the size of a fluctuation of the potential of the bottom of the conduction band rather than the time of diffusion through the skin layer. Starting from this assumption, let us consider the concentration and temperature dependences of the ratio *A*/*B*.

For relatively lightly doped samples (5 and 11), the increase in the ratio *A*/*B* is related to the increase in the sample conductivity. The lower the impurity concentration, the higher the temperature at which the ratio *A*/*B* begins to increase. Here, the condition $\delta < l$ is important, where δ is the skin depth and l is the transverse size of the sample. Otherwise, the external electromagnetic field will be uniform throughout the sample. According to Dyson, the theory is valid even at $\delta < 4l$. In this case, this ratio does not appear in the formulas determining the line distortion; it determines only the range of applicability of the formulas.

As the temperature rises, the skin layer becomes increasingly narrower, and the ratio *A*/*B* increases from unity to a certain value determined by the ratio τ_D/T_2. Investigation of the line distortion for compensated Ge showed that, for this material, the ratio *A*/*B* is close to 2.7 at high temperatures [5]. This indicates that the amplitude of fluctuations of the potential of the bottom of the conduction band is small. At high temperatures, spins do not interact with these fluctuations in Ge. However, for 4*H*-SiC, this ratio attains much larger values with increasing temperature. This is consistent with the existence of large potential fluctuations in these samples, which are apparently of technological origin. These fluctuations play the main role in ESR line distortion at temperatures up to 100 K.

For the most heavily doped samples (13 and 14), the temperature dependence of the ratio *A*/*B* is qualitatively different, and the ratio drops with increasing temperature. It is likely that the temperature dependence of conductivity for these samples is similar to that for metals. Such a dependence of the ratio *A*/*B* was observed for compensated Ge in the metallic state [5]. In those samples, the ratio *A*/*B* increases with increasing temperature. The reason for this phenomenon is that spins start to interact with increasingly smaller fluctuations as the energy decreases. To overcome this inhomogeneity, a shorter time is required. This circumstance leads to a decrease in the ratio τ_D/T_2 and, accordingly, to an increase in the ratio *A*/*B*.

Thus, the character of the temperature dependences of the ratio *A*/*B* makes it possible to determine the critical concentration for 4*H*-SiC fairly exactly. It follows from Fig. 4 that sample 11 (9.33×10^{18} cm^{-3}) still shows an increase in the conductivity with temperature (curve *2*), i.e., behaves like an insulator. However, sample 13 (1 ×

10^{19} cm^{-3}) shows a slight decrease in the ratio A/B, which is characteristic of metals and corresponds to a zero increase in conductivity with temperature. Hence, we may suggest that the concentration in sample 13 is almost critical for the insulator–metal transition in 4*H*-SiC, and it is possible that $n_C \approx 1 \times 10^{19}$ cm^{-3}.

6. ESR AND THE INSULATOR–METAL PHASE TRANSITION IN 4*H*-SIC

After discussing the main parameters of resonance lines and their variations in the vicinity of the metal–insulator phase transition, let us consider the relationship between the critical concentration N_c for the metal–insulator transition and the characteristic concentrations, revealed for them in the first and second sections, i.e., the concentrations corresponding to (i) the vanishing of the hyperfine structure (N_{ex}), (ii) the highest spin density ($N_{\max}$), (iii) antiferromagnetic pairing (N_{pair}), (iv) the change in sign for the temperature coefficient of the Dyson distortion of the line (N_{DT}), and (v) the appearance of new lines (N_M). We will go from light to heavy doping.

Let us start with the concentration N_{ex}, at which the hyperfine structure vanishes. It is well known that this phenomenon occurs when the exchange energy becomes equal to the hyperfine interaction energy [7]. Physically this means that the frequency of spin exchange between impurity atoms begins to exceed the frequency corresponding to the hyperfine interaction energy. Such an exchange can also be considered a spin diffusion via impurity centers. In this case, the internal magnetic field is averaged, and the resonance frequency corresponds to the averaged magnetic field. Figure 2 from [1] shows that the vanishing of the hyperfine structure in 4*H*-SiC becomes noticeable even at a nitrogen concentration N of about 10^{17} cm^{-3}. It is completed at $N \approx 10^{18}$ cm^{-3}. This concentration is approximately an order of magnitude lower than that for the 6*H* polytype with a deeper impurity level of nitrogen (in 6*H*, the process of vanishing of the hyperfine interaction is completed at $N \approx 10^{19}$ cm^{-3}, and the insulator–metal transition is completed at 2×10^{20} cm^{-3}). Note that the hyperfine interaction vanishes at doping levels corresponding to noticeable hopping conduction, which is determined by the overlap integral of the impurity states of the main impurities.

The next important concentration determined by us corresponds to the highest spin density that appears in ESR. For 4*H*-SiC, $N_{\max} = 6 \times 10^{18}$ cm^{-3} [1].

With a further increase in the nitrogen concentration, the spin density starts to decrease rapidly due to antiferromagnetic pairing. In Section 3.3 of [1], the nominal distance between impurity centers at which such a pairing occurs was estimated to be $R_0 = 5.1 \times 10^{-7}$ cm. The corresponding concentration $N_{pair} = 1/R_0^3 = 7.5 \times 10^{18}$ cm^{-3}. Clearly, this concentration is close to the highest spin density mentioned above. At such a concentration and zero temperature, unpaired spins detected by ESR should vanish completely provided that they are located at the same distance from each other. However, due to the random impurity distribution, the ESR signal is retained even at higher concentrations, rapidly decreasing with an increase in the concentration.

Pairing can be considered a phase transition from the paramagnetic to the antiferromagnetic phase (spin glass). Thus, with a further increase in the impurity concentration, the insulator–metal phase transition in 4*H*-SiC occurs from the antiferromagnetic insulating phase.

The following characteristic impurity concentration N_{DT} manifests itself in the temperature dependence of the behavior of the line distortion (Fig. 4). One can see from Fig. 4 that, at concentration $N_{\text{DT}} = 1 \times 10^{19}$ cm^{-3}, the sign of the temperature coefficient of the ratio A/B, which characterizes the Dyson distortion of the line shape, changes to the opposite sign (Fig. 3). It is possible that this change in sign accounts for the qualitative variation in the temperature dependences of the resistance of the samples when approaching the insulator–metal phase transition from the insulating phase. These dependences vary from exponential (far from the transition) to power-law dependences (near the transition). Such behavior is characteristic of the insulator–metal phase transition in doped semiconductors [5]. Approximately at the same concentration of uncompensated impurity centers, the resonator Q factor is smallest (Fig. 1, [1]). The reason for this fact is that the increase in the conductivity and the occurrence of a skin layer at high doping levels have opposite effects on the Q factor.

At concentration $N_M = 1.4 \times 10^{19}$ cm^{-3}, new ESR lines (III and IV) arise in strong magnetic fields. The difference between these lines and lines I and II allows us to assume that at least one of them (III) belongs to free spins, which move in the conduction band or upper Hubbard band [8].

Thus, concerning spin properties, a number of characteristic concentrations can be distinguished in the vicinity of the insulator–metal phase transition. These concentrations are governed by the magnitude of the exchange interaction. At the same time, this interaction is related to the overlap integral, which determines the point of the metal–insulator phase transition. To find this point for the 4*H*-SiC:N system under investigation, the temperature dependences of the conductivity were measured for several samples (4, 7, 9, and 14), and the results were processed according to the procedure proposed in [9]. It was found that $n_c \approx 1.5 \times 10^{19}$ cm^{-3} for 4*H*-SiC. Hence, the most characteristic sign of the formation of the metallic phase in 4*H*-SiC is the appearance of additional lines in the ESR spectrum in higher magnetic fields. Other concentrations characteristic of spin properties manifest themselves when the material is still in the insulating state. They are related to the specific features of the parameters of the spin system in the doped region, which correspond to hopping conduction.

Based on the critical concentration n_c, one can find out if the Mott criterion is satisfied for the insulator–metal phase transition [8] in 4*H*-SiC:N. This criterion can be written as $n_c^{1/3} \cdot r_B \approx 0.25$, where r_B is the Bohr radius for this material. Using the values of the effective mass and permittivity from [1], we obtain $r_B = 7.3$–9.3 Å, which yields a value of 0.23–0.18 for the Mott criterion. Such an accuracy in satisfying the Mott criterion can be considered rather high given the current accuracy in determining the parameters of 4*H*-SiC:N. Therefore, the value of critical concentration determined from electrical measurements is rather exact.

Let us try to explain the decrease in the concentration of paramagnetic centers as one approaches the insulator–metal phase transition. This phenomenon was explained above by the formation of an antiferromagnetic spin glass. In this glass, each electron is located near an atom; i.e., the electrons are spatially separated and their antiparallel coupling into pairs or clusters occurs via exchange interaction. In this case, as in any antiferromagnet, local magnetic fields arise in the sample. These fields may be responsible for the antiferromagnetic shift of resonance lines. An alternative explanation for the decrease in the concentration of paramagnetic centers is based on the concept of overlap between the upper and lower Hubbard bands (D^0- and D^--centers). The overlap means that the entire system of shallow-level impurities is divided into three subsystems: neutral paramagnetic D^0 centers, negatively charged D^--centers, and positively charged D^+ centers. In this case, the pair of electrons entering a D^--center is localized at this center and induces no local magnetic fields.

However, the explanation of the experimentally observed phenomena in terms of such a strong overlap of the Hubbard bands in the insulating state far from the transition seems unlikely. In this case, it is most likely the occurrence of the spin-glass antiferromagnetic phase that is responsible for the decrease in the concentration of paramagnetic centers.

7. CONCLUSIONS

(i) Spin relaxation in the insulating phase occurs at clusters containing charged donor and acceptor impurities (multipoles). As the impurity concentration increases, the multipole order of the clusters decreases, so spin relaxation occurs at donor–acceptor pairs near the insulator–metal phase transition.

(ii) The relaxation rate of localized spins increases as one approaches the insulator–metal phase transition, as well as with increasing temperature. At the same time, the relaxation rate of free spins in the metallic phase is independent of the impurity concentration and temperature.

(iii) The temperature dependence of the resistance of the samples shows that the insulator–metal phase transition occurs at a critical nitrogen concentration of about 1.5×10^{19} cm^{-3}. The concentration quenching of line I and the appearance of lines II and III occur at approximately the same concentration, which indicates a rearrangement of the spin system near the critical point. This rearrangement manifests itself in the transition from Curie paramagnetism to Pauli paramagnetism.

ACKNOWLEDGMENTS

We thank M.V. Alekseenko for characterizing the samples, S.V. Egorova for determining the critical concentration for the insulator–metal phase transition, and the participants of the seminar of the Laboratory of Nonequilibrium Processes in Semiconductors at the Ioffe Physicotechnical Institute for helpful discussions.

This study was supported by the Russian Foundation for Basic Research, project no. 00-02-17813; the foundation of the President of the Russian Federation, project NSh 223.2003.02; the Presidium of the Russian Academy of Sciences (the programs “Low-Dimensional Quantum Structures” and “Spin-Dependent Effects in Solids and Spintronics”); and the Ministry of Industry, Science, and Technology of the Russian Federation (the programs “Quantum Macrophysics” and “Strongly Correlated Electrons in Semiconductors, Metals, Superconductors, and Magnetic Materials”).

REFERENCES

1. A. I. Veĭnger, A. G. Zabrodskiĭ, T. V. Tisnek, and E. N. Mokhov, Fiz. Tekh. Poluprovodn. (St. Petersburg) **37**, 874 (2003) [Semiconductors **37**, 846 (2003)].
2. F. J. Dyson, Phys. Rev. **98**, 349 (1955).
3. G. Feher and A. F. Kip, Phys. Rev. **98**, 337 (1955).
4. C. P. Poole, *Electron Spin Resonance* (Wiley, New York, 1967; Mir, Moscow, 1970).
5. A. I. Veĭnger, A. G. Zabrodskiĭ, and T. V. Tisnek, Fiz. Tekh. Poluprovodn. (St. Petersburg) **34**, 46 (2000) [Semiconductors **34**, 45 (2000)].
6. B. I. Shklovskiĭ and A. L. Éfros, *Electronic Properties of Doped Semiconductors* (Nauka, Moscow, 1979; Springer, New York, 1984).
7. A. I. Veĭnger, Fiz. Tekh. Poluprovodn. (Leningrad) **1**, 20 (1967) [Sov. Phys. Semicond. **1**, 14 (1967)].
8. N. F. Mott, *Metal–Insulator Transitions* (Tailor and Francis, London, 1974; Nauka, Moscow, 1979).
9. A. G. Zabrodskiĭ and K. N. Zinov’eva, Zh. Éksp. Teor. Fiz. **86**, 727 (1984) [Sov. Phys. JETP **59**, 425 (1984)].

Translated by N. Korovin

Semiconductors, Vol. 38, No. 7, 2004, pp. 788–790. Translated from Fizika i Tekhnika Poluprovodnikov, Vol. 38, No. 7, 2004, pp. 822–824.
Original Russian Text Copyright © 2004 by Kamilov, Stepurenko, Kovalev.

ELECTRONIC AND OPTICAL PROPERTIES OF SEMICONDUCTORS

Localization of a Longitudinal Autosoliton in InSb

I. K. Kamilov, A. A. Stepurenko*, and A. S. Kovalev
Institute of Physics of Dagestan Scientific Center, Russian Academy of Sciences, Makhachkala, 367003 Russia
**e-mail: ask@iwt.ru*

Submitted December 1, 2003; accepted for publication December 30, 2003

Abstract—The current density distribution over the cross section of a sample was studied to localize a longitudinal autosoliton in the sample. It is shown that the longitudinal autosoliton is localized along the central axis of the sample or close to it. It is established that the longitudinal autosoliton is stable in a wide range of currents. *© 2004 MAIK “Nauka/Interperiodica”.*

Theoretical [1–7] and experimental [8–12] studies have shown that a dissipative structure is formed in a nonequilibrium excited electron–hole plasma produced either in *n*-GaAs by impact ionization or injection or in *n*-Ge by photogeneration, as well as in InSb by Joule heating. This structure contains local regions of extremely high density and temperature of charge carriers—autosolitons—in the form of both current layers (longitudinal autosolitons) and layers of strong electric field (transverse autosolitons). In an asymmetric electron–hole plasma ($\mu_e \neq \mu_p$ or $n_e \neq n_p$), layers of strong electric field move in the electric field in the direction of hole drift at $u = (n - p)/n > 0$ and in the direction of electron drift at $b = \mu_e/\mu_p > 1$ [13].

It is believed [11, 12] that a nonequilibrium electron–hole plasma produced by Joule heating of a sample has a radial temperature gradient and, hence, a density gradient. Transverse and longitudinal autosolitons are formed in an electric field in low- and high-density electron–hole plasmas, respectively. The velocity of transverse autosolitons was determined experimentally by the potential probe method: 3×10^2–2×10^3 cm/s in Ge [10] and ~10^3 cm/s in InSb [11, 12].

It is reasonable to assume that longitudinal autosolitons are arranged along the sample axis or close to it. To clarify this point, the current density distribution over the cross section of the sample was studied.

Compensated *p*-InSb crystals with a hole density of 10^{12} cm^{-3} and mobility μ_p = 2500–4000 cm^2 V^{-1} s^{-1} were studied at 77 K. The samples under study were parallelepipeds, with one of the end contacts partitioned into several areas to form current probes.

In this paper, we report the results of measurements for three samples: a sample $0.45 \times 0.21 \times 0.14$ cm^3 in size with an end contact partitioned into three areas (current probes) (Fig. 1a), a sample $0.66 \times 0.22 \times 0.14$ cm^3 in size with an end contact partitioned into five areas (Fig. 1b), and a sample $0.50 \times 0.3 \times 0.3$ cm^3 in size (denoted as *1*, *2*, and *3*, respectively).

To equalize the probe currents in the linear portion of the *I*–*V* characteristic, trimmer potentiometers were used. A difference in currents arises due to both the difference in the areas of current probes and the initial inhomogeneity of the crystal. Voltage pulses from current resistors were applied to the differential inputs of an oscilloscope to subtract them from each other. The resulting signal, which was passed through an interface unit and an analog-to-digital converter, was stored in a computer. A sawtooth voltage pulse was applied to the sample to study the dependence of the differential probe current on the applied voltage.

Figure 2a shows the oscillogram of the current difference between the central probe *0* and peripheral probes *1* and *2* ($I_0 - I_1$, $I_0 - I_2$) obtained by applying a sawtooth voltage to sample 1. We can see that the current from the central probe decreases in the region of subcritical voltages. The current decrease may be caused by a decrease in either the density or the mobility of carriers. Since Joule heating occurs, the decrease in the mobility in the region of the subcritical electric field reduces the current from the central probe. At the same time, even in the region of supercritical weak electric fields, the current from central probe *0* abruptly increases with respect to those from peripheral probes *1* and *2*, which indicates a sharp increase in the carrier

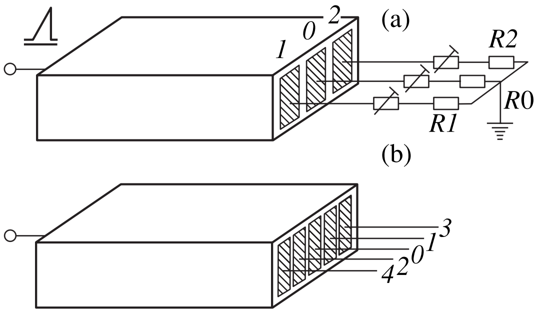

Fig. 1. (a) Sample 1 with three current probes and (b) sample 2 with five current probes.

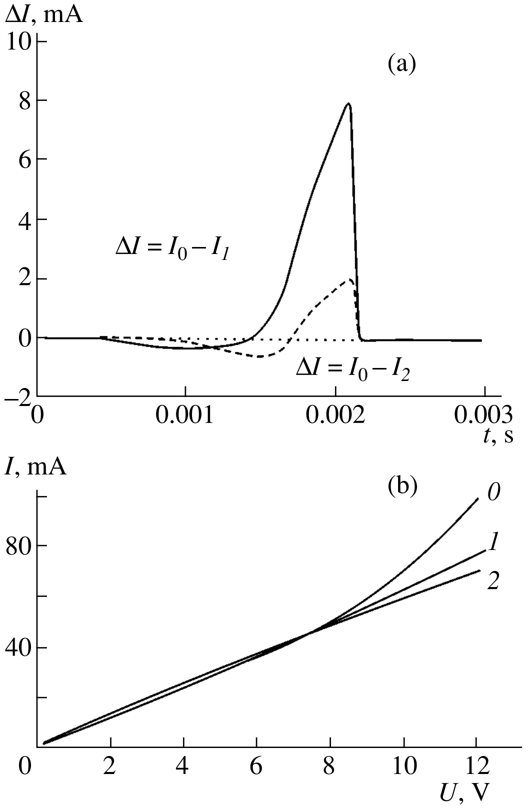

Fig. 2. (a) Oscillograms of the current difference between central (*0*) and peripheral (*1*, *2*) probes of sample 1; (b) *I–V* characteristics measured with current probes of sample 1.

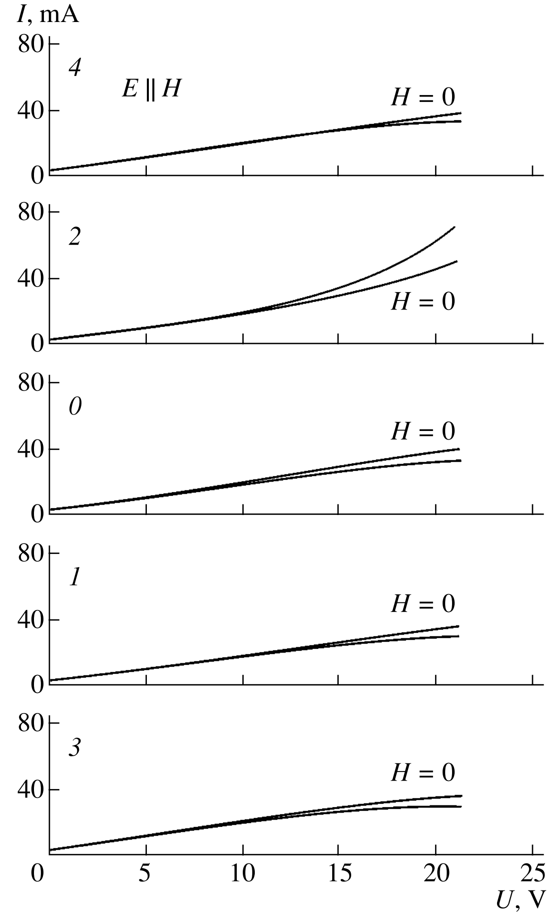

Fig. 3. *I–V* characteristics measured with current probes *0–4* of sample 2 in a longitudinal magnetic field (**H** || **E**, $H = 1.36 \times 10^4$ A/m) and without a field.

density. In [12] it was shown that the intrinsic carrier density can be high enough even at relatively low temperature ($T \approx 150$ K). The effect of nonuniform distribution of temperature and carrier density in an InSb sample upon dc Joule heating was considered in [14]. In the case of Joule heating of a sample by current pulses ($\tau = 2 \times 10^{-3}$ s, $f = 10$ Hz), the nonuniformity in the temperature distribution due to the low thermal diffusivity of InSb will be even higher if we take into account the high resistivity of the samples under study ($n = 10^{12}$ cm^{-3}, $\mu_p \approx 2500$ cm^2 V^{-1} s^{-1}). According to the results of [12, 14], Joule heating results in a temperature that is sufficient to attain intrinsic conduction and form a nonequilibrium electron–hole plasma precisely in the vicinity of the sample axis. In turn, one or several current filaments (longitudinal autosolitons) are formed, depending on the excitation level.

The *I–V* characteristic measured with central probe *0* is distinctly superlinear, while the *I–V* characteristics measured with peripheral probes *1* and *2* are linear (Fig. 2b). Figure 3 shows the *I–V* characteristics measured with the five probes of wide sample *2*. As can be seen, the *I–V* characteristic measured with the second probe is superlinear (Fig. 3, curve *2*). A weak magnetic field enhances the superlinearity of the *I–V* characteristic measured with the second probe, while the *I–V* characteristics measured with peripheral probes contain sublinear portions in the supercriticality region in a weak electric field (Fig. 3, curves *0*, *1*, *3*, *4*). This result confirms the fact (revealed by other experimental methods [15]) that the longitudinal autosoliton is cold; i.e., it is a localized region of increased carrier density and decreased temperature.

Thus, it was experimentally shown that the longitudinal autosoliton is localized along the central axis of the sample or close to it.

The value of the critical current of the longitudinal autosoliton was also measured. Short samples were used, whose longitudinal dimensions were much smaller than their transverse dimensions. Such a configuration of the sample made it possible to form only longitudinal autosolitons. Single rectangular voltage pulses 2.5 ms long were applied to the sample.

Figure 4 shows the oscillograms of a current passing through sample 3, which illustrate the dynamics of the longitudinal evolution of the autosoliton. The oscillogram shown in Fig. 4a is a characteristic pattern of formation of a longitudinal autosoliton in an electron–hole plasma produced by Joule heating ($U_1 = 0.9$ V, $I_1 = 0.0011$ A). Figure 4b shows the current oscillogram recorded at the excitation level, which is significantly higher than the initial level ($U_2 = 2.4$ V, $I_2 = 2.31$ A).

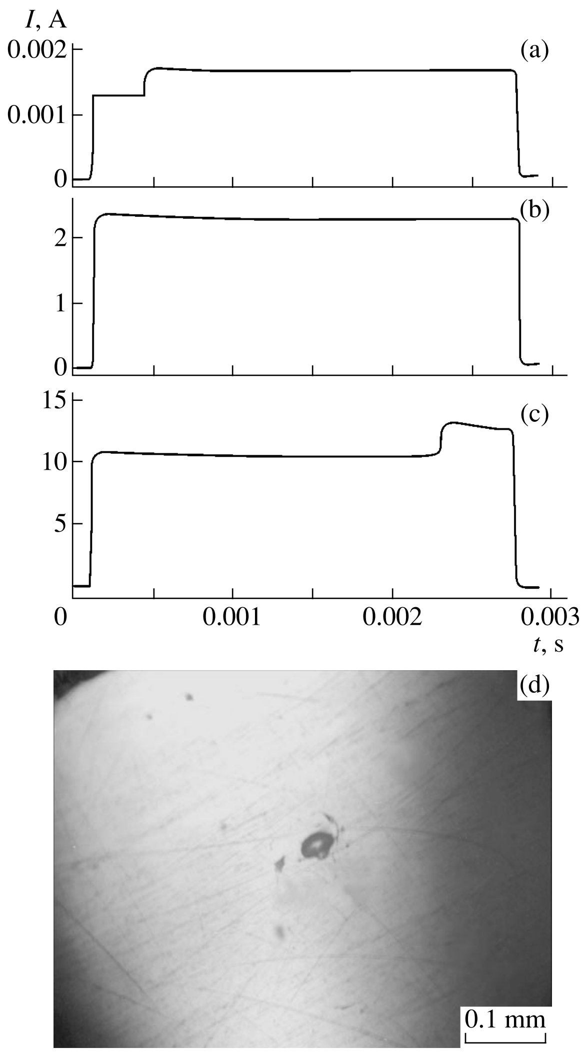

Fig. 4. (a–c) Oscillograms of a current passing through sample 3 (the applied electric field increases from (a) to (c)); (d) micrograph of the surface of sample 3 with mechanical damage.

The oscillogram in Fig. 4c illustrates a jump in the current of the longitudinal autosoliton, which results in the decay of the autosoliton, accompanied by a thermal breakdown of the sample and, hence, mechanical damage. In this case, the prebreakdown current at excitation voltage U_3 = 4 V is I_3 = 11.1 A. Figure 4d shows a micrograph of the surface of the sample (perpendicular to the current) with mechanical damage shaped like a pit located near the midpoint.

Thus, the studies performed showed the stability of longitudinal autosolitons in the range of currents I = 0.0011–11.1 A. If we take into account the transverse size of the autosoliton $\mathcal{L} = 1.6 \times 10^{-3}$ cm, the current density of the autosoliton can be as high as $j = 5.5 \times 10^6$ A/cm^2.

Apparently, such a high current density of the longitudinal autosoliton is related to the decrease in the electron temperature at the center of the autosoliton relative to the peripheral regions, which, in turn, is due to the increase in the carrier density in the localized region (autosoliton) [15]. This circumstance follows from the heat balance equation for the system of electrons in the autosoliton and the lattice [1]:

$$W = n(T_e - T_0)/\tau_\varepsilon,$$

where T_e is the electron temperature, T_0 is the lattice temperature, and τ_ε is the electron-energy relaxation time.

ACKNOWLEDGMENTS

This study was supported by the federal program of Support for Leading Scientific Schools, project no. NSh 22.53.2003.2, and the Instrument Pool of the Analytical Center of the Dagestan Scientific Center, Russian Academy of Sciences.

REFERENCES

1. B. S. Kerner and V. V. Osipov, Zh. Éksp. Teor. Fiz. **71**, 1542 (1976) [Sov. Phys. JETP **44**, 807 (1976)].
2. B. S. Kerner and V. V. Osipov, Pis'ma Zh. Éksp. Teor. Fiz. **41**, 386 (1985) [JETP Lett. **41**, 473 (1985)].
3. B. S. Kerner and V. V. Osipov, Pis'ma Zh. Éksp. Teor. Fiz. **18**, 122 (1973) [JETP Lett. **18**, 70 (1973)].
4. B. S. Kerner and V. V. Osipov, Fiz. Tekh. Poluprovodn. (Leningrad) **13**, 891 (1979) [Sov. Phys. Semicond. **13**, 523 (1979)].
5. B. S. Kerner and V. V. Osipov, Fiz. Tverd. Tela (Leningrad) **21**, 2342 (1979) [Sov. Phys. Solid State **21**, 1348 (1979)].
6. B. S. Kerner and V. V. Osipov, Fiz. Tekh. Poluprovodn. (Leningrad) **13**, 721 (1979) [Sov. Phys. Semicond. **13**, 424 (1979)].
7. A. L. Dubitskiĭ, B. S. Kerner, and V. V. Osipov, Fiz. Tverd. Tela (Leningrad) **28**, 1290 (1986) [Sov. Phys. Solid State **28**, 725 (1986)].
8. B. S. Kerner and V. F. Sinkevich, Pis'ma Zh. Éksp. Teor. Fiz. **36**, 359 (1982) [JETP Lett. **36**, 436 (1982)].
9. B. S. Kerner, V. V. Osipov, M. T. Romanenko, and V. F. Sinkevich, Pis'ma Zh. Éksp. Teor. Fiz. **44**, 77 (1986) [JETP Lett. **44**, 97 (1986)].
10. M. N. Vinoslavskiĭ, Fiz. Tverd. Tela (Leningrad) **31** (8), 315 (1989) [Sov. Phys. Solid State **31**, 1461 (1989)].
11. A. A. Stepurenko, Fiz. Tekh. Poluprovodn. (St. Petersburg) **28**, 402 (1994) [Semiconductors **28**, 243 (1994)].
12. I. K. Kamilov and A. A. Stepurenko, Phys. Status Solidi B **194**, 643 (1996).
13. V. V. Gafiĭchuk, B. S. Kerner, V. V. Osipov, and I. V. Tyslyuk, Fiz. Tverd. Tela (Leningrad) **31** (8), 46 (1989) [Sov. Phys. Solid State **31**, 1304 (1989)].
14. V. V. Antonov and L. I. Kats, Fiz. Tekh. Poluprovodn. (Leningrad) **16**, 1050 (1982) [Sov. Phys. Semicond. **16**, 672 (1982)].
15. I. K. Kamilov, A. A. Stepurenko, and A. S. Kovalev, Fiz. Tekh. Poluprovodn. (St. Petersburg) **36**, 187 (2002) [Semiconductors **36**, 180 (2002)].
16. I. K. Kamilov, A. A. Stepurenko, and A. S. Kovalev, Fiz. Tekh. Poluprovodn. (St. Petersburg) **32**, 697 (1998) [Semiconductors **32**, 625 (1998)].

Translated by A. Kazantsev

Semiconductors, Vol. 38, No. 7, 2004, pp. 791–795. Translated from Fizika i Tekhnika Poluprovodnikov, Vol. 38, No. 7, 2004, pp. 825–829.
Original Russian Text Copyright © 2004 by Gutkin, Reshchikov.

ELECTRONIC AND OPTICAL PROPERTIES OF SEMICONDUCTORS

Piezospectroscopic Study of the Emission Band of *n*-GaAs:S Peaked at about 1.2 eV

A. A. Gutkin and M. A. Reshchikov
Ioffe Physicotechnical Institute, Russian Academy of Sciences, Politekhnicheskaya ul. 26, St. Petersburg, 194021 Russia
e-mail: Agut@defect.iofiFe.ru

Submitted December 25, 2003; accepted for publication December 30, 2003

Abstract—The effect of uniaxial pressure up to 8 kbar applied along the crystallographic directions [111] and [001] on the spectra and polarization of a broad photoluminescence band of *n*-GaAs:S peaked at 1.2 eV, which is related to the trapping of electrons by $V_{Ga}S_{As}$ complexes, was studied. The dependences of the polarization of the band emission on the photon energy and temperature indicate that the initial trigonal symmetry of the $V_{Ga}S_{As}$ complex is reduced and can be monoclinic with a {011} plane of symmetry. In this case, the distortions of a complex are not reoriented and the axis of its emitting optical dipole deviates at nearly the same angle from the $\langle 111 \rangle$ and $\langle 001 \rangle$ directions lying in the plane of symmetry. Selection of the components of the photoluminescence band, split due to the uniaxial pressure, based on the piezospectroscopic behavior of the emission from anisotropic centers, confirms the model proposed for the $V_{Ga}S_{As}$ complex and shows that the rotator contribution to the emission of this complex is small. Comparison of the results obtained with the data for a similar complex, $V_{Ga}Te_{As}$, indicate a significant change in the properties of vacancy–shallow-level donor complexes when a donor of Group VI is replaced by a different donor of the same group. *© 2004 MAIK "Nauka/Interperiodica".*

1. INTRODUCTION

The broad photoluminescence band of GaAs:S peaked at about 1.2 eV is generally attributed to the radiative recombination of conduction electrons with holes captured by complexes formed by gallium vacancies (V_{Ga}) and shallow-level donors (S_{As}) [1–4]. The spectrum of this emission almost coincides with the similar luminescence spectrum of $V_{Ga}Te_{As}$ complexes in *n*-GaAs:Te [2, 3]. Since both S atoms and Te atoms form shallow-level donors in the GaAs lattice by substituting As atoms, one might expect these luminescence bands to behave similarly under uniaxial pressure. However, preliminary research on the polarization of emission of $V_{Ga}S_{As}$ complexes in *n*-GaAs:S revealed that its variation under uniaxial pressure differs significantly from the variation in the emission polarization for $V_{Ga}Te_{As}$ complexes in *n*-GaAs:Te [2, 3, 5, 6], which indicates that the distortions of $V_{Ga}S_{As}$ complexes are not aligned under uniaxial strain.

In this study, a detailed piezospectroscopic investigation of the photoluminescence of $V_{Ga}S_{As}$ complexes was performed. Based on the results obtained, the characteristics of the spatial structure of the $V_{Ga}S_{As}$ complex and the electronic state of a hole localized at this complex were determined. Comparison of the corresponding data for the $V_{Ga}S_{As}$ and $V_{Ga}Te_{As}$ complexes shows significant discrepancies between the structure and properties of complexes with similar initial composition formed by gallium vacancies and shallow-level donors in GaAs when different atoms of Group VI of the periodic table serve as donor components of a complex.

2. EXPERIMENTAL RESULTS AND QUALITATIVE ANALYSIS

Experiments were performed with sulfur-doped *n*-GaAs:S samples similar to those studied in [2, 3]. Doping was performed either by diffusing sulfur from vapor into GaAs with an electron density of about 10^{16} cm^{-3} or by adding sulfur to the melt in growing crystals by the Czochralski method. In both cases, the concentration of shallow-level donors in the surface layer, from which photoluminescence was measured, exceeded 10^{18} cm^{-3}.

The photoluminescence of samples was excited by the generation of electron–hole pairs using a He–Ne laser with a wavelength of ~0.62 μm and measured in the direction perpendicular to the external-pressure axis. The spectra contained a broad band peaked at photon energy $\hbar\omega = 1.18$ eV (at temperature $T = 2$–4 K), related to $V_{Ga}S_{As}$ complexes (Fig. 1). When uniaxial pressure $\mathbf{P}$ was applied to a sample along the [111] or [001] directions, this band was slightly broadened and shifted to larger photon energies, while the emission in the band became polarized. These changes are illustrated in Fig. 1, which, along with the spectral distribution of the luminescence intensity I at $P = 0$ and 8 kbar, shows the spectra of the polarization ratio r, which is defined as the ratio of the intensities of light with electric wave vectors $\boldsymbol{\varepsilon}$ parallel and perpendicular to the pressure axis, $I(\|)$ and $I(\perp)$, respectively. The polarization of the band emission varied in such a way that the integrated band polarization, as well as in the case $P = 0$,

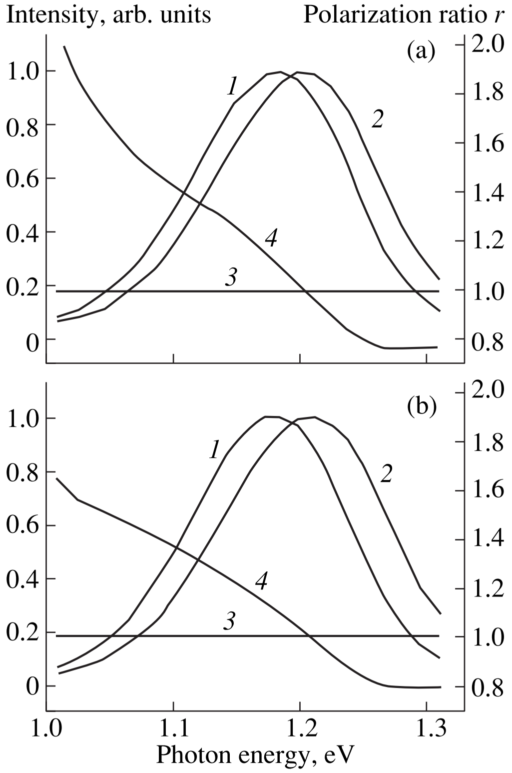

Fig. 1. Spectra of (*1*, *2*) the photoluminescence intensity I and (*3*, *4*) the polarization ratio r for $V_{Ga}S_{As}$ complexes (*1*, *3*) in an unstrained crystal ($P = 0$) and (*2*, *4*) under uniaxial pressure ($P = 8$ kbar) at $T = 2$ K. (a) $\mathbf{P} \parallel [001]$ and (b) $\mathbf{P} \perp [111]$.

was absent at low temperatures; i.e., the following relation was satisfied:

$$r^* = \int I(\parallel)d(\hbar\omega)/\int I(\perp)d(\hbar\omega) = 1.$$

Here, r^* is the integrated polarization ratio.

Such behavior of the polarization of the broad low-temperature photoluminescence band of the complexes, the symmetry of which is lower than the point symmetry of an ideal crystal, is caused by the splitting of the emission band into components due to an external uniaxial strain. These components correspond to different orientations of complexes with respect to the strain axis. The existence of this splitting under both $\mathbf{P} \parallel [111]$ and $\mathbf{P} \parallel [001]$ indicates that the symmetry of the defects under consideration is not higher than that of the monoclinic system with a {011} plane of symmetry [7].[1] This circumstance means that the $V_{Ga}S_{As}$ complex and its environment have additional distortions that are not reorientable and, thus, reduce the initial trigonal symmetry of the complex. In this case, since the dispersions of the polarization ratio under pressure applied along the [111] and [001] axes differ only slightly (Fig. 1), one might expect that the axis of the emitting dipole of the complex is deviated at approximately the same angle with respect to the ⟨111⟩ and ⟨001⟩ directions. In contrast to $V_{Ga}S_{As}$ complexes, a large dispersion of the emission polarization in the band was observed for $V_{Ga}Te_{As}$ complexes only with $\mathbf{P} \parallel [111]$, because the axis of the emitting dipole of the $V_{Ga}Te_{As}$ complex deviates only slightly from one of the ⟨111⟩ directions (the angle of deviation is ~6° [3, 5, 6]).

Another difference between the $V_{Ga}S_{As}$ and $V_{Ga}Te_{As}$ complexes, as was noted above, is the absence of the low-temperature alignment of distortion under uniaxial strain in the former, as is indicated by the absence of the integrated polarization of emission at temperatures up to ~60 K. A further increase in temperature leads to an abrupt increase in r^* at both $\mathbf{P} \parallel [111]$ and $\mathbf{P} \parallel [001]$ (Fig. 2). However, this effect is caused by the thermal transport of holes to the centers, which has an orientation characterized by the largest energy of thermal activation of hole emission under pressure [8], rather than by the alignment of the distortions of the complexes due to their reorientation. This is caused by the fact that the equilibrium integrated polarization of the band increases rather than drops with increasing temperature (Fig. 2). In Fig. 2, the results of measurements of this effect for $V_{Ga}S_{As}$ complexes are compared with similar data for $V_{Ga}Te_{As}$ complexes. As can be seen from Fig. 2, in contrast to $V_{Ga}Te_{As}$, a significant increase in r^* for the emission band of $V_{Ga}S_{As}$ with increasing temperature is observed for both $\mathbf{P} \parallel [111]$ and $\mathbf{P} \parallel [001]$. This fact shows that, for $V_{Ga}S_{As}$ complexes, significant splitting of the energy levels of centers with different orientations is observed for both strain directions, and it confirms the above assumption of approximately equal deviations of the emitting-dipole axis from the ⟨111⟩ and ⟨001⟩ directions. It is also noteworthy that, according to Fig. 1, the polarization ratio for the low-energy components of the emission band exceeds unity under uniaxial pressure. Since these components correspond to the group of complexes whose energy level is maximally spaced from the valence band, this group of centers (according to [8]) should make the largest contribution to the radiative trapping of electrons at elevated temperature. Therefore, the integrated polarization ratio should exceed unity with an increase in temperature, which is observed experimentally (Fig. 2).

3. QUANTITATIVE ANALYSIS OF THE PHOTOLUMINESCENCE SPECTRA UNDER UNIAXIAL PRESSURE

As follows from the previous section, the highest symmetry that $V_{Ga}S_{As}$ complexes can have is monoclinic with a {011} plane of symmetry [7]. This type of symmetry arises for initially trigonal complexes if the plane of symmetry of the additional distortion coincides with one of the {011} planes containing the initial

---

[1] In general, a defect whose emission bands are split under $\mathbf{P} \parallel [111]$ and $\mathbf{P} \parallel [001]$, may have a higher symmetry of orthorhombic type 1 [7]. However, a complex composed of two different components cannot have such symmetry in the GaAs lattice.

axis of the complex, i.e., the axis connecting the centers of V_{Ga} and S_{As}. If we assume that the defects under consideration have precisely this type of symmetry, then, at **P** || [111] and **P** || [001], their emission band should split into three and two components, respectively [7].

Considering the emission of centers with the symmetry mentioned above upon generation of electron–hole pairs (equiprobable excitation of centers with all orientations) in the classical dipole approximation, one can obtain relations between the intensities of these split components at different polarizations of emitted light under any experimental conditions. For light propagating perpendicular to the pressure axis [001], these relations have the form

$$I_1(\|) = I_1(\perp)[\mu_2 + a^2(1-2\mu_2)]/[\mu_2 + b^2(1-\mu_2)], \tag{1}$$

$$I_2(\|) = 2I_1(\perp), \tag{2}$$

$$I_2(\perp) = I_1(\|) + I_1(\perp). \tag{3}$$

Here, $I_1(\|)$, $I_1(\perp)$ and $I_2(\|)$, $I_2(\perp)$ are the total intensities of the first and second photoluminescence components, respectively, when the electric vector of a light wave is parallel or perpendicular to the pressure axis; μ_2 is the relative contribution of the rotator to the emission of an individual center; and a and b are the absolute values of the projection of the unit vector of the emitting-dipole axis of the complex on the $\langle 001\rangle$ crystallographic axes.

It is also clear that, if the effect of an external strain is small in comparison with the dominant intracenter interaction, the electron wave functions of the defect change only insignificantly and the effect of uniaxial pressure is only reduced to different variations in the energy of anisotropic centers with different orientations. Since the integrated polarization on the band under study did not arise at low temperatures under pressures of up to 8 kbar, the experiments performed correspond to this case. Then one would expect that the photoluminescence spectrum of centers with the same orientation with respect to the axis strain, i.e., the spectrum of each split component, would reproduce the shape of the spectrum of the entire set of centers in the absence of strain. This circumstance allows us to replace the total intensities of the components by the maximum intensity of each component in (1)–(3).

Thus, when the center under study has monoclinic symmetry with a {011} plane of symmetry, at **P** || [001], its emission spectrum with **ε** || **P** and **ε** ⊥ **P** should contain only two components. Their position is the same for both polarizations of light; the shape of the spectrum is similar to that of the spectra at $P = 0$, and the maximum relative emission intensity obeys relations (1)–(3).

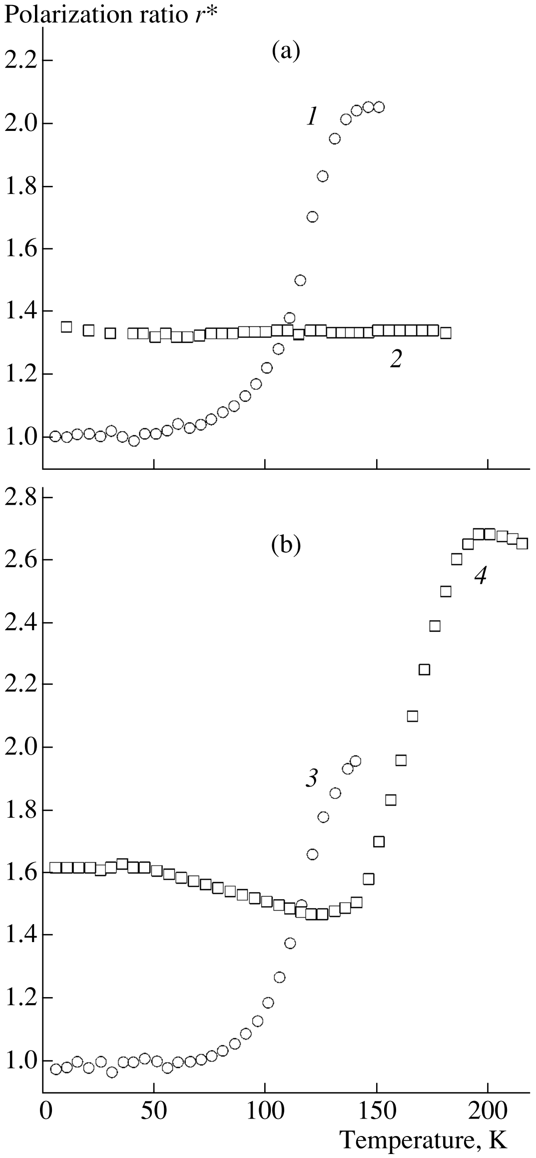

Fig. 2. Temperature dependences of the integrated polarization ratio r^* for the photoluminescence of the (*1, 3*) $V_{Ga}S_{As}$ and (*2, 4*) $V_{Ga}Te_{As}$ complexes under uniaxial pressure P = (*1*–*3*) 8 and (*4*) 10 kbar [8]. (a) **P** || [001] and (b) **P** ⊥ [111].

In this case, based on the above regularities, we can separate the experimental luminescence spectra of $V_{Ga}S_{As}$ obtained at **P** || [011] into split components using the procedure applied by us previously to $V_{Ga}Te_{As}$ complexes [9]. It was found that such a separation is possible; the corresponding results for P = 8 kbar are shown in Fig. 3. The positions of the maxima in the spectra of the components correspond to $\hbar\omega_{01} \approx 1.188$ eV and $\hbar\omega_{02} \approx 1.220$ eV (the component splitting is (32 ± 4) meV), and the relative intensity in the maxima of the components is $I_{1max}(\|) = 0.82$–0.81, $I_{1max}(\perp) = 0.09$–0.10, $I_{2max}(\|) = 0.18$–0.20, and $I_{2max}(\perp) = 0.92$–0.91.

At the same time, it turned out to be impossible to separate similar spectra obtained at **P** || [111] into two components, which one would expect for the emission spectra of monoclinic centers with a {011} plane of symmetry, which in this case are split into three components [7].

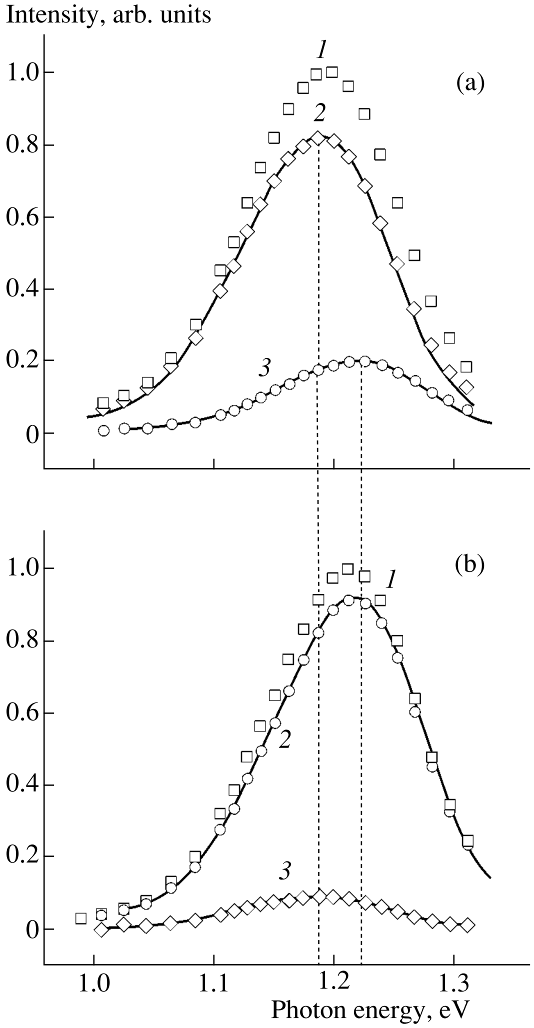

Fig. 3. Photoluminescence spectra of $V_{Ga}S_{As}$ complexes for different polarizations of measured emission under a pressure of 8 kbar applied along the [001] direction at $T = 2$ K: (*1*) experiment; (curves *2*, *3*) two components with shapes coinciding with the spectral shape at $P = 0$; and (symbols *2*, *3*) values of the emission intensities that yield the experimental spectrum in sum and fit curves *2* and *3* in the best way. (a) $\boldsymbol{\varepsilon} \parallel \mathbf{P}$ and (b) $\boldsymbol{\varepsilon} \perp \mathbf{P}$.

4. DISCUSSION AND CONCLUSIONS

To determine possible directions of the emitting-dipole axis of the complex, let us introduce designation $I_{1\max}(\|)/I_{1\max}(\perp) = \gamma$ and take into account that, for the monoclinic defect under consideration with a {011} plane of symmetry,

$$a = \sin\varphi, \quad b = (1/\sqrt{2})\cos\varphi, \qquad (4)$$

where φ in the angle between a ⟨001⟩ axis and the emitting dipole axis in the plane of symmetry of the complex. Then, the following relations can be derived from (1) and (4):

$$0 \le b^2 = [1-(\gamma-1)\mu_2/(1-2\mu_2)]/(2+\gamma) \le 1/2. \quad (5)$$

Since $0 \le \mu_2 \le 1$ and, according to the results of the previous section, $\gamma = 8.1$–9.1, inequalities (5) are satisfied only at $b^2 = 0.09$–0 and $\mu_2 = 0$–0.1.

If $b^2 \approx 0.09$ ($\mu_2 \approx 0$), $\varphi \approx \pm 64°$; i.e., the direction of the optical-dipole axis significantly differs from the ⟨111⟩ and ⟨001⟩ crystallographic axes lying in the plane of symmetry of the complex, for which $\varphi \approx \pm 35.3°$ and $\varphi = \pm 90°$, respectively. This observation is consistent with the qualitative conclusion made in Section 2.

If $b^2 \approx 0$ ($\mu_2 \approx 0.1$), $\varphi \approx \pm 90°$; i.e., the optical-dipole axis only slightly deviates from the ⟨001⟩ axis lying in the plane of symmetry of the defect. In this case, if pressure is applied along the [111] axis, the splitting of the emission components belonging to centers with different orientations should be significantly smaller than at **P** || [001]. The latter conclusion is inconsistent with the experimental data shown in Figs. 1 and 2.

Thus, the piezospectroscopic behavior of the photoluminescence band of the $V_{Ga}S_{As}$ complex is consistent with the model of a monoclinic defect with a {011} plane of symmetry, whose emitting optical dipole deviates from the ⟨111⟩ and ⟨001⟩ directions lying in this plane at approximately the same angle, while the contribution of the rotator to the center emission is small ($\mu_2 \approx 0$).

The latter two features, as well as the absence of alignment of distortions, are responsible for the significant difference between the $V_{Ga}S_{As}$ and $V_{Ga}Te_{As}$ complexes [5, 9]. These differences can also be explained considering the differences in the behavior of shallow-level donors formed by Te and S atoms substituting As atoms in AlGaAs [10]. According to calculations [10], when the content of Al is sufficiently high, the stable state of S atoms substituting As atoms in AlGaAs is the state of monoclinic symmetry with two dangling bonds and a Ga–Ga dimer, whose axis is perpendicular to the plane of symmetry of the defect (*DBB* state) rather than the state of trigonal symmetry (*DX* center), as for Te_{As}. The reason for this dissimilarity is the difference in the energies of valence *s* and *p* electrons of the Te and S atoms [10]. If we assume that the neighborhood of a gallium vacancy makes the *DX* center stable for Te_{As} and the *DBB* state stable for S_{As} (rather than the shallow-donor states) in GaAs as well, the above differences in the $V_{Ga}S_{As}$ and $V_{Ga}Te_{As}$ complexes can be qualitatively explained. However, a final conclusion about the reasons and nature of these differences can only be drawn on the basis of detailed calculations of the complexes themselves.

REFERENCES

1. E. W. Williams and H. B. Bebb, in *Semiconductors and Semimetals*, Ed. by R. K. Willardson and A. C. Beer (Academic, New York, 1972), Vol. 8, p. 321.
2. A. A. Gutkin, N. S. Averkiev, M. A. Reshchikov, and V. E. Sedov, in *Proceedings of 18th International Confer-*

ence on Defects in Semiconductors, Ed. by M. Suezawa and H. Katayama-Yoshida (Sendai, Japan, 1995); Mater. Sci. Forum **196–201**, 231 (1995).

3. A. Gutkin, M. Reshchikov, V. Sedov, and V. Sosnovskij, Proc. Est. Acad. Sci., Phys., Math. **44**, 212 (1995).
4. S. V. Bulyarskiĭ, N. S. Grushko, and A. V. Zhukov, Zh. Éksp. Teor. Fiz. **116**, 1027 (1999) [JETP **89**, 547 (1999)].
5. A. A. Gutkin, M. A. Reshchikov, and V. E. Sedov, Fiz. Tekh. Poluprovodn. (St. Petersburg) **34**, 1201 (2000) [Semiconductors **34**, 1151 (2000)].
6. N. S. Averkiev, A. A. Gutkin, E. B. Osipov, *et al.*, Fiz. Tekh. Poluprovodn. (St. Petersburg) **26**, 1269 (1992) [Sov. Phys. Semicond. **26**, 708 (1992)].
7. A. A. Kaplyanskii, J. Phys. (Paris) **28** (Suppl. 8–9), 4 (1967).
8. A. A. Gutkin and M. A. Reshchikov, Fiz. Tekh. Poluprovodn. (St. Petersburg) **37**, 287 (2003) [Semiconductors **37**, 271 (2003)].
9. A. A. Gutkin and A. V. Ermakova, Fiz. Tekh. Poluprovodn. (St. Petersburg) **37**, 908 (2003) [Semiconductors **37**, 884 (2003)].
10. D. J. Chadi and C. H. Park, in *Proceedings of 18th International Conference on Defects in Semiconductors*, Ed. by M. Suezawa and H. Katayama-Yoshida (Sendai, Japan, 1995); Mater. Sci. Forum **196–201**, 285 (1995).

Translated by Yu. Sin'kov

Semiconductors, Vol. 38, No. 7, 2004, pp. 796–799. Translated from Fizika i Tekhnika Poluprovodnikov, Vol. 38, No. 7, 2004, pp. 830–833.
Original Russian Text Copyright © 2004 by Aliev.

ELECTRONIC AND OPTICAL PROPERTIES OF SEMICONDUCTORS

Hysteresis in Ag_2Te near and within the Phase Transition Region

S. A. Aliev
Institute of Physics, National Academy of Sciences of Azerbaijan, Baku, 370143 Azerbaijan
e-mail: sarhad@physics.ab.az

Submitted July 8, 2003; accepted for publication January 8, 2004

Abstract—Electrical conductivity, the Hall coefficient, and thermoelectric power were studied and differential thermal analysis was carried out in Ag_2Te crystals near and within the range of phase transitions, in the directions of heating and cooling. A large hysteresis loop was observed. The results are discussed in terms of the theory of smeared phase transitions. Agreement between experimental data and theory is achieved in a second approximation of the inclusion function $L_2(T)$ and its derivative with respect to temperature, dL_2/dT. *© 2004 MAIK "Nauka/Interperiodica".*

1. INTRODUCTION

The electrical and thermal properties of Ag_2Te near and within the region of structural phase transition have been studied in [1–6]. The most detailed data were presented in [5, 6]. In Ag_2Te and Ag_2Se, additional phase transitions with a small change in the internal energy of the crystal were observed before and after the main transition. The experimental data were discussed in terms of the theory of smeared phase transitions [7–9]. The parameters of the phase transitions, which define the range and the degree of smearing, were calculated, and the smearing of transitions in Ag_2Te and Ag_2Se was found to be strong. It is assumed that the hysteresis of electrical and thermal properties can be observed in Ag_2Te, where phase transitions are closely spaced in temperature. In this paper, we discuss the results of differential thermal analysis, $\Delta T_y(T)$, the electrical conductivity $\sigma(T)$, the Hall coefficient $R(T)$, and the Seebeck coefficient $\alpha(T)$ in Ag_2Te, which were measured in the course of heating or cooling in the range $300 \longleftrightarrow 450$ K.

2. EXPERIMENTAL RESULTS

Three sets of Ag_2Te samples of different composition were studied: (i) stoichiometric, (ii) with an excess of Te (up to 0.75 at %), and (iii) with excess Ag (up to 0.25 at %). The experiments were performed in the setup described in [10], in which adiabatic and isothermal conditions can be created.

Figure 1a shows the temperature dependence $\sigma(T)$ for a sample with excess Ag when it is heated and cooled. It can be seen that the $\sigma(T)$ curve measured during cooling lies much lower than that obtained during heating. When the time of cooling is increased [t = 3, 4, and 6 h: curves (*1*), (*2*), and (*3*)], the $\sigma(T)$ curves run higher; in this situation the hysteresis loops become narrower, but their area remains virtually unchanged. During cooling, the $\sigma(T)$ dependences exhibit two definite steps at 400 and 382 K, which shift to a lower temperature compared to $\sigma(T)$ steps during heating (405, 415, and 425 K).

Figure 1b shows the temperature dependence of ΔT_g for the same sample. As can be seen, $\Delta T_y(T)$ curves also demonstrate two phase transitions with absorption of

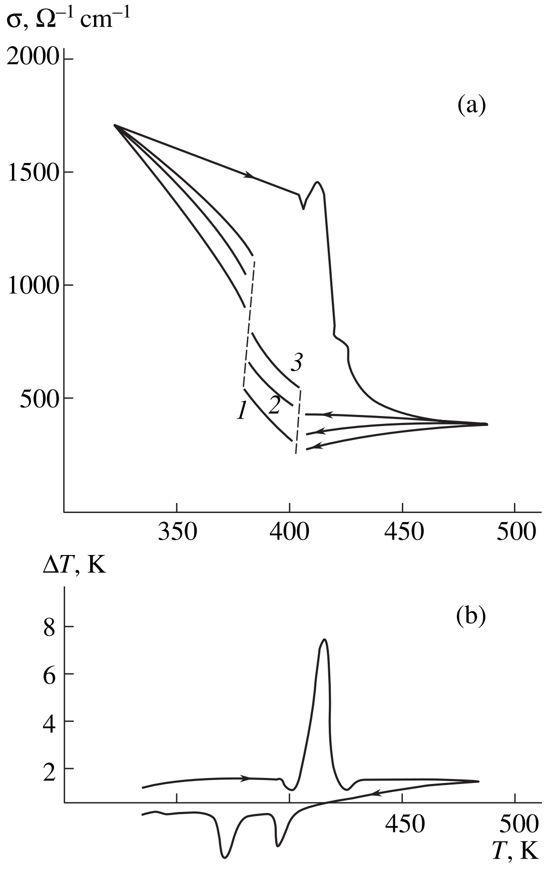

Fig. 1. Temperature dependences of (a) electrical conductivity σ and (b) ΔT in Ag_2Te with excess Ag (0.25 at %). Time of cooling: (*1*) 3, (*2*) 4, and (*3*) 6 h.

1063-7826/04/3807-0796$26.00 © 2004 MAIK "Nauka/Interperiodica"

heat. The phase transition temperatures in $\Delta T_y(T)$ in the case of cooling coincide with those observed in $\sigma(T)$. The area under the first peak is smaller than that under the second one. The phase transition temperature T_0 associated with the first peak is 15 K lower than T_0 during heating. Similar effects are observed in the temperature dependences of the Hall coefficient and thermoelectric power (Fig. 2). The phase transition temperatures during cooling coincide with those obtained from $\sigma(T)$ and $\Delta T_y(T)$, and the area of the hysteresis loop in $\alpha(T)$ is larger than those in $\sigma(T)$ and $R(T)$. Similar results were obtained for stoichiometric samples and those with excess Te.

3. ANALYSIS OF THE DATA OBTAINED

As was shown in the analysis of electrical and thermal properties of Ag_2Te and Ag_2Se [5, 6], some of these properties can be described in terms of a zeroth approximation of the inclusion function, $L_0(T)$. Specifically, it is possible to determine the mass distribution for each phase in the region of phase transition, clarify the mechanism of transformation from one phase to another, and find the change in several thermodynamic parameters and the rate dL_0/dT of the phase transition. As noted in [7, 8], in order to reveal more general properties and characteristics of the change in physical properties near and within the region of phase transition, it is necessary to analyze other terms in the expansion of $F(T)$ that determine function L. Different values of $F_n(T)$ correspond to different approximations $L_n(T)$:

$$L_n(T) = (1 + \exp F_n(T))^{-1}. \quad (1)$$

The results obtained in the zeroth approximation were used in [5, 6], so we restrict our analysis to the first and second approximations, $n = 1, 2$. In general, $L_1(T)$ has the form [7, 8]

$$L_1 = (1 + \exp[a_0(T - T_0)^{\beta} + a_1(T - T_0)^{\beta + 1}])^{-1}. \quad (2)$$

The phase transition temperature T_0 is found from the condition $L_1(T_0) = 1/2$ or $F_1(T) = 0$, which in this case leads to the solution of the equation

$$(T - T_0)^{\beta}[a_0 + a_1(T - T_0)] = 0. \quad (3)$$

The roots of this equation are as follows:

$$T_{01} = T_0, \quad T_{02} = T_{01} - \frac{a_0}{a_1} = T_0 - \frac{a_0}{a_1}. \quad (4)$$

It can be seen that two temperatures of smeared phase transition exist in this case: the first coincides with T_0, the second is shifted to the right or left of T_0, depending on the signs of a_0 and a_1. The second root tends to infinity at $a_1 \longrightarrow 0$. The temperature difference between both the phase transition points is $\Delta T_0 = T_{02} - T_{01} = -a_0/a_1$.

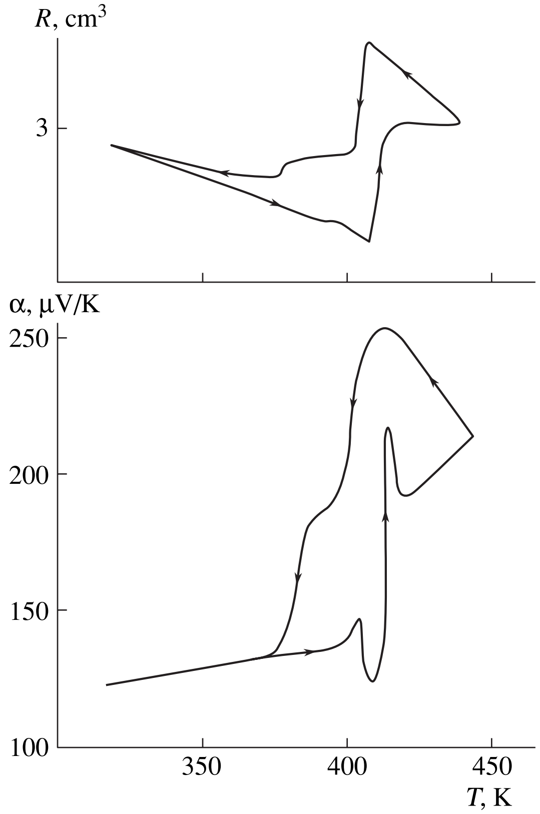

Fig. 2. Temperature dependences of the Hall [$R(T)$] and Seebeck [$\alpha(T)$] coefficients in Ag_2Te.

For a smeared phase transition ($\beta = 1$), $F_1(T)$ has the form

$$F_1(T) = a_0(T - T_0) + a_1(T - T_0)^2, \quad (5)$$

$$L_1(T) = \frac{1}{1 + \exp(T - T_0)[a_0 + a_1(T - T_0)]}, \quad (6)$$

$$\frac{dL_1}{dT} = \frac{a_0}{2[(1 + \cosh F_1(T))]}\left[1 + \frac{2a_1}{a_0}(T - T_0)\right]. \quad (7)$$

In a second approximation for smeared phase transition,

$$F_2(T) = (T - T_0)[a_0 + a_1(T - T_0) + a_2(T - T_0)^2], \quad (8)$$

$$L_2(T) = \frac{1}{1 + \exp F_2(T)}, \quad (9)$$

$$\frac{dL_2}{dT} = \frac{a_0}{2[(1 + \cosh F_2(T))]} \times \left[1 + \frac{2a_1}{a_0}(T - T_0) + \frac{3a_2}{a_0}(T - T_0)^2\right]. \quad (10)$$

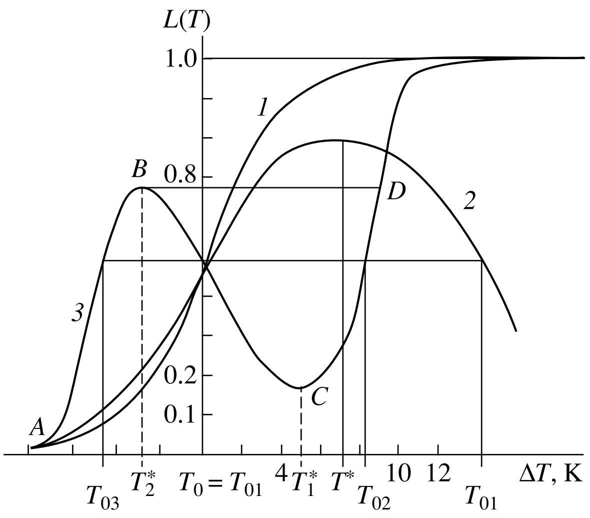

Fig. 3. Temperature dependences of the inclusion function $L(T)$ in Ag_2Te, calculated from (5) and (7). (*1*) $L_0(T)$, (*2*) $L_1(T)$, and (*3*) $L_2(T)$.

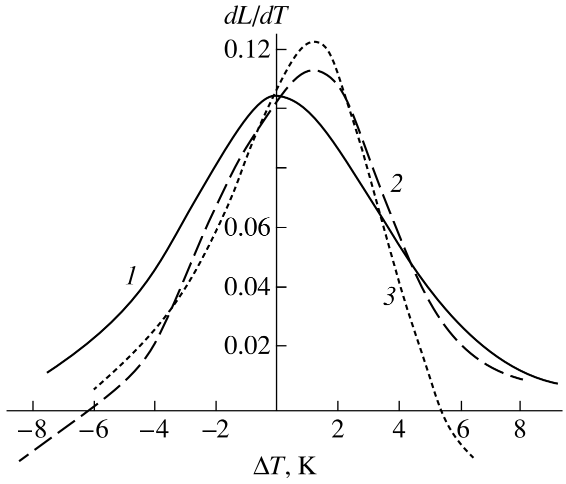

Fig. 4. Temperature dependences of the rate of phase transition in Ag_2Te, calculated from (6) and (8). (*1*) dL_0/dT, (*2*) dL_1/dT, and (*3*) dL_2/dT.

Here the phase transition temperature is determined also from the condition $F_2(T) = 0$, which yields

$$T_{02} = T_0 - \frac{a_1}{2a_2} + \sqrt{\left(\frac{a_1}{2a_2}\right)^2 - \frac{a_0}{a_2}}, \qquad (11)$$

$$T_{03} = T_0 - \frac{a_1}{2a_2} - \sqrt{\left(\frac{a_1}{2a_2}\right)^2 - \frac{a_0}{a_2}}. \qquad (12)$$

The real roots in (12) and (13) are of interest; they impose a constraint on the constant expansion coefficients a_0, a_1, and a_2. According to this constraint, the inequality $a_1^2 > 4a_0a_2$ must hold true, which occurs at $a_0 > 0$, $a_1 > 0$, and $a_2 < 0$, whence it follows that $T_{02} > T_0 > T_{03}$. The result of the negative value of a_2 is that the principal condition, the asymptotic behavior of the inclusion function L, is satisfied. At $T \ll T_0$, $L_2 \longrightarrow 0$, and at $T \gg T_0$, $L_2 \longrightarrow 1$. The last two roots, (11) and (12), coincide at $a_2 = \frac{a_1^2}{4a_0}$: $T_{02} = T_0 - \frac{a_1}{2a_2}$.

To apply Eqs. (6), (7), (9), and (10) to a specific crystal, it is necessary to know the parameters a_0, a_1, a_2, and T_0. For Ag_2Te, a_0 and T_0 were determined in [5], a_1 can be calculated based on our experimental data using relations (4), and a_2 is estimated from the condition that the roots are real.

Figures 3 and 4 show temperature dependences $L_1(T)$, $L_2(T)$, dL_1/dT, and dL_2/dT for Ag_2Te at the obtained values $a_0 = 0.42$, $a_1 = 0.03$, $a_2 = –0.01$, and $T_0 = 412$ K. For comparison, zeroth-approximation curves $L_0(T)$ and dL_0/dT are also shown. As can be seen, $L_1(T)$ is quite different from $L_0(T)$. The maximum value of $L_1(T)$ is reached at temperature $T^* = T_0 - \frac{a_0}{3a_1}$, which lies between the two temperatures of a smeared phase transition ($T_{01} > T^* > T_{02}$). According to [7, 8], this behavior of $L_1(T)$ may make physical sense if a single phase exists in a certain temperature range ($\Delta T = T_{02} - T_{01}$). This is not the case for our experimental data for Ag_2Te and the temperature dependence $L_0(T)$ (Fig. 3), because the mechanism of transition from the α- to the β-phase has been established [5] and there is no range of existence (ΔT) of such a phase in Ag_2Te in the region of the phase transition. Evidence that such regions exist (during phase transition) was presented in research devoted to Rochelle salts [8]. Clearly, this is just one of the possibilities; in general, more detailed research is necessary. Figure 3 also shows the temperature dependence $L_2(T)$. The extreme values of $L_2(T)$ correspond to temperatures

$$T_1^* = T_0 - \frac{a_1}{3a_2} + D \quad \text{and} \quad T_2^* = T_0 - \frac{a_1}{3a_2} - D, \qquad (13)$$

where $D = \frac{1}{3a_1}\sqrt{a_1^2 - 3a_0a_2}$.

The condition $T_1^* > T_0 > T_2^*$ is satisfied at the values of a_0, a_1, and a_2 given above. Functions $F_1(T_1^*)$ and $F_2(T_2^*)$ can be determined from T_1^* and T_2^*. Calculations show that the extreme value of $F_2(T_1^*)$ corresponds to the minimum, and $F_2(T_2^*)$, to the maximum of $L_2(T)$.

As can be seen in Fig. 3, $L_2(T)$ for Ag_2Te is asymmetrical. The asymmetry of the phase transition in Ag_2Te is also apparent in the temperature dependences of the phase transition rate, dL_1/dT and dL_2/dT (Fig. 4). These data also show that in smeared phase transitions the maximum of the phase transition rate shifts from T_0

to a higher temperature, and its value is higher than that for dL_0/dT. An additional phase transition with heat absorption is clearly observed in dL_2/dT dependences. The asymmetry of electrical and thermal properties in the phase transition in Ag_2Te is also observed experimentally, especially outside the range of smearing of the phase transition [5]. All these data indicate that the fine structure of smeared phase transitions appear in higher-order approximations of the inclusion function.

A physical interpretation of $L_2(T)$ was offered in [8]. One possibility is that a new phase appears in the region *AB* (Fig. 3), disappears in the region *BC*, and arises again in *CD*. The authors reckon that this situation is hardly probable, although it may be possible if several transitions occur closely enough to each other along the temperature axis. However, a more likely scenario is that the region *BC* corresponds to a metastable state of the system in a specific temperature range. For this case, we can draw straight lines *BD* and *AC* and obtain the hysteresis loop *ABCD*; its width is given by

$$h = T_{03} - T_{02} = 2\sqrt{\left(\frac{a_1}{2a_2}\right)^2 - \frac{a_0}{a_2}}. \qquad (14)$$

It follows from (14) that hysteresis can appear only when $a_1^2 > 4a_0a_2$. Based on the experimental data, we conclude that both these interpretations can not only be applied to Ag_2Te, but may even complement each other, because phase transitions that lie close enough along the temperature axis have been revealed in this material and hysteresis effects are observed in its electrical and thermal properties. Note that there is good agreement between the calculated and experimental values of T_{02} and T_{03}, and the width of the hysteresis loop *h*, which was obtained in the experiments on some kinetic coefficients, is broader than $h = 14$ K calculated from Eq. (14). Clearly, this result was predictable, because in a real situation the area of the hysteresis loop is affected by various factors, such as the time of cooling, the degree of approximation to the adiabatic or isothermal conditions of the experiment, the energy loss to contact wires, and so on.

Additional information on the hysteresis in a phase transition can be obtained from the calculation of the quantity of heat released or absorbed in the phase transition on heating or cooling. This can be done from the known $\Delta T_y(T)$ in the region of the phase transition using relation [5]:

$$Q = \frac{khbM}{vm}, \qquad (15)$$

where *h* and *b* are the height and width at the half-maximum peaks, respectively; *M*, the molecular mass; and *v*, the rate of heating. For the sample under study, we obtained the following: on heating, $Q_{408\,\mathrm{K}} = 2$ J, $Q_{415\,\mathrm{K}} = 20$ J, and $Q_{425\,\mathrm{K}} = 1.3$ J; on cooling, $Q_{400\,\mathrm{K}} = 2.2$ J and $Q_{380\,\mathrm{K}} = 5.6$ J. The heat released in the main smeared phase transition ($\alpha' \longrightarrow \beta'$) is seven times larger than the heat absorbed in the accompanying phase transitions $\alpha \longrightarrow \alpha'$ and $\beta' \longrightarrow \beta$. Note that the total change in the internal energy of the crystal on heating is three times larger than it is on cooling. These specific features can be explained as follows: near the smeared phase transition, in the region $\alpha_{405} \longrightarrow \alpha'_{408}$, a weak ordering of the hexagonal sublattice of Ag_2Te occurs, which consumes a small portion of external energy. A structural reconstruction $\alpha'_{408} \longrightarrow \beta'_{418}$ then occurs, which releases energy within the crystal. Finally, in the region $\alpha'_{418} \longrightarrow \beta'_{428}$, the reconstruction of the crystal into a face-centered cubic lattice with energy absorption is completed. This reasoning is consistent with the general concept of a structural phase transition [11]. According to this concept, when a low-symmetry crystal is transformed into a high-symmetry crystal, the main transition may be accompanied by displacement-type transitions (disordering of a sublattice). The observation of two distinct phase transitions on cooling confirms the occurrence of an additional phase transition in Ag_2Te. We believe that the fact that there is no third phase transition can be attributed to its very small energy (1.3 J). The significantly smaller (by a factor of 3) change in the internal energy of the crystal when it is cooled compared to when it is heated can be attributed to hysteresis, which is associated with energy loss.

REFERENCES

1. S. A. Aliev and Z. F. Agaev, Izv. Akad. Nauk SSSR, Neorg. Mater. **25**, 241 (1989).
2. S. A. Aliev and F. F. Aliev, Izv. Akad. Nauk SSSR, Neorg. Mater. **24**, 1389 (1989).
3. S. A. Aliev and F. F. Aliev, Izv. Akad. Nauk SSSR, Neorg. Mater. **25**, 241 (1989).
4. S. A. Aliev, F. F. Aliev, and G. P. Pashaev, Neorg. Mater. **29**, 1073 (1993).
5. S. A. Aliev, F. F. Aliev, and Z. S. Gasanov, Fiz. Tverd. Tela (St. Petersburg) **40**, 1693 (1998) [Phys. Solid State **40**, 1540 (1998)].
6. S. A. Aliev, Z. S. Gasanov, Z. F. Agaev, and R. D. Guseĭnov, Izv. Nats. Akad. Nauk Azerb., Ser. Fiz.–Mat. Tekh. Nauk **5**, 81 (2002).
7. B. N. Rolov, *Washed out Phase Transitions* (Latv. Gos. Univ., Riga, 1978).
8. B. N. Rolov and V. É. Yurkevich, *Physics of Washed out Phase Transitions* (Rostov. Gos. Univ., Rostov-on-Don, 1983).
9. B. N. Rolov, Izv. Akad. Nauk Latv. SSR, Ser. Fiz. Tekh. Nauk, 433 (1983).
10. S. A. Aliev and D. G. Arasly, Izv. Akad. Nauk Az. SSR, Ser. Fiz.–Tekh. Mat. Nauk **6**, 97 (1982).
11. M. J. Berger, Kristallografiya **16**, 1084 (1971) [Sov. Phys. Crystallogr. **16**, 959 (1971)].

Translated by D. Mashovets

Semiconductors, Vol. 38, No. 7, 2004, pp. 800–806. Translated from Fizika i Tekhnika Poluprovodnikov, Vol. 38, No. 7, 2004, pp. 834–840.
Original Russian Text Copyright © 2004 by Murel', Obolenskiĭ, Fefelov, Kiseleva.

SEMICONDUCTOR STRUCTURES, INTERFACES, AND SURFACES

Resistance of Proton-Irradiated GaAs Photodetectors to Combined Gamma and Neutron Radiation

A. V. Murel'*, S. V. Obolenskiĭ^, A. G. Fefelov**, and E. V. Kiseleva****
**Institute of the Physics of Microstructures, Russian Academy of Sciences, Nizhni Novgorod, 603950 Russia*
***Lobachevskiĭ State University, pr. Gagarina 23, Nizhni Novgorod, 603950 Russia*
^e-mail: Obolensk@rf.unn.ru

Submitted December 16, 2003; accepted for publication December 30, 2003

Abstract—Characteristics of proton-irradiated epitaxial *i*-GaAs structures with an interdigitated system of electrodes are studied before and after exposure to combined γ and neutron radiation. In order to reduce the dark current of photodetectors, the electrodes were metallized on proton-irradiated *i*-GaAs structures and were then fused for 30 min at 300°C, which led to a partial recovery of the epitaxial-layer conductivity. It is shown on the basis of measurements of spectral dependences of the structures' photosensitivity that the photosensitivity of the proton-irradiated structures is insensitive to the effect of combined γ and neutron radiation if the energies of optical photons are close to the band-gap energy. It is therefore suggested that these structures can be used in the fabrication of radiation-resistant photodetectors. © *2004 MAIK "Nauka/Interperiodica".*

1. INTRODUCTION

Devices with unprecedentedly good characteristics are often used in the design of systems that operate under conditions of nuclear radiation in order to ensure a safety margin that compensates the radiation-induced degradation.

In cases where this safety margin is insufficient, various compensating circuits that are designed to compensate the radiation effects are used. However, this is a serious problem of circuitry engineering because of the different behavior of the circuit components exposed to nuclear radiation. At the same time, in a number of applications, the characteristics of devices are not themselves subject to any significant requirements except the need for the device parameters to be stable under irradiation with high doses. Implementing such characteristics makes it possible to attain a gain in the characteristics of the device in general by simplifying the circuitry used. The beneficial effect manifests itself most clearly in the design of microwave devices, in which the use of compensating circuits is difficult.

Photoresistors are often used to fabricate microwave photodetectors, as they have smaller values of interelectrode capacitance compared to photodiodes. The design of radiation-resistant photodetectors based on photoresistors is complicated by the fact that high-quality undoped crystals are conventionally used to operate regions of these devices [1], and such crystals can hardly withstand radiation. The lifetime and mobility of charge carriers change significantly as a result of irradiation with doses of γ-ray photons as low as 10^4–10^5 R and with doses of neutrons as low as 10^{12}–10^{13} cm^{-2} [2]. Accordingly, the photosensitivity defined as the ratio between the photocurrent and dark current also decreases. At the same time, if we disregard the absolute value of photosensitivity and only require that this photosensitivity be constant after exposure to high doses of nuclear radiation, we can use materials with a high inherent defect concentration (preferably, one to two orders of magnitude higher than that introduced by external nuclear radiation) for active regions of detectors. In this case, apart from an increase in the radiation resistance, one can attain a gain in the cutoff frequency of the photodetector operation due to the short lifetime of charge carriers in the irradiated material [1, 2].

A large number of studies have been devoted to studying the effects of technology-related proton radiation and spurious γ and neutron radiation (separately) on semiconductor structures and devices [2–19]. However, the complex effect of various types of radiation is nonadditive [6]; i.e., the processes of formation and stabilization of defects and their complexes and clusters in a solid depend heavily on the properties of the starting material [7]. The defects in a crystal can become the centers that capture mobile defects [7], multiple irradiation of semiconductor (reirradiation) can reduce its resistivity [8], and so on. Thus, the radiation resistance of semiconductor structures that initially contain a high concentration of specially introduced radiation defects and are then subjected to irradiation with other types of particles or photons should differ significantly from that of a defect-free material or a material exposed once again to the same type of radiation. In this study, we analyze the variations in the characteristics of epitaxial GaAs structures as a result of irradiation simultaneously with γ-ray photons and neutrons. The structures had an interdigitated system of contacts and were irradiated preliminarily with protons. The neutron-radi-

1063-7826/04/3807-0800$26.00 © 2004 MAIK "Nauka/Interperiodica"

Table 1. Parameters of the samples according to an analysis of temperature dependences of the *I–V* characteristics for different types of radiation

Sample no.	Radiation type*: dose, R; fluence, cm^{-2}	Metal–semiconductor barrier height, eV	Activation energy determined from the resistance at the initial portion of the *I*(*V*) curve, eV (charge-carrier concentration, cm^{-3})	Volume resistance of the samples, Ω
Φ0	Starting sample (the structure irradiated with protons and partially annealed)	0.380	0.35 (6.2×10^{11})	1.5×10^6
Φ1	γ: 10^5 R	0.380	0.35 (6.2×10^{11})	1.5×10^6
Φ2	γ: 10^6 R	0.525	0.617 (2×10^7)	5×10^6
Φ3	γ: 10^7 R	0.527	0.617 (2×10^7)	3×10^8
Φ4	γ: 10^4 R+ *n*: 10^{13} cm^{-2}	0.368	0.313 (2.6×10^{12})	1×10^7
Φ5	γ: 10^5 R+ *n*: 10^{14} cm^{-2}	0.461	0.633 (1.1×10^7)	1×10^9

* γ is irradiation with γ-ray photons; *n*, irradiation with neutrons.

ation spectrum was bell-shaped in the energy range 0.03–3 MeV; the mean neutron energy was 1.5 MeV.

2. SAMPLES AND SOURCES OF HIGH-ENERGY RADIATION

We used epitaxial GaAs structures with an interdigitated system of contacts (16 × 17 pins) as starting samples. The structure period was 25 μm, the interpin gap was 10 μm, and the pin length was 75 μm. The epitaxial layer was grown by vapor-phase epitaxy on a high-purity semi-insulating GaAs substrate with a resistivity of 10^8 Ω cm; the layer was 0.6 μm thick and had an electron concentration on the order of 10^{14} cm^{-3}. Before metallization, the structures were irradiated with 30-, 60-, and 90-keV protons (with doses of 4×10^{13} cm^{-2} at each energy; each irradiation took 40 min). A conventional AuGe–Au eutectic was used for metallization, after which the ohmic contacts were fused for 30 min at 300°C in an argon atmosphere.

According to Brudnyi and Potapov [8], the highest GaAs resistivity achievable with proton irradiation (10^8 Ω cm or higher) is attained after exposure to proton radiation with a dose of ~10^{14} cm^{-2}. Heat treatment at 400–450°C leads to nearly complete annealing of radiation defects [5]. In this study, we used a heat treatment at lower temperatures (300°C). As a result, the resistivity of the proton-irradiated layer recovered only to values on the order of 10^4 Ω cm, which was sufficient for high-quality isolation of peripheral regions in discrete devices and interdevice isolation in monolithic integrated circuits (MICs) [20]. It is important that only thermally stable defects remain in the structure after the heat treatment used in this study, which makes it possible to use this technology to fabricate photodetectors in GaAs MICs that contain high-power field-effect transistors whose active region is heated to 150–200°C by the flowing current [21].

Assuming that the nonadditivity of the effects of various types of radiation manifests itself most clearly at high rates of defect production, we chose a pulsed nuclear reactor in our experimental studies of radiation resistance of the samples under the most severe conditions. The width of a pulse of the neutron and γ radiation was 350 μs, the fluence of neutrons in a pulse was 1×10^{14} cm^{-2}, and the dose of accompanying γ-ray photons per pulse was about 100 kR. The energy spectrum of neutrons and γ-ray photons in the range from 10 keV to 6 MeV was bell-shaped; the mean neutron energy was 1 MeV. We also used a continuous isotope source of γ radiation (based on ^{60}Co, with an energy of γ-ray photons of 1 MeV and a dose of 10^6 R per 24 h). Below, we disregard the accumulation of Ge and Se in the GaAs lattice due to nuclear transmutations, since the doses used in our experiments are three to four orders of magnitude lower than those typically used for transmutational doping [9]. The temperature of the sample was no higher than 320 K during irradiation. The parameters that characterize irradiation of the samples are listed in Table 1.

3. EXPERIMENTAL

In order to determine the charge-carrier concentration in GaAs and the height of the Schottky barrier, we studied the current–voltage (*I–V*) characteristics of the samples in relation to temperature. Nonuniformities in the distribution of dark electrical conductivity were evaluated by measuring the resistance of various sections of the interdigitated structure. The nonuniformity in the distribution of photoconductivity in the samples was evaluated by scanning the light spot (focused optical emission of an incandescent lamp) over the gap in the interdigitated system of electrodes.

Experimental *I–V* characteristics of the samples are shown in Fig. 1. Apparently, the anomalous behavior of

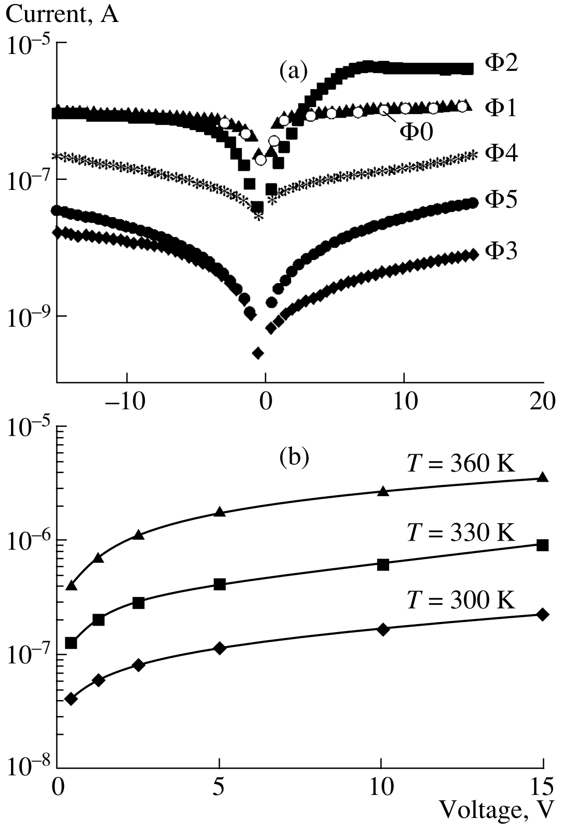

Fig. 1. Dark *I*–*V* characteristics of the samples: (a) comparison of *I*–*V* characteristics of samples exposed to different types of radiation and (b) temperature dependence of the *I*–*V* characteristic for sample Φ4.

sample Φ2, in which the *I*–*V* characteristic that was initially symmetric with respect to the change in sign of the voltage became asymmetric after irradiation, is related to technology-induced differences between the contacts. Below, when analyzing the characteristics of this sample, we use the right-hand portion of the *I*(*V*) curve; this portion corresponds to a higher conductivity of the sample and, thus, minimizes the parasitic contact phenomena owing to the forward connection of the degraded contact.

The spread in the values of dark conductivity in the interdigitated structures amounted to 5–8% of the conductivity itself. Nonuniformities in the conductivity distribution in the structures were no larger than 17%, as was determined by scanning the surface of the structure with an optical beam.

In order to evaluate the leakage currents through the substrate at room temperature, we measured the dark and photoinduced *I*–*V* characteristics of reference samples that were formed on the same semi-insulating substrate, were not preliminary irradiated with protons, and had a similar interdigitated system of electrodes.

We studied the characteristics of radiation defects using photoinduced current transient spectroscopy (PICTS). The sample was placed in the chamber for measurements and was maintained at a fixed temperature in the range 300–360 K and at a constant bias voltage. Simultaneously, the sample was periodically exposed to optical pulses at a wavelength that corresponded to the predominant band-to-band generation of charge carriers. The resulting photocurrent was amplified using a fast-response amplifier and was then digitized.

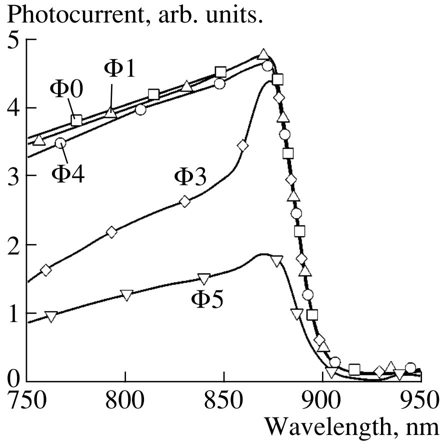

Fig. 2. Dependence of the photocurrent in the samples on the wavelength of optical radiation.

The results of measuring the spectral photosensitivity of the samples are shown in Fig. 2. Two groups of samples were identified in the course of the measurements. In the first group (Φ0, Φ1, and Φ4), the photosensitivity decreases steadily starting with the largest value that corresponds to the long-wavelength cutoff of the photoeffect as the wavelength of optical radiation decreases. In the second group (Φ3, Φ5), the rate of decrease in photosensitivity is appreciably higher at wavelengths of 850–870 nm than at wavelengths of 750–850 nm.

4. PROCESSING THE EXPERIMENTAL DATA

4.1. Distribution of Radiation Defects in the Sample

On the basis of experimental data [5] and the results of original calculations using the Monte Carlo method (the TRIM software package), we may state that point defects are produced in a semiconductor structure as a result of irradiation with protons. Most of these defects are located within a layer about 1 μm thick. A decrease in the defect concentration is observed near the surface; this defect distribution can be made more uniform to a certain extent by diffusion and partial recombination of point defects during the technological operation of fusing the ohmic contacts.

Irradiation with γ-ray photons gave rise to a nearly uniform distribution of point defects across the sample thickness owing to a larger penetration depth for γ-ray photons in GaAs (~1 cm). In contrast to the irradiation with protons and γ-ray photons, neutron radiation gives rise to point-defect clusters that are 20–30 nm in size [2] and are also uniformly distributed over the volume of GaAs (the penetration depth of neutrons in GaAs is ~10 cm for a neutron energy of 1 MeV).

The estimations showed that, for the highest doses of neutron and γ-ray radiation, the total concentration of point defects produced by irradiation with neutrons and γ-ray photons amounted to 10–30% of the concentration of defects that remained in the sample after irradiation with protons and subsequent heat treatment. The concentration of clusters of radiation defects generated by neutron radiation is lower by a factor of 250 than the point-defect concentration [10]. In addition, as follows from Table 1, irradiation with both neutrons and γ-ray photons led to an increase in the sample's resistivity of two to three orders of magnitude. Note that the concentration of stable radiation defects was estimated on the basis of the data of [2] for the case of the generation of these defects in undamaged material. At the same time, as was mentioned above, the concentration of defects in the case of combined irradiation cannot be determined by a simple summation and should be controlled using independent measurements, which is accomplished in this study using the PICTS method.

4.2. *Processing the I–V Characteristics of the Samples*

The results of measuring both the dark and photoinduced *I–V* characteristics at room temperature showed that the resistance of the reference samples (formed on the semi-insulating substrate) before and after exposure to combined γ and neutron radiation was much higher than that of the samples irradiated with protons (with subsequent annealing) before and after combined irradiation with neutrons and γ-ray photons. This behavior suggests that the current in the samples irradiated with protons flows directly within the epitaxial layer with the radiation defects and does not penetrate into the substrate.

In order to process the temperature dependences of the dark *I–V* characteristics, we used the method suggested in [11]. We define the voltage across the sample as

$$V = V_1 + V_b + V_2 = V_1 + IR_b + V_2,$$

where V is the applied voltage, V_1 and V_2 represent the potential drop across the metal–semiconductor contact regions, V_b is the potential drop across the semiconductor bulk, I is the reverse current, and R_b is the bulk resistance of the semiconductor.

Taking into account that the current through the Schottky contact is defined as $I = I_s[1 - \exp(-qV_1/kT)]$ when thermionic emission is dominant, we obtain

$$V = IR_b - (kT/q)\ln(1 - I/I_s).$$

At low bias voltages (such that I is less than $0.9I_s$), the potential drop V_1 is very small (less than 0.6 V) and is negligible compared to the applied voltage. Under these conditions, all applied bias voltage drops mainly across the GaAs bulk, so that the GaAs bulk resistance controls the current through the entire structure. In this situation, the *I–V* characteristic obeys Ohm's law; i.e., $V = IR_b$. At the same time, the term $|\ln(1 - I/I_s)|$ increases at high voltages (in which case $I \longrightarrow I_s$) and governs the voltage dependence of the current.

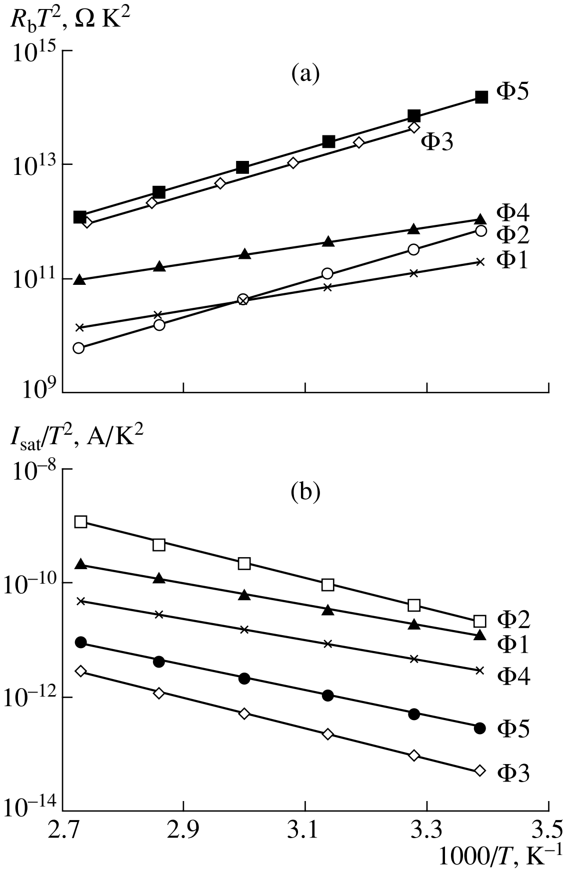

Fig. 3. Temperature dependences of (a) volume resistance of the samples and (b) saturation current of the Schottky barrier.

An analysis of experimental data shows that the measured *I–V* characteristic is described by a linear function to a high degree of accuracy in the voltage range 0–0.5 V. In this region, we determined the bulk resistance R_b and its temperature dependence (Fig. 3a), which can be adequately approximated using the expression [11] $R_b \propto T^{-2}\exp[-q(E_c - E_F)/kT]$ in the vicinity of room temperature. As a result, we managed to determine the position of the Fermi level and the concentration of charge carriers in the semiconductor bulk (Table 1). The height of the Schottky barrier was estimated from the temperature dependence of the saturation current (Fig. 3b).

In Table 1, we list the corresponding activation energies and charge-carrier concentrations and the heights of the metal–semiconductor barriers determined using these energies (the barrier height increases as the dose of γ-ray radiation increases).

Table 2. Comparison of the GaAs deep-level parameters obtained in this study with published data

Data obtained in this study				Published data*		
level depth, eV	capture cross section, cm^2	amplitude of the PICTS signal, arb. units	type of radiation	level depth, eV	type of radiation	reference
				0.14		[15]
0.148 ± 0.014	5×10^{-18}	0.15		0.15		[18]
0.207 ± 0.004	2×10^{-13}	0.07		0.17–0.22		[15]
0.305 ± 0.012	2×10^{-15}	0.2	Protons	0.2	Protons	[18]
0.323 ± 0.028	5×10^{-13}	0.3	(Φ0)	0.25		[18]
0.623 ± 0.029	7×10^{-13}	0.5		0.25–0.29		[15]
				0.34		[15]
				0.36		[14]
				0.08		[12]
0.115 ± 0.003	5×10^{-17}			0.12		[12]
0.213 ± 0.018	2×10^{-14}	1.2	Protons + γ-ray photons	0.13		[12]
0.259 ± 0.030	1×10^{-17}	1.4		0.14	γ-ray photons	[2]
0.272 ± 0.016	2×10^{-16}	1.5	(Φ3)	0.20		[12]
0.312 ± 0.012	1×10^{-15}	1.1		0.30		[4]
		0.9		0.31		[12]
				0.38		[14], [2], [17]
				0.5		[13]
			Protons + γ-ray photons + neutrons	0.52		[16]
0.690 ± 0.149	3×10^{-12}	7.2		0.58	Neutrons	[16]
0.942 ± 0.041	4×10^{-10}	6.5		0.63		[16]
			(Φ5)	0.72		[13]
				0.75		[16]

* Published data are given only for levels whose depth roughly coincides with that determined experimentally in this study.

This behavior may be explained by the fact that most of the point defects produced in the sample as a result of irradiation with γ-ray photons accumulates gradually at the semiconductor surface near the interface with the metal. In contrast, the capture of the point defects by clusters produced by neutron radiation to some extent inhibits the drain of point defects to the surface.

A certain increase in the charge-carrier concentration at low (10^{13} cm^{-2}) fluences of neutron radiation can be caused by the process of formation of stable radiation-defect clusters that accumulate point defects from the surrounding space. Despite this process, the conductivity of the samples apparently decrease steadily owing to a decrease in the charge-carrier mobility as a result of scattering at the space-charge region that surrounds the defect-containing clusters.

Kozlov and Kozlovskiĭ [5] discussed the effect of proton radiation on the AuGe–n^+-GaAs interface. It was shown that irradiation with protons could give rise to processes that were similar to those involved in the formation of a fused ohmic contact when the thickness of the metal layer was chosen such that the defects were mainly produced in the vicinity of the AuGe–n^+-GaAs interface. In this study, only a variation in the barrier height was observed when the sample was irradiated with γ-ray photons. This behavior is caused by the fact that γ radiation is absorbed in the entire semiconductor bulk (i.e., mostly away from the metal–semiconductor interface) and the formation of an ohmic contact to *i*-GaAs is hampered by the light doping of this material.

4.3. Processing the PICTS Data

The deep-level parameters determined reliably from processed PICTS data are listed in Table 2.

The effect of the combined (proton, γ, and neutron) radiation is nonadditive: as the dose of γ-ray photons increases, the defects and their complexes produced by irradiation with protons are rearranged (possibly redistributed) so that defects with shallower levels are formed. A comparison of the data obtained with published results [2, 4, 12–18] (Table 2) shows that combined proton–γ radiation gives rise to the defects with shallower levels. These defects have smaller cross sections for the capture of charge carriers and cannot be centers of efficient recombination of photoexcited charge carriers.

A classical pattern of the origination of a high concentration of defects is observed in the case of irradiation with fast neutrons. These defects introduce deep levels into the band gap, feature large cross sections for charge-carrier capture (the so-called *U* band in the DLTS spectrum [13]), and are efficient recombination centers.

4.4. Processing Experimental Data on the Spectral Photosensitivity of the Samples

The assumptions above concerning the characteristics of the recombination are confirmed by an analysis of variations in the photosensitivity of the samples. The photosensitivity was calculated as the ratio between the increment of current in the samples under illumination and the dark current (Fig. 2).

In the region of the maximum photocurrent of the sample (wavelength range 840–870 nm), the depth of absorption of optical radiation is about 1 μm [7]. Thus, the value of photocurrent is affected by the defects that are contained in the entire volume of the material irradiated with protons. In contrast, photons are absorbed in the surface layer of the sample (with a layer thickness of about 0.1 μm) at wavelengths shorter than 0.8 μm [7]; i.e., the generation–recombination of the charge carriers and photocurrent as a whole are affected to a great extent by defects located in the vicinity of the surface.

As the neutron-radiation fluence increases (samples Φ4 and Φ5), the photocurrent in the starting sample decreases almost to the same extent in the entire range of absorbed-radiation wavelengths (Fig. 2), since the radiation-defect clusters that most affect the recombination of charge carriers are distributed uniformly in the material and are almost immobile. The traps corresponding to the clusters have levels near the midgap and exhibit a large capture cross section, which causes a substantial increase in the rates of both the surface and volume recombination.

It can be seen from Fig. 3 that a slight variation in photosensitivity is observed only in the range 840–870 nm for sample Φ3; in other words, the effect of γ radiation is only slight if the entire volume of the sample is photoexcited and is significant if the excitation is restricted to the surface region. This fact cannot be accounted for by an increase in the efficiency of recombination near the surface of the sample since deep-level transient spectroscopy shows that the concentration and efficiency (capture cross section) of traps decrease when the samples are irradiated with γ-ray photons.

Note that the peak in the spectral dependence of photocurrent cannot be accounted for by the charge-carrier diffusion from the proton-irradiated layer into the substrate since the diffusion coefficient is small in GaAs samples with a high concentration of defects. It was shown previously [2] that the charge-carrier lifetime was on the order of 10 ps in GaAs with a very high concentration of defects. This lifetime corresponds to a diffusion length of about 0.1 μm, whereas the absorption depth for optical radiation varies from 0.1 to 1 μm, depending on the wavelength.

Apparently, the observed increase in the surface-recombination efficiency is mainly caused by a change in the surface potential as a result of irradiation with γ-ray photons. A decrease in the tangential electric-field component in the surface layer to some extent suppresses the process of separation of nonequilibrium charge carriers and, thus, leads to an increase in the recombination rate. This conclusion is indirectly confirmed by the variation observed in the height of the Schottky barrier (Table 1).

As is well known, the dark current of diodes increases owing to an increase in the thermal-generation rate as a result of irradiation of *p*–*n* junctions with neutrons and γ-ray photons [19]. At the same time, the photocurrent in the diodes decreases owing to a decrease in the charge-carrier lifetime [2]; i.e., the photosensitivity decreases drastically. The situation for semiconductor photoresistors is different: variations in the dark current and photocurrent have the same “sign” due to an increase in the resistivity as a result of irradiation [2], so that the value of the variation in photosensitivity is controlled by the relation between the rates of increase in the resistivity of the semiconductor and the decrease in the lifetime of charge carriers. Typically, these rates are not equal to each other and, moreover, depend on the fluence in the case of irradiation with neutrons [19], so the dependence of the charge-carrier lifetime on the neutron fluence starts to level off at fluences higher than 10^{13} cm^{-2} [19]. Estimations based on previous data [2, 19] show the ratio between the charge-carrier lifetime in *i*-GaAs and the resistivity of this material changes by a factor of 2 even for neutron-radiation fluences of about 1.5×10^{13} cm^{-2}.

An insignificant decrease in the photosensitivity of the structure is observed in the wavelength region near 870 nm for the samples under study when they are irradiated with γ-ray photons, and a decrease by only a factor of 2 is observed when they are irradiated with neutrons at a fluence of 10^{14} cm^{-2}. The latter observation suggests that variations in the resistivity of the sample and the charge-carrier lifetime in samples exposed to combined γ–neutron radiation vary synchronously owing to the aforementioned effects of the rearrangement and redistribution of defects.

Thus, the design and fabrication technology suggested by us for interdigitated structures on a proton-irradiated epitaxial layer of undoped GaAs makes it possible to fabricate photodetectors with high radiation resistance to combined irradiation with γ-ray photons and neutrons.

5. CONCLUSIONS

On the basis of the results reported in this paper, we can draw the following conclusions.

(i) The presence of radiation defects causes a decrease in the charge-carrier concentration and an increase in the resistance of the samples by two orders of magnitude.

(ii) The accumulation of radiation defects at the metal–semiconductor interface causes an increase in the potential-barrier height, which has a significant effect on the dark saturation current of the structures.

(iii) The decrease in the photosensitivity of the structures as a result of irradiation with high fluences of neutrons is related to the capture and rapid recombination of charge carriers at the levels introduced by defects in the vicinity of clusters of radiation defects generated by fast neutrons.

(iv) As the dose of γ radiation increases, the defect complexes formed during irradiation with protons (the levels corresponding to the PICTS peaks at temperatures $T = 300$–320 K) are destroyed, and shallow levels with characteristic temperatures of about 100–200 K and a relatively small capture cross section appear. At the same time, under combined irradiation with γ-ray photons and neutrons, the opposite occurs: the formation of shallow levels is suppressed, and levels are formed that are characteristic of irradiation with neutrons and have large capture cross sections and PICTS peaks at 320–340 K.

(v) The photosensitivity of the structures under consideration is radiation-resistant if the incident photons have an energy that almost coincides with the band gap. This behavior is accounted for by synchronism in the rates of variation of dark resistivity and photocurrent amplitude in the samples irradiated with γ-ray photons and simultaneously with γ-ray photons and neutrons.

(vi) These results make it possible to recommend the design and technology suggested above for the fabrication of radiation-resistant photodetectors.

REFERENCES

1. S. M. Sze, *Physics of Semiconductor Devices*, 2nd ed. (Wiley, New York, 1981; Énergiya, Moscow, 1973).
2. E. R. Astvatsatur’yan, D. V. Gromov, and V. M. Lomako, *Radiation Effects in Devices and Integrated Circuits Based on Gallium Arsenide* (Universitetskoe, Minsk, 1992).
3. R. Zuleeg, in *GaAs Microelectronics*, Vol. 11 of *VLSI Electronics Microstructure Science*, Ed. by N. G. Einspruch and W. R. Wisseman (Academic, Orlando, 1985) [in *Gallium Arsenide in Microelectronics*, Ed. by V. N. Mordkovich (Mir, Moscow, 1988)].
4. A. V. Bobyl’, R. V, Konakova, V. K. Kononov, *et al.*, Élektron. Tekh., Ser. 8: Upr. Kach. Stand., No. 4, 31 (1992).
5. V. A. Kozlov and V. V. Kozlovskiĭ, Fiz. Tekh. Poluprovodn. (St. Petersburg) **35**, 769 (2001) [Semiconductors **35**, 735 (2001)].
6. S. V. Obolenskiĭ, Fiz. Khim. Obrab. Mater., No. 2, 5 (2001).
7. V. S. Vavilov and N. A. Ukhin, *Radiation Effects in Semiconductors and Semiconductor Devices* (Atomizdat, Moscow, 1969).
8. V. N. Brudnyĭ and A. I. Potapov, Fiz. Tekh. Poluprovodn. (St. Petersburg) **35**, 1423 (2001) [Semiconductors **35**, 1361 (2001)].
9. V. N. Brudnyĭ, N. G. Kolin, D. I. Merkurisov, and V. A. Novikov, Fiz. Tekh. Poluprovodn. (St. Petersburg) **35**, 739 (2001) [Semiconductors **35**, 708 (2001)].
10. V. P. Klad’ko and V. P. Plyatsko, Fiz. Tekh. Poluprovodn. (St. Petersburg) **32**, 261 (1998) [Semiconductors **32**, 235 (1998)].
11. Y. L. Luo, T. P. Chen, S. Fang, and C. D. Beling, Solid State Commun. **101**, 715 (1997).
12. D. V. Lang, in *Point Defects in Solids* (Plenum, New York, 1975; Mir, Moscow, 1979).
13. V. A. Novikov and V. V. Peshev, Fiz. Tekh. Poluprovodn. (St. Petersburg) **32**, 411 (1998) [Semiconductors **32**, 366 (1998)].
14. S. A. Goodman, F. D. Auret, M. Ridgway, and G. Myburg, Nucl. Instrum. Methods Phys. Res. B **148**, 446 (1999).
15. C. Chiossi, F. Nava, C. Canali, *et al.*, Nucl. Instrum. Methods Phys. Res. A **388**, 379 (1997).
16. V. N. Brudnyĭ, N. G. Kolin, V. A. Novikov, *et al.*, Fiz. Tekh. Poluprovodn. (St. Petersburg) **31**, 811 (1997) [Semiconductors **31**, 686 (1997)].
17. V. N. Brudnyĭ and V. V. Peshev, Fiz. Tekh. Poluprovodn. (St. Petersburg) **37**, 22 (2003) [Semiconductors **37**, 20 (2003)].
18. F. Nava, P. Vanni, A. Cavallini, *et al.*, Nucl. Phys. B **61**, 432 (1998).
19. F. P. Korshunov, G. V. Gatal’skiĭ, and G. M. Ivanov, *Radiation Effects in Semiconductor Devices* (Nauka i Tekhnika, Minsk, 1978).
20. S. V. Obolenskiĭ and V. D. Skupov, Pis’ma Zh. Tekh. Fiz. **26** (16), 1 (2000) [Tech. Phys. Lett. **26**, 645 (2000)].
21. M. Shur, *GaAs Devices and Circuits* (Plenum, New York, 1987; Mir, Moscow, 1991).

Translated by A. Spitsyn

Semiconductors, Vol. 38, No. 7, 2004, pp. 807–811. Translated from Fizika i Tekhnika Poluprovodnikov, Vol. 38, No. 7, 2004, pp. 841–845.
Original Russian Text Copyright © 2004 by Strokan, Ivanov, Savkina, Lebedev, Kozlovskiĭ, Syvajarvi, Yakimova.

SEMICONDUCTOR STRUCTURES, INTERFACES, AND SURFACES

Radiation Resistance of Transistor- and Diode-Type SiC Detectors Irradiated with 8-MeV Protons

N. B. Strokan*, A. M. Ivanov*^, N. S. Savkina*, A. A. Lebedev*,
V. V. Kozlovskiĭ, M. Syvajarvi***, and R. Yakimova*****
**Ioffe Physicotechnical Institute, Russian Academy of Sciences, Politekhnicheskaya ul. 26, St. Petersburg, 194021 Russia*
^e-mail: alexandr.ivanov@mail.ioffe.ru
***St. Petersburg Polytechnical University, Politekhnicheskaya ul. 29, St. Petersburg, 195251 Russia*
****Linköping University, 58133 Linköping, Sweden*

Submitted January 19, 2004; accepted for publication January 26, 2004

Abstract—Nuclear-particle detectors based on SiC with a structure composed of an n^+-type substrate, a *p*-type epitaxial layer, and a Schottky barrier are studied. Structures with a ~10-μm-thick 6*H*-SiC layer exhibit transistor properties, whereas those with a ~30-μm-thick 4*H*-SiC layer exhibit diode properties. It is established that a more than tenfold amplification of the signal is observed in the transistor-type structure. The amplification is retained after irradiation with 8-MeV protons with a dose of at least 5×10^{13} cm^{-2}; in this case, the resolution is ≤10%. Amplification of the signal was not observed in the structures of diode type. However, there were diode-type detectors with a resolution of ≈3%, which is acceptable for a number of applications, even after irradiation with the highest dose of 2×10^{14} cm^{-2}. *© 2004 MAIK “Nauka/Interperiodica”.*

1. INTRODUCTION

Recently, much attention has been paid to silicon carbide SiC in studies of materials for semiconductor nuclear-radiation detectors. This is related to the progress made in growing SiC films with characteristics that are acceptable for fabricating detectors. In the context of nuclear-radiation detectors, SiC properties, such as a high threshold energy for defect production (a prerequisite for radiation resistance) and a wide band gap, are very attractive. The wide band gap reduces both the excess current generated in the detector volume and the related noise by several orders of magnitude. As a result, SiC detectors maintain normal operation at temperatures as high as 500°C [1], which, combined with high chemical stability, makes these detectors unique for special applications.

In this paper, we report the results of studying the radiation resistance of detectors based on SiC films and subjected to irradiation with 8-MeV protons up to doses of 5×10^{13} or 2×10^{14} cm^{-2}, depending on the type of detector structure. In these conditions, the concentration of primary radiation defects is in the range $(2–8) \times 10^{16}$ cm^{-3}, which exceeds the difference concentration of initial impurities by more than an order of magnitude. It seems important to find out to what extent the introduction of defects affects the performance of detectors.

The films had *p*-type conductivity and were obtained by sublimation epitaxy on heavily doped n^+-type substrates. We used two groups of films, with thicknesses $d \approx 10$ μm and $d \approx 30$ μm. The films of the first group, which had the structure of a 6*H*-SiC polytype, were obtained at the Ioffe Physicotechnical Institute and had a difference concentration of acceptor and donor impurities $(N_a - N_d) \leq 7.5 \times 10^{14}$ cm^{-3}. The thicker films were grown at Linköping University (Sweden) and had a 4*H*-SiC polytype structure with $(N_a - N_d) = (3–5) \times 10^{15}$ cm^{-3}.

A Schottky barrier was formed at the surface of *p*-type films using magnetron-sputtering deposition of Ni; this barrier served as the *n*-type contact. A reverse bias voltage *U* was then applied to the barrier, and the structures were tested in a mode that detects the separate α particles of natural decay. We used the standard instrumentation for the method of pulse-height analysis to determine the energy *E* measured by the detector as a function of the reverse bias *U* applied to the barrier with the α-particle energy in the range 3.5–5.4 MeV.

As was reported by Lebedev *et al.* [2], amplification of the signal, which is characteristic of transistor structures, was observed for detectors based on films with $d \approx 10$ μm. As the bias *U* increased, the signal $E(U)$ increased superlinearly and was several tens of times greater than the energy absorbed in the detector. At the same time, the signal $E(U)$ leveled off at values of *E* close to the energy of α particles for detectors based on thicker films with $d \approx 30$ μm (these films were also more heavily doped). This leveling-off is characteristic of the design of detectors in the diode version and indicates that the extent *W* of the field region of the collector–base junction is insufficient for the transistor effect to appear. As a result, tests of the structures based on films of the aforementioned types made it possible to provisionally separate the detectors into transistor and diode types.

Comparison of the contributions of Si and C atoms to the absorption of the proton energy

Atoms in the film	Energy absorbed by atoms, keV	Number of collisions with a proton*	Mean energy in collisions, eV
Si	51.6	276	187
C	14.7	113	130

* Collisions leading to the formation of vacancies are taken into account.

Previously (see [3]), a high degree of compensation for the SiC conductivity was observed at doses $\approx 10^{15}$ cm^{-2} in studies of the effect of irradiation with 1-GeV protons on diode structures based on *n*-type 6*H*-SiC films with $N_d - N_a \approx 4 \times 10^{15}$ cm^{-3}.[1] It is important to examine to what extent the aforementioned doses affect the run $E(U)$ of the signal at the output of the transistor formed on *p*-type 6*H*-SiC film. Thus, the starting dose for irradiating transistors with 8-MeV protons was taken to be 10^{13} cm^{-2}.

The starting dose was increased to 10^{14} cm^{-2} (equivalent to $\approx 10^{16}$ cm^{-2} relativistic protons) for diodes. In addition to the increase in doses, it was expected that the compensation of conductivity would increase the values of W and make it possible to obtain transistors with a thick base.

Apart from the aforementioned measurements of signals induced by α particles $E(U)$, we also measured the dependences of the structures' capacitance on the bias $C(U)$. All the measurements were carried out at room temperature.

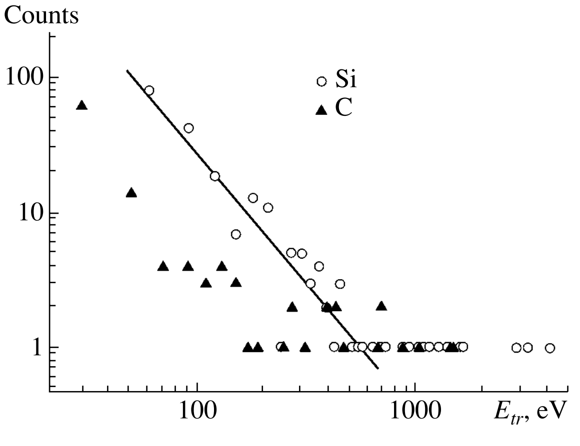

Fig. 1. Distribution of energy transferred to the atoms of the silicon carbide film in the passage of 8-MeV protons. The thickness of the film is 30 μm; the sampling statistic is reported for 985 protons.

2. SPECIAL FEATURES OF INTERACTION BETWEEN PROTONS AND SIC FILMS

As is well known, the production of radiation defects in semiconductors by nuclear particles involves two stages. The first stage involves two processes. First, the atoms of the matrix are displaced as a result of direct interaction with the particle. A collision cascade then develops; in this process, the defects are produced by primary recoil atoms that acquire sufficient energy from the incident particle. In the second stage, the primary vacancies and interstitials become involved in various physicochemical reactions (mainly with the defects existing in the matrix). The first stage can be simulated in detail using the TRIM software package [4].

As applied to the case under consideration, we simulated the result of the passage of protons with E_p = 8 MeV through a SiC film with d = 30 μm. The values of the displacement-threshold energy were taken to be 35 and 20 eV for Si and C, according to the published data [5, 6]. The calculation showed that, despite the lower value of threshold energy for C atoms, the main fraction of the vacancies produced is related to Si atoms. This circumstance is caused by the quadratic dependence of the proton-scattering cross section on the atomic number of the element. A comparison of the role of Si and C atoms in the collisions that occur is illustrated in the table (the result of the passage of 985 protons through the films was traced).

As follows from the table, the total number of collisions (leading to the production of vacancies) per incident proton is equal to (276 + 113)/985 = 0.40. However, vacancy–interstitial pairs are also generated in the course of subsequent cascades caused by recoil atoms, which leads to a value of 1.28 vacancies per incident proton (with a statistical sample of $\approx 2 \times 10^4$ protons).

It is significant that the energy is transferred to atoms in small portions in collisions with protons (see Fig. 1 and the rightmost column of the table). A decrease in the number of events with an increase in the energy (E_{tr}) transferred in a collision occurs for Si atoms in proportion to $1/E_{\text{tr}}^{1.92}$ according to the approximation (see the straight line in Fig. 1). This dependence is almost consistent with the analytical dependence proportional to $1/E_{\text{tr}}^2$.

3. RESULTS OF IRRADIATION OF TRANSISTOR STRUCTURES

3.1. Measurements of Capacitance

It was assumed in measurements of the transistor capacitance as a function of the voltage at the collector

---

[1] The differential cross section of the Rutherford scattering of protons at the target atoms with a transfer of energy in the range from E_{tr} to $E_{\text{tr}} + dE_{\text{tr}}$ is inversely proportional to the product $E_p E_{\text{tr}}^2$, where E_p is the proton energy. Therefore, a dose of 1-GeV relativistic protons is equivalent to a dose of 8-MeV protons that is lower by approximately a factor of 100.

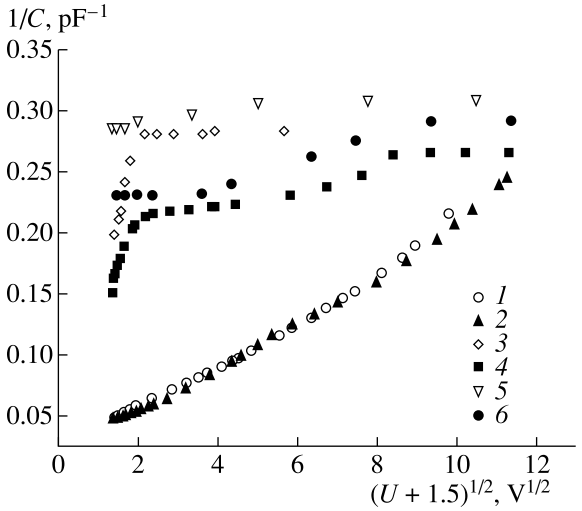

Fig. 2. Dependence of the capacitance of transistor structures on the bias voltage applied to the collector for different doses of irradiation with protons. Curves *1*, *3*, and *5* correspond to sample *22*, and curves *2*, *4*, and *6* correspond to sample *33*. Curves *1* and *2* represent the data for unirradiated samples. Curves *3*, *4* and *5*, *6* represent the results of measurements for samples irradiated with doses of 1×10^{13} and 2×10^{13} cm^{-2}, respectively.

$C(U)$ that the emitter capacitance (C_{em}) remained unchanged. Since

$$1/C(U) = 1/C_{em} + 1/C(U)_{col}, \qquad (1)$$

where $C(U)_{col}$ is the collector capacitance, the quantity $N_a - N_d$ can be determined from the value of the squared derivative[2]

$$[d(1/C)d\sqrt{U}]^2 \propto 1/(N_a - N_d). \qquad (2)$$

As was expected, the effective concentration of charged impurities changed considerably as a result of irradiation with a proton dose of 10^{13} cm^{-2}. This change was due to the compensation of the film's conductivity and manifested itself in the modified shape of the $C(U)$ curve, where a leveled-off portion appeared (Fig. 2). The values of $N_a - N_d$ calculated using formula (2) from the linear portion $1/C = f(U^{1/2})$ decreased from $(7.1–7.5) \times 10^{14}$ to $(1.8–2.6) \times 10^{13}$ cm^{-3} for samples *22* and *33*, respectively.

An increase in the proton dose to 2×10^{13} cm^{-2} (and then to 5×10^{13} cm^{-2}) resulted in a higher degree of compensation, so that the contact potential difference was sufficient to attain the saturation of the values of capacitance.

3.2. Measurements of the Signal in Detecting α Particles

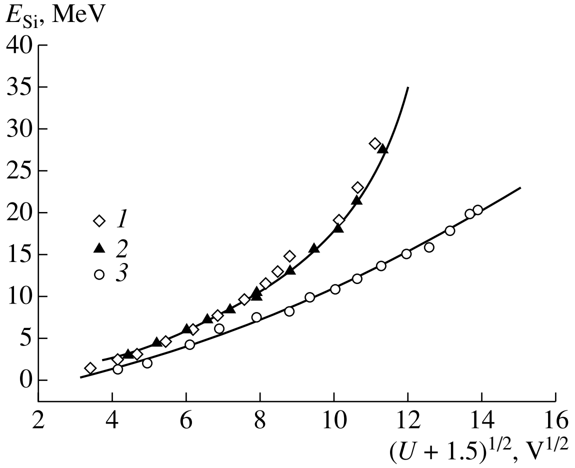

Fig. 3. Mean amplitude in the signal spectrum for a transistor structure as a function of the collector bias voltage for several doses of irradiation with protons. Sample *33*: α particles with an energy of 3.5 MeV are detected. The doses of protons are (*1*) 1.0×10^{13}, (*2*) 2.0×10^{13}, and (*3*) 5.0×10^{13} cm^{-2}.

We used α particles with an energy of 3.5 MeV and a range of ~10 μm in SiC; this range coincided with the thickness of the detector base. The aforementioned energy value was obtained by slowing down the ^{238}Pu α particles in the 20-mm air gap between the source and the detector. We measured the average pulse height in the spectrum, the spectrum shape, and the full width of the spectral line at half-maximum (FWHM). The number of channels in the pulse-height analyzer was 4000. The energy interval per channel was determined using a silicon detector.

The dependence of the average pulse height on the bias is shown in Fig. 3, where 1.5 V allows for the contact potential difference. If the charge introduced into the detector by an α particle is not amplified, a linear dependence, $E \propto W \propto (U + 1.5)^{1/2}$, should be observed for the variables used (in the approximation of a spatially uniform charge generation). It can be seen from Fig. 3 that the superlinear increase in the signal $E(U)$ is replaced by an almost linear increase as the proton dose is increased from 1×10^{13} to 5×10^{13} cm^{-2}. However, the amplitude of the signal is as large as 45 MeV (taking into account that the average energy for the formation of an electron–hole pair in SiC is equal to 7.7 eV [7]); this amplitude is tenfold greater than the energy introduced into the detector base.

The shape of the spectral line was Gaussian, and the FWHM as a function of the bias remained in general almost unchanged as the dose increased (see Fig. 4). A difference can be observed only for the portions where the smallest values of FWHM are attained (FWHM < 10%). For example, biases $U \approx 50$ V are needed to attain the smallest value of FWHM after irradiation with 2×10^{13} cm^{-2} of protons. In contrast, this value is attained at $U > 100$ V for a proton dose of 5×10^{13} cm^{-2}. According to Fig. 2, these values of U significantly exceed those required to deplete the base.

---

[2] In the case of diodes, one typically uses the derivative of the square of $1/C$: $[d(1/C^2)/dU] \propto 1/(N_a - N_d)$.

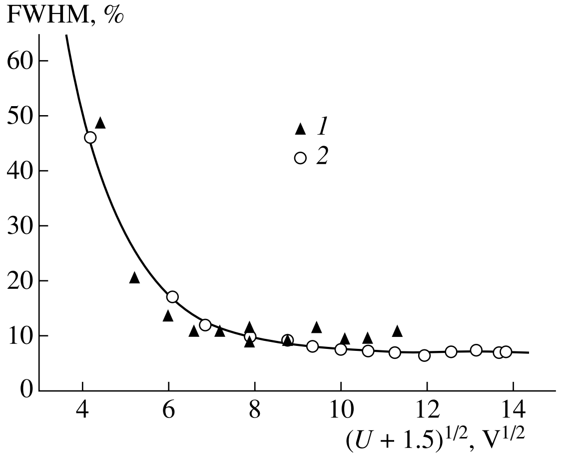

Fig. 4. Spectral-line width for a transistor structure as a function of the collector bias voltage for different doses of irradiation with protons. Sample *33*: α particles with an energy of 3.5 MeV are detected. The doses of protons are (*1*) 2.0×10^{13} and (*2*) 5.0×10^{13} cm^{-2}.

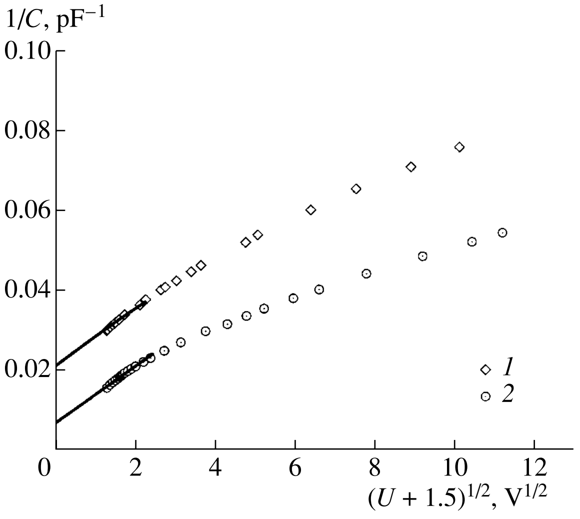

Fig. 5. Dependences of the capacitance of a diode structure on the bias voltage after irradiation with protons with a dose of 10^{14} cm^{-2}. Curves *1* and *2* correspond to samples IV-*3* and III-*5*, respectively. The weak-field region manifests itself when the curves are extrapolated to zero on the horizontal axis.

4. RESULTS OF IRRADIATING THE DIODE STRUCTURES

4.1. Measurements of Capacitance

After irradiation with a proton dose of 10^{14} cm^{-2}, the samples could be divided into two groups, according to the shape of dependences $C = f(U)$. For the samples of the first group, C depended on U; however, extrapolation of the initial portion of curve $1/C = f[(U + 1.5)^{1/2}]$ to $U + 1.5 = 0$ did not yield the value $1/C = 0$ (see Fig. 5). This observation indicates that a specific region appears in the structure whose size does not depend on bias. Ryvkin *et al.* [8] introduced the term "weak-field region" (W_W), since the voltage drop across this region is equal to the difference between the Fermi level and the compensating level and remains so irrespective of U. In the case under consideration, the values of W_W were no larger than 5 μm, so the electric-field strength was estimated to be $F \approx 1$ kV/cm.

The capacitance was independent of the bias U for the samples of the second group; i.e., the conductivity compensation is more profound in this case.

4.2. Measurements of the Signal in Detecting α Particles

High-voltage biases (up to 1 kV) could be applied to diodes of the second group; thus, we were able to monitor the charge transport in strong fields and analyze both the amplitude and shape of the spectral line. We used α particles with energy $E_\alpha = 5.4$ MeV. The charge-collection efficiency (CCE) was as high as 0.8, and the resolution was limited by the FWHM (≤2%). The shape of the line was Gaussian.

However, we failed to obtain a dependence of the signal on bias, which is typically observed for transistor structures. According to estimations, the width of the zone of a strong field ($F \approx 70$ kV/cm) was $W \leq 15$ μm, which was found to be insufficient for emitter–collector interaction with a base width of 30 μm.

An increase in the proton dose to 2×10^{14} cm^{-2} did not lead to changes in the shape of the dependences of CCE and FWHM on bias either, but it did affect the values of these quantities. Diodes III-*5* (which retained the value CCE ≈ 0.8) and VI-*4* (in which the values of CCE decreased appreciably) were opposite with respect to CCE(U) dependence (Fig. 6, curves *2*, *4*). Both the aforementioned trends manifested themselves in the curves for sample IV-*3*, where two groups of signals (curves *1*, *3*) were observed simultaneously. The CCE(U) dependence according to the lower peak for sample IV-*3* (IV-3_{min}) was similar to that for sample VI-*4*, whereas this dependence for the higher peak (IV-3_{max}) almost coincided with the case of CCE ≈ 0.8.

The energy resolution also degraded and in the best case (diodes III-*5* and IV-*3*) was limited to FWHM = 3%. It is significant that the values of FWHM = $f(U)$ were identical for both peaks of sample IV-*3*. This circumstance makes it possible to account for the presence of two peaks according to Fig. 6. The conductivity is compensated with different rates over the area of the sample owing to the nonuniform distribution of impurities in the starting film. In general, the diode is divided into several detectors with individual conditions of signal formation. Diode IV-*3* can be represented as two detectors, in one of which the base is not completely depleted. As is well known [9], the presence of a high-resistivity base leads to a decrease in the signal by a factor of W/d, which is characteristic of peak IV-3_{min} in sample IV-*3*.

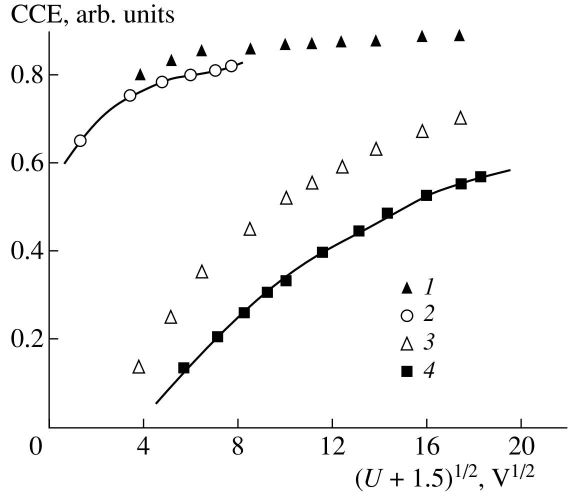

Fig. 6. Charge-collection efficiency (CCE) as a function of the bias voltage in a diode structure after irradiation with protons with a dose of 2×10^{14} cm^{-2}. Curves *1–4* correspond to spectral lines of samples IV-3_{max}, III-*5*, IV-3_{min}, and VI-*4*, respectively (see the text).

Finally, diode VI-*4*, which exhibited the lowest CCE, also featured the worst resolution (FWHM = 7%).

5. CONCLUSION

The results of this study clarify the limits of normal operation of detectors based on *p*-SiC films (6*H* and 4*H* polytypes) irradiated with 8-MeV protons with doses as high as 5×10^{13} and 2×10^{14} cm^{-2} for transistor- and diode-type structures, respectively. Even at the highest doses, the detectors can still be used for the spectrometry of α particles. The resolution of the transistor-type detectors amounts to ≤10% (with signal amplification greater than a factor of 10). As for diode detectors, there is a group of them that has a resolution of about 3%, which is acceptable for most applications.

Both values for the upper limit of the aforementioned doses correspond to the introduction of primary defects with a concentration that exceeds the starting concentrations of uncompensated impurities by more than an order of magnitude. In the case of diode-type detectors, the concentration of primary defects is as high as 8×10^{16} cm^{-3}. Such a high concentration of defects reduces the lifetime of nonequilibrium charge carriers, which manifests itself in a decrease in the efficiency of the charge transport.

Simultaneously, the presence of the structure defects gives rise to a beneficial effect: a decrease in the charge of uncompensated impurities (compensation of the conductivity of *p*-type films). However, the degree of compensation was found to be insufficient to deplete diode structures with a base thickness ≈30 μm, which prevented the observation of the signal amplification characteristic of transistor-type detectors.

The results obtained are qualitatively close to those of previous research [3] carried out on 6*H*-SiC films with *n*-type conductivity. However, further studies are required in order to compare the radiation resistance of *n*- and *p*-SiC films in more detail.

ACKNOWLEDGMENTS

This study was carried out as part of the RD50 (CERN) program and was supported in part by a grant from the President of the Russian Federation (grant no. NSh-2223.2003.02) and INTAS (grant no. 01-603). Thick films were grown within the framework of a joint grant with the Swedish Academy of Sciences.

REFERENCES

1. E. V. Kalinina, G. F. Kholuyanov, D. V. Davydov, *et al.*, Fiz. Tekh. Poluprovodn. (St. Petersburg) **37**, 1260 (2003) [Semiconductors **37**, 1229 (2003)].
2. A. A. Lebedev, N. B. Strokan, A. M. Ivanov, *et al.*, Appl. Phys. Lett. **79**, 4447 (2001).
3. A. M. Ivanov, N. B. Strokan, D. V. Davydov, *et al.*, Appl. Surf. Sci. **184**, 431 (2001).
4. *Ion Implantation: Science and Technology*, Ed. by J. F. Ziegler (Academic, Orlando, 1984).
5. W. Jiang, S. Thevuthasan, W. J. Weber, and R. Grotzschel, Nucl. Instrum. Methods Phys. Res. B **161–163**, 501 (2000).
6. S. Lazanu, I. Lazanu, E. Borchi, and M. Bruzzi, Nucl. Instrum. Methods Phys. Res. A **485**, 768 (2002).
7. A. M. Ivanov, E. V. Kalinina, A. O. Konstantinov, *et al.*, Pis'ma Zh. Tekh. Fiz. **30** (14), 1 (2004).
8. S. M. Ryvkin, L. L. Makovski, N. B. Strokan, *et al.*, IEEE Trans. Nucl. Sci. **15** (3), 226 (1968).
9. V. K. Eremin, N. B. Strokan, and N. I. Tisnek, Fiz. Tekh. Poluprovodn. (Leningrad) **8**, 1157 (1974) [Sov. Phys. Semicond. **8**, 751 (1974)].

Translated by A. Spitsyn

Semiconductors, Vol. 38, No. 7, 2004, pp. 812–817. Translated from Fizika i Tekhnika Poluprovodnikov, Vol. 38, No. 7, 2004, pp. 846–851.
Original Russian Text Copyright © 2004 by Zolotovskaya, Posnov, Prokosin, Yumashev, Gurin, Alexeenko.

LOW-DIMENSIONAL SYSTEMS

Nonlinear Properties of Phototropic Media on the Basis of Cu_xSe Nanoparticles in Quartz Glass

S. A. Zolotovskaya*^, N. N. Posnov*, P. V. Prokosin*, K. V. Yumashev*,
V. S. Gurin, and A. A. Alexeenko*****
**International Laser Center, Minsk, 220013 Belarus*
^e-mail: zolotovskaya@rambler.ru
***Institute of Physicochemical Problems, Belarussian State University, Minsk, Belarus*
****Gomel State University, Gomel, 246699 Belarus*

Submitted October 30, 2003; accepted for publication November 26, 2003

Abstract—Energy and kinetic characteristics of theinduced transparency in quartz sol–gel glasses containing copper selenide nanoparticles of different stoichiometry are studied. The dependence of the nonlinear optical properties of the glass samples on the chemical composition of copper selenide particles, which gives rise to an additional absorption band in the near-infrared region and determines its spectral position, is established. It is found that the time of relaxation of the induced transparency increases and the peak absorption cross section decreases as the absorption maximum shifts to the low-energy spectral region. *© 2004 MAIK “Nauka/Interperiodica”.*

1. INTRODUCTION

Semiconductor nanoparticles introduced into a dielectric matrix are currently being intensively studied [1, 2]. Indeed, a variety of quantum-confinement effects in such materials determines the specific features of the optical response of nanoparticles and makes these optical materials with novel properties promising for applications [3–6]. The character of the quantum-confinement effects is determined not only by the size of nanoparticles but also by their chemical nature, crystalline structure, the state of the surface, and the degree of order in the material. The spectroscopic properties of I–VIII (for example, Cu and Ag chalcogenides), II–VI (CdS, CdSe), III–V (GaAs, InP), and IV–VI (PbS, PbSe) compounds in the form of nanoparticles have been largely established. Particles with sizes that allow for the formation of a crystalline lattice usually form nanocrystalline phases with invariable composition and almost single-crystal structure. Some other semiconductors, including copper and silver chalcogenides, have more complex crystalline structures and their chemical compositions do not necessarily obey the strict rules of stoichiometry [7–12]. In this case, the size-dependent properties of nanoparticles depend not only on the particle size but also on stoichiometry, the state of the surface, and the presence of intrinsic defects and impurities. An example of such a material is copper selenide Cu_xSe, which exists as a series of stable and metastable phases under normal conditions, with the stoichiometry coefficient x varying from 1 to 2. The presence of nonstoichiometric phases with $x < 1$ or $x > 2$ is also possible [13–15]. The variation in x produces a substantial change in the band gap E_g (from 1.8 to 1.1 eV for x varying from 2 to 1, respectively) [16–20] and, furthermore, the parameters of the energy-band structure cannot be unambiguously determined from the data of different authors. The variation in the stoichiometry of copper selenide is accompanied by a change in the crystalline structure. Moreover, the phases of different stoichiometry exhibit a series of phase transitions as temperature varies. There is lack of data on copper selenide in the form of nanoparticles; there are only indications that it is possible to synthesize Cu_xSe for $1 \le x \le 2$ using the sonochemical method in water [21], $Cu_{2-x}Se$ in a nonaqueous medium [22], and $Cu_{2-x}Se$ using the microwave activation method [23]. These studies also contain no data on the energy-band structure or on the optical properties of the materials. However, there are numerous studies dealing with copper selenide in the form of thin films [13], which are promising for photoelectric devices, but the properties of individual particles may differ considerably from those of films. Previously, it was shown that Cu_xSe can be formed in quartz (thin film or bulk)matrices obtained from organosilicon precursors by the sol–gel method. According to [24–26], the optical properties of copper selenide nanoparticles are to some extent unique compared to those of the compounds mentioned above, which are traditionally used in quantum-confinement studies. In addition to interband transitions, the spectra include a highly intense absorption band in the near-infrared (IR) region, which may be attributed to the formation of intraband levels due to surface oxidation of nanoparticles. The Cu_xSe nanoparticles in dielectric matrices (glass, transparent polymer) exhibit phototropic properties; i.e., the initial optical absorption can increase to saturation and then return to the initial value with a characteristic recovery time.

In this study, we consider the optical properties of phototropic media: quartz glasses fabricated using sol–gel technology with inclusions of copper selenide (Cu_xSe) nanoparticles. The energy and kinetic characteristics of the induced transparency in glasses with nanoparticles of different composition in the near-IR region are obtained, and a possible mechanism for the induced transparency that provides an interpretation of the optical properties observed is suggested.

2. PREPARATION OF SAMPLES

Quartz glass samples containing Cu_xSe nanoparticles were fabricated by a series of operations typical of the well-known sol–gel method based on tetraethylorthosilicate (TEOS) hydrolysis and modified to facilitate the formation of nanoparticles of the required composition [27–29]. The main steps of this method are as follows. Polysilicon acid sol was prepared by mixing TEOS, ethyl alcohol, water, and a small amount of HCl, which served as a hydrolysis catalyst. A solid filler in the form of SiO_2 particles with diameter 20–50 nm (aerosil) was introduced into the sol to form a homogeneous mixture, which transforms into the gel state as a result of the neutralization of sol by a water solution of ammonia (0.1 mol/l) to pH ≈ 6; the gels obtained were kept in plastic containers with a specified configuration. After drying in air, the gels were subjected to annealing at different temperatures (from 600 to 1100°C), which provided an opportunity to control the porosity of the gel before introducing copper salts as doping components. As a result, we obtained porous xerogels consisting of SiO_2 (with a small amount of residual hydroxide groups). To introduce copper to xerogels, the latter were impregnated with an alcohol solution of $Cu(NO_3)_2$ at a concentration of $(3–10) \times 10^{-3}$ mol/l. After being died in air, the samples were subjected to thermal treatment in a hydrogen flow at 600°C for 1 h and placed into quartz cells, which contained a specified amount of elementary selenium sufficient to produce a selenium partial pressure of about 1 atm at the peak temperature 1200°C. The cells were sealed and heated to 1200°C, in accordance with the chosen rate of temperature increase. As a result, the glass samples were stained by Cu_xSe nanoparticles. For optical measurements, we chose five samples, which differed in the temperature conditions of xerogel treatment and in copper content. The fact that the composition of the nanoparticles appeared to be close to that of copper selenide Cu_2Se was confirmed in earlier studies using Rutherford backscattering and high-resolution transmission electron microscopy (TEM) [27, 29]. The presence of copper selenide nanoparticles in glasses after the final stage of sintering was also confirmed by the TEM measurements (a UEM-100LM system) carried out by examination of carbon replicas taken directly from the freshly cleaved surfaces of the glasses under study. The particles were almost spherical with diameter ranging from 20 to 50 nm for all the glass samples, which is clearly seen in Fig. 1.

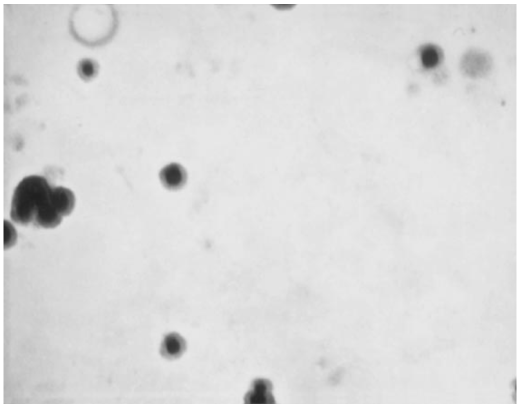

Fig. 1. A typical micrograph of nanoparticles formed in the glass samples; 20000× magnification.

3. THE OPTICAL EXPERIMENT

The kinetics of the induced transparency was measured by the picosecond pump–probe technique using an absorption spectrometer on the basis of a passively mode-locked laser. We used $YAlO_3:Nd^{3+}$ laser pulses with a duration of 15 ns and a wavelength of 1.08 μm (fundamental harmonic) as pump radiation. The energy density at the sample surface was about 14 mJ/cm^2. Depending on the sample under study, the wavelength of the probe radiation was 1.08 μm or 1.29 μm (the second harmonic of the induced Raman scattering in $KGd(WO_4)_2$ for pumping radiation wavelength 1.08 μm). The induced change in optical absorption can be defined as

$$\Delta OD = -\log\frac{T(t_d)}{T_0},$$

where $T(t_d)$ and T_0 are the transmittances of the irradiated and unirradiated samples, respectively.

The saturation of absorption was studied using the one-beam technique and by measuring the dependence of the absorption coefficient at a wavelength of 1.54 μm on the intensity of pump pulses of duration 80 ns generated by a passively Q-switched erbium glass laser. A $MgAl_2O_4:Co^{2+}$ crystal was used as the passive Q switch of the laser [30].

4. RESULTS AND DISCUSSION

Figure 2 shows the linear absorption spectra for a number of samples of glasses that contain copper selenide nanoparticles. It can be seen that the position of the near-IR absorption band varies from sample to sample, whereas the general appearance of the spectra is similar for the entire series of samples: in addition to the band in the visible region mentioned above, an absorption edge typical of semiconductor materials

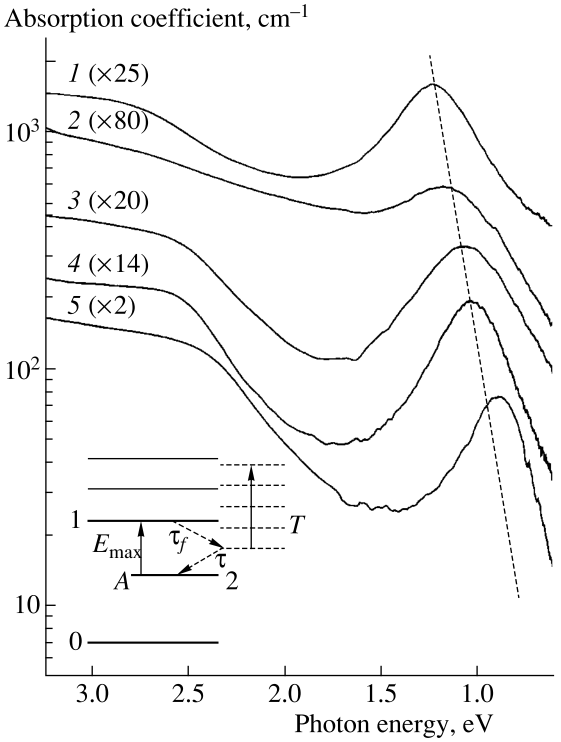

Fig. 2. Absorption spectra of the glass samples numbered in accordance with the table; the inset shows the energy diagram of Cu_xSe nanoparticles.

appears. By measuring the position of the edge, we determined the band gap E_g. For different samples, the absorption peaks were observed at E_{max} = (sample *1*) 1.23, (*2*) 1.17, (*3*) 1.07, (*4*) 1.03, and (*5*) 0.89 eV (see Table). The band gap E_g was determined assuming that there are indirect allowed transitions and using the dependences of the absorption coefficient on the photon energy in the form $\alpha\hbar\omega = f[(\hbar\omega - E_g)^2]$ [31].

Note that, for some of the samples studied, the quantity E_{max} changes systematically; however, there is no correlation with E_g, although for a number of copper selenides of different stoichiometry a change in E_g is observed as the Cu/Se ratio increases [16–20]. Therefore, the special feature of our samples that is responsible for the position of the absorption peak is the energy level position in the band gap (level *A* in the diagram; Fig. 2, inset) rather than the change in the stoichiometry of copper selenide. The levels can correspond to defect or impurity states and, in particular, to nanoparticle surface states because of the well-known fact that the fraction of atoms at the surface in nanosize particles is considerably larger than that in a bulk crystalline or amorphous material. In copper chalcogenides, some special features of their chemical properties can give rise to additional states in view of the tendency of copper to form compounds with different stoichiometry and different valence states. In other words, an internal electron transfer without a change in the total charge state of the particles is possible, which is shown in the energy diagram as a process involving the levels in the band gap. As we proceed from sample *1* to sample *5*, the intraband level apparently approaches the bottom of the conduction band (Fig. 2, inset), which produces a variation in optical properties: the absorption-band energy decreases and the relaxation time increases.

Figure 3 illustrates the kinetics of the induced transparency in the glass samples under study. The relaxation kinetics of the induced transparency is exponential and can be expressed in the form

$$\Delta OD(t_d) = \Delta OD(0)\exp(-t/\tau), \qquad (1)$$

where τ is the characteristic relaxation time. The value of τ varies from sample to sample from 0.15 to 1.24 ns (see table). Analyzing the relation between the relaxation time and the absorption peak E_{max}, we note that longer relaxation times correspond to the peaks with lower energies (Fig. 4), which can be explained by the closer position of the intraband level to the bottom of the conduction band (Fig. 2, inset).

Figure 5 shows the dependence of the absorption coefficient of the glass samples under study on the pump intensity. A decrease in absorption (induced transparency) is observed for all the samples. The residual absorption α_B in the state with increased transparency normalized to the initial absorption α_0 at a given wavelength is in the range 0.35–0.89. Solid curves in Fig. 5 represent the results of simulation using the fast-relaxation absorber model [32], where the absorption coefficient is described as

$$\alpha(I_0) = \frac{\alpha_0 - \alpha_B}{1 + \dfrac{I_0}{I_S}} + \alpha_B, \qquad (2)$$

Spectral and kinetic characteristics of sol–gel glasses with Cu_xSe nanoparticles

Sample	E_{max}, eV	E_g, eV	τ, ns	I_S, MW/cm^2 ($\hbar\omega$ = 0.8 eV)	α_B/α_0 ($\hbar\omega$ = 0.8 eV)	σ_{max}, 10^{-17} cm^2
1	1.23	2.0	0.3	–	–	15.06*
2	1.17	1.4	0.15	5.5	0.89	17.60
3	1.07	1.8	0.24	–	–	–
4	1.03	2.0	0.95	5	0.56	3.0
5	0.89	1.8	1.24	7	0.35	0.87

* The value was obtained from data on the absorption saturation at $\hbar\omega$ = 1.17 eV [26].

where I_S is the saturation intensity. The values of α_B/α_0 and I_S corresponding to the closest correlation between the numerical results and the experiment are listed in the table. The residual absorption can be attributed to the effect of absorption by the excited states [33].

Using the obtained set of data on the absorption of Cu_xSe nanoparticles in glass samples, we can plot the dependence of the residual absorption α_B in the state with induced transparency on the difference between the pump photon energy $\hbar\omega = \hbar\omega_{\text{pump}}$ and the maximum $E_{\max}$ of the absorption band considered (Fig. 6). The residual absorption is minimal in the spectral region corresponding to the absorption peak and increases as the pump frequency is detuned from the absorption peak. Figure 6 also shows the data obtained in [26] for sample *1* for pumping with a different photon energy of $\hbar\omega_{\text{pump}} = 1.17$ eV. These data are consistent with the results of this study and readily fit the behavior of $\alpha_B(\hbar\omega_{\text{pump}})/\alpha_0(\hbar\omega_{\text{pump}})$ as a function of $E_{\max} - \hbar\omega_{\text{pump}}$.

Using the saturation intensities I_S and the relaxation times τ, we calculated the absorption cross sections σ for the photon energies $\hbar\omega_{\text{pump}}$ from the well-known expression $\sigma = \hbar\omega_{\text{pump}}/2I_S\tau$. Using the relationship

$$\frac{\alpha_0^{\max}}{\alpha(\hbar\omega_{\text{pump}})} = \frac{\sigma_{\max}}{\sigma(\hbar\omega_{\text{pump}})}, \qquad (3)$$

where $\alpha_0^{\max}$ is the absorption coefficient at the maximum of the band, we determined the peak values of the absorption cross sections $\sigma_{\max}$ for the low-energy band (see table). As we shift the absorption band to higher photon energies by changing the pump photon energy, the corresponding peak absorption cross section increases (Fig. 4) and becomes significantly larger for the samples with absorption peaks corresponding to the shortest wavelengths. We may assume that the energy levels (Fig. 2, inset) that are responsible for the peaks with shorter wavelengths and have larger absorption cross sections have a different origin from the levels whose absorption cross section is an order of magnitude smaller. The fact that the intraband levels fall into two categories is also confirmed by the considerable difference in their relaxation times: levels of the first type are characterized by $\tau \approx 1$ ns and lower values of $\sigma_{\max}$, while those of the second type have $\tau < 400$ ps and larger $\sigma_{\max}$ (Fig. 4, table).

The energy levels under consideration are formed due to chemical changes in copper selenide nanoparticles (at the surface or at defects that involve a change in the valence of copper atoms). It is therefore possible to correlate their discrete character to a specific chemical model. It should be noted that a size dependence of the energy levels would indicate a continuous change in the properties. Hence, it follows that copper selenide nanoparticles that have similar stoichiometry and similar values of E_g can exist in different chemical states, which control the position of the intraband level and cause additional absorption in the low-energy region.

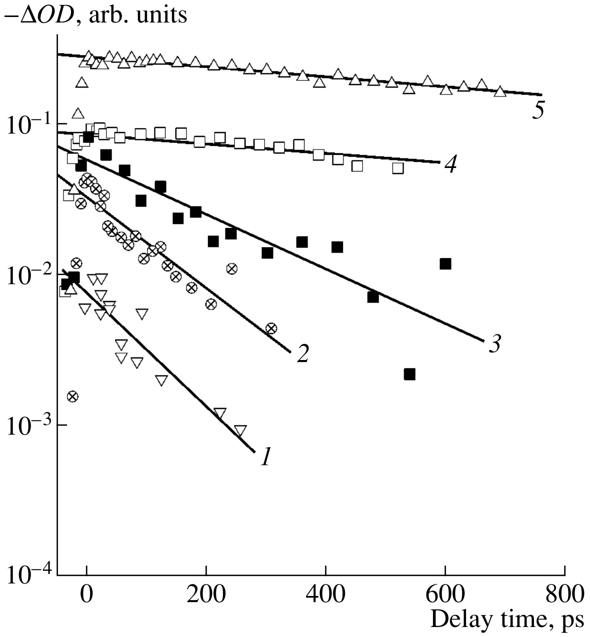

Fig. 3. Kinetics of the induced change in the absorption ΔOD of quartz glasses containing Cu_xSe nanoparticles. Pump pulse parameters: photon energy 1.15 eV, pulse duration 15 ps. Probe photon energy: (sample *1*) 1.38, (*2*, *3*, *5*) 1.15, and (*4*) 0.96 eV. Experimental data are indicated by dots; the results of simulation are represented by solid curves. Numbers by the curves correspond to the sample numbers in the table.

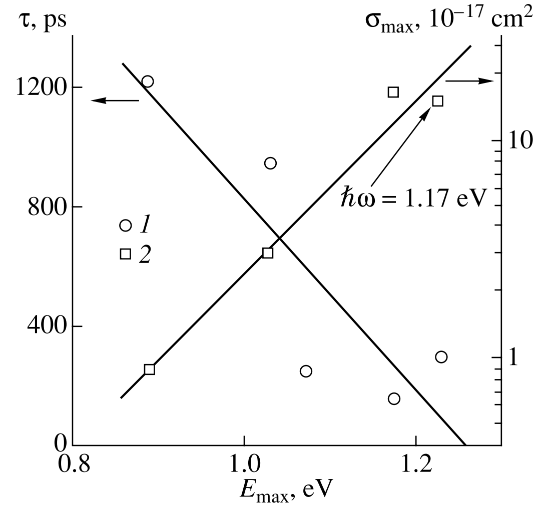

Fig. 4. (*1*) Time of relaxation of the induced transparency τ and (*2*) the peak cross section $\sigma_{\max}$ vs. the absorption peak energy $E_{\max}$ for the samples of glasses containing Cu_xSe nanoparticles.

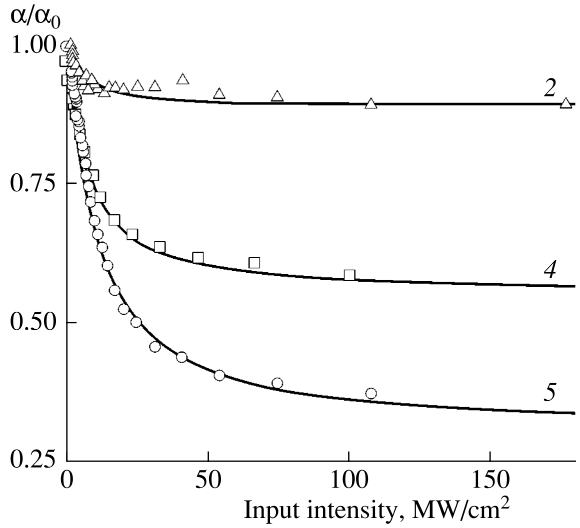

Fig. 5. Absorption coefficient of glasses containing Cu_xSe nanoparticles vs. the intensity of the pump pulses with photon energy $\hbar\omega = 0.8$ eV and duration 80 ns. Experimental data are indicated by dots; the results simulation are represented by solid curves. Numbers by the curves correspond to the sample numbers in the table.

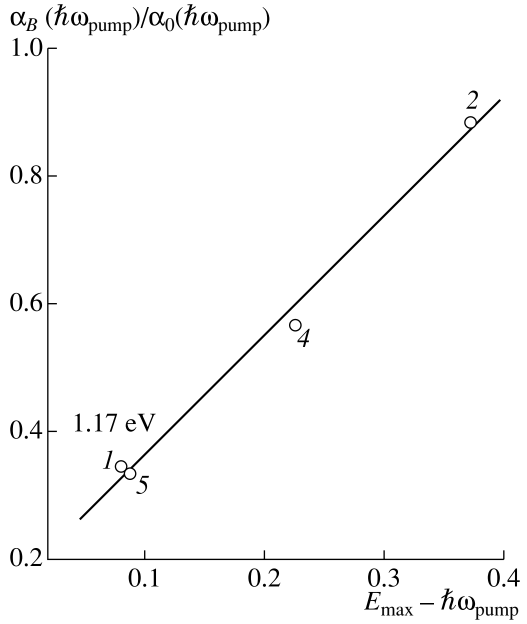

Fig. 6. Residual absorption in the state with induced transparency α_B/α_0 vs. the spectral position of the line of the excitation radiation $E_{max} - \hbar\omega_{pump}$. Numbers by the curves correspond to the sample numbers in the table. For samples *2*, *4*, and *5*, $\hbar\omega = \hbar\omega_{pump} = 0.8$ eV; for sample *1*, 1.17 eV (indicated in the plot).

5. CONCLUSION

Samples of quartz glasses containing copper selenide nanoparticles were fabricated using sol–gel technology, and the characteristics of their linear absorption in the visible and IR regions were studied. We investigated the energy and the kinetic characteristics of the induced transparency in glasses with Cu_xSe nanoparticles of different stoichiometry in the presence of laser pumping with frequencies that are efficiently absorbed due to the low-energy spectral band. Different glasses feature different positions of low-energy peak absorption; for example, as the peak position varies from 1.23 to 0.89 eV, the characteristic time of relaxation of the induced transparency corresponding to the absorption saturation in the band considered increases from 0.15 to 1.24 ns and the peak absorption cross section decreases from 1.7×10^{-17} to 8.7×10^{-18} cm^2. This behavior is related to the appearance of intraband levels of different chemical nature.

ACKNOWLEDGMENTS

This study was supported by the state program for basic research "The Development of the Scientific Grounds of Synthesis and the Study of Properties of Inorganic Materials and Disperse Systems" of the Ministry of Education of Belarus. We are grateful to A.V. Kaparikha for help in performing the TEM studies.

REFERENCES

1. S. V. Gaponenko, *Optical Properties of Semiconductor Nanocrystals* (Cambridge Univ. Press, Cambridge, 1998).
2. A. D. Yoffe, Adv. Phys. **42**, 173 (1993); Adv. Phys. **50**, 1 (2001).
3. *Nanomaterials: Synthesis, Properties and Applications*, Ed. by A. S. Edelstein and R. C. Cammarata (Inst. of Physics, Bristol, 1996).
4. C. N. R. Rao, J. Mater. Chem. **9** (1), 1 (1999).
5. U. Woggon, *Optical Properties of Semiconductor Quantum Dots* (Springer, Berlin, 1998).
6. G. T. Perovskiĭ, A. A. Zhilin, V. S. Shashkin, and A. A. Onushchenko, Opt. Zh. **65** (12), 29 (1998) [J. Opt. Tech. **65**, 974 (1998)].
7. V. V. Gorbachev, *I–IV Semiconductor Compounds* (Metallurgiya, Moscow, 1980).
8. A. A. Babitsyna, T. A. Emel'yanova, M. A. Chernitsyna, and V. T. Kalinnikov, Zh. Neorg. Khim. **20**, 3093 (1975).
9. R. M. Murray and R. D. Heyding, Can. J. Chem. **53**, 878 (1975); Can. J. Chem. **54**, 841 (1976).
10. R. D. Heyding, Can. J. Chem. **44**, 1233 (1966).
11. Z. Vucic, O. Milat, V. Horvatic, and Z. Ogorelec, Phys. Rev. B **24**, 5398 (1981).
12. Z. Ogorelec and B. Celustka, J. Phys. Chem. Solids **30**, 149 (1969).
13. K. L. Chopra and S. R. Das, *Thin Film Solar Cells* (Plenum, New York, 1983; Mir, Moscow, 1986).
14. H. Ueda, M. Nohara, K. Kitazawa, *et al.*, Phys. Rev. B **65**, 155104 (2002).
15. Y. Cheng, T. J. Emge, and J. G. Brennan, Inorg. Chem. **35**, 7339 (1996).
16. V. V. Gorbachev, Neorg. Mater. **28**, 2310 (1992).

17. G. P. Sorokin, Yu. M. Papshev, and P. T. Oush, Fiz. Tverd. Tela (Leningrad) **7**, 2244 (1965) [Sov. Phys. Solid State **7**, 1810 (1965)].
18. G. B. Abdullaev, A. N. Aliyarova, and G. A. Asadov, Phys. Status Solidi **21**, 461 (1967).
19. K. C. Sharma, R. P. Sharma, and J. C. Garg, Indian J. Pure Appl. Phys. **28**, 590 (1990).
20. B. Vengalis, L. Valatska, N. Shiktorov, and A. Yukna, Lit. Fiz. Sb. **27**, 561 (1987).
21. Sh. Xu, H. Wang, J.-J. Zhu, and H.-Y. Chen, J. Cryst. Growth **234**, 263 (2002).
22. W. Wang, Y. Geng, P. Yan, *et al.*, J. Am. Chem. Soc. **121**, 4062 (1999).
23. J. Zhy, O. Oalchik, S. Chen, and A. Gedanken, J. Phys. Chem. B **104**, 7344 (2000).
24. K. V. Yumashev, A. M. Malyarevich, P. V. Prokoshin, *et al.*, Appl. Phys. B **65**, 545 (1997).
25. K. V. Yumashev, N. N. Posnov, I. A. Denisov, *et al.*, J. Opt. Soc. Am. B **17**, 572 (2000).
26. K. V. Yumashev, V. S. Gurin, P. V. Prokoshin, *et al.*, Phys. Status Solidi B **224**, 815 (2001).
27. V. S. Gurin, V. B. Prokopenko, A. A. Alexeenko, *et al.*, Int. J. Inorg. Mater. **3**, 493 (2001).
28. V. S. Gurin, V. B. Prokopenko, A. A. Alexeenko, *et al.*, Mater. Sci. Eng. C **15**, 93 (2001).
29. V. S. Gurin, V. B. Prokopenko, A. A. Alexeenko, and A. V. Frantskevich, J. Mater. Chem. **11**, 149 (2001).
30. K. V. Yumashev, I. A. Denisov, N. N. Posnov, *et al.*, Appl. Phys. B **70**, 179 (2000).
31. V. V. Sobolev and V. V. Nemoshkalenko, *Methods of Computational Physics in the Theory of Solids. Electronic Structure of Semiconductors* (Naukova Dumka, Kiev, 1988).
32. W. Rudolph and H. Weber, Opt. Commun. **34**, 491 (1980).
33. G. Tamulaitis, V. Gulbinas, G. Kodis, *et al.*, J. Appl. Phys. **88**, 178 (2000).

Translated by A. Sidorova

Semiconductors, Vol. 38, No. 7, 2004, pp. 818–823. Translated from Fizika i Tekhnika Poluprovodnikov, Vol. 38, No. 7, 2004, pp. 852–857.
Original Russian Text Copyright © 2004 by Tyschenko, Rebohle.

LOW-DIMENSIONAL SYSTEMS

Radiative Recombination in Ge^+-Implanted SiO_2 Films Annealed under Hydrostatic Pressure

I. E. Tyschenko* and L. Rebohle**
**Institute of Semiconductor Physics, Siberian Division, Russian Academy of Sciences, Novosibirsk, 630090 Russia*
e-mail: tys@isp.nsc.ru
Fax: (+7) 3832332771
***Nanoparc GmbH, D-01454 Dresden-Rossendorf, Deutschland*

Submitted November 5, 2003; accepted for publication December 3, 2003

Abstract—Photoluminescence (PL) spectra and PL excitation spectra were recorded at room temperature from SiO_2 films implanted with Ge^+ ions and annealed at temperature T_a = 450–1100°C under hydrostatic pressure P = 12 kbar. The emergence of features in the violet and green bands of the PL and PL excitation spectra correlates with the formation of hydrostatically strained Ge nanocrystals. The shift of the PL bands to higher energies, which occurs as the annealing temperature is raised to $T_a \geq 800$°C, can be attributed to a shift of the energy levels related to the radiative recombination centers, which is caused by the increasing deformation potential. The observed PL is accounted for by the enhanced probability of direct radiative transitions in Ge nanocrystals with an X-like conduction band. *© 2004 MAIK "Nauka/Interperiodica".*

1. INTRODUCTION

The increasing interest in the synthesis and study of the properties of nanocrystalline Ge (nc-Ge), a material which emits light in the visible spectral range and is competitive with direct-gap semiconductors (such as GaAs and AlGaAs), has been stimulated by the specific band structure of this material. First, it has quite a wide band gap [1]; second, the small difference between the energies of direct and indirect transitions ensures small times of radiative recombination of quantum-confined electrons and holes in nc-Ge [1, 2]. Photoluminescence (PL) in the violet (3.1–4.3 eV) and green (~2.2–2.4 eV) spectral ranges was experimentally observed in SiO_2 films containing Ge [2–9]. The characteristics of these bands strongly depended on the Ge content in the SiO_2 matrix and on the conditions of subsequent thermal treatment. Violet PL peaks at 3.1 and 4.3 eV dominated in the spectra of SiO_2 films with a low (≤3 at %) content of Ge, annealed at temperatures $T_a \approx 500$°C [8]. These peaks are mostly attributed [10–12] to radiative transitions between the singlet (S) and triplet (T) states, $S_1 \longrightarrow S_0$ and $T_1 \longrightarrow S_0$, in the set of energy levels of a neutral oxygen vacancy bound to two Ge atoms in the SiO_2 matrix. Regarding the nature of the green PL band, there is still no consensus among researchers. In several studies it was attributed to radiative recombination of quantum-confined electrons and holes in nc-Ge [2, 5, 6]. However, the absence of a clearly pronounced correlation between the size of the nanocrystals and the position of the PL peak has stimulated the search for alternative sources of the green PL band. For example, the recombination of quantum-confined electrons and holes in Ge nanoclusters about 2 nm in size or less, which have no crystalline structure [7]. At the same time, we have recently shown [13, 14] that SiO_2 films containing amorphous Ge nanoclusters about 2 nm in size do not luminesce in the visible part of the emission spectrum. The interface between nc-Ge and the SiO_2 matrix was also mentioned as a possible source of the PL band at ~2.38 eV [8], although another group of authors [2, 9] considers the interface as a channel of nonradiative recombination of electrons and holes generated in nc-Ge. Earlier, we found that the appearance of a green band in PL from SiO_2 films with rather low Ge content (0.67–3 at % Ge), annealed at high (T_a = 1130°C) temperature under hydrostatic pressure (P = 12 kbar), correlates with the formation of uniformly strained Ge nanocrystals [13, 14]. In this study, we present the results of a detailed investigation of the PL emission and excitation spectra in the visible range for SiO_2 films implanted with Ge^+ ions and annealed under pressure.

2. EXPERIMENTAL

Ge nanocrystals were formed in 500-nm-thick SiO_2 films that were thermally grown on (100) n-Si wafers with a resistivity of 5–10 Ω cm. Oxide films were implanted first with Ge^+ ions with an energy of 450 keV, followed by ions with an energy of 230 keV, with doses of 3.0×10^{16} and 1.8×10^{16} cm^{-2}, respectively. The energies and doses used allowed a homogeneous distribution of Ge in SiO_2 films to be formed at depths of ~0.1–0.35 μm. The content of Ge in this layer was ~3 at %. After the implantation, samples were annealed in an Ar atmosphere at temperatures T_a = 450–

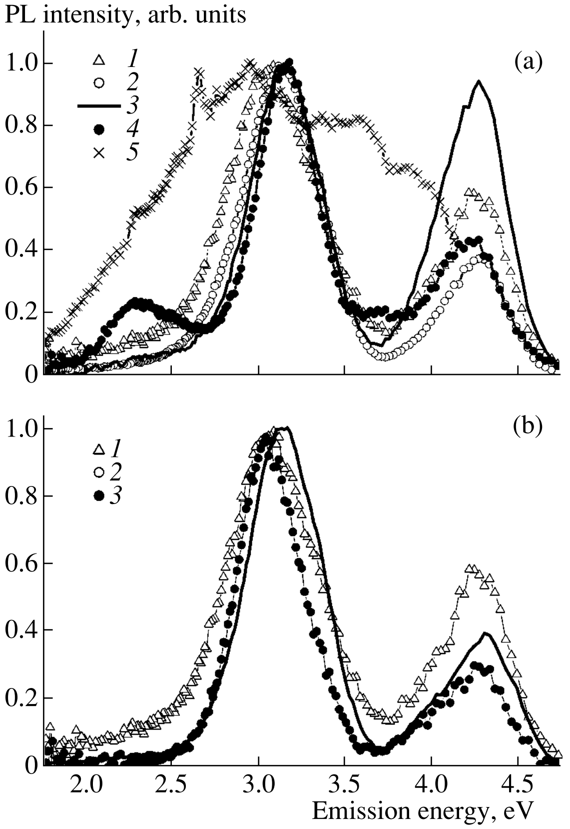

Fig. 1. PL spectra of SiO$_2$ films implanted with Ge$^+$ ions (*1*) before and (*2*–*5*) after annealing in an Ar atmosphere for 5 h. (a) Annealing under 12 kbar pressure at temperatures T_a = (*2*) 450, (*3*) 600, (*4*) 800, and (*5*) 1100°C. (b) Annealing at atmospheric pressure at T_a = (*2*) 600 and (*3*) 1000°C. The energy of the exciting light was 5.16 eV.

1100°C for 5 h. The annealing was performed in a high-pressure furnace under hydrostatic pressure P = 12 kbar, as well as in an atmospheric-pressure furnace. In the high-pressure furnace, the annealing procedure was as follows. A sample was placed into the furnace, the pressure was raised to 12 kbar, and then the sample was heated to the necessary temperature. The final stage was performed in the reverse order: first, the heating was switched off, and then the pressure was reduced. This sequence allowed us to exclude the recovery stage, so that the structural transformations that occurred during the high-pressure annealing were fixed at room temperature. The PL and PL excitation spectra were recorded at room temperature with a Spex Furomax spectrometer and Hamamatsu R928 photodetector.

3. RESULTS

Figure 1a shows PL spectra normalized to maximum intensity, which were excited by light with an energy of 5.16 eV in SiO$_2$ films implanted with Ge$^+$ ions. The spectra were recorded before and after the annealing at T_a = 450–1100°C under 12 kbar pressure. The PL spectra recorded immediately after the Ge$^+$ implantation demonstrate two peaks at 3.1 and 4.3 eV, with an FWHM of ~0.6 and 0.53 eV, respectively. These peaks are the only peaks that remain in the PL spectra after annealing at T_a = 450 and 600°C. When the annealing temperature is raised to 800°C, a new peak at ~2.3 eV appears in the green range in addition to the peaks mentioned above. When T_a is further increased to 1100°C, the clearly pronounced peaks observed after annealing at lower temperatures disappear, and a broad PL band is formed in the range ~2–4 eV. In this situation, the PL intensity increases in the low-energy (<3 eV) range, whereas the peak at 4.3 eV virtually disappears. Annealing under atmospheric pressure does not cause a similar transformation of the PL peaks (Fig. 1b). Up to T_a = 1000°C, only two peaks at 3.1 and 4.3 eV are observed in the emission spectra, and increasing T_a only changes their intensity.

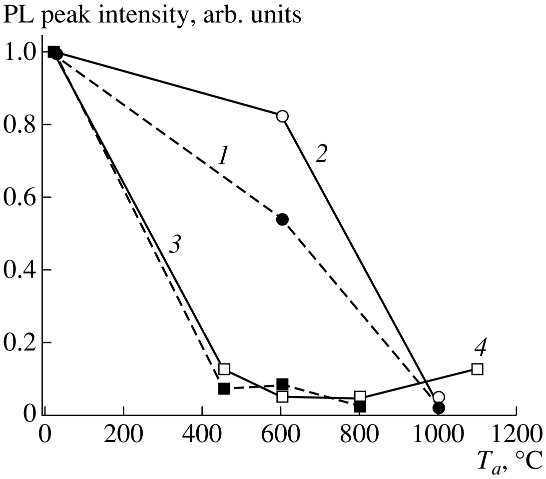

Fig. 2. Intensities of PL peaks with energies (*1*, *3*) 4.3 and (*2*, *4*) 3.1 eV as functions of the temperature T_a of annealing (*1*, *2*) at atmospheric pressure and (*3*, *4*) at P = 12 kbar.

Figure 2 shows the intensities of the 3.1- and 4.3-eV peaks as functions of T_a for annealing under atmospheric pressure and at P =12 kbar. Different behaviors are observed for samples annealed at pressures of 1 bar and 12 kbar. In the first case, the data obtained coincide with those published earlier [8]; i.e., a significant decrease in the PL intensity is observed only for T_a > 600°C. For samples annealed at P =12 kbar, the intensity of violet PL peaks decreased by nearly an order of magnitude, starting from T_a = 450°C, and then slowly decayed as T_a was raised to 800°C. As T_a was further increased to 1100°C, the intensity of the PL peak at 3.1 eV increased again, whereas the peak at 4.3 eV virtually disappeared.

To reveal the nature of the PL peaks observed, we studied their excitation spectra. Figure 3 shows excitation spectra for the 3.1-eV emission peak. The PL excitation spectra recorded immediately after the implantation of Ge$^+$ ions exhibit only one peak at ~5.0 eV. Sub-

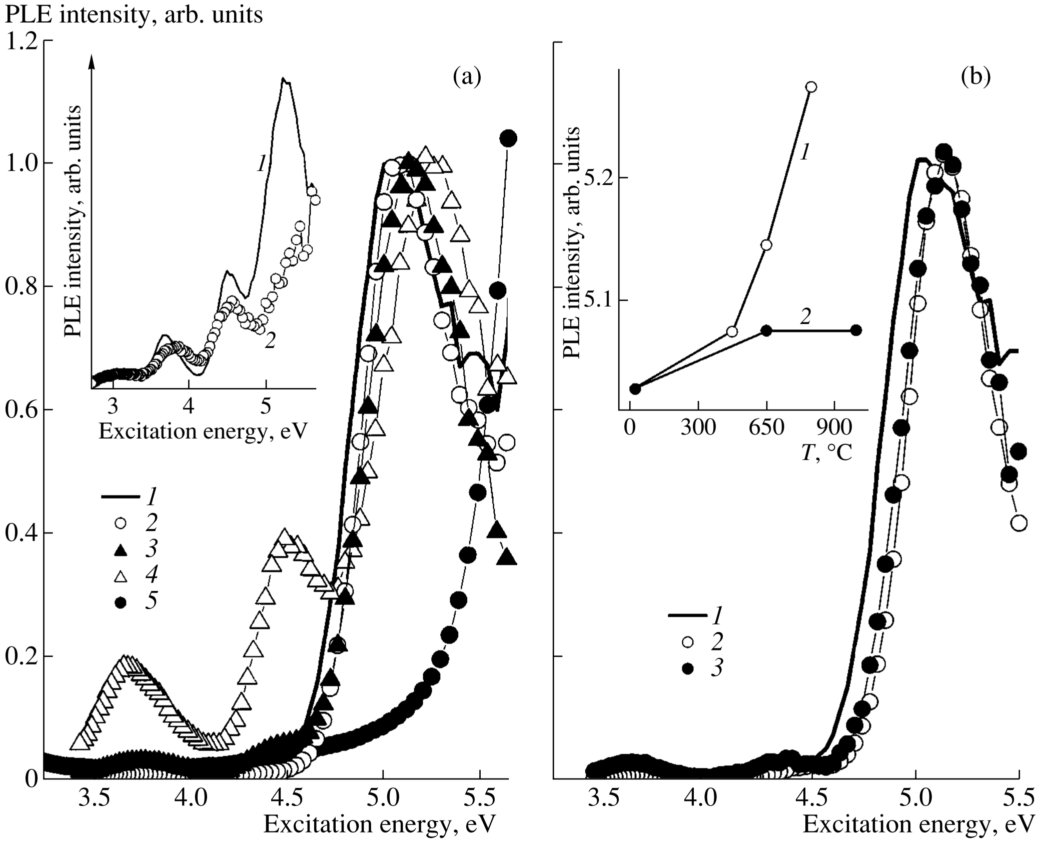

Fig. 3. Excitation spectra of a 3.1-eV PL peak for SiO_2 films implanted with Ge^+ ions (*1*) before and (*2*–*5*) after annealing in an Ar atmosphere for 5 h. (a) Annealing under 12 kbar pressure at temperature T_a = (*2*) 450, (*3*) 600, (*4*) 800, and (*5*) 1100°C. Inset: PL excitation spectra for SiO_2 films implanted with Ge^+ ions and annealed at T_a = 1100°C for peaks at (*1*) 3.1 eV and (*2*) 2.3 eV. (b) Annealing at atmospheric pressure at T_a = (*2*) 600, (*3*) 1000°C. Inset: energy of the peak in the excitation spectrum of the 3.1-eV PL peak as a function of the temperature of annealing under (*1*) 12 kbar and (*2*) 1 bar pressure.

sequent annealing under hydrostatic pressure causes a blue shift of this peak (Fig. 3a), and after annealing at T_a = 800°C the energy of the excitation peak for the violet PL band is 5.24 eV. Note that, in the range of relatively low (<800°C) annealing temperatures, the shape of the excitation spectrum for the violet PL band is not changed compared to the spectrum of unannealed samples. After annealing at T_a = 800°C, the excitation spectrum has, apart from the main peak at 5.24 eV, two peaks at 4.5 and 3.7 eV with lower intensity. The occurrence of these peaks correlates with the formation of the green PL peak in the relevant emission spectrum (Fig. 1a). It is remarkable that the 4.5- and ~3.7-eV peaks are also seen in the excitation spectrum of the green PL band (Fig. 3a, inset), whereas the distinct high-energy (5.24 eV) peak is not observed there. Note that the 4.5- and ~3.7-eV peaks observed in the excitation spectrum of the green PL band are somewhat broader than those in the excitation spectrum of the violet PL band. A radical change in the excitation spectrum for the violet PL band was observed after the annealing at T_a = 1100°C (Fig. 3a). In this case, no distinct peaks are observed, and the intensity of the violet emission increases exponentially as the energy of the excitation light increases. As mentioned above, in the case of annealing under atmospheric pressure (Fig. 3b), the excitation spectrum for the violet PL band shows a single peak at ~5.1 eV. The position of this peak did not change when T_a increased from 600 to 1000°C (Fig. 3b, inset).

4. DISCUSSION

In the discussion of the nature of the observed PL bands, we draw attention to the fact that significant differences between the PL spectra of samples annealed under atmospheric pressure and those annealed under hydrostatic compression start to appear after annealing at $T_a \geq 800$°C. Only two peaks, at about 3.1 and 4.3 eV, are observed for relatively low T_a, regardless of the pressure. In both cases, the intensity of these peaks reaches its maximum under excitation by photons with an energy of 5.1 eV. The differences were observed only in the dependences of the intensity of peaks of violet PL on T_a at low annealing temperatures (Fig. 2).

In the literature [8, 15], the nature of the 3.1- and 4.3-eV PL peaks is attributed (respectively) to transitions between the levels of the triplet and the ground singlet ($T_1 \longrightarrow S_0$) states, and between those of the excited and the ground singlet ($S_1 \longrightarrow S_0$) states of a molecule-like ≡Ge–Ge≡ center or, in other words, of a neutral oxygen vacancy bound to two Ge atoms in a SiO_2 matrix [15]. The differences observed in the dependences of the PL intensity on T_a in the range 20–600°C can be explained as follows. For annealing at atmospheric pressure, the intensity of these PL peaks first increases as the SiO_2 matrix is ordered and the ≡Ge–Ge≡ centers are formed up to $T_a \approx 500$°C. Then, at higher annealing temperatures, Ge atoms are concentrated in nanoclusters with subsequent crystallization, and the intensity of the violet PL begins to decrease [8, 15]. In the case of annealing under elevated pressure, the clustering of Ge is accelerated [13, 14]. Rapid formation of the competing centers of radiative or nonradiative recombination under annealing can reduce the efficiency of radiative recombination via the ≡Ge–Ge≡ center. As a result, we observe the decrease in the PL intensity of the 3.1- and 4.3-eV bands, which starts as early as at $T_a = 450$°C.

In our experiments, the effect of hydrostatic pressure on the state of the centers responsible for PL increases as T_a increases. Pressure can stimulate the formation of PL centers with hydrostatically strained bonds. We believe that this effect causes the blue shift of the peak in the excitation spectrum for the violet PL (Fig. 3a), which can be attributed to the shift of the energy levels of singlet and triplet states of a neutral oxygen vacancy, induced by the deformation potential. Furthermore, high-temperature annealing under pressure leads to the formation of hydrostatically strained Ge nanocrystals. Their formation correlates with the appearance of the green PL band in the spectra excited with a 337-nm line from an N_2 laser [13, 14]. Additional peaks at 4.5 and ~3.7 eV appear in the excitation spectra of PL at 3.1 and 2.3 eV (Fig. 3a), and these peaks coincide with the peaks in the excitation spectrum of the green PL. Thus, the formation of a low-intensity peak at about 2.3 eV in the emission spectrum may indicate the beginning of the formation of Ge nanocrystals. Hence, the appearance of two additional bands in the excitation spectrum of the 3.1-eV peak may be related to the additional excitation of carriers from the band of the Ge nanocrystals to the levels of neutral oxygen vacancies localized near the interface between a nanocrystal and the SiO_2 matrix. It is worth noting that, in the case of annealing under atmospheric pressure at 800°C, only Ge nanoclusters with an average size of about 2 nm and without a distinct crystal structure are formed [16].

Radical distinctions between the PL spectra of samples annealed under atmospheric and elevated pressure were observed for T_a = 1000–1100°C (Fig. 1). For the case of annealing at P = 1 bar, the emission spectra do not undergo any fundamental changes; only the intensity of the PL peaks related to recombination on the ≡Ge–Ge≡ center decreases. In contrast, the PL spectrum is significantly modified after annealing under elevated pressure. Instead of isolated peaks in the violet and near-UV spectral ranges, a broad band of PL is formed, which extends over almost the whole the visible range. Note especially that a peak with an energy of 4.3 eV is not observed in this case. This indicates that the PL in the UV range is most probably related not to the ≡Ge–Ge≡ center, but to some other centers.

The lack of distinct peaks in the excitation spectrum recorded after annealing at $T_a = 1100$°C (Fig. 3a, spectrum *5*) also indicates that a wide variety of other centers take part in the excitation of radiative recombination. In our previous research [13, 14] we showed that annealing at 1100°C under a pressure of 12 kbar stimulates the formation of hydrostatically compressed Ge nanocrystals, and their size distribution is broader than that after annealing under atmospheric pressure. After cooling, the average hydrostatic pressure within these nanocrystals was ~19.7 kbar, as estimated from the shift of the optical phonon frequency. The correlation between the features that arise in the PL emission and excitation spectra and the structural transformations allows us to attribute the observed green PL (after annealing at $T_a = 800$°C, $P = 12$ kbar) and the broad PL band (1100°C, 12 kbar) with the recombination of quantum-confined electrons and holes in hydrostatically strained Ge nanocrystals. Due to specific conditions of the mode of high-pressure annealing used (see above), the residual stress in nanocrystals annealed at $T_a = 800$°C must be less than that after annealing at $T_a = 1100$°C. This may be one of the reasons for the difference in the positions of the PL peak: its energy in the first case (2.38 eV) is lower than in the second (Fig. 1a).

To clarify the mechanism of the observed PL, we estimated (in terms of the effective mass approximation) the energies of transitions $L_1 \longrightarrow \Gamma'_{25}$, $X_1 \longrightarrow \Gamma'_{25}$, and $\Gamma'_2 \longrightarrow \Gamma'_{25}$ as functions of the size of unstrained and hydrostatically strained (for $P = 19.7$ kbar) Ge nanocrystals. These data are shown in Fig. 4. The effective mass in the $\langle 111 \rangle$ direction of the Ge Brillouin zone is large; therefore, its contribution to the quantization energy is negligible. Thus, the energy of the $\Gamma'_2 \longrightarrow \Gamma'_{25}$ transition was treated as the energy of a 2D-confined electron–hole pair [17]:

$$E_c = \frac{\hbar^2}{2\mu_\perp}\left(\frac{2.405}{R}\right)^2 - \frac{3.513e^2}{\varepsilon R}, \qquad (1)$$

where R is the radius of a nanocrystal; $\mu_\perp = 0.045m_0$, the effective mass of the electron–hole pair in the $\langle 111 \rangle$ direction of the Ge Brillouin zone; and ε, the dielectric constant of Ge nanocrystals (we assume $\varepsilon = 15.8$, as in bulk Ge). In the calculation of energies of $X_1 \longrightarrow \Gamma'_{25}$ and $\Gamma'_2 \longrightarrow \Gamma'_{25}$ transitions, the quantum confinement of electron and hole states [2] was taken into account.

Comparison of the energy of the observed emission band with calculated energy spacings shows that the energy of the observed emission band most probably

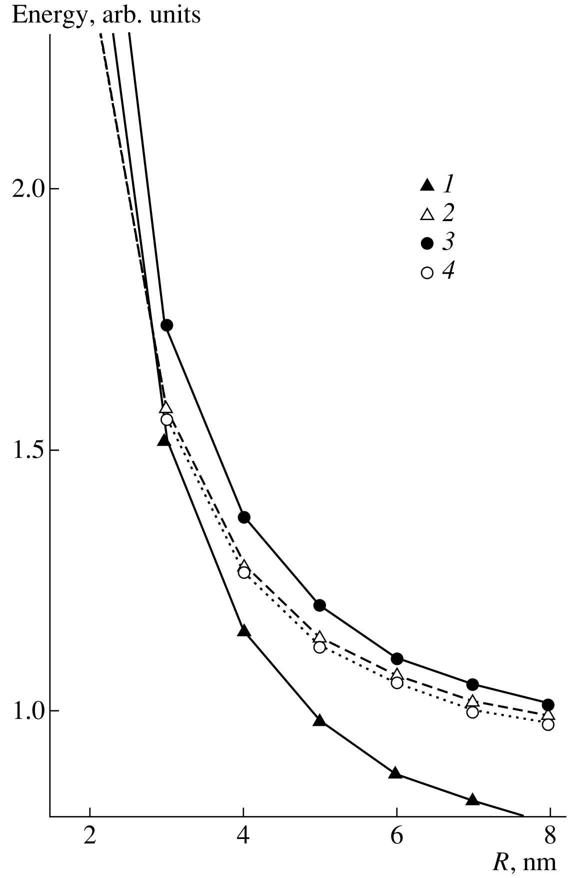

Fig. 4. Energies of indirect transitions (*1, 3*) $L_1 \longrightarrow \Gamma'_{25}$ and (*2, 4*) $X_1 \longrightarrow \Gamma'_{25}$ calculated in the effective mass approximation as functions of the radius of the nanocrystal for nc-Ge: (*1, 2*) stress-free and (*3, 4*) hydrostatically strained at P = 19.7 kbar.

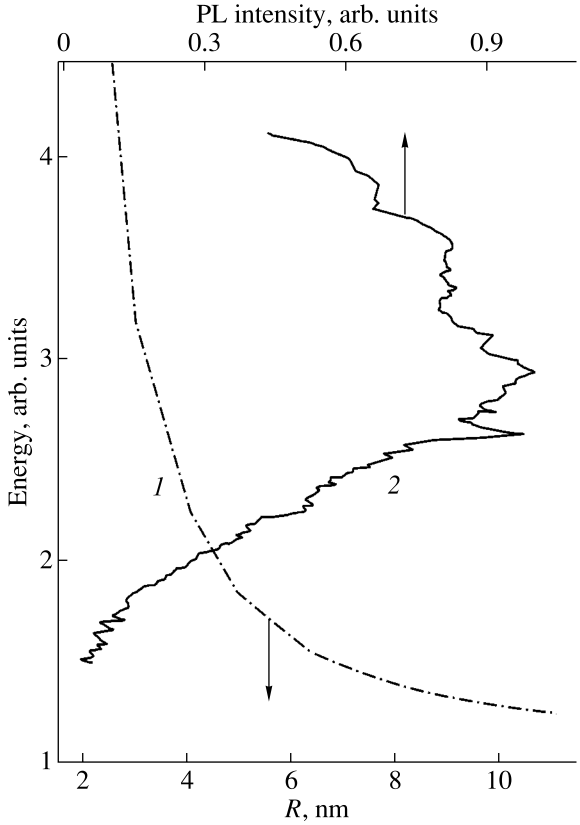

Fig. 5. (*1*) Calculated energy of the direct transition $\Gamma_2 \longrightarrow \Gamma'_{25}$ for uniformly strained (P = 19.7 kbar) nc-Ge as a function of the radius of the nanocrystal; (*2*) experimentally observed PL spectrum for SiO_2 films implanted with Ge^+ ions and annealed in an Ar atmosphere for 5 h at T_a = 1100°C under 12 kbar pressure.

corresponds to direct radiative transitions $\Gamma'_2 \longrightarrow \Gamma'_{25}$ with a radius of less than 6 nm (Fig. 5). Note that the difference in the energy of direct transitions for unstrained and uniformly strained nanocrystals is about 0.3 eV. Nevertheless, despite the fact that the size of the unstrained nanocrystals was even smaller than that of the strained ones, PL was observed only in the latter case. This can be accounted for by the data presented in Fig. 4, which shows the energies of the $L_1 \longrightarrow \Gamma'_{25}$ and $X_1 \longrightarrow \Gamma'_{25}$ transitions as functions of the radius of unstrained and hydrostatically strained nanocrystals. It can be seen that, in unstrained nanocrystals, the transition $L_1 \longrightarrow \Gamma'_{25}$ remains the one with minimum energy, as in the case of bulk Ge. However, when the size of a nanocrystal is reduced, the difference between the energies of the $L_1 \longrightarrow \Gamma'_{25}$ and $X_1 \longrightarrow \Gamma'_{25}$ transitions decreases, and at $R < 2.7$ nm the conduction band of a nanocrystal becomes *X*-like. Therefore, recombination should now proceed via point X_1, which corresponds to the minimum energy at the boundary of the Brillouin zone in the ⟨100⟩ direction. This is similar to the results of theoretical calculations in [18]. The conduction band of strained nanocrystals is *X*-like for all the values of their radius (up to R = 11 nm) considered in our study. This should affect the processes of relaxation of photoexcited electrons and holes; i.e., the recombination of electrons and holes via L_1 and X_1 minima of the conduction band involves the emission or absorption of a phonon, and the limiting value of the phonon energy in Ge is E_{ph} = 37 meV. The energy spacing between the levels of electron states $\Delta E = (dE/dk)/D$ should increase as the size of the nanocrystal decreases (dE/dk is the dispersion dependence of the electron energy; k, the wave vector; and D, the size of the crystal). This means that, at some value of D, ΔE can exceed the limiting phonon energy; therefore, the relaxation of an electron to the minimum of the conduction band in an indirect transition demands the involvement of two or more phonons. Since the probability of multiphonon processes in Ge is low, the lifetime of an excited electron state increases, which, in turn, can raise the probability of direct radiative transitions $\Gamma'_2 \longrightarrow \Gamma'_{25}$. Since the density of electron states in the ⟨111⟩ direction of the Brillouin zone of Ge is higher than that in the ⟨100⟩ direction, the condition $\Delta E > E_{\text{ph}}$ in X-like nanocrystals must be fulfilled more easily than in L-like nanocrystals. In terms of this model, it is understandable that there is no clearly pronounced dependence between the position of the PL peak and the size of strained nanocrystals, which was observed by several authors [2, 5–7].

5. CONCLUSION

We have studied PL and PL excitation spectra of SiO$_2$ films implanted with Ge$^+$ ions and annealed at temperatures T_a = 450–1100C under hydrostatic pressure P = 12 kbar. The spectra were recorded at room temperature. The emergence of features in the violet and green bands of the PL and PL excitation spectra correlates with the formation of uniformly strained Ge nanocrystals. The blue shift of PL bands for $T_a \geq 800°$C is attributed to the deformation-induced shift of the energy levels of radiative-recombination centers. The PL observed is accounted for by the enhanced probability of direct radiative transitions in Ge nanocrystals with an X-like conduction band.

ACKNOWLEDGMENTS

The authors are grateful to Dr. W. Skorupa for assistance in the implantation of Ge ions, Prof. A. Misiuk for assistance in the high-pressure annealing, and Dr. A.B. Talochkin for valuable discussions.

REFERENCES

1. T. Takagahara and K. Takeda, Phys. Rev. B **46**, 15578 (1992).
2. Y. Maeda, Phys. Rev. B **51**, 1658 (1995).
3. W. Skorupa, R. A. Yankov, I. E. Tyschenko, *et al.*, Appl. Phys. Lett. **68**, 2410 (1996).
4. J. P. Wilcoxon, P. P. Provencio, and G. A. Samara, Phys. Rev. B **64**, 035417 (2001).
5. L. Yue and Y. He, J. Appl. Phys. **81**, 2910 (1997).
6. H. A. Atwater, K. V. Shcheglov, S. S. Wong, *et al.*, Mater. Res. Soc. Symp. Proc. **321**, 363 (1994).
7. S. Hayashi, J. Kanazawa, M. Takaoka, *et al.*, Z. Phys. D **26**, 144 (1993).
8. L. Rebohle, J. von Borany, R. A. Yankov, *et al.*, Appl. Phys. Lett. **71**, 2809 (1997).
9. G. A. Kachurin, L. Rebole, I. E. Tyschenko, *et al.*, Fiz. Tekh. Poluprovodn. (St. Petersburg) **34**, 23 (2000) [Semiconductors **34**, 21 (2000)].
10. H. Hosono, Y. Abe, D. L. Kinser, *et al.*, Phys. Rev. B **46**, 11445 (1992).
11. J. Y. Zhang, X. M. Bao, Y. H. Ye, and X. L. Tan, Appl. Phys. Lett. **73**, 1790 (1998).
12. M. Martini, F. Meinardi, A. Paleari, *et al.*, Phys. Rev. B **57**, 3718 (1998).
13. I. E. Tyschenko, A. B. Talochkin, A. G. Cherkov, *et al.*, Fiz. Tekh. Poluprovodn. (St. Petersburg) **37**, 479 (2003) [Semiconductors **37**, 462 (2003)].
14. I. E. Tyschenko, A. B. Talochkin, A. G. Cherkov, *et al.*, Solid State Commun. (in press).
15. L. Rebohle, J. von Borany, H. Fröb, and W. Skorupa, Appl. Phys. B **71**, 131 (2000).
16. L. Rebohle, I. E. Tyschenko, J. von Barany, *et al.*, Mater. Res. Soc. Symp. Proc. **486**, 175 (1998).
17. K. L. Teo, S. N. Kwok, P. Y. Yu, and S. Guha, Phys. Rev. B **62**, 1584 (2000).
18. F. A. Reboredo and A. Zunger, Phys. Rev. B **62**, R2275 (2000).

Translated by D. Mashovets

Semiconductors, Vol. 38, No. 7, 2004, pp. 824–829. Translated from Fizika i Tekhnika Poluprovodnikov, Vol. 38, No. 7, 2004, pp. 858–863.
Original Russian Text Copyright © 2004 by Borisenko.

LOW-DIMENSIONAL SYSTEMS

The Effect of Acoustic Phonon Confinement on Electron Scattering in GaAs/Al$_x$Ga$_{1-x}$As Superlattices

S. I. Borisenko
Kuznetsov Siberian Physicotechnical Institute, Tomsk, 634050 Russia
e-mail: sib@elefot.tsu.ru

Submitted July 22, 2003; accepted for publication December 15, 2003

Abstract—The relaxation time of quasi-two-dimensional (quasi-2D) electrons in the lowest miniband of the GaAs/Al$_{0.35}$Ga$_{0.65}$As superlattice is calculated for the case of scattering by acoustic phonons. It is shown that electron scattering is affected only slightly by the quantization of the phonon spectrum in terms of the elasticity theory. The scattering is well described based on the phonon spectrum of the bulk semiconductors that form the superlattice. *© 2004 MAIK "Nauka/Interperiodica".*

1. INTRODUCTION

The effect of quantum confinement of the phonon subsystem on electron scattering in heterostructures that consist of isolated GaAs/Al$_x$Ga$_{1-x}$As quantum wells (QWs) and the corresponding superlattices (SLs) is the subject of a number of studies. However, in most of these studies, polar optical phonons were considered [1–11]. These studies showed that the quantization of the spectra of polar optical phonons can be used to increase the electron mobility determined by scattering by polar optical phonons in SLs near room temperature, compared to the corresponding mobility in bulk semiconductors [12]. However, the question of a possible increase in the total electron mobility limited by phonon scattering due to the quantization of the spectrum of polar optical phonons is problematic, since, in the structures under consideration, the scattering of electrons by acoustic phonons is substantially enhanced [13]. There are practically no studies on the effect of quantization of the acoustic phonon spectrum on electron scattering. In [14], this problem was solved using the theory of elasticity for an isolated QW in the isotropic-continuum approximation. An important approximation in this study is the boundary conditions corresponding to the free heteroboundaries of the QW.

In our study, the effect of the quantization of acoustic phonons on the scattering and mobility of quasi-2D electrons in the lowest miniband of the GaAs/Al$_x$Ga$_{1-x}$As SL is considered. We calculate the spectrum of acoustic phonons using the method suggested in [14]. However, our boundary conditions at heteroboundaries imply the continuity of displacements and of the normal components of the stress tensor taking into account the Bloch periodicity relative to the SL period.

2. CALCULATION OF THE FREQUENCY SPECTRUM AND DISPLACEMENT VECTORS FOR ACOUSTIC VIBRATIONS IN A SUPERLATTICE

We will calculate the frequency spectrum and the displacement field $\mathbf{u}(\mathbf{r})$ for an SL that consists of GaAs/Al$_x$Ga$_{1-x}$As QWs using the Green–Christoffel equation in the isotropic-continuum approximation ($c_{12} + 2c_{44} - c_{11} = 0$),

$$\frac{\partial^2 \mathbf{u}}{\partial t^2} = v_\perp^2 \Delta \mathbf{u} + (v_\parallel^2 - v_\perp^2)\nabla(\nabla \mathbf{u}), \tag{1}$$

where $v_\perp = \sqrt{c_{44}/\rho}$ and $v_\parallel = \sqrt{c_{11}/\rho}$ are the velocities of transverse and longitudinal acoustic phonons (these velocities depend on the z coordinate with the period d along the SL axis). As boundary conditions for the solutions of Eq. (1), we will take into account the continuity of displacements and the normal components of the stress tensor at the heteroboundaries of the SL and also the fact that the displacement vector obeys the Bloch theorem with respect to the variable along the symmetry axis of the SL. We will seek the solution of Eq. (1) in the form of normal vibrations (with regard to the isotropy of the medium),

$$\mathbf{u}_{\nu\mathbf{q}}(\mathbf{r}) = \frac{A_{\nu\mathbf{q}}}{\sqrt{\rho(z)V}}\mathbf{s}_{\nu\mathbf{q}}(z)\cdot e^{iq_\perp x}, \tag{2}$$

where $\mathbf{q} = (q_\perp, 0, q_z)$ is the phonon wave vector; $\mathbf{s}_{\nu\mathbf{q}}(z)$ are the vector functions satisfying the Bloch theorem and the normalization condition

$$\frac{1}{d}\int_{-b}^{a}\frac{\mathbf{s}^*_{\nu\mathbf{q}}(z)\mathbf{s}_{\nu'\mathbf{q}}(z)}{\rho(z)}dz = \frac{d}{a\rho_a + b\rho_b}\delta_{\nu\nu'}; \tag{3}$$

$\rho(z)$ is the material density (a periodic function with a period of the SL); $A_{\nu\mathbf{q}}$ is the complex normal coordinate

1063-7826/04/3807-0824$26.00 © 2004 MAIK "Nauka/Interperiodica"

of the vibrational mode with the number ν; $q_\perp$ is the magnitude of the wave vector in the plane perpendicular to the SL axis; q_z is the component of the wave vector along the SL symmetry axis; a and b are the widths of the QW and of the potential barrier of the SL; $d = a + b$ is the SL period; and ρ_a and ρ_b are the material densities in the QW and in the potential barrier, respectively.

If formula (2) is taken into account, the solution of Eq. (1) is reduced to finding the eigenvalues and the vectors of the differential operator $\hat{D}$ that obey the boundary conditions

$$\hat{D}\mathbf{u}_\nu = -\omega_\nu^2\mathbf{u}_\nu, \tag{4}$$

where

$$\hat{D} = \begin{pmatrix} v_\perp^2\frac{\partial^2}{\partial z^2} - v_\parallel^2 q_\perp^2 & 0 & iq_\perp(v_\parallel^2 - v_\perp^2)\frac{\partial}{\partial z} \\ 0 & v_\perp^2\frac{\partial^2}{\partial z^2} - v_\perp^2 q_\perp^2 & 0 \\ iq_\perp(v_\parallel^2 - v_\perp^2)\frac{\partial}{\partial z} & 0 & v_\parallel^2\frac{\partial^2}{\partial z^2} - v_\perp^2 q_\perp^2 \end{pmatrix}.$$

For acoustic phonon displacements that have nonzero divergence, the system of secular equations for the function $\mathbf{s} = \exp(iqz)\cdot\mathbf{e}$ assumes the form

$$\begin{cases} (v_\perp^2 q^2 + v_\parallel^2 q_\perp^2 - \omega^2)e_x + q_\perp q(v_\parallel^2 - v_\perp^2)e_z = 0 \\ q_\perp q(v_\parallel^2 - v_\perp^2)e_z + (v_\parallel^2 q^2 + v_\perp^2 q_\perp^2 - \omega^2)e_z = 0. \end{cases} \tag{5}$$

The solution of system (5) is represented by the four values of the parameter q that correspond to the four values of the vector $\mathbf{e} = (e_x, 0, e_z)$:

$$\begin{aligned} q_{1,2} &= \pm Q_1 = \pm\sqrt{\left(\frac{\omega}{v_\perp}\right)^2 - q_\perp^2}, \\ q_{3,4} &= \pm Q_2 = \pm\sqrt{\left(\frac{\omega}{v_\parallel}\right)^2 - q_\perp^2}; \end{aligned} \tag{6}$$

$$\begin{aligned} \mathbf{e}_1 &= \frac{(-Q_1, 0, q_\perp)}{\sqrt{q_\perp^2 + Q_1^2}}, \quad \mathbf{e}_2 = \frac{(Q_1, 0, q_\perp)}{\sqrt{q_\perp^2 + Q_1^2}}, \\ \mathbf{e}_3 &= \frac{(q_\perp, 0, Q_2)}{\sqrt{q_\perp^2 + Q_2^2}}, \quad \mathbf{e}_4 = \frac{(-q_\perp, 0, Q_2)}{\sqrt{q_\perp^2 + Q_2^2}}. \end{aligned} \tag{7}$$

Using formulas (6), we find the relationship between Q_1 and Q_2:

$$v_\perp^2(Q_1^2 + q_\perp^2) = v_\parallel^2(Q_2^2 + q_\perp^2). \tag{8}$$

Taking into account (6) and (7), we write formula (2) for the required functions in the general case as

$$\mathbf{u}_{\nu\mathbf{q}}(\mathbf{r}) = \frac{A_{\nu\mathbf{q}}}{\sqrt{\rho(z)V}}e^{i\mathbf{q}_\perp\mathbf{r}_\perp}\sum_i c_{\nu\mathbf{q}i}(z)e^{iq_{\nu\mathbf{q}i}(z)z}e_{\nu\mathbf{q}i}(z), \tag{9}$$

where $c_{\nu\mathbf{q}i}(z)$ are constants that have the values $c_{\nu\mathbf{q}i1}$ and $c_{\nu\mathbf{q}i2}$ in the QW and the potential barrier, respectively. These values, and the spectrum of normal mode eigenfrequencies $\omega_{\nu\mathbf{q}}$, represent a solution of the system of equations that satisfies the boundary conditions (1) and the normalization condition (3) (see Appendix).

3. CALCULATION OF THE SCATTERING PROBABILITY

We calculated the scattering probability in the Born approximation by representing an approximate electron wave function as a Bloch sum over ground-state wave functions in an infinitely deep QW of the SL [13]:

$$\psi_\mathbf{k}(\mathbf{r}) = \sqrt{\frac{d}{V}}e^{i\mathbf{k}_\perp\mathbf{r}_\perp}\sum_n e^{ik_z dn}\varphi(z - dn), \tag{10}$$

where

$$\varphi(z) = \begin{cases} \sqrt{\frac{2}{a}}\sin\left(\frac{\pi}{a}z\right), & 0 \le z < a, \\ 0, & -b < z < 0. \end{cases} \tag{11}$$

Taking into account (9)–(11), we can use the deformation potential approximation for the energy of interaction between electrons and acoustic phonons to write the following expression for the probability of elastic scattering of the lowest-miniband electron with wave vector $\mathbf{k}$ to the state $\mathbf{k}'$:

$$w_{\nu\mathbf{q}}(\mathbf{k}, \mathbf{k}') = w_\nu(\mathbf{q})\delta[E(\mathbf{k}') - E(\mathbf{k})]\delta_{\mathbf{k}', \mathbf{k}-\mathbf{q}}.$$

Here,

$$w_\nu(\mathbf{q}) = w_\nu(q_\perp, q_z) = \frac{2\pi k_0 T D_a}{\hbar c_{11a}V}f^2\left(\frac{aQ_{\nu\mathbf{q}21}}{2}\right), \tag{12}$$

D_a and c_{11a} are the deformation potential of the bottom of the conduction band and the elastic modulus that correspond to the material of the QW, and

$$f(\xi_{\nu\mathbf{q}}) = \frac{\pi^2\sin(\xi_{\nu\mathbf{q}})}{\xi_{\nu\mathbf{q}}(\pi^2 - \xi_{\nu\mathbf{q}}^2)}\left|c_{\nu\mathbf{q}31} - e^{-2i\xi_{\nu\mathbf{q}}}c_{\nu\mathbf{q}41}\right|. \tag{13}$$

4. CALCULATION OF THE RELAXATION TIME

For an SL whose lowest miniband is narrow, we calculate the times of transverse and longitudinal relaxation in the elastic-scattering approximation using the well-known formulas [13]

$$\frac{1}{\tau_\perp(E)} = \sum_{\mathbf{k}',\nu,\mathbf{q}} w_{\nu\mathbf{q}}(\mathbf{k},\mathbf{k}')\left(1-\frac{\mathbf{k}'_\perp\mathbf{k}_\perp}{k_\perp^2}\right) = \sum_\nu \frac{1}{\tau_{\perp\nu}(E)}, \tag{14}$$

$$\frac{1}{\tau_\parallel(E)} = \sum_{\mathbf{k}',\nu,\mathbf{q}} w_{\nu\mathbf{q}}(\mathbf{k},\mathbf{k}')\left(1-\frac{\sin(k'_z d)}{\sin(k_z d)}\right) = \sum_\nu \frac{1}{\tau_{\parallel\nu}(E)}, \tag{15}$$

where $E = \hbar^2 k_\perp^2/2m_\perp^*$ is the energy of the transverse motion of an electron in the miniband. After integration with respect to the electron wave vector in the final state and some transformations, expressions (14) and (15) can be reduced to the following form convenient for numerical integration:

$$\begin{aligned}\frac{1}{\tau_{\perp\nu}(E)} &= \frac{V}{4\pi^3 E}\int_0^{2k_\perp}\int_0^{\pi/d}\frac{w_\nu(q_\perp,q_z)}{\sqrt{4k_\perp^2-q_\perp^2}}q_\perp^2\,dq_\perp dq_z\\ &= \frac{Vm_\perp^*}{4\pi^3\hbar^2 E}\int_0^{4E}\int_0^{\pi/d}\frac{w_\nu(x,q_z)}{\sqrt{4E-x}}x^{1/2}\,dx\,dq_z,\end{aligned} \tag{16}$$

$$\begin{aligned}\frac{1}{\tau_{\parallel\nu}(E)} &= \frac{Vk_\perp^2}{4\pi^3 E}\int_0^{2k_\perp}\int_0^{\pi/d}\frac{w_\nu(q_\perp,q_z)}{\sqrt{4k_\perp^2-q_\perp^2}}[1-\cos(q_z d)]\,dq_\perp dq_z\\ &= \frac{Vm_\perp^*}{4\pi^3\hbar^2}\int_0^{4E}\int_0^{\pi/d}\frac{w_\nu(x,q_z)[1-\cos(q_z d)]}{\sqrt{4E-x}}x^{-1/2}\,dx\,dq_z,\end{aligned} \tag{17}$$

where $x = \hbar^2 q_\perp^2/2m_\perp^*$.

5. THE APPROXIMATION OF A BULK ISOTROPIC SPECTRUM OF ACOUSTIC PHONONS

In the approximation of a bulk isotropic spectrum of acoustic phonons, the variables in expression (12) for the scattering probability take the values $c_{\nu\mathbf{q}31} = 1$, $c_{\nu\mathbf{q}41} = 0$, and $Q_{\nu\mathbf{q}21} = q_z + 2\pi\nu/d$. Taking (14)–(17) into account, we obtain the following known result for longitudinal and transverse relaxation times [13]:

$$\frac{1}{\tau_\perp} = \frac{1}{\tau_\parallel} = \frac{1}{\tau_0} = \frac{3k_0Tm_\perp^*D_a^2}{2\hbar^3 ac_{11a}}. \tag{18}$$

Taking (16)–(18) into account, we can write expressions (14) and (15) in a form convenient for analysis:

$$\frac{1}{\tau_i} = \frac{1}{\tau_0}\chi_i(E), \tag{19}$$

where

$$\chi_\perp(E) = \frac{1}{2\pi E}\int_0^{4E}\frac{\varphi_\perp(x)}{\sqrt{4E-x}}x^{1/2}\,dx, \tag{20}$$

$$\chi_\parallel(E) = \frac{1}{\pi}\int_0^{4E}\frac{\varphi_\parallel(x)}{\sqrt{4E-x}}x^{-1/2}\,dx, \tag{21}$$

$$\varphi_\perp(E) = \frac{2a}{3\pi}\sum_\nu\int_0^{\pi/d} f^2(\xi_{\nu\mathbf{q}})\,dq_z, \tag{22}$$

$$\varphi_\parallel(E) = \frac{2a}{3\pi}\sum_\nu\int_0^{\pi/d} f^2(\xi_{\nu\mathbf{q}})[1-\cos(q_z d)]\,dq_z. \tag{23}$$

Here, the functions $\chi_i(E)$ are dimensionless and depend parametrically on a and b. In the approximation of a bulk isotropic spectrum of acoustic phonons, functions (20)–(23) become constants,

$$\chi_\perp(E) = \chi_\parallel(E) = \varphi_\perp(E) = \varphi_\parallel(E) = 1.$$

6. CALCULATION OF THE MOBILITY

It is known [13] that the mobility of quasi-2D electrons in the lowest miniband of the SL can be represented as

$$\begin{aligned}\mu_{xx} &= \mu_{yy} = \mu_\perp = e\langle\tau_\perp\rangle/m_\perp,\\ \mu_{zz} &= \mu_\parallel = e\langle\tau_\parallel\rangle/\langle m_\parallel\rangle,\end{aligned} \tag{24}$$

where $\langle\tau_\perp\rangle$, $\langle\tau_\parallel\rangle$, and $\langle m_\parallel\rangle$ are the transverse relaxation time, the longitudinal relaxation time, and the longitudinal effective mass, respectively, averaged over the energy of the transverse motion. For nondegenerate electron gas, taking (20), (21) into account, we obtain

$$\langle\tau_\perp\rangle = \int_0^\infty \tau_\perp(x)\mathrm{e}^{-x}x\,dx = \tau_0\int_0^\infty \chi_\perp^{-1}(x)\mathrm{e}^{-x}x\,dx, \tag{25}$$

$$\langle\tau_\parallel\rangle = \int_0^\infty \tau_\parallel(x)\mathrm{e}^{-x}\,dx = \tau_0\int_0^\infty \chi_\parallel^{-1}(x)\mathrm{e}^{-x}\,dx, \tag{26}$$

$$\frac{1}{\langle m_\parallel\rangle} = \frac{\Delta^2 d^2}{2\hbar^2 k_0 T}, \tag{27}$$

where $x = E/k_0T$ and Δ is the width of the lowest miniband of the SL conduction band in the approximation of weakly interacting QWs.

7. ANALYSIS OF THE RESULTS OF THE CALCULATION

Numerical calculation of electron relaxation for scattering by acoustic phonons was performed for the

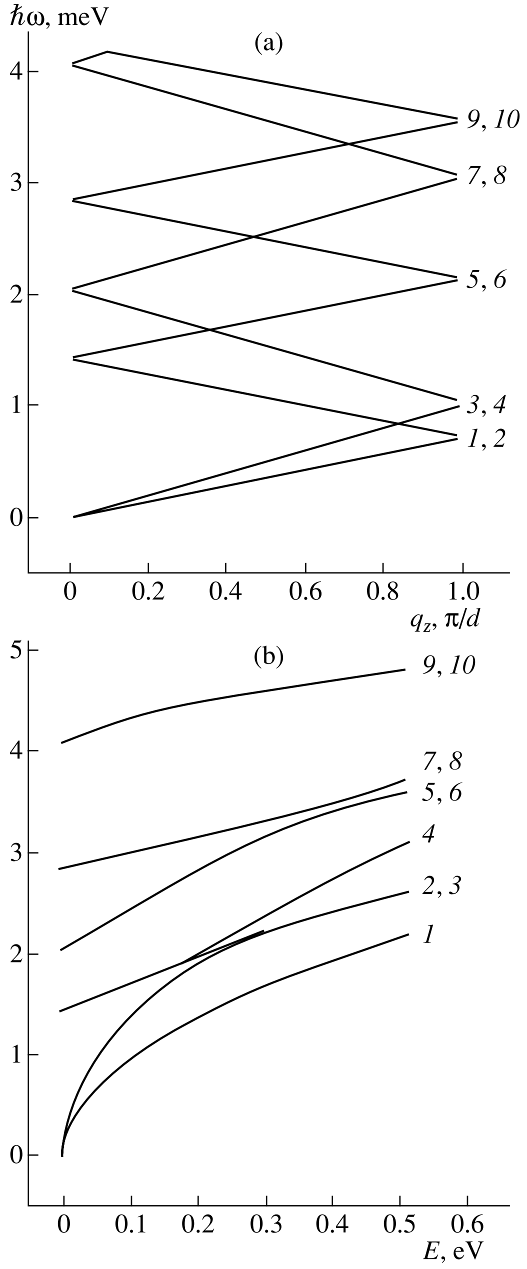

Fig. 1. Dispersion of the acoustic phonon energy $\hbar\omega$ in superlattices shown (a) as a function of q_z at $q_\perp = 0$ and (b) as a function of $E = \hbar^2 q_\perp^2/2m_\perp^*$ at $q_\| = 0$; (*1*–*10*) are the numbers of the lowest minimodes of acoustic phonons.

isoperiodic GaAs/$Al_{0.35}Ga_{0.65}As$ SL in the approximation of elastic scattering and nondegenerate quasi-2D electron gas in the lowest miniband. We used the following parameters for the calculation of the frequency spectrum and displacements corresponding to acoustic phonons in the isotropic-continuum approximation [15]: $c_{11a} = 12.21 \times 10^{10}$ N/m^2, $c_{44a} = 5.99 \times 10^{10}$ N/m^2, and $\rho_a = 5.36$ g/cm^3 for GaAs; $c_{11b} = c_{11a} + 0.14x$, $c_{44b} = c_{44a} - 0.05x$, and $\rho_b = \rho_a - 1.6x$ for the GaAs/$Al_xGa_{1-x}As$ alloy. The transverse effective mass was assumed to be equal to the electron effective mass in GaAs, $m_\perp^* = 0.067m_0$. Figures 1a and 1b show the energy spectra of the ten lowest minimodes of acoustic phonons for a symmetric SL with $a = b = 5$ nm. Because of the small difference in the parameters of gallium arsenide and the alloy that describe the elastic properties of single crystals, the calculated spectra differ only slightly from the spectra of bulk isotropic crystals, with the velocities of longitudinal and transverse vibrations averaged according to the formula

$$v_i = \frac{v_{ia}\rho_a a + v_{ib}\rho_b b}{\rho_a a + \rho_b b}. \qquad (28)$$

Figure 2a shows the functions $\varphi_\perp(E)$ (curve *1*) and $\varphi_\|(E)$ (curve *2*) calculated using formulas (22) and (23). For the calculation of these functions, the total number of minimodes taken into account was 25. According to Fig. 2a, the quantum confinement of acoustic phonons appears as a weak dispersion and anisotropy of these functions of electron energy. The latter feature is absent in the approximation of a bulk spectrum of acoustic phonons. This dispersion gives rise to a weak dispersion and anisotropy of the longitudinal and transverse relaxation times determined by the functions $\chi_i(E)$ and to the temperature dependence of the relaxation time averaged over energy. Figure 3 shows the temperature dependences of the transverse (curve *1*) and longitudinal (curve *2*) relaxation times averaged over energy and calculated using formulas (25) and (26). In the temperature range $T = 77$–400 K, the times decrease steadily with increasing temperature.

Figures 2b and 2c show the dispersion of the functions $\varphi_i(E)$ calculated for an asymmetric SL with the parameters $a = 3$ nm, $b = 5$ nm and $a = 5$ nm, $b = 3$ nm, respectively. Calculation using the relaxation times averaged over energy shows that the quantities $\langle \chi_i^{-1} \rangle$ depend only slightly on the QW width and the potential barrier thickness in the range of parameters considered.

8. CONCLUSIONS

From an analysis of the results of our calculations, we can draw the following conclusions: (i) the effect of quantum confinement on the spectrum of acoustic phonons only slightly affects electron scattering in GaAs/$Al_xGa_{1-x}As$ SLs and gives rise to a slight decrease in scattering, a corresponding temperature dependence, and anisotropy of the relaxation time and mobility; (ii) disregarding these effects, we can describe well the electron scattering by acoustic phonons in SLs in the bulk phonon spectrum approximation.

These conclusions suggest that it is problematic to increase the electron mobility limited by phonon scattering via the effect of quantum confinement on polar scattering in low-dimensional GaAs/$Al_xGa_{1-x}As$ heterostructures in the room temperature region. This situation arises because, in contrast to bulk GaAs, electron

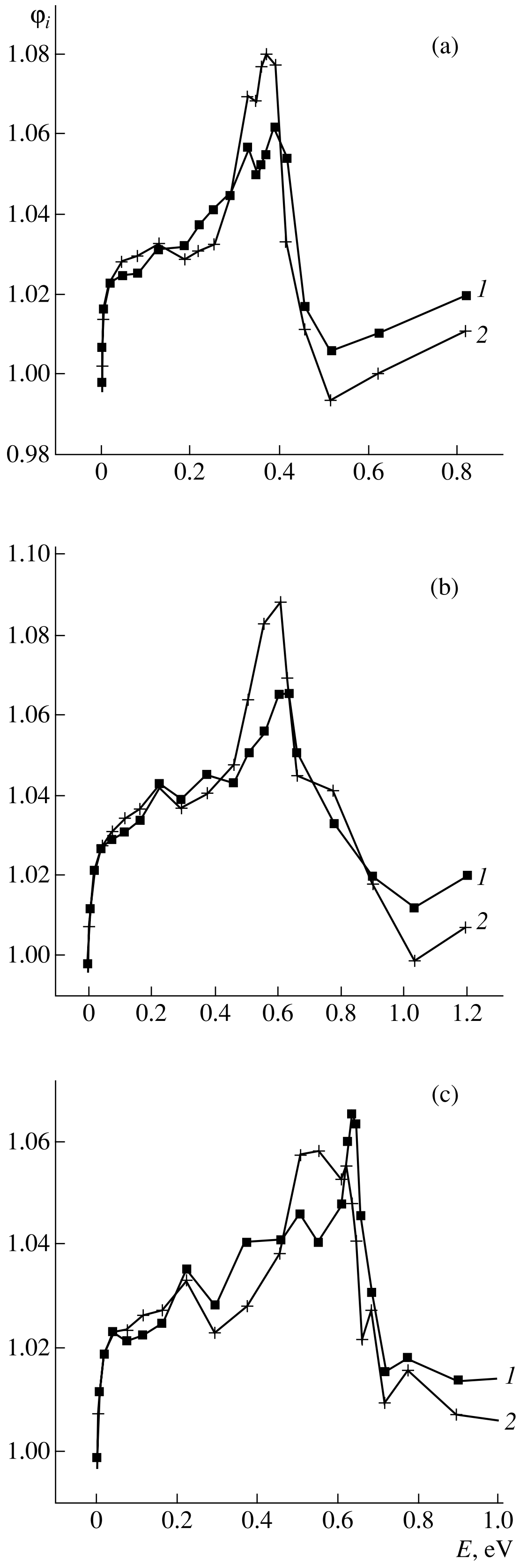

Fig. 2. Dispersion of the functions (*1*) $\varphi_\perp(E)$ and (*2*) $\varphi_\parallel(E)$. (a) a = 5 nm and b = 5 nm; (b) a = 3 nm and b = 5 nm; and (c) a = 5 nm and b = 3 nm.

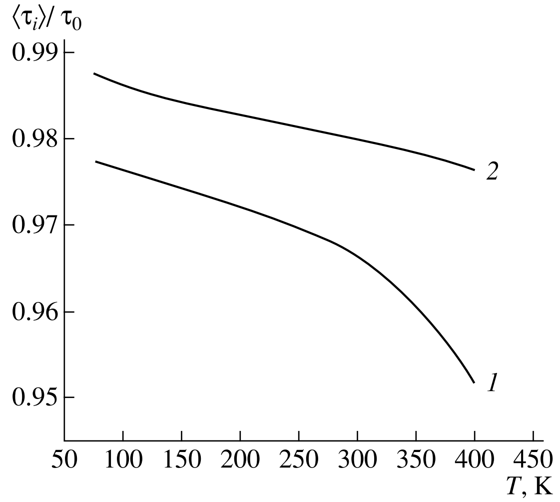

Fig. 3. Temperature dependence of the relaxation time averaged over energy for a = 5 nm and b = 5 nm: (*1*) $\tau_\perp/\tau_0$ and (*2*) $\tau_\parallel/\tau_0$.

scattering by acoustic phonons in the low-dimensional heterostructures considered can be dominant at room temperature due to quantum confinement of the electronic subsystem.

APPENDIX

A system of eight linear equations that make it possible to solve Eq. (1) is obtained from the boundary conditions and the Bloch theorem for the displacements and the normal component of the stress tensor. This system has the following form:

$$\frac{1}{\sqrt{\rho_1}}\sum_i e_{i1x}c_{i1} = \frac{1}{\sqrt{\rho_2}}\sum_i e_{i2x}c_{i2}, \tag{A.1}$$

$$\frac{1}{\sqrt{\rho_1}}\sum_i e_{i1z}c_{i1} = \frac{1}{\sqrt{\rho_2}}\sum_i e_{i2z}c_{i2}, \tag{A.2}$$

$$\begin{aligned}&\sqrt{\rho_1}v_{\perp1}^2\sum_i(q_\perp e_{i1z}+q_{i1}e_{i1x})\cdot c_{i1}\\ &= \sqrt{\rho_2}v_{\perp2}^2\sum_i(q_\perp e_{i2z}+q_{i1}e_{i2x})\cdot c_{i2},\end{aligned} \tag{A.3}$$

$$\begin{aligned}&\sqrt{\rho_1}\sum_i[q_\perp(v_{\parallel1}^2-2v_{\perp1}^2)e_{i1x}+q_{i1}v_{\parallel1}^2e_{i1z}]\cdot c_{i1}\\ &= \sqrt{\rho_2}\sum_i[q_\perp(v_{\parallel2}^2-2v_{\perp2}^2)e_{i2x}+q_{i2}v_{\parallel2}^2e_{i2z}]\cdot c_{i2},\end{aligned} \tag{A.4}$$

$$\frac{1}{\sqrt{\rho_1}}\sum_i e^{iq_{i1}a}e_{i1x}c_{i1} = \frac{e^{iq_zd}}{\sqrt{\rho_2}}\sum_i e^{-iq_{i2}b}e_{i2x}c_{i2}, \tag{A.5}$$

$$\frac{1}{\sqrt{\rho_1}}\sum_i e^{iq_{i1}a} e_{i1z}c_{i1} = \frac{e^{iq_zd}}{\sqrt{\rho_2}}\sum_i e^{-iq_{i2}b} e_{i2z}c_{i2}, \tag{A.6}$$

$$\begin{gathered}\sqrt{\rho_1}\,v_{\perp 1}^2\sum_i e^{iq_{i1}a}(q_\perp e_{i1z} + q_{i1}e_{i1x})\cdot c_{i1} \\ = e^{iq_zd}\sqrt{\rho_2}\,v_{\perp 2}^2\sum_i e^{-iq_{i2}b}(q_\perp e_{i2z} + q_{i1}e_{i2x})\cdot c_{i2},\end{gathered} \tag{A.7}$$

$$\begin{gathered}\sqrt{\rho_1}\sum_i e^{iq_{i1}a}[q_\perp(v_{\parallel 1}^2 - 2v_{\perp 1}^2)e_{i1x} + q_{i1}v_{\parallel 1}^2 e_{i1z}]\cdot c_{i1} \\ = e^{iq_zd}\sqrt{\rho_2} \\ \times\sum_i e^{-iq_{i2}b}[q_\perp(v_{\parallel 2}^2 - 2v_{\perp 2}^2)e_{i2x} + q_{i2}v_{\parallel 2}^2 e_{i2z}]\cdot c_{i2},\end{gathered} \tag{A.8}$$

where

$$c_i(z) = \begin{cases} c_{i1}, & 0 \le z < a \\ c_{i2}, & -b \le z < 0, \end{cases} \quad i = 1, \ldots, 4. \tag{A.9}$$

For $q_\perp = 0$, this system of equations can be separated into two independent 4×4 systems, one of which determines the spectra of longitudinal vibrations and the other, the spectra of transverse vibrations. These systems correspond to the solution of the well-known transcendental equation [16]

$$\begin{gathered}\cos(q_zd) = \cos\frac{\omega a}{v_{ia}}\cos\frac{\omega b}{v_{ib}} \\ -\frac{1}{2}\left(\frac{\rho_b v_{ib}}{\rho_a v_{ia}} + \frac{\rho_a v_{ia}}{\rho_b v_{ib}}\right)\sin\frac{\omega a}{v_{ia}}\sin\frac{\omega b}{v_{ib}}.\end{gathered} \tag{A.10}$$

Numerical methods are generally used to find nontrivial solutions to the above 8×8 system of equations, since the problem cannot be reduced to the solution of a simple equation of the (A10) type.

REFERENCES

1. B. K. Ridley, Phys. Rev. B **39**, 5282 (1989).
2. G. Q. Hai, F. M. Peeters, and J. T. Devreese, Phys. Rev. B **48**, 4666 (1993).
3. G. Q. Hai, F. M. Peeters, and J. T. Devreese, Phys. Rev. B **62**, 10572 (2000).
4. V. V. Bondarenko and F. F. Sizov, Phys. Low-Dimens. Semicond. Struct., Nos. 8–9, 123 (1995).
5. D. N. Mirlin and A. F. Rodina, Fiz. Tverd. Tela (St. Petersburg) **38**, 3201 (1996) [Phys. Solid State **38**, 1749 (1996)].
6. X. Zianni, C. D. Simserides, and G. P. Triberis, Phys. Rev. B **55**, 16324 (1997).
7. C. R. Bennett, M. A. Amato, N. A. Zakhleniuk, *et al.*, J. Appl. Phys. **83**, 1499 (1998).
8. J. Pozela, A. Namajunas, K. Pozela, and V. Jucience, Physica E (Amsterdam) **5**, 108 (1999).
9. B. A. S. Camacho, Phys. Status Solidi B **220**, 53 (2000).
10. K. Pozela, Fiz. Tekh. Poluprovodn. (St. Petersburg) **35**, 1361 (2001) [Semiconductors **35**, 1305 (2001)].
11. G. J. Warren and P. N. Butcher, Semicond. Sci. Technol. **1**, 133 (1986).
12. I. Dharssi and P. N. Butcher, J. Phys.: Condens. Matter **2**, 119 (1990).
13. S. I. Borisenko, Fiz. Tekh. Poluprovodn. (St. Petersburg) **36**, 861 (2002) [Semiconductors **36**, 808 (2002)].
14. N. Bannov, V. Aristov, V. Mitin, and M. A. Stroscio, Phys. Rev. B **51**, 9930 (1995).
15. Landolt–Börnstein, *Numerical Date and Functional Relationships in Science and Technology*, Ed. by O. Madelung (Springer, Berlin, 1987), New Ser. 3, Vol. 22a.
16. P. Y. Yu and M. Cardona, *Fundamentals of Semiconductors*, 3rd ed. (Springer, Berlin, 2001; Fizmatlit, Moscow, 2002).

Translated by I. Zvyagin

Semiconductors, Vol. 38, No. 7, 2004, pp. 830–832. Translated from Fizika i Tekhnika Poluprovodnikov, Vol. 38, No. 7, 2004, pp. 864–866.
Original Russian Text Copyright © 2004 by Gorskiĭ.

LOW-DIMENSIONAL SYSTEMS

Kapitsa Effect in Crystals with Superlattices

P. V. Gorskiĭ

Chernivtsi National University, Chernivtsi, 58000 Ukraine

Submitted November 20, 2003; accepted for publication December 23, 2003

Abstract—It is shown that the longitudinal Kapitsa effect in crystals with superlattices can be explained taking into account Landau quantization and its influence on carrier scattering by the deformation potential of acoustic phonons. Formulas for the Kapitsa coefficient are derived for various degrees of electron gas degeneracy. © *2004 MAIK “Nauka/Interperiodica”.*

For a long time there was no adequate physical interpretation of the linear relation between magnetic field and magnetoresistance (the Kapitsa effect, discovered in 1929) [1]. However, in 1972 Dreizin and Dykhne [2] showed that the Kapitsa law for polycrystalline samples can be derived by averaging the so-called polar diagram of the magnetoresistance of a single crystal, taking into account scattering at crystal boundaries in magnetic fields that are sufficiently high such that $(\Omega\tau)^{1/3} \gg 1$ (Ω is the cyclotron frequency and τ is the electron-momentum relaxation time). The polar diagram characterizes the dependence of the magnetoresistance on the rotation angle of the magnetic field vector in the plane perpendicular to the single-crystal symmetry axis. Previously, this fact was established experimentally by Alekseevskii and Gaidukov [3]. The possibility of observing the Kapitsa effect strongly depends on the relation between the radius of the cyclotron orbit of an electron and its free path limited by the crystallite boundaries.

However, such an interpretation of the Kapitsa effect is valid only in the quasi-classical approximation and only for transverse magnetoresistance. The longitudinal Kapitsa effect, which takes place simultaneously with the transverse effect, should not exist in this approximation. However, the longitudinal Kapitsa effect can be explained taking into account Landau quantization and its effect on carrier scattering, which is the subject of this study.

We consider the Kapitsa effect in crystalline superlattices in a configuration in which electric and magnetic fields are parallel to the superlattice C axis, which is perpendicular to the layers. We describe the carrier motion along the C axis using the tight-binding approximation and the motion in the direction normal to the C axis using the effective-mass method [4]. Therefore, the electron energy in a superlattice in the case of Landau quantization is written as

$$E_{nk_z} = \mu^* B(2n+1) + \Delta(1 - \cos ak_z), \qquad (1)$$

where n is the Landau level index; k_z is the quasi-momentum component along the C axis; B is the magnetic field; $\mu^* = \mu_B \frac{m_0}{m^*}$; μ_B is the Bohr magneton; m_0 is the free electron mass; m^* is the electron mass across the C axes; Δ is the half-width of the narrow conduction miniband for carrier motion along the C axis; and a is the distance between the translationally equivalent layers of the crystal, whose planes are perpendicular to the C axis.

When taking into account the effect of the magnetic field on carrier scattering, we assume that the magnetic field is sufficiently strong to suppress scattering-induced transitions between the Landau subbands. In this case, the following conditions must be satisfied for scattering by the lattice deformation potential:

$$k(T \le \mu^* B,) \qquad (2)$$

$$\Delta \le \mu^* B. \qquad (3)$$

If we set $m^* = 0.1m_0$ and $\Delta = 0.01$ eV [5], conditions (2) and (3) at $T = 88$ K [1] are satisfied for magnetic fields $B \ge 7$ T. However, when studying the dependence of the magnetoresistance of metals on magnetic field, Kapitsa dealt with magnetic fields of up to 30 T. It is shown in [6] that, if conditions (2) and (3) are satisfied, the relaxation time can be introduced when calculating the longitudinal resistance. Furthermore, this relaxation time can be considered inversely proportional to the density of electronic states per Landau subband in the magnetic field.

The corresponding proportionality factor was calculated in [6] for 0–0 intraband transitions. However, in the case of electron scattering by the lattice deformation potential, this factor is the same for all the n–n transitions in the two limiting cases corresponding to induced and spontaneous scattering. Which mechanism is dominant depends on the dimensionless parameter

$$\kappa = 2\left(\frac{\pi k T a_B}{hs}\right)^2,$$

1063-7826/04/3807-0830$26.00 © 2004 MAIK “Nauka/Interperiodica”

where T is the temperature, s is the averaged velocity of sound in the plane of the crystal layers, and

$$a_B = \left(\frac{h}{2\pi|eB|}\right)^{1/2}$$

is the magnetic length; the other notation is conventional. If $\kappa \gg 1$ or $\kappa \ll 1$, induced or spontaneous scattering is dominant, respectively. If $s = 5 \times 10^3$ m/s, it turns out that induced scattering is dominant at liquid-nitrogen temperature in fields below 30 T. In this case the monotonic part of the dependence of the crystal's conductance on the magnetic field can be described by (see [7])

$$\sigma_{zz}(B) = \frac{16\pi^2\tau_0 e^2 m^* a\overline{W}}{h^4 kT|\mu^* B|}\left\{\int\limits_{W(x)\le\zeta} dx|W'(x)|^3\right.$$

$$+\sum_{l=1}^{\infty}(-1)^l h_l^{\sigma}\left[\int\limits_{W(x)\le\zeta} dx|W'(x)|^3\exp\left(l\frac{W(x)-\zeta}{kT}\right)\right. \quad (4)$$

$$\left.\left.-\int\limits_{W(x)\ge\zeta} dx\left|W'(x)^3\right|\exp\left(l\frac{\zeta-W(x)}{kT}\right)\right]\right\},$$

$$h_l^{\sigma} = \frac{\mu^* Bl/kT}{\sinh(\mu^* Bl/kT)}. \quad (5)$$

In formula (4), $W(x) \equiv W(ak_z)$ is the carrier dispersion relation in the direction perpendicular to the layers, $W'(x)$ is the derivative, ζ is the chemical potential measured from the bottom of the miniband, τ_0 is a constant describing the scattering intensity in the crystal, and $\overline{W} = \Delta$ is the half-width of the miniband in the direction perpendicular to the layers. Integration in formula (4) is performed only over positive values of x. Using this formula and the dispersion relation (1), we consider the Kapitsa effect in crystals with superlattices. Using the relations from [6], we express τ_0 in terms of the deformation potential constant Ξ, the crystal density ρ, and the velocity of sound s in the plane of the layers.

First, when analyzing formula (4), we note that the dependence of the crystal resistivity on the magnetic field is linear if there is a high degree of degeneracy when $\zeta/\Delta \gg 1$, since in this situation the corrections to the term linear in B are exponentially small. We then obtain the final formula for ρ_{zz}:

$$\rho_{zz} = \frac{3\pi}{4}\frac{h\Xi^2 kT|\mu^* B|}{e^2\Delta^3\rho s^2 a^2}. \quad (6)$$

The second case takes place for carrier densities and temperatures such that $\zeta = \Delta$; i.e., the chemical potential lies in the middle of the allowed miniband. Then ρ_{zz} is obtained by doubling expression (6). In this case, the sum over l in (4) is identically equal to zero.

The third case corresponds to nondegenerate electron gas for which $\zeta < 0$ and $|\zeta|/kT \gg 1$. In this case, by also taking into account the effect of Landau quantization on the chemical potential, we obtain the final formula for the longitudinal magnetoresistance:

$$\rho_{zz} = \frac{\pi\Xi^2 B I_0\left(\frac{\Delta}{kT}\right)}{4n_0 a^3 e\rho s^2}\left(\Delta\cosh\frac{\Delta}{kT} - kT\sinh\frac{\Delta}{kT}\right)^{-1}, \quad (7)$$

where n_0 is the carrier density and $I_0(x)$ is the Bessel function of the imaginary argument. The transition to the effective mass approximation in this formula corresponds to a larger Δ/kT ratio. Then, taking into account the asymptotic form of the Bessel function $I_0(x)$ [8], we obtain the following asymptotic formula for the magnetoresistance:

$$\rho_{zz} \propto B\sqrt{T}. \quad (8)$$

The temperature dependence given by this formula is similar to the one that follows from the classical Drude model (only for the resistance without a magnetic field) [9]. However, in the case of classical statistics and the quadratic dispersion law of electrons, this model should yield correct results if the carrier scattering geometry is approximately one-dimensional, which it is in a strong quantizing magnetic field [10]. An additional condition for the validity of formula (4) for crystals with superlattices is $hs/2\pi a_B \ll \Delta$. Setting $s = 5 \times 10^3$ m/s and $\Delta = 0.01$ eV, we find that this condition can be violated only when $B \ge 6100$ T. Note that, if we consider collisions with impurities and/or point defects instead of electron–phonon collisions as the scattering mechanism, formula (4) would change such that the factor before the expression in the braces would no longer depend on the magnetic field and temperature, and the longitudinal resistance would level off with high fields. Hence, for both scattering mechanisms the dependence of the resistance on the magnetic field with sufficiently strong fields would be written as

$$\rho_{zz}(B) = \rho_i + KB, \quad (9)$$

where ρ_i is the part of the resistance related to impurities and K is the Kapitsa coefficient.

In a weak field, where the relaxation time may be considered independent of the magnetic field, the magnetoresistance is quadratically dependent on the magnetic field regardless of the scattering mechanism, since the factor h_l^{σ} (even in a magnetic field) is determined by the thermodynamic properties of the electron gas in a magnetic field rather than by fine details of the scattering mechanisms.

In conclusion, we summarize the conditions for observing the Kapitsa effect and estimate the Kapitsa coefficient for some materials. We note that, if $\Delta = 0.01$ eV and $m^* = 0.1m_0$, the observation of the Kapitsa effect requires magnetic fields greater than 10 T. If

$m^* = 0.01m_0$, fields higher than 1 T are required. In this case, the temperature can vary from 4.2 to 77 K. In some cases, i.e., when there are very small transverse effective masses of charge carriers, the effect can be observed even at room temperature. However, in this case, the interband transitions must be suppressed and the induced scattering must be dominant; i.e., conditions (2) and (3), as well as the condition $\kappa \gg 1$, must be satisfied. Then, in strongly degenerate semiconductors and semimetals, the Kapitsa coefficient can be determined using formula (6). For example, for $T = 4$ K, $\Xi = 1$ eV, $m^* = 0.01m_0$, $\Delta = 0.01$ eV, $\rho = 5 \times 10^3$ kg/m^3, $a = 10$ nm, and $s = 5 \times 10^3$ m/s, the Kapitsa coefficient is equal to 1.56×10^{-7} Ω cm/T, which corresponds to a carrier concentration of about 4.16×10^{16} cm^{-3} or higher. In nondegenerate layered semiconductors, the Kapitsa coefficient can be determined using formula (7). For the above values of the energy-band parameters and deformation potential, a carrier concentration of $n_0 = 10^{15}$ cm^{-3}, and a temperature of 88 K, the Kapitsa coefficient is 1.37×10^{-4} Ω cm/T. We note that, if the crystal band parameters are known, then by studying the longitudinal Kapitsa effect we can determine the amplitude of the deformation potential and, hence, the effective interaction responsible (according to the Bardeen–Cooper–Schrieffer theory) for the superconducting transition [11]. Thus, Kapitsa's assumption that the effect is related to superconductivity is confirmed, at least for the longitudinal effect. There is no such relation for the transverse effect in its conventional interpretation.

In addition, we can draw the following conclusion from the results of the calculation. If the Fermi surface of the crystal corresponds to a warped circular (elliptical) cylinder or ellipsoid, then the conditions of validity for the derived formulas and, hence, the observability of the longitudinal Kapitsa effect are best satisfied for electric and quantizing magnetic field orientations along the cylinder axis or the major axis of the ellipsoid.

REFERENCES

1. P. L. Kapitsa, *Strong Magnetic Fields* (Nauka, Moscow, 1988).
2. A. M. Dreĭzin and Yu. A. Dykhne, Zh. Éksp. Teor. Fiz. **63**, 242 (1972) [Sov. Phys. JETP **36**, 127 (1972)].
3. N. E. Alekseevskiĭ and Yu. P. Gaĭdukov, Zh. Éksp. Teor. Fiz. **35**, 554 (1958) [Sov. Phys. JETP **8**, 383 (1959)].
4. R. F. Fivaz, J. Phys. Chem. Solids **28**, 839 (1967).
5. F. G. Bass, A. A. Bulgakov, and A. P. Tetervov, *High-Frequency Properties of Semiconductors with Superlattices* (Nauka, Moscow, 1989).
6. V. F. Gantmakher and Y. B. Levinson, *Carrier Scattering in Metals and Semiconductors* (Nauka, Moscow, 1984; North-Holland, Amsterdam, 1987).
7. P. V. Gorskiĭ, Fiz. Nizk. Temp. **12**, 584 (1986) [Sov. J. Low Temp. Phys. **12**, 329 (1986)].
8. E. Jahnke, F. Emde, and F. Lösch, *Tables of Higher Functions*, 7th ed. (Teubner, Stuttgart, 1968; McGraw-Hill, New York, 1960; Nauka, Moscow, 1968).
9. C. Kittel, *Introduction to Solid State Physics*, 5th ed. (Wiley, New York, 1976; Nauka, Moscow, 1978).
10. A. M. Zlobin and P. S. Zyryanov, Zh. Éksp. Teor. Fiz. **58**, 952 (1970) [Sov. Phys. JETP **31**, 513 (1970)].
11. M. Cohen, G. Gladstone, M. A. Jensen, and J. R. Schrieffer, *Superconductivity*, Ed. by R. Parks (Marcel Dekker, New York, 1969; Mir, Moscow, 1972).

Translated by A. Kazantsev

Semiconductors, Vol. 38, No. 7, 2004, pp. 833–836. Translated from Fizika i Tekhnika Poluprovodnikov, Vol. 38, No. 7, 2004, pp. 867–871.
Original Russian Text Copyright © 2004 by Kryzhanovskaya, Gladyschev, Blokhin, Musikhin, Zhukov, Maksimov, Zakharov, Tsatsul'nikov, Ledentsov, Werner, Guffart, Bimberg.

Optical and Structural Properties of InAs Quantum Dot Arrays Grown in an $In_xGa_{1-x}As$ Matrix on a GaAs Substrate

N. V. Kryzhanovskaya*^, A. G. Gladyschev*, S. A. Blokhin*, Yu. G. Musikhin*,
A. E. Zhukov*, M. V. Maksimov*, N. D. Zakharov, A. F. Tsatsul'nikov*,**
N. N. Ledentsov*, P. Werner**, F. Guffart***, and D. Bimberg*****
**Ioffe Physicotechnical Institute, Russian Academy of Sciences, St. Petersburg, 194021 Russia*
^e-mail: kryj@mail.ioffe.ru
***Max-Planck Institut für Mikrostrukturphysik, Halle, Deutschland*
****Institut für Festkörperphysik, Technische Universität Berlin, Deutschland*

Submitted January 15, 2004; accepted for publication January 19, 2004

Abstract—Structural and optical properties of InAs quantum dots (QDs) deposited on the surface of a thick InGaAs metamorphic layer grown on a GaAs substrate have been studied. The density and lateral size of QDs are shown to increase in comparison with the case of QDs grown directly on a GaAs substrate. The rise of In content in the InGaAs layer results in the red shift of the photoluminescence (PL) line, so that with 30 at % indium in the metamorphic layer the PL peak lies at 1.55 μm. The PL excitation spectroscopy of the electronic spectrum of QDs has shown that the energy separation between the sublevels of carriers in QDs decreases as the In content in the InGaAs matrix increases. © *2004 MAIK "Nauka/Interperiodica".*

1. INTRODUCTION

The effect of the substrate material on the details of the formation of quantum dots (QDs) in the Stranski–Krastanow growth process is one of the most interesting and important problems in modern semiconductor technology. Despite significant progress in experimental [1] and theoretical [2] studies of the physics of self-organized formation of QDs, the dependences of density, lateral size, and height and shape of QDs on the lattice constant and surface energy of the substrate material are not clearly understood. Experimental study of these processes is hindered by the fact that only certain types of substrates are available. For example, the use of InGaAs substrates to grow structures in the InGaAs–InAlGaAs system has not become widespread. Furthermore, systematic experiments of this kind would require InGaAs substrates with a varied In content.

We recently demonstrated the possibility of growing thick InGaAs layers with quite high crystalline and optical quality on GaAs substrates [3–6]. To ensure the transition from the lattice constant of GaAs to that of the $In_xGa_{1-x}As$ layer, a metamorphic $In_xGa_{1-x}As$ buffer layer was deposited between them. In the growth of the $In_xGa_{1-x}As$ buffer, a special technique that reduces the density of dislocations was used [7], which provided a sufficiently low density of dislocations penetrating into the optically active region and high planarity of all the heterointerfaces. Thus, the stress-free $In_xGa_{1-x}As$ layer plays the role of the substrate material for further growth, and the In content in this layer can be varied in a wide range. This technique was used in [4], and 1.52 μm lasing was obtained in a laser based on QDs that were grown on a thick metamorphic $In_{0.2}Ga_{0.8}As$ layer on a GaAs substrate. We now report on a detailed study of the effect of the composition of an $In_xGa_{1-x}As$ ($0 \le x \le 0.30$) layer on which InAs QDs are grown on the density, size, shape, and energy spectrum of the QDs.

2. EXPERIMENTAL

The structures were MBE-grown on (100) *n*-GaAs substrates in a Riber 32P system with a solid-state As source. First, the intermediate 0.5-μm-thick $In_xGa_{1-x}As$ ($x = 0$–0.30) buffer layer intended for ensuring the transition from GaAs to InGaAs lattice constant was grown at a temperature of 400°C. The growth temperature was then raised to 500°C, and the active region of the structure was grown; it was a 0.2-μm-thick $In_xGa_{1-x}As$ layer (hereinafter the matrix) confined on both sides by $In_{0.2}Ga_{0.8}As/In_{0.2}Al_{0.8}As$ superlattices to prevent the leakage of carriers to the surface and the buffer layer. QDs were located in the middle of the $In_xGa_{1-x}As$ layer; their growth sequence was as follows. First, seed islands were formed by depositing 2.6 monolayers (ML) of InAs; then they were overgrown with an $In_yGa_{1-y}As$ ($y = x + 0.2$) layer with an effective thickness of 5 nm.

A study by transmission electron microscopy (TEM) in the diffraction-contrast mode was performed on a Philips CM microscope with a 100-kV acceleration voltage. Dark-field images of a structure were obtained in (200) reflection directed in parallel to the growth surface.

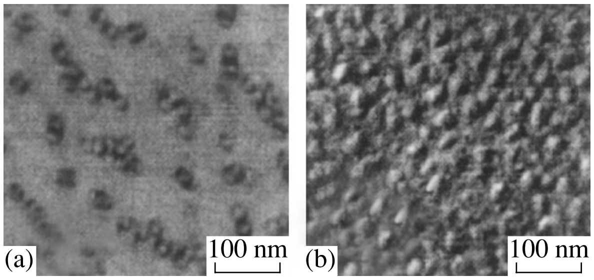

Fig. 1. Planar TEM images of QDs for structures with (a) GaAs and (b) $In_{0.2}Ga_{0.8}As$ matrices.

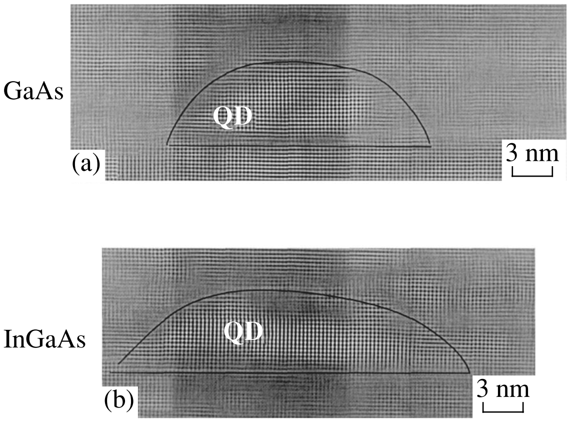

Fig. 2. Cross-sectional HRTEM images of QDs for structures with (a) GaAs and (b) $In_{0.2}Ga_{0.8}As$ matrices.

A JEM 4010 microscope with a 400-kV acceleration voltage was used for the high-resolution transmission electron microscopy (HRTEM). The Fourier filtration was applied in the analysis of the images obtained. In the reconstruction of images, (200) reflections and the transmitted beam were used.

Photoluminescence (PL) of the structures was excited by an Ar-ion laser (W = 1500 W/cm^2, λ = 514 nm) and studied in the temperature range 10–300 K. The PL excitation spectra were recorded under excitation from the light of a halogen incandescent lamp that was passed through a monochromator. The signal was detected using a monochromator and a cooled Ge diode.

3. RESULTS AND DISCUSSION

Figures 1a and 1b show TEM images of QD arrays grown on GaAs and $In_{0.2}Ga_{0.8}As$ surfaces, respectively. As can be seen from these figures, the surface density of QDs is significantly higher in the case of deposition on an $In_{0.2}Ga_{0.8}As$ layer than on GaAs. This increase in the QD density with a constant scatter in size is desirable and opens the way to attaining a higher gain on the ground state in QD lasers [8].

HRTEM data (Figs. 2a, 2b) showed that the growth of QDs on a metamorphic $In_xGa_{1-x}As$ layer also causes an increase in the lateral size of islands with the retention of their height. The lateral size is 19 nm for GaAs and 26 nm for the $In_{0.2}Ga_{0.8}As$ matrix (Figs. 2a and 2b, respectively). Note that RHEED patterns, which were recorded during the growth of the structure, indicate that the formation of QDs (the transition to 3D growth) occurs after the deposition of InAs with an effective thickness of 1.7 ML on a GaAs matrix and 1.5 ML for the case of $In_{0.2}Ga_{0.8}As$. Thus, in the latter case the formation of QDs consumes more material. One may assume that the increase in the density of QDs and their lateral size can be caused both by the activated decomposition of $In_xGa_{1-x}As$ with a high InAs content ($x = 0.4$) at the overgrowth stage and by possible segregation of In on the surface of the $In_xGa_{1-x}As$ buffer layer.

When the material of the matrix is changed from GaAs to $In_xGa_{1-x}As$, the PL line corresponding to the emission associated with the QD ground state (asterisked in the spectra) is red-shifted (Fig. 3). With a 30% InAs content in the matrix material, the PL peak lies at 1.55 μm. This shift of QD PL to lower energies may be caused by several factors. First, the decrease in compressive stress in QDs when the matrix material is changed lowers the energy of the bottom of the conduction band. Second, the increase in the lateral size of QDs also brings down the quantization levels. Furthermore, when the InAs content in the matrix material increases, the band gap of the matrix decreases, and, consequently, the penetration of carrier wave functions into the potential barrier is diminished; thus, the carrier levels in QDs are reduced. At the stage of QD overgrowth, the presence of a stressed $In_xGa_{1-x}As$ layer with large x (tensile-strained in the vertical direction and with lower elasticity) also depresses stress fields in InAs QDs and brings down the levels. All these effects can contribute to the red shift of the PL line [9].

When the InAs content in the matrix is less than 20%, no decrease in the integral efficiency of PL was observed up to high excitation densities, which is consistent with the localization of penetrating dislocations in the buffer layer. When the InAs content in the matrix is raised to over 25%, the PL intensity decreases; this is related to the partial penetration of residual dislocations from the buffer to the upper layers and to the formation of dislocated QDs in the overgrowth of initial islands with an InGaAs layer with a rather high (>45%) In content [10, 11]. Both effects are observed in TEM images of these structures.

The PL spectrum of a sample with QDs in an $In_{0.2}Ga_{0.8}As$ matrix recorded at high excitation density (Fig. 4, dashed line) demonstrates lines corresponding to ground and excited states, as well as the line of PL from a quantum well (QW) formed by the wetting layer and the $In_{0.4}Ga_{0.6}As$ layer used for overgrowth of the seed islands. The peak at 1.185 eV corresponds to the emission from the $In_{0.2}Ga_{0.8}As$ matrix. Owing to inhomogeneous broadening of the ensemble of QDs, it is difficult to determine precisely the peak energies in the

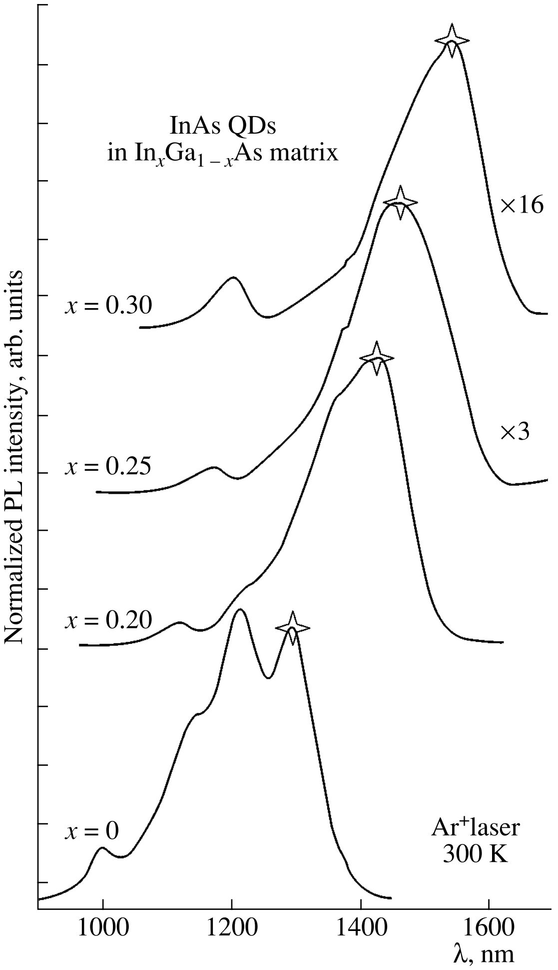

Fig. 3. Normalized PL spectra of InAs QDs deposited on In$_x$Ga$_{1-x}$As layers with different InAs contents (x).

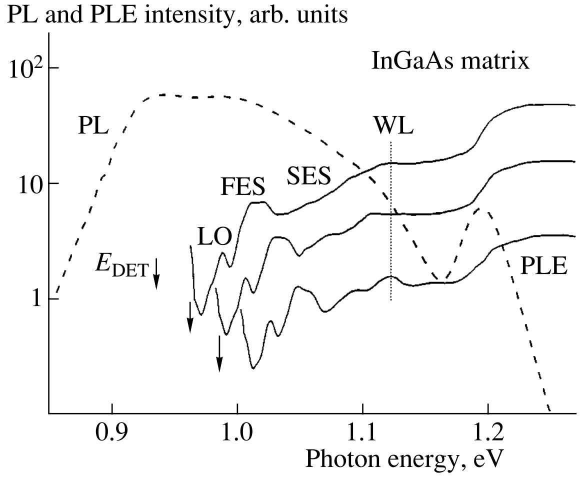

Fig. 4. PL spectrum of InAs QDs deposited on an In$_x$Ga$_{1-x}$As layer, recorded under excitation with an Ar laser (1.5 kW/cm^2) (dashed line). PL excitation spectra recorded at the detection energies E_{DET} = 0.94, 0.96, and 0.985 eV (solid line).

PL spectrum. A more detailed determination of the energies of optical transitions is possible when luminescence excitation spectroscopy is used, which makes it possible to study the relaxation and recombination processes in QDs with a definite energy of the ground state (to be more precise, in the ensemble of dots for which the ground state energy lies within the spectral resolution of the optical system, typically several millielectronvolts). Since lateral transport between QDs is absent at low temperatures, the PL excitation spectra recorded along the profile of a PL line contain information on the energy spectrum of QDs with different energies of the ground state, i.e. for QDs of different size.

Figure 4 shows PL excitation spectra recorded at the temperature T = 10 K at different detection energies E_{DET} = 0.94, 0.96, and 0.985 eV (marked with arrows). These excitation spectra exhibit peaks corresponding to absorption in the InGaAs matrix and in the QW formed by the wetting layer and covering the In$_y$Ga$_{1-y}$As layer (Fig. 4, WL) and the absorption associated with the excited states (Fig. 4, SES, FES). The complex structure of the peaks of the excited states can be explained based on the following considerations. As was shown theoretically in [12], several electron and hole levels exist in pyramidal-shaped InAs–GaAs QDs that are quite large. It is well known also that the degeneracy of levels in pyramidal QDs with a square base is completely removed by the Coulomb interaction and piezoelectric effect [12]. Therefore, a great number of levels appear in the QD energy spectrum, although the probabilities of optical transitions between some of these can be quite low (partially forbidden transitions). As a result, optical transitions with similar energies in the ensemble of QDs can behave as a single “effective transition,” and the absorption line of this “effective excited state” will be a superposition of inhomogeneously broadened lines of transitions involving the excited states with similar energies.

The peaks of separate transitions in PL excitation spectra, which lie within the limits of the “second effective excited state,” are resolved much worse. This may be related to the great number of these closely spaced transitions and to their stronger inhomogeneous broadening. Moreover, because of the possible fluctuations of the QD shape, several excited states may, in general, correspond to a single ground state.

Note that carrier relaxation processes must be considered in the interpretation of peaks in the PL excitation spectra [13]. The high relative intensity of peaks associated with certain excited states is caused by the fact that the energy difference between these states and the ground state is a multiple of the energy of longitudinal optical (LO) phonons, which facilitates the relaxation of carriers from these excited states [14]. In the case under study, the PL excitation spectrum also shows a peak related to the phonon relaxation; this peak is located 35 meV from the detection energy and corresponds to the LO phonon energy in the GaAs–InAs system.

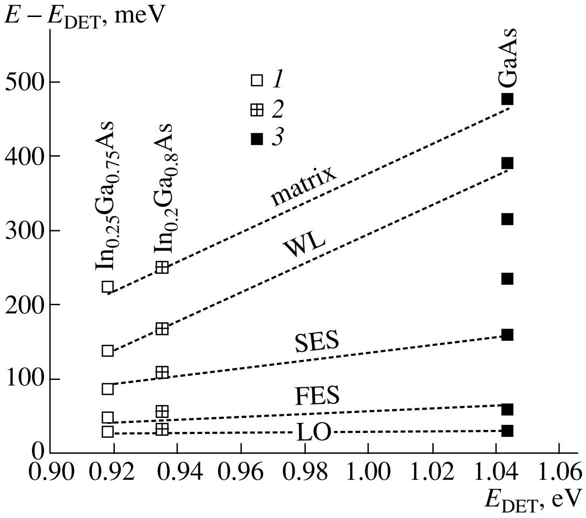

Fig. 5. Energies of peaks in the PL excitation spectra for QDs in (*1*) $In_{0.25}Ga_{0.8}As$, (*2*) $In_{0.2}Ga_{0.8}As$, and (*3*) GaAs matrices. For convenience, the detection energy E_{DET} is subtracted.

Figure 5 shows the energies of peaks in the PL excitation spectrum of QDs in $In_{0.25}Ga_{0.75}As$, $In_{0.2}Ga_{0.8}As$, and GaAs matrices; for convenience they are shifted by the detection energy. In all cases, the detection of the PL excitation spectra was performed at the energy of the PL peak corresponding to transitions from the QD ground state. It can be seen that, in the case of QDs deposited on InGaAs layers, the increase in the In content causes a decrease in the energy of carrier localization, defined as the difference between the matrix band gap and the energy of optical transition from the QD ground state. The energy separation between the energies of excited states and the ground state also decreases. This fact can be attributed to a decrease in the energy separation between the sublevels of electrons (holes) in a QD as its lateral size increases, while the number of sublevels seems to increase [15].

4. CONCLUSION

Structural and optical properties of InAs QDs in an $In_xGa_{1-x}As$ ($0 \le x \le 0.3$) matrix have been studied. The dots were formed on the surface of a thick $In_xGa_{1-x}As$ metamorphic layer grown on a GaAs substrate. The density and lateral size of QDs is higher when they are grown on an InGaAs metamorphic layer than when they are grown on GaAs. The height of dots remains approximately constant. The peak wavelength in the QD emission spectrum depends on the composition of the matrix material; it can be varied in a controlled manner from 1.3 μm (at $x = 0$) to 1.55 μm ($x = 0.3$), and a high efficiency of luminescence is retained. The energy spectrum of QDs was studied by means of PL excitation spectroscopy. When the InAs content in the matrix is increased, the localization energy of QDs (the difference between the energy of QD ground state and the matrix band gap) decreases, and the energy separation between the ground and excited states also decreases.

ACKNOWLEDGMENTS

This study was carried out as part of a joint project of the Ioffe Institute, Russian Academy of Sciences, and NSC-Nanosemiconductor-GmbH (Germany). N.V.K. acknowledges the support of the INTAS "Young Scientist Fellowship" program.

REFERENCES

1. D. Bimberg, M. Grundmann, and N. N. Ledentsov, *Quantum Dot Heterostructures* (Wiley, Chichester, 1999).
2. V. A. Shchukin, N. N. Ledentsov, and D. Bimberg, *Epitaxy of Nanostructures* (Springer, Berlin, 2004).
3. V. A. Odnoblyudov, A. Yu. Egorov, A. R. Kovsh, *et al.*, Fiz. Tekh. Poluprovodn. (St. Petersburg) (in press).
4. A. E. Zhukov, S. S. Mikhrin, E. S. Semenova, *et al.*, Fiz. Tekh. Poluprovodn. (St. Petersburg) **37**, 1143 (2003) [Semiconductors **37**, 1119 (2003)].
5. A. E. Zhukov, A. P. Vasil'ev, A. R. Kovsh, *et al.*, Fiz. Tekh. Poluprovodn. (St. Petersburg) **37**, 1461 (2003) [Semiconductors **37**, 1411 (2003)].
6. N. N. Ledentsov, F. R. Kovsh, A. E. Zhukov, *et al.*, Electron. Lett. **39**, 1126 (2003).
7. N. N. Ledentsov, U.S. Patent No. 6,653,166 (2003).
8. L. V. Asryan, M. Grundmann, N. N. Ledentsov, *et al.*, IEEE J. Quantum Electron. **37**, 418 (2001).
9. F. Guffarth, R. Heitz, A. Schliwa, *et al.*, Phys. Rev. B **64**, 85305 (2001).
10. B. V. Volovik, A. F. Tsatsul'nikov, D. A. Bedarev, *et al.*, Fiz. Tekh. Poluprovodn. (St. Petersburg) **33**, 990 (1999) [Semiconductors **33**, 901 (1999)].
11. M. V. Maximov, A. F. Tsatsul'nikov, B. V. Volovik, *et al.*, Phys. Rev. B **62**, 16671 (2000).
12. O. Stier, M. Grundmann, and D. Bimberg, Phys. Rev. B **59**, 5688 (1999).
13. N. N. Ledentsov, M. Grundmann, N. Kirstaedter, *et al.*, in *Proceedings of 22nd International Conference on Physics of Semiconductors, Vancouver, Canada, 1994*, Ed. by D. J. Lockwood (World Sci., Singapore, 1995), Vol. 3, p. 1855.
14. R. Heitz, O. Stier, I. Mukhametzhanov, *et al.*, Phys. Rev. B **62**, 11017 (2000).
15. N. N. Ledentsov, M. Grundmann, N. Kirstaedter, *et al.*, in *Proceedings of 7th International Conference on Modulated Semiconductor Structures* (Madrid, 1995); Solid-State Electron. **40**, 785 (1996).

Translated by D. Mashovets

Semiconductors, Vol. 38, No. 7, 2004, pp. 837–841. Translated from Fizika i Tekhnika Poluprovodnikov, Vol. 38, No. 7, 2004, pp. 872–876.
Original Russian Text Copyright © 2004 by Karachinsky, Novikov, Gordeev, Zegrya.

LOW-DIMENSIONAL SYSTEMS

Mechanism of Dicke Superradiance in Semiconductor Heterostructures

L. Ya. Karachinsky*, I. I. Novikov, N. Yu. Gordeev, and G. G. Zegrya
Ioffe Physicotechnical Institute, Russian Academy of Sciences, St. Petersburg, 194021 Russia
**e-mail: Karach@switch.ioffe.ru*

Submitted October 10, 2003; accepted for publication January 20, 2004

Abstract—Dicke superradiance is regarded as an intermediate phase in the transition from spontaneous to stimulated emission in semiconductor laser heterostructures. A phenomenological model that describes the formation of superradiant domains (“macrodipoles”) in the active region of heterostructures is suggested. It is shown that the characteristic emission time of these domains falls within the subpicosecond range. © *2004 MAIK “Nauka/Interperiodica”.*

1. INTRODUCTION

Recently, the resonance interaction of nonequilibrium carriers in semiconductor laser heterostructures via the electromagnetic field of their emission in recombination has attracted increasing interest [1–7]. Resonance processes of this kind, which have been well studied for solid-state and gas lasers, are called “Dicke superradiance” [8]. This effect is due to the small distance between radiative centers compared to the emission wavelength, and it appears in the generation of short pulses of coherent light, with the emission intensity proportional to the squared number of radiative centers involved in the process. The interest in this phenomenon is mainly due to the fact that it allows us to explain in terms of superradiance the results of various experiments that cannot be accounted for using the conventional concepts of how semiconductor lasers operate. It has been predicted theoretically that the phenomenon of superradiance can be used to generate ultrashort high-power pulses of electromagnetic radiation in different wavelength ranges and to develop semiconductor lasers based on indirect-bandgap semiconductors, such as silicon and germanium [9].

Measurements of the autocorrelation functions of the emission of dc-pumped injection lasers, performed using a high-sensitivity optical autocorrelator [10], demonstrated that superradiance pulses are formed both above and below the lasing threshold [11, 12]. Parameters of the superradiance pulses were estimated, and the upper bound to the duration of a superradiance pulse was found to be 400 fs.

We subsequently derived an analytical equation for the form-factor of the homogeneous broadening of the spectrum of laser heterostructures with the use of the simplest expressions of the theory of superradiance in two-level systems. Good agreement with the experimental data obtained by studying the electroluminescence from an InGaAs/GaAs quantum well (QW) laser heterostructure at 77 K has been observed [4–6, 13]. It has been shown that, for such a structure, the collective emission by carriers predominates even at room temperature at certain driving current densities. [5]. Studies of how the parameters of the emission spectra depend on driving current density and temperature made it possible to estimate the characteristic time of the collective interaction of carriers to be 20–35 fs in a wide range of temperatures and driving currents [4–6, 13].

An analytical expression for describing the inhomogeneously broadened emission spectrum of quantum dot (QD) structures has also been derived in terms of the theory of superradiance in two-level systems [6, 14]. This expression describes with high precision the experimental emission spectra of InGaAs/AlGaAs QD laser heterostructures, measured at 77 K in a wide range of driving current densities. The characteristic superradiance time, calculated from the experimental data using the analytical equation obtained, was found to be about 15 fs [6, 14].

Despite recent attempts (see, e.g., [2, 7]) to analyze theoretically the specific features of superradiance in semiconductor heterostructures, no rigorous theoretical model for describing phenomena of this kind has been suggested so far. The goal of this study was to construct a phenomenological model that would describe the appearance of superradiance in the active region of laser heterostructures and the subsequent evolution of superradiance processes.

2. THEORETICAL MODEL

Let us assume that the density of nonequilibrium carriers (electrons and holes) in the active region of a laser (in a QW) may fluctuate around some average value in the x direction (see figure). This can lead to the formation of domains with increased density of nonequilibrium carriers. In this case, the imaginary part of

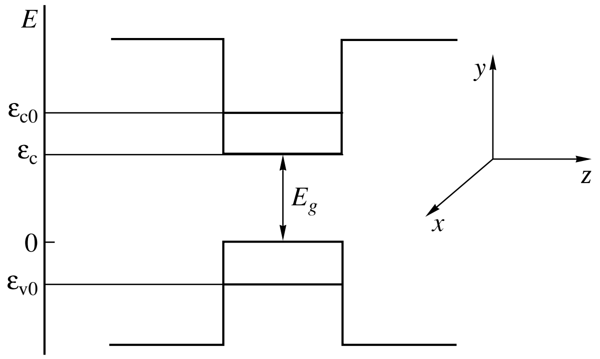

Band diagram of a laser heterostructure.

the dielectric susceptibility, Imχ, will be positive within a domain, negative outside it, and zero at its boundary. This will lead to localization of the electromagnetic field within the domains, because the dielectric constant within the domain will in this case exceed that in the outside (i.e., the domain is optically denser than its environment). Let us use the fact that χ depends on carrier density. Thus, to calculate the domain size, we need to write an equation for Imχ taking into account its dependence on the nonequilibrium carrier density and equate this expression to zero. The corresponding coordinate $x = x_0$ will be an estimate of the size of the domains formed. In our calculations, we will use the density matrix formalism [15].

Let us consider a domain. The polarization vector $P(t)$ is related to the single-particle density matrix operator ρ by the following expression [15]:

$$P(x, t) = eN(x)\sum_{mm'}\iint r_{m'm}(p, p')\rho_{mm'}(p, p', x, t)dpdp'. \tag{1}$$

Here e is the elementary charge; N, the 3D electron density; $r_{m'm}$, the dipole matrix element of the interband transition; and $\rho_{mm'}$, the matrix elements of the density matrix operator ρ.

We will consider below only four components of the density matrix: ρ_{vv} describes the state of an electron in the valence band, ρ_{cc} describes the state of an electron in the conduction band, ρ_{vc} describes a transition from the conduction band (state c) to the valence band (state v), and ρ_{cv} describes a transition from v to c. We will restrict our analysis to only direct interband transitions, when $r_{vv} = r_{cc} = 0$. The matrix element of an interband transition between electron and hole levels can be written as

$$r_{cv}(q_c, q_v) = r_{vc}(q_c, q_v) = r_{vc}(q)\delta_{q_c - q_v, 0}, \tag{2}$$

where q is the longitudinal momentum of carriers [$q = (q_y, q_x)$ and the z axis is perpendicular to the QW plane]. As a result, the expression for the polarization vector can be written as

$$P(x, t) = \frac{en(x)}{a}\int r_{vc}(q)[\rho_{vc}(q, x, t) - \rho_{cv}(q, x, t)]dq. \tag{3}$$

This expression takes into account only the ground states of electrons and holes. Here, $n(x)$ is the 2D electron density, and a is the QW width.

The off-diagonal components of the density matrix are found from the following system of equations:

$$i\hbar\frac{\partial\rho_{vc}}{\partial t} = \hbar\omega_{vc}\rho_{vc} - \frac{i\hbar}{T_{vc}}\rho_{vc} - eE[r, \rho]_{vc}, \tag{4}$$

$$i\hbar\frac{\partial\rho_{cv}}{\partial t} = \hbar\omega_{cv}\rho_{cv} - \frac{i\hbar}{T_{cv}}\rho_{cv} - eE[r, \rho]_{cv}, \tag{5}$$

where $\omega_{cv} = E_c - E_v/\hbar$; E_c and E_v are the energies of electrons and holes, respectively; and E is the strength of the electric field of the wave. As ρ is a Hermitian operator, it is necessary that the condition $T_{vc} = T_{cv} = \tau$ be satisfied. The constant τ, named the time of transverse dipole relaxation, is related to the line width of the optical transition. To solve Eqs. (4) and (5) for ρ_{cv} and ρ_{vc}, we use the approximation of the first harmonic of the electromagnetic field. As a result, we have

$$\rho_{vc}(q, x, t) = -\frac{e}{\hbar}D(q, x)\frac{r_{vc}(q)Ee^{i\omega t}}{\omega_{vc} - \omega - i/\tau}, \tag{6}$$

$$\rho_{cv}(q, x, t) = -\frac{e}{\hbar}D(q, x)\frac{r_{cv}(q)Ee^{i\omega t}}{\omega_{cv} - \omega - i/\tau}, \tag{7}$$

where $D(q) = \rho_{cc} - \rho_{vv}$ is the difference of the occupancies of levels in the conduction and valence bands. Let us rewrite D in terms of the distribution functions of electrons in the conduction and valence bands, f_c and f_v, respectively:

$$D(q, x) = \frac{2}{(2\pi)^2 n(x)}[f_c(q, x) - f_v(q, x)]. \tag{8}$$

We now use the definition of the dielectric susceptibility χ:

$$P(x, t) = \chi(x, \omega)E. \tag{9}$$

The imaginary part of the dielectric susceptibility can be expressed in terms of the dielectric constant as follows:

$$\varepsilon''(x, \omega) = 4\pi\mathrm{Im}\chi(x, \omega).$$

The gain coefficient $g(x, \omega)$ is related to $\varepsilon''(x, \omega)$ by the expression [16]

$$g(x, \omega) = -\frac{\omega}{c}\frac{\varepsilon''}{\sqrt{k_0}}, \tag{10}$$

where k_0 is the static dielectric constant. If we substitute the expression for $\varepsilon''(x, \omega)$ into (10) and use relations (3) and (6)–(8), we obtain the following expression for the gain coefficient $g(x, \omega)$:

$$g(x, \omega) = \frac{16\pi}{\sqrt{k_0}} \frac{e^2}{\hbar c} \frac{\hbar\omega}{a}$$

$$\times \int \frac{d^2 q}{(2\pi)^2} (r_{cv} e)^2 [f_c(q, x) - f_v(q, x) - 1] \tag{11}$$

$$\times \frac{\delta_\tau}{(E_c - E_v - \hbar\omega)^2 + \delta_\tau^2},$$

where $\delta_\tau = \hbar/\tau$. In (11), we take into account the fact that $f_v(x, q) = 1 - f_h(x, q)$, where $f_v(x, q)$ is the distribution function of electrons in the valence band. The dipole matrix element r_{cv} can be conveniently expressed as

$$r_{cv} = \frac{\int j_{cv} dx}{\hbar\omega}. \tag{12}$$

Here, j_{cv} is the probability flux density:

$$j_{cv} = i\gamma(u_c^* v_v + u_v v_c^*), \tag{13}$$

where $u(r)$ and $v(r)$ are the smooth envelopes of the Bloch functions of s and p type [15],

$$\gamma^2 \approx (\hbar/2m_c)E_g,$$

m_c is the electron effective mass, and E_g is the band gap.

After expression (1) is integrated, and taking into account

$$\frac{1}{\pi} \frac{\delta_\tau}{(E_c - E_v - \hbar\omega)^2 + \delta_\tau^2}\Bigg|_{\delta_\tau \to 0} \longrightarrow \delta_\tau(E_c - E_v - \hbar\omega), \tag{14}$$

the equality $\mathrm{Im}\chi = 0$ becomes equivalent to the following expression:

$$\frac{1}{\exp\left(-\frac{\tilde{\mu}_n}{T}\right) + 1} + \frac{1}{\exp\left(-\frac{\tilde{\mu}_p}{T}\right) + 1} - 1 = 0, \tag{15}$$

where $\tilde{\mu}_n = \mu_n - \varepsilon_{c0}$ and $\tilde{\mu}_p = \mu_p - \varepsilon_{v0}$ are the quasi-Fermi energies of electrons and holes, reckoned from the conduction and valence bands, respectively. From expression (15) we have

$$\tilde{\mu}_n + \tilde{\mu}_p = 0. \tag{16}$$

Let us assume that the electron–hole plasma in the domain is quasi-neutral. In this case, the 2D densities of electrons (n) and holes (p) in the QW are equal. They can be written as follows [17]:

$$n = N_c \ln\left[\exp\left(-\frac{\tilde{\mu}_n}{T}\right) + 1\right], \tag{17}$$

$$p = \frac{m_h}{m_c} N_c \ln\left[\exp\left(-\frac{\tilde{\mu}_p}{T}\right) + 1\right], \tag{18}$$

where $N_c = m_c T/\pi\hbar$ is the 2D density of states for the conduction band in the QW; m_c and m_h are the electron and hole effective masses, respectively; and T is temperature.

It should be noted that the degree of degeneracy of electrons in the QW is very high, whereas the degeneracy of holes is negligibly small. Taking this into account, we can simplify expressions (17) and (18) to obtain

$$\tilde{\mu}_n = \frac{\pi\hbar^2}{m_c} n, \tag{19}$$

$$\tilde{\mu}_p = T \ln\left(\frac{p\pi\hbar^2}{m_h T}\right). \tag{20}$$

Taking into account the quasi-neutrality of the electron–hole plasma in the domain and expressions (16), (19), and (20), we obtain the following condition for the equality of the gain coefficient $g(x, \omega)$ to zero:

$$\frac{\tilde{\mu}_n}{T} \exp\left(\frac{\tilde{\mu}_n}{T}\right) = \frac{m_h}{m_c}. \tag{21}$$

We should remember here that the electron density n depends on the coordinate x, i.e., $n = n(x)$. Substituting the explicit expression for $\tilde{\mu}_n$ in terms of density into (21), we obtain the final equation for finding x_0 at which the gain coefficient $g(x, \omega)$ becomes zero:

$$\frac{\pi \frac{\hbar^2}{m_c} n(x)}{T} \exp\left(\frac{\pi \frac{\hbar^2}{m_c} n(x)}{T}\right) = \frac{m_h}{m_c}. \tag{22}$$

Thus, we find x_0 and thereby estimate the size of domains with increased density of nonequilibrium carriers.

To determine the spatial distribution of the density of nonequilibrium carriers within the domain, we use the continuity equation. The domain is a region with increased density of nonequilibrium carriers, and this region has a finite size. It was shown in [18] that, if the strong degeneracy of electrons is taken into account in the case of bimolecular recombination (and holes are nondegenerate), the continuity equation takes the following form:

$$\frac{2}{3} \frac{\mu_h}{e} \frac{d}{dx}\left(\tilde{\mu}_n \frac{dN(x)}{dx}\right) = \frac{\gamma N^2(x)}{4}, \tag{23}$$

where μ_h is the hole mobility, $N(x)/2 = n(x)$, and γ is the coefficient of bimolecular recombination. This equation was derived using the condition for quasi-neutrality of the electron–hole plasma ($n = p$).

To solve Eq. (23) and find the dependence $n(x)$ within the domain, we make the following substitution of variables:

$$\xi = x N_{ch}^{1/2}, \tag{24a}$$

$$\psi = \frac{N(x)}{N_{ch}}. \tag{24b}$$

Here,

$$N_{ch} = \frac{3\gamma e m_c}{8\mu_h \pi \hbar^2}. \tag{25}$$

As a result, Eq. (23) takes the form

$$\frac{d}{d\xi}\left(\psi\frac{d\psi}{d\xi}\right) = \psi^2. \tag{26}$$

With (26) multiplied by $\frac{d\psi}{d\xi}$ and the total differential separated out, we obtain

$$\psi^2\left(\frac{d\psi}{d\xi}\right)^2 = \frac{1}{2}\psi^4 + C_1, \tag{27}$$

where C_1 is the integration constant. To find C_1, we use the boundary condition that the density of nonequilibrium electrons at the domain boundary is equal to the uniform density in the QW, which is known; i.e.,

$$\psi|_{\xi \to \xi_0} \longrightarrow \psi_0 = \frac{2n_0}{N_{ch}}, \tag{28a}$$

$$\xi_0 = x_0 N_{ch}^{1/2}, \tag{28b}$$

where n_0 is the "background" density of nonequilibrium electrons, which is determined by the driving current, and ξ_0 and x_0 are the domain boundaries in the new and old variables, respectively. Since $\frac{d\psi_0}{d\xi} = 0$, expression (27) yields the first integration constant C_1 as

$$C_1 = -\frac{1}{2}\psi_0^4. \tag{29}$$

We now solve Eq. (27) for ψ and obtain

$$\psi = \left\{\frac{\exp[-\sqrt{2}(\xi + C_2)] + \psi_0^4 \exp[\sqrt{2}(\xi + C_2)]}{2}\right\}^{1/2}, \tag{30}$$

where C_2 is the integration constant. To find C_2, we use the condition that the dependence of the density of nonequilibrium carriers on the coordinate should have a maximum at the center of the domain (at $\xi = 0$) and then decay toward the domain boundaries. This condition is expressed as

$$\left.\frac{d\psi}{d\xi}\right|_{\xi = 0} = 0.$$

After the derivative of expression (30) with respect to the variable ξ is taken and the second boundary condition is used, we obtain the following expression for finding C_2:

$$\psi_0^4 e^{\sqrt{2}C_2} - e^{-\sqrt{2}C_2} = 0. \tag{31}$$

From (31) we readily find that

$$C_2 = -\sqrt{2}\ln\psi_0. \tag{32}$$

Let us revert to the initial variables. When we use expressions (24a), (24b), (28a), and (32), as well as the fact that $n(x) = N(x)/2$, we obtain the expression for the density of nonequilibrium electrons within the domain as a function of the coordinate x:

$$n(x) = \frac{N_{ch}}{2\sqrt{2}}\left\{\exp[-\sqrt{2}(xN_{ch}^{1/2} - \sqrt{2}\ln\psi_0)] + \left(\frac{2n_0}{N_{ch}}\right)^4 \exp[\sqrt{2}(xN_{ch}^{1/2} - \sqrt{2}\ln\psi_0)]\right\}^{1/2}. \tag{33}$$

We now substitute (33) into (22) and numerically solve the resulting equation for x for the case of an $\mathrm{In_{0.15}Ga_{0.85}As}$ QW 100 Å thick. For this purpose, we use the following values of the numerical parameters:

$$m_c = 0.515 \times 10^{28}\ \mathrm{g}, \quad m_h = 4.505 \times 10^{-28}\ \mathrm{g},$$

$$T = 0.026\ \mathrm{eV}, \quad \gamma = 3 \times 10^{-4}\ \mathrm{cm^2\ s^{-1}},\ \text{and}$$

$$\mu_h = 200\ \mathrm{cm^2/(V\ s)}.$$

The background density of electrons (equal to that of holes) $n_0 = 10^{12}$ cm^{-2}. The numerical calculations indicate that Eq. (10) is satisfied when $x \approx 0.5$ μm. The doubled value of x_0 (1 μm) is the estimate of the size of a domain with an increased density of nonequilibrium carriers, which may be formed in the active region of the heterostructure as a result of carrier density fluctuations. The size we obtained can in turn be used to estimate the characteristic emission time of such a domain.

3. DISCUSSION

The above analysis shows that, as the density of nonequilibrium carriers in the active region of a heterostructure increases, the system breaks down into domains after a certain critical value is reached (n_0 in the case in question), and a nonequilibrium second-order phase transition thereby occurs. The domains are stable objects that have a characteristic mesoscopic size, which depends only on the parameters of the semiconductor, as was established above. Each domain is a QW region in which the emission is localized because the dielectric constant within the domain exceeds that in the outside. The domain is an optically denser medium because the imaginary part of the dielectric constant is positive within the domain and equal to zero at its boundary. This means that a kind of "feedback" arises within a single domain, and as a result the domain emits coherent light as a single whole (all emitters within the domain are in phase). At the same time, the total emission of the laser heterostructure below the lasing threshold remains incoherent, because the domains in the active region are not in phase with one another.

Thus, we considered the process of spontaneous formation of coherently emitting domains in the active region of a semiconductor laser. The distinctive feature of the "Dicke superradiance" is the spontaneous phasing of emitting carriers without any external coherent action on the system [19]. It is reasonable to assume that the recombination of nonequilibrium carriers in the domains formed occurs precisely in the superradiant mode. On the basis of this assumption, let us estimate the characteristic emission time typical of domains of this kind. For this purpose, we use the criterion that relates the maximum size of the superradiant region, $L_{\max}$, to the characteristic superradiance time, τ_{SR} (see, e.g., [19]):

$$L_{\max} = V\tau_{SR}, \tag{34}$$

where V is the speed of light within the material. If we substitute the previously obtained estimate of the size of the domain with an increased density of nonequilibrium carriers and the speed of light within the material, $V = 0.97 \times 10^{10}$ cm/s, into expression (34), we estimate the characteristic superradiance time to be $\tau_{SR} = 10$ fs. Note that this value agrees well with the previously obtained experimental estimates [4–6, 13].

As the density of nonequilibrium carriers increases further, the concentration of domains in the active region of the semiconductor laser (n_d) increases and, at a certain density of nonequilibrium carriers, the domains start to overlap. This occurs when the condition $n_d^{1/3} 2x_0 \approx 1$ is satisfied. In this case, a phase transition from superradiant to stimulated emission takes place.

4. CONCLUSION

Dicke superradiance was analyzed as an intermediate phase in the transition from spontaneous to stimulated emission in semiconductor laser heterostructures. A phenomenological model is suggested that describes the formation of superradiant domains ("macrodipoles"), in which the electromagnetic field is localized, in the active region of the heterostructures. The size of domains of this kind was estimated using the density matrix formalism, which made it possible to evaluate the characteristic emission time of these domains to be about 10 fs. This value agrees well with the results of previous autocorrelation and spectral experiments, which further supports the model suggested. In our next paper, we will present the electromagnetic theory of superradiance, which will make it possible to estimate not only the characteristic superradiance time, but also the intensity of superradiance and its delay time.

ACKNOWLEDGMENTS

This study was supported by the Russian Foundation for Basic Research (grant nos. 01-02-17764, 04-07-90148, and 04-07-16786), the Russian Academy of Sciences, and the Ministry of Industry, Science, and Technology of the Russian Federation. L.Ya.K. thanks INTAS for financial support (grant YSF no. 2001/2-97), and L.Ya.K. and I.I.N. gratefully acknowledge the financial support of the Dinastiya Foundation and the Moscow International Center for Basic Physics.

REFERENCES

1. P. P. Vasil'ev, H. Kan, H. Ohta, and T. Hiruma, Phys. Rev. B **64**, 195209 (2001).
2. A. A. Belyanin, V. V. Kocharovsky, Vl. V. Kocharovsky, and D. S. Pestov, Proc. SPIE **4605**, 356 (2001).
3. A. I. Klimovskaya, Yu. A. Driga, E. G. Gule, and O. A. Pikaruk, Fiz. Tekh. Poluprovodn. (St. Petersburg) **37**, 706 (2003) [Semiconductors **37**, 681 (2003)].
4. S. V. Zaitsev, N. Yu. Gordeev, L. Ya. Karachinsky, *et al.*, Jpn. J. Appl. Phys. **38**, 4772 (1999).
5. S. V. Zaĭtsev, N. Yu. Gordeev, L. A. Graham, *et al.*, Fiz. Tekh. Poluprovodn. (St. Petersburg) **33**, 1456 (1999) [Semiconductors **33**, 1309 (1999)].
6. S. V. Zaitsev, N. Yu. Gordeev, L. Ya. Karachinsky, *et al.*, Appl. Phys. Lett. **76**, 2514 (2000).
7. P. P. Vasil'ev, Kvantovaya Élektron. (Moscow) **29**, 4 (1999).
8. R. H. Dicke, Phys. Rev. **93**, 99 (1954).
9. A. A. Belyanin, I. G. Kalugin, V. V. Kocharovskiĭ, and Vl. V. Kocharovskiĭ, Izv. Ross. Akad. Nauk, Ser. Fiz. **63**, 369 (1999).
10. A. M. Georgievskiĭ and S. V. Zaĭtsev, Prib. Tekh. Éksp. **39**, 132 (1996).
11. S. V. Zaitsev and A. M. Georgievski, in *Proceedings of International Conference of SPIE on Optical Diagnostics of Materials and Devices for Opto-, Micro-, and Quantum Electronics* (Kiev, Ukraine, 1995), p. 319.
12. S. V. Zaĭtsev and A. M. Georgievskiĭ, Fiz. Tekh. Poluprovodn. (St. Petersburg) **32**, 366 (1998) [Semiconductors **32**, 332 (1998)].
13. A. M. Georgievskiĭ, S. V. Zaĭtsev, N. Yu. Gordeev, *et al.*, Fiz. Tekh. Poluprovodn. (St. Petersburg) **33**, 847 (1999) [Semiconductors **33**, 779 (1999)].
14. N. Yu. Gordeev, S. V. Zaĭtsev, V. I. Kopchatov, *et al.*, Pis'ma Zh. Tekh. Fiz. **26** (6), 78 (2000) [Tech. Phys. Lett. **26**, 259 (2000)].
15. G. G. Zegrya, in *Antimonide Related Strained Layer Heterostructures*, Ed. by M. O. Manasreh (Gordon and Breach, Neward, 1997).
16. G. G. Zegrya and N. A. Gun'ko, Fiz. Tekh. Poluprovodn. (St. Petersburg) **32**, 843 (1998) [Semiconductors **32**, 749 (1998)].
17. A. S. Polkovnikov and G. G. Zegrya, Phys. Rev. B **58**, 4039 (1998).
18. B. L. Gel'mont, V. A. Elyukhin, G. G. Zegrya, *et al.*, Fiz. Tekh. Poluprovodn. (Leningrad) **20**, 2061 (1986) [Sov. Phys. Semicond. **20**, 1289 (1986)].
19. A. Allen and J. H. Eberly, *Optical Resonance and Two-Level Atoms* (Wiley, New York, 1975; Atomizdat, Moscow, 1978).

Translated by M. Tagirdzhanov

Semiconductors, Vol. 38, No. 7, 2004, pp. 842–848. Translated from Fizika i Tekhnika Poluprovodnikov, Vol. 38, No. 7, 2004, pp. 877–883.

Manifestation of Size-Related Quantum Oscillations of the Radiative Exciton Recombination Time in the Photoluminescence of Silicon Nanostructures

A. V. Sachenko*, Yu. V. Kryuchenko*, I. O. Sokolovskiĭ*, and O. M. Sreseli**
**Lashkarev Institute of Semiconductor Physics, National Academy of Sciences of Ukraine, Kiev, 03028 Ukraine*
***Ioffe Physicotechnical Institute, Russian Academy of Sciences, Politekhnicheskaya ul. 26, St. Petersburg, 194021 Russia*
e-mail: Olga.Sreseli@mail.ioffe.ru

Submitted January 27, 2004; accepted for publication January 29, 2004

Abstract—The spectra of steady- and nonsteady-state photoluminescence in silicon nanostructures are calculated using the envelope-function method. The distinguishing feature of this calculation is that it takes into account an additional size-related quantum effect that manifests itself in the nonmonotonic (oscillatory) dependence of the time of radiative pseudodirect (phononless) exciton transitions on the nanocrystallite size. This is due to the oscillating overlap integral of the electron wave functions of the X valleys in the conduction band and the hole wave functions of the Γ valley in the valence band. The mesoscopic effect, which manifests itself in an appreciable broadening of the energy spectrum of small nanocrystals because of the fact that the fluctuations of both the structure of heteroboundaries and the atomic arrangement of nanocrystals become significant, is also taken into account. The potential application of this approach in interpreting experimental photoluminescence spectra in low-dimensional silicon is analyzed.

1. INTRODUCTION

It is now widely acknowledged that exciton radiative recombination in nanocrystallites (NCs) is the mechanism of photoluminescence (PL) in low-dimensional silicon. However, the existing theoretical models fail to describe many important features of the PL spectra in silicon NCs, such as the presence of several fundamental PL bands, the difference in their width in the short- and the long-wavelength spectral regions, the PL spectrum evolution in time, and so on.

In this study, we make a new attempt to simulate the PL characteristics of silicon nanostructures using the envelope-function method on the basis of the exciton recombination in NCs but now taking an additional effect into account. This effect stems from the indirect structure of the energy band of the initial silicon and gives rise to an oscillatory dependence of the exciton radiative lifetime on the size of NCs. It is shown that, in NCs of a certain size, this time can be fairly short (from several tens to several hundreds of nanoseconds). Therefore, even over a wide range of NC sizes, the main contribution to PL is made by NCs whose size corresponds to the shortest radiative recombination times. Since the size-related quantum effect relates a specific mean energy of radiative transitions to each size of NC, the PL spectra should contain only a few highly intense bands corresponding to comparatively narrow ranges of NC sizes. Note that, generally speaking, this mechanism should be effective in all low-dimensional silicon structures, from quantum wells to quantum dots. The differences that appear with a decrease in dimensionality are the following: (i) the PL bands shift toward short wavelengths, (ii) the oscillator strength of the pseudodirect (phononless) exciton transitions increases as a consequence of the increasing electron and hole localization in space, and (iii) the phonon-related broadening of the PL features becomes less pronounced because of the quantization of the phonon spectrum and the relative decrease in the fraction of radiative exciton transitions with the involvement of phonons.

Experimental steady-state PL spectra of silicon NCs most often appear as a single broad band. Two bands are observed much more rarely, and only in isolated rare cases are three bands observed. Therefore we expect to attain a better agreement with experiment by taking into consideration the mesoscopic broadening of the PL bands in small NCs as a result of an increase in the fluctuations of the atomic arrangement in the NC and at heteroboundaries and the corresponding smearing of the optical transitions within the NC ensemble.

Our aim is to study the PL steady-state spectra and the PL kinetics in relation to the exciton radiative lifetime, which oscillates with the size of the NC, and to analyze the effect of the mesoscopic broadening of the energy spectrum of small silicon NCs (their size D is mainly restricted to $D < 3$ nm).

2. THEORETICAL BACKGROUND

It has been shown [1] that the probability of radiative phononless exciton transitions in silicon NCs is an oscillating function of their characteristic size D. This behavior is a consequence of a change in the overlap integral of the wave functions of electrons in the *X* valley of the conduction band and holes in the Γ valley of the valence band; i.e., it is a consequence of the indirect character of the structure of the energy band in the initial silicon (in direct-gap semiconductors, no oscillations are observed). In terms of the model based on infinitely high barriers, the oscillation period is approximately 0.64 nm. In [2] the period of radiative phononless exciton transition τ_{rx} in silicon quantum wires surrounded by a SiO_x matrix was calculated as a function of their diameter *D* (see Fig. 1, inset). It can be seen that, with an increase in the degree of oxidation *x*, the oscillatory dependence $\tau_{rx}(D)$ shifts to larger thicknesses. The minima of τ_{rx} rapidly decrease as the wires become thinner. This behavior is caused by an increase in the degree of localization, which is equivalent to the increase in the degree of smearing of the wave functions of electrons in the *X* valley and holes in the Γ valley in reciprocal space and the resulting increase in the overlap integral (and, accordingly, in the probability of direct radiative phononless electron–hole recombination). In other words, the deepening of the minima is related to an increase in the probability that the excess electron momentum in the *X* valley will be transferred directly to the nanostructure as a whole (or that a hole in the Γ valley will acquire the excess momentum from the nanostructure) without the involvement of phonons. Phonons are known to ensure the conservation of momentum during the emission of radiation in indirect-gap bulk materials (including silicon) and, therefore, are involved in the formation of the radiative channel even in the zeroth order. The efficiency of this mechanism increases as the quantum wire becomes thinner.

Similar results for the matrix element of the radiative electron–hole transition and the radiative recombination time in porous silicon were obtained in [3].

Generally speaking, apart from the effect described above, which stems from dimensional quantization in the direction perpendicular to the quantum wire and from an increase in the contribution of states of appropriately oriented *X* valleys to pseudodirect transitions, one should also expect an increase in the contribution of longitudinal band states (along the wire) to the direct radiative process. This contribution is due to the rearrangement of the band structure in this direction as the wire thickness *D* decreases. For example, in threads with small *D*, the bottom of the one-dimensional conduction band must shift to the Γ point [4]. Both contributions that enhance the probability of direct radiative transitions were discussed in review [5]. Since this rearrangement of the band structure makes a monotonic contribution to the probability of direct radiative transitions with a decrease in *D*, it should smooth out the oscillations of the total time of radiative recombination $\tau_{rx}(D)$: the greatest smoothing corresponds to the region of the smallest *D*.

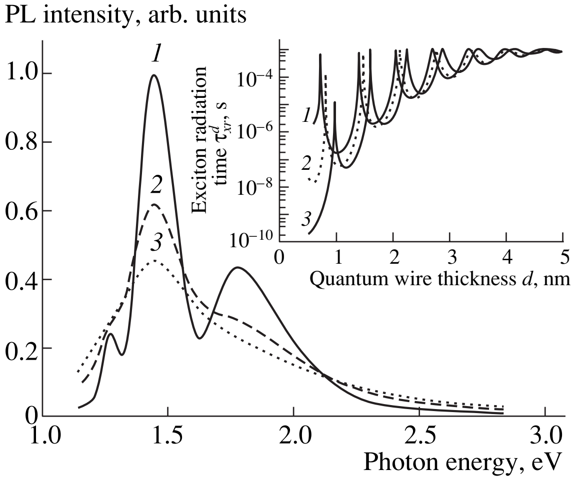

Fig. 1. Calculated steady-state PL spectra of nanostructures containing silicon quantum wires with an average transverse size of 2.1 nm. Calculation parameters: variance of wire thicknesses σ = 0.4 nm; broadening parameter Γ_0 = (*1*) 0.02, (*2*) 0.07, and (*3*) 0.12 eV. Curves in the inset are plotted for the barrier SiO_x layer with *x* = (*1*) 1.5, (*2*) 1.75, and (*3*) 2.

We restrict our theoretical analysis to the case of comparatively thin wires, when the exciton binding energy is large (≥0.3 eV) and it is possible to disregard the presence of free electron–hole pairs at room temperature, in accordance with the results obtained in [6]. The equation of generation–recombination balance for a wire with diameter *D* has the form

$$\frac{dn_x(D)}{dt} + \frac{n_x(D)}{\tau_x(D)} = cD^2 I[1 - \exp(-\alpha(D)L)], \quad (1)$$

where $n_x(D)$ is the total number of excitons in the quantum wire (exciton concentration integrated along the wire length *L*) in the lowest exciton subband; *I* is the radiation intensity; $\alpha(D)$ is the absorption coefficient; $c \approx 1$ is the form factor ($c = 1$ and $c = \pi/4$ for the quantum wires of square and circular cross sections, respectively); and $\tau_x(D)$ is the total lifetime of excitons in the wire:

$$1/\tau_x(D) = 1/\tau^d_{rx}(D) + 1/\tau^i_{rx}(D) + 1/\tau_{nx}(D).$$

Here, $\tau_{nx}(D)$ is the nonradiative lifetime of excitons and $\tau^d_{rx}(D)$ and $\tau^i_{rx}(D)$ are the characteristic times of radiative pseudodirect (without phonons) and indirect (with phonons involved) exciton transitions in the quantum wire, respectively.

In the steady state, the solution to equation (1) is expressed by the function

$$n_x(D) = cD^2 I[1 - \exp(-\alpha(D)L)]\tau_x(D), \quad (2)$$

whereas the intensity of the exciton luminescence at the corresponding exciton transition energy *E*(*D*) (the dependences *E*(*D*) were calculated in [1]) is given by

$$\Im_{PL}(E) = cD^2 I[1 - \exp(-\alpha(D)L)]\tau_x(D)/\tau_{rx}(D), \quad (3)$$

where $\tau_{rx}(D)$ is the total characteristic time of exciton radiative transition determined by the rule for the summation of reciprocal quantities:

$$1/\tau_{rx}(D) = 1/\tau^{i}_{rx}(D) + 1/\tau^{d}_{rx}(D).$$

On the assumption that a multimode ensemble of wires in an NC is described by the sum of Gaussian distributions in the vicinity of several main thicknesses $\bar{D}_i$ ($i = 1, 2, 3, \ldots n$) and that the individual PL lines have Lorentzian shapes, the spectral density of the exciton PL has the form

$$\begin{aligned} I_{PL}(E) &= \int \sum_{i=1}^{n} a_i \Im_{PL}(\xi) f_G(D(\xi), \bar{D}_i, \sigma_i) \\ &\quad \times \frac{\partial D}{\partial \xi} \frac{\Gamma(\xi)}{(E-\xi)^2 + \Gamma(\xi)^2/4} d\xi, \end{aligned} \tag{4}$$

where $f_G(D, \bar{D}_i, \sigma_i) = (1/\sqrt{2\pi}\sigma_i)\exp[-(D - \bar{D}_i)^2/2\sigma_i^2]$, a_i is the weighting coefficient of the respective Gaussian function, $\Gamma(\xi)$ is the broadening parameter that depends on the transition energy (i.e., on the quantizing size D), and the thickness D in the integrand is considered a function of the exciton transition energy, i.e., a function inverse to $E(D)$.

The relaxation kinetics of the intensity of a PL line with the energy $E(D)$ after a short (compared to the characteristic time $\tau_x(D)$) excitation pulse with duration t_i is defined by the expression

$$\begin{aligned} \Im_{PL}(E, t) &= cD^2 I[1 - \exp(-\alpha(D)L)][t_i/\tau_{rx}(D)] \\ &\quad \times \exp(-t/\tau_x(D)). \end{aligned} \tag{5}$$

With the size distribution of quantum wires given by function $f_G(D, \bar{D}, \sigma)$, the decay kinetics of the PL integrated intensity can be described as

$$\begin{aligned} I^{PL}_{\text{int}}(t) &= c \int_{D_{\min}}^{D_{\max}} (\xi^2 I[1 - \exp(-\alpha(\xi)L)] \\ &\quad \times \exp(-t/\tau_x(\xi)) t_i/\tau_{rx}(\xi)) f_G(\xi, \bar{D}, \sigma) \partial\xi. \end{aligned} \tag{6}$$

Similarly to expression (4), the spectral density of excitonic PL detected with the delay t_d after a short-pulse excitation of the ensemble of quantum wires can be written in the following form:

$$\begin{aligned} I_{PL}(E, t_d) &= \int \sum_{i=1}^{n} a_i \Im_{PL}(\xi, t_d) f_G(D(\xi), \bar{D}_i, \sigma_i) \\ &\quad \times \frac{\partial D}{\partial \xi} \frac{\Gamma(\xi) d\xi}{(E-\xi)^2 + \Gamma(\xi)^2/4}, \end{aligned} \tag{7}$$

where the quantity $\Im_{PL}(\xi, t)$ is defined by (5).

3. RESULTS AND DISCUSSION

Let us consider the effect produced by the oscillatory dependences $\tau_{rx}(D)$ on the PL spectra. When plotting the steady-state PL spectra, we used the dependence $\tau_{rx}(D)$ calculated in [2] for the case of quantum wires Si–SiO$_2$ and the dependence of the exciton transition energy on the wire thickness obtained in [1]. The case of strong absorption ($\alpha(D)L \gg 1$) was analyzed.

It follows from [4] that, when the size distribution of quantum wires is given by a single Gaussian function $f_G(D, \bar{D}, \sigma)$ with small width (e.g., $\sigma = 0.1$ nm), the steady-state PL spectrum appears as a narrow emission band. If the size distribution of wires is multimodal (for example, described by a set of narrow Gaussian functions) and the half-widths of the Γ lines in the exciton spectra of wires are small, each of the Gaussian distributions included in the set will correspond to a band in the PL spectrum. This mechanism is responsible for the formation of a multimodal PL spectrum if one disregards the oscillations of $\tau_{rx}(D)$. In terms of this approach, the bands broaden as the spread of the wire thickness increases, and they can begin to overlap, thus forming a single PL band with several peaks. However, the main feature of our approach, which takes into account the effect of $\tau_{rx}(D)$ oscillations, is that it allows the formation of several (up to three) PL bands in the spectrum even for a unimodal wire size distribution (for example, described by a Gaussian function with mean size $\bar{D} = 2$ nm).

Our calculations for wires with square and circular cross sections showed that, by varying D in the range 1–3.5 nm, we can obtain five main PL bands with energies in the intervals 1.15–1.17, 1.22–1.26, 1.38–1.45, 1.74–1.88, and 2.30–2.55 eV.

Note that a similar situation should take place for PL in a material containing quantum dots; i.e., as in the case with quantum wires, the main reason for the appearance of a multiband PL spectrum may be the presence of minima in the dependence $\tau_{rx}(D)$, which are caused by the indirect-gap structure of the initial silicon. Compared to the PL spectra of the silicon quantum wires, the PL spectra of quantum dots are shifted to shorter wavelengths. Our estimations based on the dependences of the electron–hole transition energy and the exciton binding energy in silicon quantum dots on their diameter obtained in [7, 8] showed that the PL spectrum of silicon quantum dots in the SiO$_2$ matrix may feature six bands located near 1.26, 1.34, 1.59, 2.06, 2.52, and 2.98 eV.

Let us compare the calculated energies of the main PL bands for silicon NCs with experimental data. The PL spectrum of porous silicon films obtained in [9–11] contained bands with energies 1.3–1.4, 1.7–1.9, 2.1, 2.3, and 2.9 eV. The PL spectrum of nanocrystalline silicon films (with nanocrystals in the form of quantum dots) detected in [12, 13] featured almost all of the bands mentioned above. Therefore, the experimental

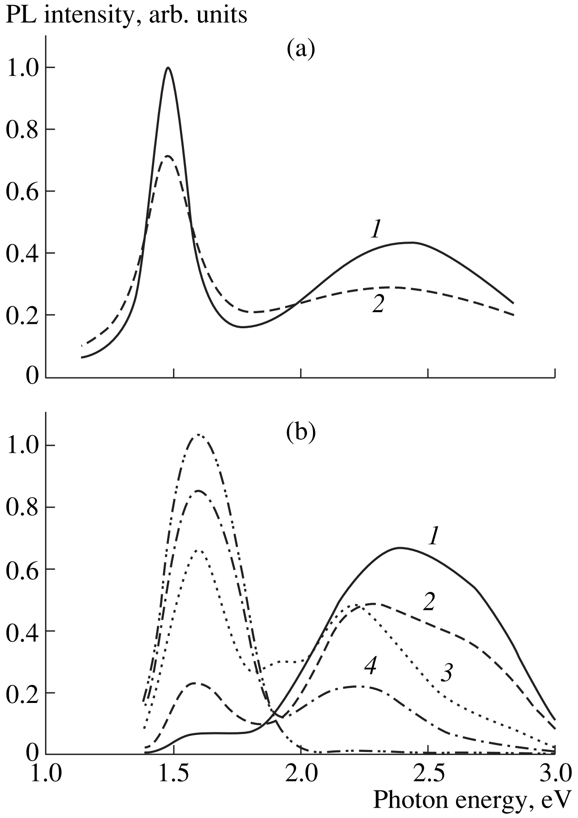

Fig. 2. Steady-state PL spectra of silicon nanostructures: (a) calculation by formula (4) for bimodal Gaussian distribution of wire thicknesses ($a_1 = 2.5$, $\overline{D}_1 = 1.2$ nm, $a_2 = 1.0$, $\overline{D}_2 = 2.1$ nm, and the same variance $\sigma = 0.1$ nm) with broadening parameter Γ_0 = (*1*) 0.04 and (*2*) 0.07 eV; (b) experimental data for different sizes of NC; the curves are numbered in order of increasing mean size of NCs.

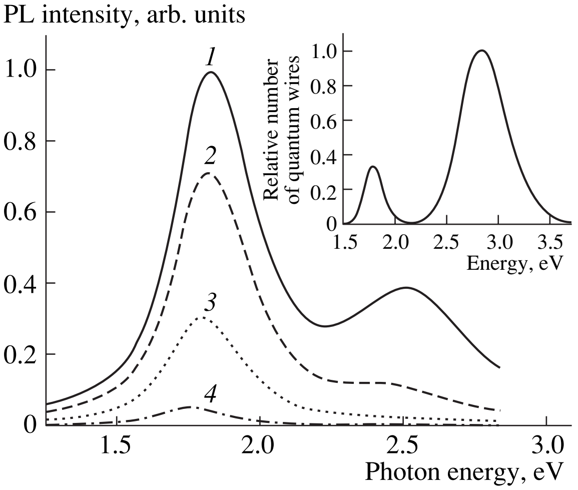

Fig. 3. Steady-state PL spectra of nanostructures containing a bimodal Gaussian distribution of silicon quantum wires; the spectra were calculated by formula (7) with different time delays t_d ($a_1 = 3.0$, $\overline{D}_1 = 1.0$ nm, $a_2 = 1.0$, $\overline{D}_2 = 1.7$ nm, and the same variance $\sigma = 0.1$ nm). Other calculation parameters: $\Gamma_0 = 0.07$ eV and time delay t_d = (*1*) 100, (*2*) 200, (*3*) 500, and (*4*) 1300 ns. The inset shows the energy distribution of exciton radiative transitions corresponding to the size distribution under consideration.

energies of transitions fall into the intervals calculated above for the main bands of silicon NCs, which arise because of the nonmonotonic dependence $\tau_{rx}(D)$. A number of the bands calculated above, in particular, the bands with energies 1.3–1.4, 1.92, 2.3, and 2.84 eV, were observed in the electroreflection spectra of silicon NCs [14, 15], while others (for example, the bands with energies 2.1 and 2.4 eV) were observed in the absorption spectra [16].

Note that, in order to compare the PL spectra and the absorption (or electroreflection) spectra of silicon NCs correctly, it is necessary to take into account the special features of PL excitation. In the case of conventional excitation by a nitrogen laser, in almost all quantum wires (with the exception of those that are thinner than 1 nm) the excitation of free electron–hole pairs precedes their binding into excitons. The absorption coefficient is quite large ($>10^4$ cm^{-1}), which makes it possible to restrict the analysis of PL to the case of strong absorption. If the same NCs are excited by photons with energies that correspond to the excitonic absorption band, the absorption coefficient will depend substantially on both the wire diameter and the accuracy of matching to the peak of the absorption band corresponding to this diameter. The PL of the structures with quantum dots also has its own special features, specifically, the fact that it is in principle impossible to realize the case of strong absorption.

Note that the transition energies in silicon quantum dots estimated disregarding the exciton effect are shifted considerably to shorter wavelengths compared to the experiment. Specifically, according to the calculation, the maximal energy of transition between purely electronic and purely hole states in the quantum dots of the experimentally studied structures should range from 3.8 to 4 eV, and the minimal energy is expected to be about 1.5 eV. At the same time, the corresponding experimental values were in the ranges 2.8–3.0 and 1.2–1.4 eV, respectively.

Figure 1 shows the spectral dependences of steady-state PL in silicon quantum wires as calculated by formula [4] for an NC size distribution given by the Gaussian function with mean value $\overline{D} = 2.1$ nm and a fairly large variance ($\sigma = 0.4$ nm). When calculating the spectra shown in Figs. 1–4, we approximated the mesoscopic effect associated with the fluctuations in the heteroboundary structure by using a size-dependent (i.e., dependent on the transition energy $E(D)$ due to the size-related quantum effect) parameter of excitonic-band broadening $\Gamma(E) = \Gamma_0(D_0/D)^3$, $D_0 = 3$ nm. It was also assumed that $\tau_{nx}(D) = \tau_{n0}(D/3)^2$ and $\tau_{n0} = 3$ μs. As can be seen from Fig. 1, with small values of Γ_0, the PL

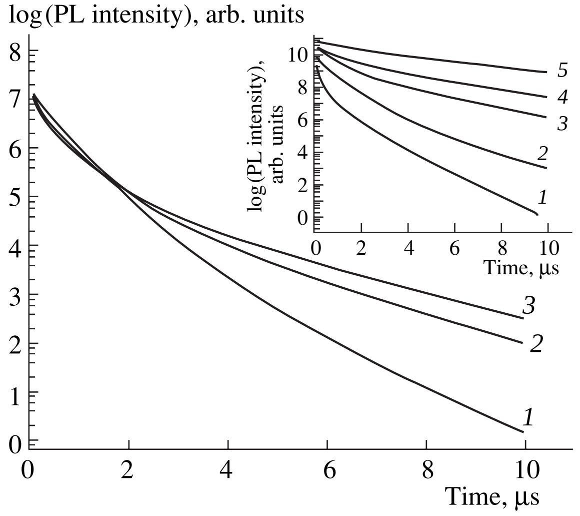

Fig. 4. Relaxation kinetics of the integrated intensity of PL calculated for a bimodal Gaussian distribution in the ensemble of quantum wires. Calculation parameters: $\bar{D}_1$ = 1 nm, $\bar{D}_2$ = 1.7 nm, $a_1 = 1$, $a_2 = 1$, and σ = (*1*) 0.1, (*2*) 0.3, and (*3*) 0.5 nm. The inset illustrates the PL relaxation kinetics in a unimodal Gaussian ensemble of quantum wires. The calculation parameters σ and $\bar{D}$ = (*1*) 0.1 and 1 nm, (*2*) 0.2 and 1.4 nm, (*3*) 0.3 and 1.8 nm, (*4*) 0.4 and 2.2 nm, and (*5*) 0.5 and 3 nm, respectively.

spectrum contains three of the five bands mentioned above as a result of oscillations of the dependence $\tau_{rx}(D)$. As Γ_0 increases, at first, the dips in the calculated PL spectra flatten and only the inflection points remain; then, at a sufficiently high value of Γ_0, the PL spectrum becomes featureless.

Figure 2a shows the steady-state PL spectra calculated for the case where the distribution of quantum wire thicknesses is described by two Gaussian functions centered at $\bar{D}$ = 1.0 and $\bar{D}$ = 2.4 nm. It can be seen from Fig. 2a that, since mesoscopic broadening is taken into account, the high-energy PL band appears to be significantly broader than the low-energy band. The experimental steady-state PL spectra obtained in [11] (Fig. 2b) for quantum dots in the SiO$_x$ matrix are further evidence of the fact that the high-energy band is indeed much more broadened than the low-energy band. The observation of two bands in steady-state PL spectra is only possible when the number of small NCs is sufficiently large. A somewhat different situation arises when PL spectra are detected with a time delay. With short delays t_d, the contribution of small NCs to a PL spectrum may be major even with a small number of such NCs, since they are characterized by shorter radiative-recombination times than larger NCs. As t_d increases, the relationship between the contributions that NCs of different sizes make to PL changes in favor of larger NCs and, when the number of small NCs is not large (compared to that of large NCs), only the long-wavelength band remains. This fact is illustrated by Fig. 3, which shows PL spectra calculated by formula (7) with different time delays t_d for silicon quantum wires with a size distribution described by two Gaussian functions (the corresponding distribution of wires over the excitonic radiative-transition energies $E(D)$ is shown in the inset). It can be seen that, with an increase in t_d, the PL bands actually shift to longer wavelengths and, with sufficiently large values of t_d, the spectrum contains only the long-wavelength band. A similar type of time-resolved PL spectra is typical of both porous silicon films and structures with silicon quantum dots.

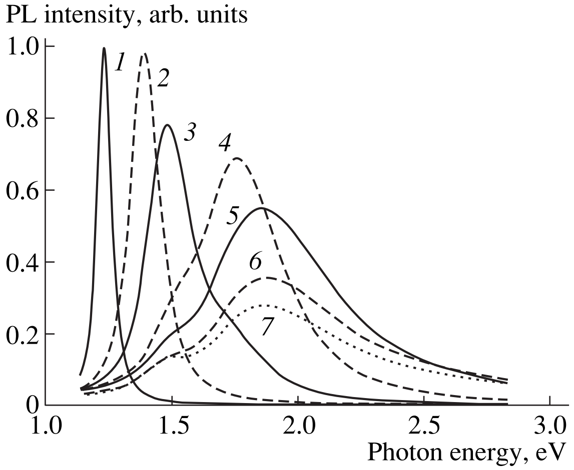

Fig. 5. Steady-state PL spectra for nanostructures containing a unimodal Gaussian ensemble of silicon quantum wires. Calculation parameters: Γ_0 = 0.02 eV; σ and $\bar{D}$ = (*1*) 0.1 and 3.0 nm, (*2*) 0.1 and 2.5 nm, (*3*) 0.15 and 2.1 nm, (*4*) 0.2 and 1.8 nm, (*5*) 0.3 and 1.5 nm, (*6*) 0.4 and 1.3 nm, and (*7*) 0.5 and 1.2 nm.

Figure 4 shows the kinetic dependences of the integrated PL intensity calculated by formula (6) for silicon quantum wires in the case where their size distribution is similar to that in Fig. 3. It can be seen that, in this case, the PL kinetics is closely approximated by “stretched” exponential functions, which is consistent with the experimental data. As the value of σ increases, the PL relaxation at the initial stage occurs more quickly and at the final stage slows down more severely. Therefore, for small NCs, the PL relaxation becomes nonexponential with smaller σ than for large NCs. At the same time, the PL relaxation can be close to exponential under certain conditions, specifically, for sufficiently large NCs with moderately large values of σ (see Fig. 4, inset).

Let us now analyze the positions of bands in the PL spectrum of silicon nanostructures in relation to the size of the nanostructures taking into account the oscillations of $\tau_{rx}(D)$ and the excitonic-band broadening $\Gamma(D)$. As can be seen from Fig. 5, with large mean sizes of NCs, the PL bands corresponding to the minima of $\tau_{rx}(D)$ are located with a high density along the energy axis. However, with a small variance in the size of NCs σ, they are clearly separated. Therefore, a decrease in the mean size of NCs leads to the usual shift of the peak of the PL band to higher energies (curves *1*, *2*). With smaller mean sizes, the individual bands become broader and start to overlap (curves *3*, *4*). Finally, for the smallest NCs, the band broadening is even more pronounced (due to both the mesoscopic effect, which is taken into account by parameter Γ, and the relative increase in the role of the size variance), and the peak position on the energy axis stabilizes, i.e., becomes size-independent (curves *5–7*). In special cases, even a decrease in the energy of the PL band is possible. This effect can be caused by a number of factors: (i) the amorphization of the smallest NCs; (ii) satisfying the condition $E_g^* > h\nu$, where E_g^* is the optical energy gap renormalized due to the size-related quantum effect and $h\nu$ is the photon energy of excitation radiation; and (iii) the complete oxidation of the smallest NCs.

In order to verify the theoretical model described above, we fabricated and experimentally studied two different porous silicon samples: sample *1*, from heavily doped *p*-type (100) silicon, ρ = 10–20 mΩ cm ($p = 4 \times 10^{18}$–10^{19} cm^{-3}), obtained by etching in an electrolyte with a low water content (HF : *Et* : H_2O = 1 : 2 : 1, and sample *2*, from *p*-type (100) silicon, ρ = 12 Ω cm ($p = 10^{15}$ cm^{-3}), obtained by etching in a standard electrolyte (HF : *Et* = 1 : 1). The samples had different degrees of oxidation: sample *2* was more oxidized due to postanodic treatment.

The PL spectra were measured with time resolution (the instant of detection was delayed relative to the excitation pulse). Laser pulses with a wavelength of λ = 337 nm, a duration of 10 ns, and a repetition rate of 100 Hz were used as the excitation radiation. The PL spectra were measured at room temperature using a computerized setup on the basis of an MDR-2 monochromator, a V9-5 stroboscopic voltage converter (strobe-pulse width 4 ns), and a FEU-79 photomultiplier as a detector.

The time-resolved experimental PL spectra obtained for porous silicon samples are plotted by the solid curves in Fig. 6a (sample *1*) and Fig. 6b (sample *2*). Using our theoretical approach (Fig. 6, dotted curves), we managed to fit the spectral position of the low-energy band, its shape, and the decrease in the intensity with increasing delay time to the experimental data.

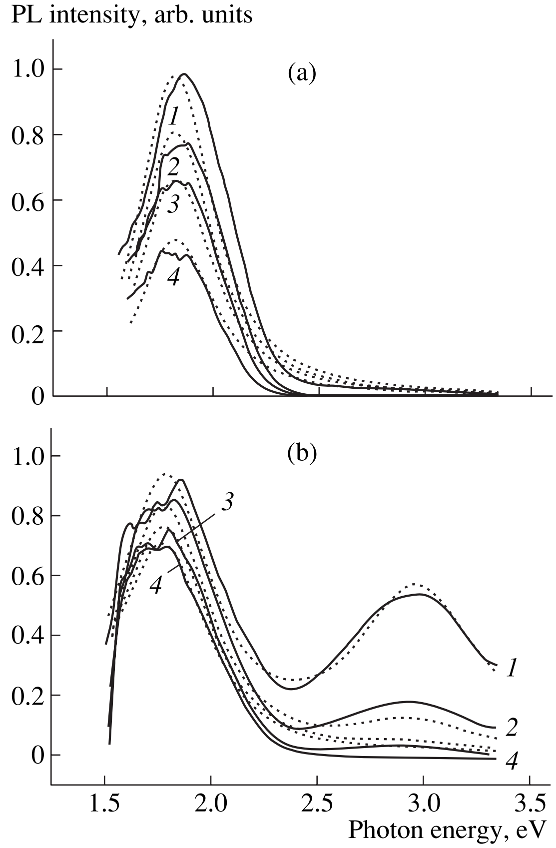

Fig. 6. Time-resolved PL spectra of porous silicon: experiment (solid curves) with (a) sample *1* with delay time t_d = (*1*) 0.2, (*2*) 0.5, (*3*) 0.8, and (*4*) 1.3 μs; (b) sample *2* with t_d = (*1*) 0.1, (*2*) 0.2, (*3*) 0.3, and (*4*) 0.4 μs; calculation (dashed curves) for a mean quantum wire thickness of 1.75 nm and a mean quantum dot size of 0.7 nm.

At the same time, it is not possible in principle to fit the position of the high-energy PL band and the decrease in its intensity with increasing delay time to the experiment within the framework of a model in which porous silicon is considered as simply an ensemble of quantum wires. Therefore, using previous results [17], we assumed that the high-energy band with a peak at 2.95 eV in the PL spectra of porous silicon films is related not only to the quantum wires in these films but also to the small-size quantum dots. The modifications of our model for quantum dots includes the following: (i) the term D^2 is replaced by $\alpha(D)D^3$ in equations (1)–(3), (ii) the matrix element of radiative transition calculated for quantum dots is used instead of that calculated for quantum wires, and (iii) the dot-size dependence of the exciton optical transition energy of the quantum dots obtained in [7, 8] is employed. This modification enabled us to fit our model to the experiment in the first-order approximation for both the low- and the high-energy parts of the PL spectra (Fig. 6b).

CONCLUSION

The results of this study suggest that the experimentally observed “fast” band 2.9–3 eV in the PL spectra of porous silicon and SiO_x films is related to the photoluminescence of quantum dots of very small size (≈1 nm in diameter) rather than to the luminescence of SiO_x. The model suggested above enables one to predict the energy position of this band and accounts for its large width and the very slight change in the position of the peak as the delay time increases. Furthermore, one may assume that the corresponding band observed in nonporous silicon (including quartz) is of similar nature.

Indeed, for this band to be present, the silicon oxide only needs to contain silicon clusters with linear dimensions of about 1 nm, which is quite possible in reality.

The analysis performed suggests that the multimode character of the PL spectra, their special features with different size distributions of NCs, as well as their relaxation behavior, are associated with the size-related quantum oscillations of the excitonic radiative-recombination time. It is also shown that, in order to provide for a satisfactory fit of the calculated PL spectra to those observed in the experiment (especially in the high-energy part), one should take into account the strong mesoscopic broadening of the high-energy bands, which prevents the simultaneous appearance of several bands in the PL spectra of silicon NCs. This broadening is caused by intense fluctuations of the optical energy gap in small NCs.

ACKNOWLEDGMENTS

We are grateful to Prof. D.V. Korbutyak and É.B. Kaganovich for discussions of the results.

This study was supported by the Ministry of Science and Education of Ukraine (project no. F 7/284-2001) and INTAS (grant no. Call 2001 NANO-0444). O.M. Sreseli acknowledges the support of the “Solid Nanostructure Physics” program of the Ministry of Industry, Science, and Technology of the Russian Federation and the “Low-Dimensional Quantum Structures” program of the Presidium of the Russian Academy of Sciences.

REFERENCES

1. Yu. V. Kryuchenko and A. V. Sachenko, Physica E (Amsterdam) **14**, 299 (2002).
2. D. V. Korbutyak, Yu. V. Kryuchenko, I. M. Kupchak, and A. V. Sachenko, Semicond. Phys. Quantum Electron. Optoelectron. **6**, 172 (2003).
3. M. S. Hyberstein, Phys. Rev. Lett. **72**, 1514 (1994).
4. G. D. Sanders and Y. C. Chang, Phys. Rev. B **45**, 9202 (1992).
5. M. S. Bresler and I. N. Yassievich, Fiz. Tekh. Poluprovodn. (St. Petersburg) **27**, 871 (1993) [Semiconductors **27**, 475 (1993)].
6. A. V. Sachenko and Yu. V. Kryuchenko, Fiz. Tekh. Poluprovodn. (St. Petersburg) **38**, 102 (2004) [Semiconductors **38**, 99 (2004)].
7. D. Delley and E. F. Steigmeyer, Appl. Phys. Lett. **67**, 2370 (1995).
8. T. Takagahara, Phys. Rev. B **47**, 4569 (1993).
9. G. Polisskiĭ, O. M. Sreseli, A. V. Andrianov, and F. Kokh, Fiz. Tekh. Poluprovodn. (St. Petersburg) **31**, 365 (1997) [Semiconductors **31**, 304 (1997)].
10. H. Miruno, H. Koyama, and N. Koshida, Appl. Phys. Lett. **69**, 3779 (1996).
11. É. B. Kaganovich, É. G. Manoĭlov, I. R. Bazylyuk, and S. V. Svechnikov, Fiz. Tekh. Poluprovodn. (St. Petersburg) **37**, 353 (2003) [Semiconductors **37**, 336 (2003)].
12. M. Baran, B. Bulakh, N. Korsunska, *et al.*, Semicond. Phys. Quantum Electron. Optoelectron. **6**, 282 (2003).
13. N. Koshida and N. Matsumoto, Mater. Sci. Eng. R **40**, 169 (2003).
14. T. Toyama, Y. Kotani, A. Shimodo, and H. Okamoto, Appl. Phys. Lett. **74**, 3323 (1999).
15. E. F. Venger, R. Yu. Golineĭ, L. A. Matveeva, and A. V. Vasin, Fiz. Tekh. Poluprovodn. (St. Petersburg) **37**, 104 (2003) [Semiconductors **37**, 103 (2003)].
16. F. Buda, J. Kohanoff, and M. Parrinello, Phys. Rev. Lett. **69**, 1272 (1992).
17. H. Foll, M. Christophersen, J. Carstensen, and G. Hasse, Mater. Sci. Eng. R **39**, 93 (2002).

Translated by A. Sidorova

Semiconductors, Vol. 38, No. 7, 2004, pp. 849–854. Translated from Fizika i Tekhnika Poluprovodnikov, Vol. 38, No. 7, 2004, pp. 884–889.
Original Russian Text Copyright © 2004 by Masalov, Samarov, Volkodav, Emel'chenko, Bazhenov, Bozhko, Karpov, Gruzintsev, Yakimov.

AMORPHOUS, VITREOUS, AND POROUS SEMICONDUCTORS

Ultraviolet Luminescence of ZnO Infiltrated into an Opal Matrix

V. M. Masalov*, É. N. Samarov*, G. I. Volkodav*†, G. A. Emel'chenko*^, A. V. Bazhenov*, S. I. Bozhko*, I. A. Karpov*, A. N. Gruzintsev, and E. E. Yakimov****

**Institute of Solid-State Physics, Russian Academy of Sciences, Chernogolovka, Moscow oblast, 142432 Russia*
^e-mail: emelch@issp.ac.ru
***Institute of Microelectronics Technology and High-Purity Materials, Russian Academy of Sciences, Chernogolovka, Moscow oblast, 142432 Russia*

Submitted December 22, 2003; accepted for publication December 25, 2003

Abstract—Technology for the infiltration of zinc oxide into a three-dimensional opal lattice using chemical deposition from a solution was developed. Samples of ZnO–opal composites, whose luminescence at room temperature mainly occurs in the ultraviolet spectral range, were obtained. The filling ratio was monitored by two different techniques: (i) checking the increase in the mass of the sample and (ii) checking the shift of the peak in the optical reflection spectrum of samples filled with ZnO in comparison with the initial opal matrices. The results obtained by these two methods are consistent with each other. Optimum conditions for synthesizing ZnO-filled opals in order to attain the highest intensity of ultraviolet luminescence were determined. It was shown that using "raw" opals, whose voids are incompletely filled with the semiconductor material, leads to a severalfold increase in the intensity of the edge excitonic emission band at room temperature. The results obtained can be used in the development of efficient directed laser light sources in the ultraviolet spectral range based on the "photonic crystal" effect. © *2004 MAIK "Nauka/Interperiodica".*

1. INTRODUCTION

The development of effective methods for implementing the "photonic crystal" concept in order to fabricate high-efficiency light-emitting devices (lasers and LEDs) with characteristics superior to those of currently existing ones is a problem of current interest for modern photonic technology, which is based on utilizing photons (i.e., light) instead of electrons as carriers of information. The concept of the photonic band gap (PBG), which was developed in [1, 2], implies that light waves in the PBG spectral range cannot propagate through the photonic crystal, cannot experience total reflection when they are incident on the crystal from the outside, and cannot be emitted inside the crystal because of a lack of corresponding optical modes. These properties originate from the three-dimensional modulation of the refractive index in the photonic crystal, which is a periodic structure composed of dielectric unit elements. In this context, in order to produce an efficient light-emitting device, one needs to form a bound photonic state within such a structure, thus introducing a spectrally narrow allowed level into the PBG. The energy of this level must be tuned to the emission photon energy of the laser or LED. The first report on the experimental realization of PBG material was published in 1991 [3], and those results corresponded to the microwave region of the spectrum (13–15 GHz). A photonic crystal exhibiting PBG in the infrared region (1.35–1.95 μm) was demonstrated only in 1999 [4]. Now researchers are actively seeking ways of fabricating novel light emitters and passive elements for optoelectronics on the basis of photonic crystals.

The predicted high efficiency of, for example, LEDs of this kind is based on the possibility of designing the necessary optical modes within a photonic crystal and controlling their directions of propagation. Commercially available LEDs based on semiconductors with an internal quantum efficiency of up to 99.7% have a low external efficiency (about 2–4%) [5]. The limit is set by the small width of the emission cone (16° for GaAs). The rest of the light is lost due to total internal reflection and emission in the "idle" directions. The concept of the photonic crystal allows all spontaneous emission to be channeled into the operating modes of the device. In principle, the external efficiency of such a device can be as high as the internal efficiency of the material (more than 90%). There are a number of methods for fabricating photonic crystals, mainly adopted from the silicon industry. They include electron lithography, masking, ion etching, electrochemical methods, selective oxidation, etc. All of these time-consuming and expensive techniques can only produce two-dimensional (quasi-two-dimensional) structures, which do not provide full realization of the potential offered by the physics of photonic crystals for device applications. The main method that allows fabrication of ordered three-dimensional structures is based on matrix technology. It is based on filling regular lattices of voids in natural or artificial matrixes, such as zeolite, asbestos, or opal crystals, with different substances [6].

---

† Deceased.

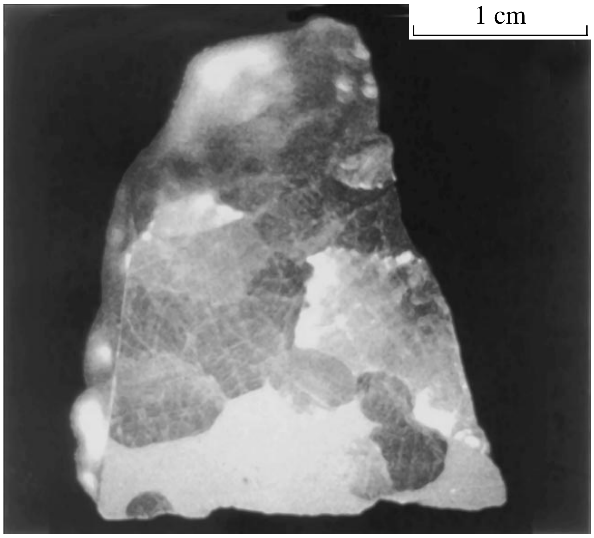

Fig. 1. Optical photograph of the domain structure of an opal sample; the size of the SiO_2 particles equals 260 nm.

Matrix methods have been widely used to synthesize mesoporous and macroporous ceramics [7–10]; polymers [11]; semiconductor sublattices of Te, GaAs, HgSe, and CdS clusters [12, 13]; and inverted opals from CdSe [14], Si [15], and Ge [16]. This approach, based on the use of synthetic opal, was suggested in [12].

It was shown that crystalline GaN can be grown in the voids of an opal matrix [17]. A number of studies were devoted to the emission properties of organic molecules, semiconductor nanocrystals, and rare-earth ions embedded in an opal matrix [12, 18, 19]. In our recent study [20] it was found that a ZnO–opal structure obtained by depositing a thin layer of ZnO onto an opal film exhibits ultraviolet (UV) excitonic luminescence originating from quantum dots formed in the second nearest layer to the surface of the opal film.

Producing high-quality nanostructures using zinc oxide with emission mainly in the UV region is necessary for the development of high-power semiconductor light sources in this spectral region. This semiconductor compound has a wide band gap (equal to 3.4 eV [21]), direct interband transitions, and low resistivity, which favors its use for the fabrication of semiconductor LEDs [22] and transparent contacts and windows for solar cells [23, 24]. Zinc oxide has the same optical, electrical, and structural parameters as gallium nitride, but is simpler in terms of growth technology and more stable during operation.

The goal of this study is (i) to grow samples of synthetic opals filled with ZnO that exhibit luminescence mainly in the UV region and (ii) to study the influence of the parameters of the synthesis process on the spectral characteristics of the emission.

2. INFILTRATION OF ZINC OXIDE INTO AN OPAL MATRIX

Filling of the voids in an opal matrix was carried out by impregnation with a solution of zinc nitride $Zn(NO_3)_2 \cdot nH_2O$ and subsequent decomposition of the nitride into oxide upon thermal treatment. Note that, in addition to zinc nitride, which is readily soluble in water and ethyl alcohol, there are a number of organic zinc compounds suitable for this procedure [25]. They include zinc stearate $Zn(C_{18}H_{35}O_2)_2$ (melting temperature T_m = 130°C), acetylacetonate $Zn(C_5H_7O_2)_2$ (T_m = 138°C), and acetate $Zn(C_2H_3O_2)_2 \cdot 2H_2O$ (T_m = 235°C). The presence of large carbon radicals in these molecules hinders their penetration into small voids. Zinc formate $Zn(HCO_2)_2 \cdot 2H_2O$ has the least number of “useless” atoms, but it exhibits lower solubility in water (5.2 wt %) and is not soluble in alcohol. Preliminary experiments showed that zinc acetate has a lower penetration ability than zinc nitrate in the process of opal matrix impregnation.

According to the solubility diagram of zinc nitrate in water [26], zinc nitrate exists only in the form of crystal hydrate $Zn(NO_3)_2 \cdot nH_2O$, where the number of water molecules varies from nine to one as the temperature varies from –32 to +70°C. The temperature for the impregnation process was varied in the range 55–70°C, where zinc nitrate contains one or two water molecules. Zinc nitrate for the process was prepared by the standard reaction of metallic zinc with nitric acid (both reagents of chemical purity grade) [27].

Opal samples of two types were used: “raw” samples, which were treated only by drying at temperatures of up to 150°C, and “baked” samples, which, in addition to drying, were thermally treated at ~1000°C for 5 h in air. Samples of dimensions $\sim 5 \times 4 \times 3$ mm^3 were cut with their large facet parallel to the sedimentation direction. Ordered domains (clearly distinguished in the reflected light as uniformly colored regions) then occupied, as a rule, more than 50% of each facet (see Fig. 1). The size of the silicon dioxide spheres varied in different samples from 260 to 320 nm.

The duration of the impregnation procedure was varied from 1.5 h for the first impregnation to 20 h for the final treatment. After the impregnation procedure was finished, the crust of zinc nitride crystals was cleaned off the samples. The samples were then dried and heated to 450–600°C in order to induce decomposition of the nitride into oxide. Then, another impregnation treatment was carried out, and the entire process was repeated many times.

In Fig. 2, typical weight-increase curves for samples subjected to successive impregnation treatment and annealing are shown. Curve *1* corresponds to a raw sample and curve *2*, to a baked sample. The number of impregnation–annealing cycles is plotted on the abscissa, and the ratio of the increase in mass Δm to the initial mass m_0 is the ordinate. Note that both curves flatten out after about 20 impregnation–annealing cycles; however, the value of the final mass increase differs considerably in the two cases, which indicates unambiguously that the two types of sample have different porosities.

Theoretically, the largest possible increase in the mass of a sample with an ideal close-packed lattice of spheres can be calculated from the following relationship, assuming complete filling of the voids with ZnO:

$$\Delta m_{\max} = PV_{\mathrm{op}}\rho_{\mathrm{ZnO}} = Pm_0\rho_{\mathrm{ZnO}}/\rho_{\mathrm{op}}. \quad (1)$$

Here, P is the sample porosity (the fraction of the volume occupied by the voids), m_0 is the initial mass of the sample, ρ_{ZnO} is the density of zinc oxide, and ρ_{op} is the apparent density of the opal.

The porosity of the structure, which consists of close-packed spheres, equals 0.26. This is the case of baked opal, whose spheres are monolithic. In raw opal, each sphere in turn consists of first-generation SiO_2 particles aggregated into a close-packed lattice. Thus, each sphere has a porosity of 0.26, and the raw opal sample as a whole has a porosity of 0.45. So the apparent density equals 1.64 g/cm^3 for baked opal and 1.21 g/cm^3 for raw opal. These values are close to those of the opal densities obtained experimentally by X-ray porosimetry [28] (1.65 and 1.28 g/cm^3 for baked and raw opals, respectively) and by pycnometry (our measurements yield 1.64 and 1.23 g/cm^3 for baked and raw opals, respectively).

Using the values 5.6, 1.64, and 1.21 g/cm^3 for the densities of zinc oxide, baked opal, and raw opal, respectively, we find that the largest possible mass increase is theoretically $\Delta m_{\max} = 0.89m_0$ for baked opal and $\Delta m_{\max} = 2.08m_0$ for raw opal.

Returning now to the analysis of the mass-increase curves in Fig. 2, we note that the experimentally measured increase in the mass of baked opal upon impregnation was $1.1m_0$ (curve *1*). This value agrees satisfactorily with that calculated in the model of a close-packed structure ($0.89m_0$), taking into account the contribution of the zinc oxide crust formed on the surface of the sample to the increase in mass. According to our estimate, for the size of samples under study this contribution can be as high as $0.2m_0$. In addition, samples always have cavities that are not related to the lattice structure (cracks etc.). The increase in the mass of the raw opal sample (curve *2*) was $1.55m_0$, which is considerably smaller than the theoretical limit ($2.08m_0$). This indicates that nanovoids between the first-generation SiO_2 particles are only partially (41%) filled with ZnO. This is easily explained if one bears in mind that the size of first-generation SiO_2 particles is 5–7 nm, the size of the voids between them is 1–3 nm, and the inlet-channel size of these voids is 0.75–1.0 nm, which is comparable to the size of nitrate or hydrate complexes of zinc (0.4–0.6 nm) [29]. As the inlet channel of a nanovoid becomes partially filled with ZnO, the opening of the channel becomes smaller than the size of a zinc complex, and nanovoid filling stops.

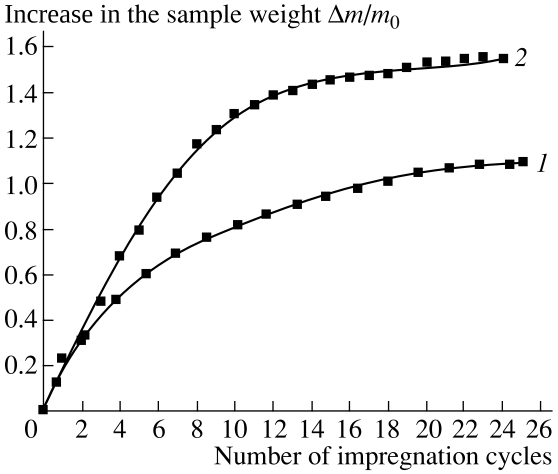

Fig. 2. Weight increase in samples subjected to successive cycles of impregnation and annealing for (*1*) baked and (*2*) raw opal.

3. REFLECTION SPECTRA

The optical reflection spectra were recorded using a prism monochromator coupled to an optical microscope. Photoelectric detection was performed using a computer-controlled CCD array detector. The spectral sensitivity range of the setup was 400–1100 nm. A tungsten-filament incandescent lamp SIRSh-40 was used as the light source. The smallest probed area on the surface of the sample was 40×40 μm^2. In the samples under study, the {111} plane of the bulk opal crystal was tilted by about 30° from the plane of the sample's surface. The spectra were recorded under normal incidence of light on the {111} plane.

In the spectral range examined, there is a single line in the reflection spectra of all the samples under study. The reflection spectra of baked and raw opals are shown in Figs. 3a and 3b, respectively. The wavelength of the peak reflection in samples of baked opal before their filling with ZnO (Fig. 3a, dashed curve) $\lambda = 492$ nm corresponds to the Bragg condition $\lambda = 2dn_{\mathrm{eff}}$, where the value of the effective refractive index $n_{\mathrm{eff}} = 1.35$ agrees satisfactorily with the calculated one. For an fcc lattice (which is the case under consideration), the distance between the planes in the $\langle 111 \rangle$ direction $d = 0.816D_{\mathrm{SiO_2}}$, where the diameters of SiO_2 spheres $D_{\mathrm{SiO_2}} = 225$ and 285 nm in baked and raw opals, respectively. It should be taken into account that, in unfilled raw opal, the volume fraction of SiO_2 $f_1 = 0.55$ and porosity $f_2 = 0.45$, while in baked opal $f_1 = 0.74$ and $f_2 = 0.26$. The calculated effective refractive index of raw opal $n_{\mathrm{eff}} = 1.267$. The spectral position of the reflection peak in unfilled samples of raw opal (Fig. 3b, dashed curve) $\lambda = 587$ nm corresponds to the Bragg condition $\lambda = 2dn_{\mathrm{eff}}$, where the value of the effective

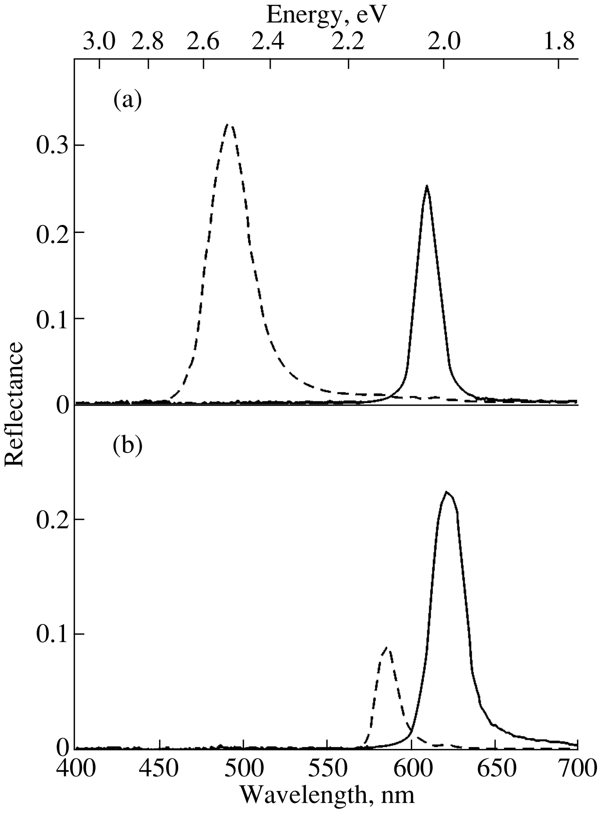

Fig. 3. Room-temperature reflection spectra of (a) baked and (b) raw opals. Dashed lines correspond to starting samples that were not filled with ZnO; solid lines correspond to samples containing ZnO in the voids of the opal matrix (filling ratio α = (a) 1 and (b) 0.31).

refractive index n_{eff} agrees satisfactorily with the calculated value.

As the voids between the spheres of an opal crystal are filled with ZnO, the reflection peak shifts to longer wavelengths due to an increase in n_{eff}. In the general case of a three-component system, n_{eff} is defined by the expression

$$n_{\text{eff}}^2 = n_1^2 f_1 + n_2^2 f_2 + n_3^2 f_3. \tag{2}$$

Here, $n_1 = 1.45$, $n_2 = 1$, and $n_3 = 2.2$ are the refractive indices and f_1, f_2, and f_3 are the volume fractions of SiO_2, air, and ZnO, respectively ($f_1 + f_2 + f_3 = 1$).

It follows from (2) that, for baked opal with voids filled completely with ZnO ($f_2 = 0$), $n_{\text{eff}} = 1.68$. For the sphere diameter $D_{SiO_2} = 225$ nm, the reflection peak in such a structure should appear at $\lambda = 616$ nm, which agrees well with the experimentally observed value $\lambda = 610$ nm (Fig. 3a, solid curve). The raw opal sample is partially filled with ZnO; the filling ratio determined from the increase in mass amounts to 31% of the calculated largest possible value. The reflection peak in this sample appears at 623 nm (Fig. 3b, solid curve). From the shift in the spectral position of the reflection peak caused by the filling of the voids, it is easy to calculate the effective refractive index of the partially filled sample $n_{\text{eff2}} = n_{\text{eff1}}\lambda_2/\lambda_1 = 1.345$ (where $n_1 = 1.27$, $\lambda_1 = 587$ nm, and $\lambda_2 = 623$ nm). Thus, the void filling ratio equals $\alpha = f_3/(f_2 + f_3) = f_3/0.45 = 0.37$ (37%), which differs insignificantly from the value determined from the increase in mass (31%).

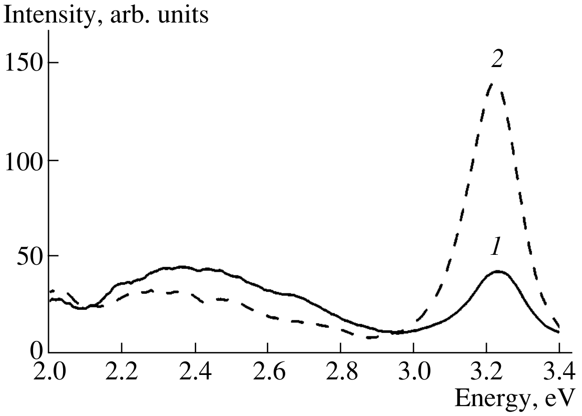

Fig. 4. Room-temperature luminescence spectra of bulk raw opal containing ZnO in the voids of the opal lattice (filling ratio $\alpha = 0.31$), recorded (*1*) before and (*2*) after 30-min annealing at 800°C in air.

4. LUMINESCENCE SPECTRA

Room-temperature photoluminescence (PL) spectra of ZnO-filled opals were analyzed. An LGI-505 pulsed nitrogen laser was used as the excitation source (wavelength, 337.1 nm; pulse duration, 10 ns; and peak power, 1.5 kW). The PL was excited within a rectangular spot 0.2×0.3 mm^2 in area. The spectra were recorded using an MDR-6 double monochromator under computer control, which provided a spectral resolution of no worse than 1 meV for the slit widths used.

To determine the contribution of the opal matrix to the luminescence, emission from unfilled and filled samples with different filling ratios ($\alpha = 0.31$ and $\alpha = 1$) was studied. It should be noted that the samples of unfilled opal did not exhibit any intrinsic luminescence irrespective of the baking conditions. In order to improve the quality of the crystal structure and the stoichiometry of zinc oxide, filled opals were annealed at 800°C in air for 30 min. These conditions of high-temperature annealing are optimal for increasing the intensity of the UV emission of ZnO [23].

Figure 4 shows the PL spectra of raw opal filled with ZnO ($\alpha = 0.31$) before (curve *1*) and after (curve *2*) high-temperature annealing. In both cases, the spectra are dominated by bands of green impurity-related emission (with a peak at 2.35 eV) and UV excitonic emission (with a peak at 3.23 eV). However, in the spectra of unannealed samples of filled raw opal, both bands are of comparable intensity, while after annealing the

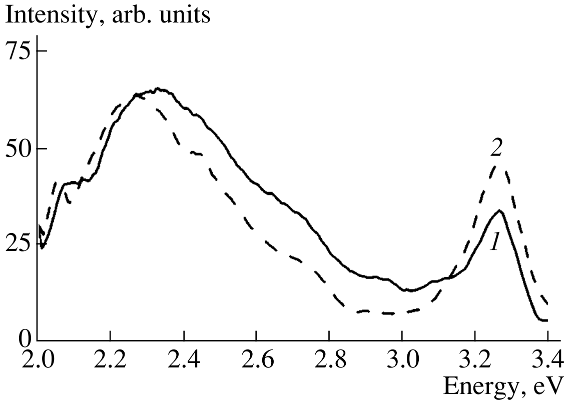

Fig. 5. Room-temperature luminescence spectra of bulk baked opal containing ZnO in the voids of the opal lattice (filling ratio $\alpha = 1$), recorded (*1*) before and (*2*) after 30-min annealing at 800°C in air.

intensity of the UV emission increases severalfold. In the latter case, nearly all the radiative recombination of laser-excited electrons occurs via bound-exciton states of ZnO.

In the PL spectra of baked opal filled with ZnO ($\alpha = 1$), the broad band of green impurity-related emission (with a peak at 2.35 eV) has the highest intensity both for unannealed samples and those annealed in air at 800°C (Fig. 5). The UV peak originating from excitonic luminescence also increases slightly upon annealing (curve *2*). The presence of green emission in ZnO is evidence of crystal-lattice point defects of zinc-vacancy and oxygen-vacancy type [30]. Radiative transitions of electrons from levels of donor intrinsic-defects (V_O) to levels of acceptor intrinsic-defects (V_{Zn}) are responsible for the broad luminescence band, which is inhomogeneously broadened due to a spread in the distances between the defects in donor–acceptor pairs of this type. At the same time, the intense UV emission of ZnO at room temperature in raw opal (Fig. 4) is indicative of its better stoichiometry and higher quality crystal structure.

Thus, the process using raw opal, whose voids are filled incompletely ($\alpha = 0.31$), results in the formation of higher quality ZnO embedded in the opal matrix compared to the process using baked opal, whose voids are completely filled ($\alpha = 1$). In the former case, the intensity of the UV emission is three times higher than in the latter case (Figs. 4, 5, curves *2*). Taking into account that the mass of ZnO in completely filled opal is more than three times greater than the mass of ZnO in partially filled opal, we conclude that the efficiency of the UV luminescence in raw opal is an order of magnitude higher.

This effect can be explained by the effect of two factors: the presence of the nanovoids at the spheres of raw opal and the presence of voids in partially filled ($\alpha = 0.31$) opal. In our opinion, the hexagonal lattice of nanovoids can play an ordering role in the crystallization of ZnO, which also has a hexagonal crystal lattice. As a result, ZnO layers of higher crystal quality grow on textured surfaces of SiO_2 spheres in raw opal during annealing. In addition, the presence of voids that remain in opal partially filled with ZnO facilitates the access of oxygen in the process of high-temperature annealing (Fig. 4, curves *1*, *2*), and the composition of the grown layers becomes closer to stoichiometric.

5. CONCLUSION

Thus, we described a method for the controlled filling of voids in an opal matrix with zinc oxide and determined the optimum conditions for synthesizing ZnO within the opal structure in order to attain the highest intensity of UV luminescence from ZnO. We demonstrated that the use raw opals, whose voids are incompletely filled with the semiconductor material, leads to a severalfold increase in the intensity of edge excitonic luminescence at room temperature. The results obtained can be used in the development of efficient directed laser light sources in the UV spectral region using the photonic crystal effect.

ACKNOWLEDGMENTS

This study was supported by INTAS (project no. 2002-796), the Russian Foundation for Basic Research (project no. 01-02-97024), and the Ministry of Industry, Science, and Technology of Russia (contract no. 40.012.1.1.11.54).

REFERENCES

1. S. John, Phys. Rev. Lett. **58**, 2486 (1987).
2. E. Yablonovitch, Phys. Rev. Lett. **58**, 2059 (1987).
3. E. Yablonovitch, T. J. Gmitter, R. D. Meade, *et al.*, Phys. Rev. Lett. **67**, 3380 (1991).
4. J. G. Fleming and S. Y. Lin, Opt. Lett. **24**, 49 (1999).
5. T. F. Kraus and R. M. De La Rue, Prog. Quantum Electron. **23**, 51 (1999).
6. V. N. Bogomolov, Usp. Fiz. Nauk **124**, 171 (1978) [Sov. Phys. Usp. **21**, 77 (1978)].
7. P. Yang, T. Deng, D. Zhao, *et al.*, Science **282**, 2244 (1998).
8. O. D. Velev, T. A. Jede, R. F. Lobo, and A. M. Lenhoff, Nature **389**, 447 (1997).
9. B. T. Holland, C. E. Blanford, and A. Stein, Science **281**, 538 (1998).
10. J. E. G. J. Wijnhoven and W. L. Vos, Science **281**, 802 (1998).
11. S. A. Johnson, P. J. Ollivier, and T. E. Mallouk, Science **283**, 963 (1999).
12. V. N. Astratov, V. N. Bogomolov, A. A. Kaplyanskii, *et al.*, Nuovo Cimento D **17**, 1349 (1995).
13. D. J. Norris and Yu. A. Vlasov, Adv. Mater. **13**, 371 (2001).
14. Yu. A. Vlasov, N. Yao, and D. J. Norris, Adv. Mater. **11**, 165 (1999).

15. A. Blanco, E. Chomski, S. Grabtchak, *et al.*, Nature **405**, 437 (2000).
16. H. Miguez, F. Meseguer, C. Lopez, *et al.*, Langmuir **16**, 4405 (2000).
17. V. G. Golubev, D. A. Kurdyukov, A. V. Medvedev, *et al.*, Fiz. Tekh. Poluprovodn. (St. Petersburg) **35**, 1376 (2001) [Semiconductors **35**, 1320 (2001)].
18. S. V. Gaponenko, V. N. Bogomolov, E. P. Petrov, *et al.*, J. Lightwave Technol. **17**, 2128 (1999).
19. S. G. Romanov, T. Maka, C. M. Sotomayor Torres, *et al.*, Appl. Phys. Lett. **79**, 731 (2001).
20. A. N. Gruzintsev, V. T. Volkov, G. A. Emel'chenko, *et al.*, Fiz. Tekh. Poluprovodn. (St. Petersburg) **37**, 330 (2003) [Semiconductors **37**, 314 (2003)].
21. Y. Chen, D. M. Bagnall, Z. Zhu, *et al.*, J. Cryst. Growth **181**, 165 (1997).
22. Y. R. Ray, W. J. Kim, and H. W. White, J. Cryst. Growth **219**, 419 (2000).
23. A. N. Georgobiani, A. N. Gruzintsev, V. T. Volkov, and M. O. Vorob'ev, Fiz. Tekh. Poluprovodn. (St. Petersburg) **36**, 284 (2002) [Semiconductors **36**, 265 (2002)].
24. J. R. Tuttle, M. A. Contreras, T. J. Gillespie, *et al.*, Prog. Photovoltaics **3**, 235 (1995).
25. *Handbook of a Chemist*, 3rd ed. (Khimiya, Leningrad, 1971), Vol. 2.
26. A. N. Kirgintsev, L. N. Trushnikova, and V. G. Lavrent'eva, *Solubility of Inorganic Materials in Water: a Handbook* (Khimiya, Leningrad, 1972).
27. Yu. V. Karyakin and I. I. Angelov, *Pure Chemical Materials* (Khimiya, Moscow, 1974).
28. V. V. Ratnikov, Fiz. Tverd. Tela (St. Petersburg) **39**, 956 (1997) [Phys. Solid State **39**, 856 (1997)].
29. H. B. Gray, *Electrons and Chemical Bonding* (Benjamin, New York, 1964; Mir, Moscow, 1967).
30. A. N. Gruzintsev, V. T. Volkov, I. I. Khodos, *et al.*, Mikroélektronika **31**, 234 (2002).

Translated by M. Skorikov

Semiconductors, Vol. 38, No. 7, 2004, pp. 855–860. Translated from Fizika i Tekhnika Poluprovodnikov, Vol. 38, No. 7, 2004, pp. 890–895.
Original Russian Text Copyright © 2004 by Biryulin, Turinov, Yakimov.

PHYSICS OF SEMICONDUCTOR DEVICES

Leakage Currents over the Surface of CdHgTe-Based Photodiodes

P. V. Biryulin*^, V. I. Turinov*, and E. B. Yakimov**
**Scientific and Production Association (NPO) Istok, Fryazino, Moscow oblast, 141190 Russia*
^e-mail: birulin@si.ru
***Institute of Microelectronic Technology and Ultrahigh-Purity Materials,*
Russian Academy of Sciences, Chernogolovka, Moscow oblast, 142432 Russia
e-mail: yakimov@impt-hptm.ac.ru

Submitted August 21, 2003; accepted for publication December 24, 2003

Abstract—The leakage current I_p over the surface of $Cd_xHg_{1-x}Te$-based photodiodes that have a cutoff wavelength of the photosensitivity spectrum of λ_{co} = 9.8–11.6 μm and are fabricated by implanting Zn^{++} ions into the *p*-type solid solution is investigated. The surface character of the I_p current is indicated by a coordinate shift of the peak in the sensitivity profile of n^+–p junctions, which is measured in a scanning mode by the beam of a CO_2 laser with a wavelength of 10.6 μm, with an increase in voltage *U* across the photodiode and the shift of spectral characteristics to shorter wavelengths with increasing *U*. *© 2004 MAIK "Nauka/Interperiodica".*

The properties of *p*–*n* junctions based on narrow-gap $Cd_xHg_{1-x}Te$ solid solutions depend heavily on the conditions of the synthesis and growth of crystals, as well as on the technology used for fabricating *p*–*n* junctions [1]. There are also difficulties such as the presence of high random shunting conductivity associated with bulk microinhomogeneities formed during crystal growth [2]. Such defects can also affect processes in the fabrication of *p*–*n* junctions. The phenomena of shunting, which cause the degradation of the *p*–*n* junctions with time, are also associated with the nature of the surface of $Cd_xHg_{1-x}Te$. At this surface, accumulation layers in *n*-type material and inversion layers in *p*-type material are formed [3, 4]. There is also the problem of mercury loss from the surface during technological operations. Many of these problems have already resolved, and the technology of crystal growth and the fabrication of *p*–*n* junctions have reached such a level that the emphasis of research has now shifted to the properties of $Cd_xHg_{1-x}Te$ based *p*–*n* junctions [5].

The reverse current of photodiodes (PDs) (I_Σ) is the sum of the diffusion component (I_d), the generation–recombination current in the space-charge region (SCR) (I_{gr}), the photocurrent (I_f), the tunnel component (I_t), and the leakage current (I_p) both over the surface and in the bulk due to defects in experimental PDs.

In this study, we focus our attention on the current I_p since this current is the cause of the low differential resistance R_d in experimental $Cd_xHg_{1-x}Te$-based PDs. To reveal the dominant currents for various reverse biases *U*, theoretical current–voltage (*I*–*U*) characteristics with varying current components were plotted to attain agreement between theoretical and experimental *I*–*U* characteristics. The measurements were carried out for PDs fabricated using p-$Cd_xHg_{1-x}Te$ samples

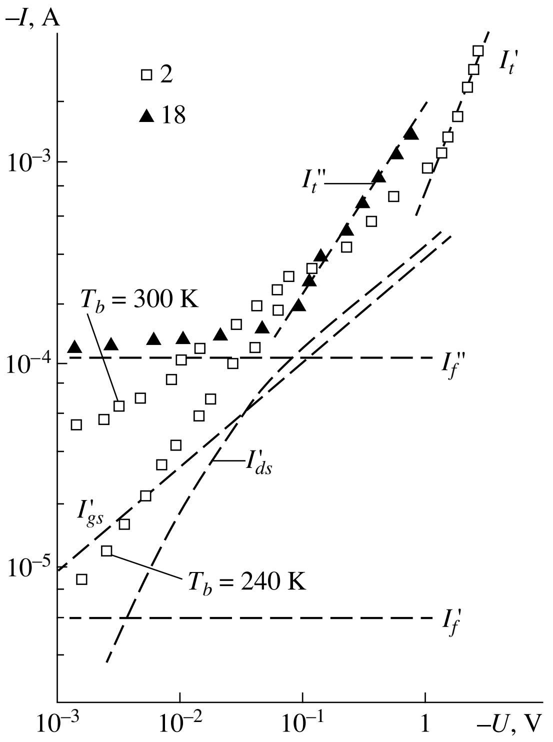

Fig. 1. Bias-voltage dependences of reverse currents of CdHgTe-based photodiodes 2 and 18. The graphic symbols correspond to the experiment, and the lines correspond to the calculation of components of the current. Photodiode 2: $I'_t = I'_{d0} = 6 \times 10^{-7}$ A; $I'_{g0} = 1.2 \times 10^{-8}$ A; I'_f (T_b = 240 K); I'_{ds} and I'_{gs} are calculated using formulas (4) and (5), respectively; $S = 1.5 \times 10^4$ cm/s. Photodiode 18: $I''_t = I''_{d0}$ = 2.5×10^{-6} A; $I''_{g0} = 1 \times 10^{-7}$ A; I''_f (T_b = 300 K); $S = 2.4 \times$ 10^4 cm/s.

Parameters of the $Cd_xHg_{1-x}Te$ samples and photodiodes based on these compounds

$Cd_xHg_{1-x}Te$ sample	PD number	L_n, μm	λ_{co}, μm	R_0A, Ω cm^2	R_d^{max}, kΩ (–U, μV)	p_p, 10^{16} cm^{-3}
A1: $p = 1.1 \times 10^{15}$ cm^{-3}, $\mu_p = 447$ cm^2/(V s) $\tau_n = 7 \times 10^{-8}$ s; A1: $p = 5.3 \times 10^{14}$ cm^{-3}, $\mu_p = 647$ cm^2/(V s)	2	$\frac{100}{35}$	10.0	0.68	5.6 (405)	1.3
	4	–	9.9	0.71	37 (300)	0.8
	5	–	9.8	0.72	55 (135)	0.6
	7	$\frac{90}{35}$	–	0.61	18.4 (50)	0.25
B3: $p = 1.5 \times 10^{16}$ cm^{-3} $\mu_p = 523$ cm^2/(V s), $\tau_n = 1 \times 10^{-7}$ s; B4: $p = 6.6 \times 10^{14}$ cm^{-3} $\mu_p = 520$ cm^2/(V s)	9	$\frac{70}{104}$	–	0.89	35 (135)	0.3
	11	$\frac{90}{104}$	9.8	0.32	23 (150)	0.22
	12	$\frac{120}{104}$	10.1	0.81	1200 (160)	1.2
	14	–	9.9	0.63	32 (126)	0.11
C1: $p = 1 \times 10^{16}$ cm^{-3}, $\mu_p = 463$ cm^2/(V s), $\tau_n = 3 \times 10^{-8}$ s	3	–	10.1	0.54	3.6 (130)	0.4
	18	$\frac{200}{62}$	10.8	0.17	8.7 (90)	1.5
	21	–	9.94	0.32	16.2 (68)	3.5
D1: $p = 1.8 \times 10^{16}$ cm^{-3}, $\mu_p = 491$ cm^2/(V s), $\tau_n = 4 \times 10^{-8}$ s, D2: $p = 9 \times 10^{14}$ cm^{-3}, $\mu_p = 471$ cm^2/(V s)	10	–	11.6	0.21	12 (65)	1.0
	13	–	11.48	0.38	23.5 (48)	–
	15	–	11.29	0.59	17.6 (49)	–
	16	–	11.28	0.62	27 (69)	–
	17	–	–	0.42	16.2 (50)	–
G1: $p = 2.8 \times 10^{16}$ cm^{-3}, $\mu_p = 492$ cm^2/(V s), $\tau_n = 8 \times 10^{-8}$ s	8	$\frac{160}{116}$	–	0.35	15 (47)	1.1
	19	$\frac{100}{116}$	11.48	0.39	20.6 (50)	1.0
	20	$\frac{130}{116}$	11.8	0.44	15 (47)	0.37

Note: The diameter of n^+–p junctions defined by the photomask is 300 μm. The parameters of the $Cd_xHg_{1-x}Te$ samples are determined from measurements at $T = 78$ K. λ_{co} is the cutoff wavelength of the photosensitivity spectrum at a level of 0.5 of the peak value. R_0A is the specific differential resistance for zero bias, and R_d^{max} is the peak differential resistance.

obtained by thermal conversion of n-type samples. The parameters of the p-$Cd_xHg_{1-x}Te$ samples, namely, the hole concentration p, hole mobility μ_p, and electron lifetime τ_n, are listed in the table. The base n^+-type region was fabricated by implanting Zn^{++} ions with an energy of 120 keV and a dose of 1×10^{15} cm^{-2}. The depth of the n^+-p junction was estimated to be ~(0.5–0.8) μm. ZnS film was used as a protective mask for the n^+–p junctions.

The diffusion current I_d flows through the asymmetric n^+–p junction [6]. In this case, the contribution of minority carriers of a heavily doped n^+-region to this current can be disregarded:

$$I_d = I_{d0}[\exp(-qU/kT) - 1],$$

$$I_{d0} = (qn_i^2/N_a)(kT\mu_n/q\tau_n), \qquad (1)$$

where q is the elementary charge; k is the Boltzmann constant; T is the absolute temperature; n_i is the electron concentration in an intrinsic semiconductor; and N_a, μ_n, τ_n are the acceptor concentration, electron mobility, and electron lifetime for the p-region of the junction, respectively.

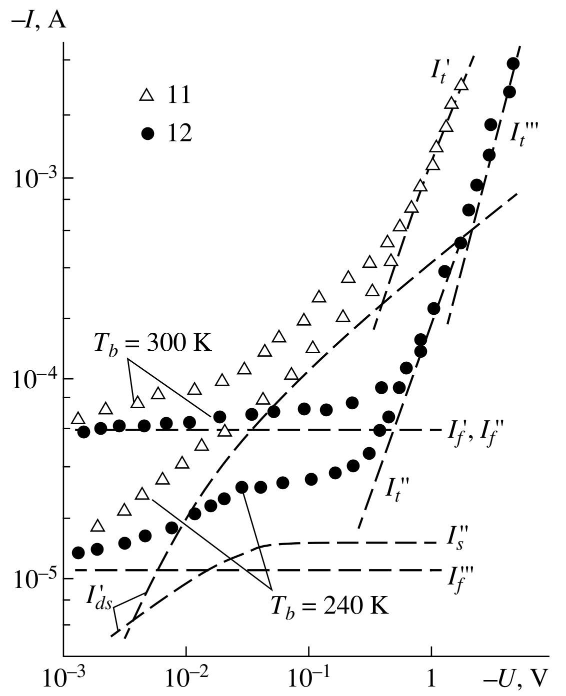

Fig. 2. Bias-voltage dependences of reverse currents of CdHgTe-based photodiodes 11 and 12. The graphic symbols correspond to the experiment, and the lines correspond to the calculation of components of the current. Photodiode 11: $I'_t = I'_{d0} = 1.1 \times 10^{-6}$ A; $I'_{g0} = 8.9 \times 10^{-7}$ A; $I'_f = I''_f$ (T_b = 300 K); I'_{ds} is calculated using formula (4); $S = 2.1 \times 10^4$ cm/s. Photodiode 12: $I''_t = I''_{d0} = 1.8 \times 10^{-7}$ A; $I''_{g0} = 3 \times 10^{-9}$ A; I''_f (T_b = 300 K) and I''_f (T_b = 240 K); I''_s is calculated using formula (6); $S = 1.5 \times 10^4$ cm/s.

For the generation–recombination currents I_{gr}, since they are much smaller than the other currents, only numerical values for $U > kT/q$ [7] are given in the captions to Figs. 1–3:

$$I_{g0} = (n_i A W_0/\tau_0)(kT/U_{bi}), \quad \tau_0 = (\tau_{n0}\tau_{p0})^{1/2}, \quad (2)$$

where W_0 is the width of the SCR; τ_{n0} and τ_{p0} are the lifetimes of minority carriers (electrons and holes) under thermodynamic equilibrium in the p- and n^+-regions of the junction, respectively; U_{bi} is the built-in voltage; and A is the junction area.

The expression for the photocurrent of a detector, which is induced by the background radiation with a spectral density W_λ (the Plank relationship), takes the following form:

$$I_f = q\sin^2(\theta/2)(1/2\pi\hbar c)\int\limits_{\Delta\lambda} W_\lambda \tau(\lambda)\eta(\lambda)d\lambda, \quad (3)$$

where θ is the PD linear angle of view, c is the speed of light in free space, $\hbar$ is the reduced Planck constant, λ is the radiation wavelength, $\tau(\lambda)$ is the spectral transmission coefficient of the PD cryostat window and antireflecting coating at the p–n junction, and $\eta(\lambda)$ is the spectral quantum efficiency [8].

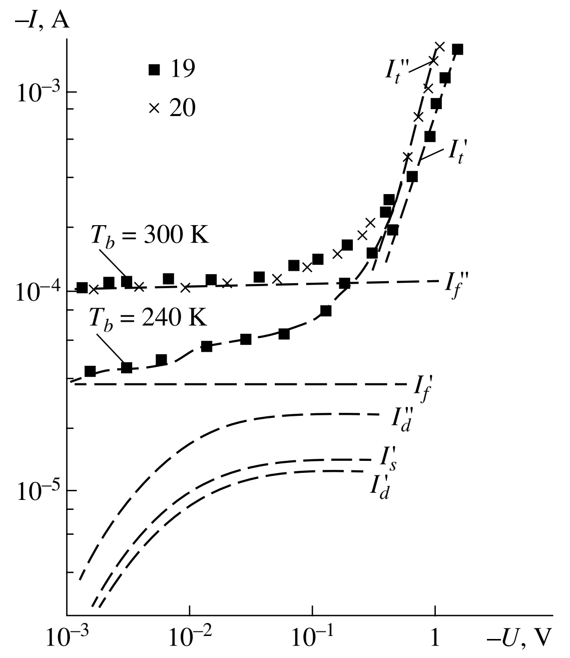

Fig. 3. Bias-voltage dependences of reverse currents in CdHgTe-based photodiodes 19 and 20. The graphic symbols correspond to the experiment, and the lines correspond to the calculation of components of the current. Photodiode 19: $I'_t = I'_{d0} = 1.2 \times 10^{-5}$ A; $I'_{g0} = 5.9 \times 10^{-9}$ A; I'_f (T_b = 240 K); I'_s is calculated using formula (6); I'_d is calculated using formula (1); $S = 3 \times 10^3$ cm/s. Photodiode 20: $I''_t = I''_{d0} = 2.3 \times 10^{-5}$ A; $I''_{g0} = 1.3 \times 10^{-8}$ A; I''_f (T_b = 300 K); I''_d is calculated with formula (1); $S = 1.5 \times 10^3$ cm/s.

Let us consider the current I_p for the leakage over the surface [9–11], first, the current I_d, or the surface diffusion current in a channel [10]:

$$I_{ds} = [2\sigma d^2 I_d(kT/q)]^{1/2} \times [\exp(qU/kT) - (qU/kT) - 1]^{1/2}, \quad (4)$$

where σ is the conductivity of the surface channel; d is the channel width; and I_d is the diffusion current through the n^+–p junction, which is determined by relationship (1).

In addition, let us consider the generation–recombination current in a channel I_{gs} [9], which is expressed in terms of the difference of reduced potentials at the surface and in a bulk $(Y_s - Y_b)$, the carrier mobility in the channel μ_s, and the rate of the generation–recombination process G in a unit volume of the semiconductor:

$$I_{gs} = d[(\exp 2B - 1)/(\exp 2B + 1)][G\mu_s kT\varepsilon_0\varepsilon_s]^{1/2} \times \exp[-(Y_s - Y_b)/2]U^{1/2}, \quad (5)$$

where $G = n_i/2\tau_n$, $B = l[qG\exp(Y_s)/2\mu_s n_i kT]^{1/2}$, l is the channel length, $Y_b = -E_{fb}/kT$, and ε_0 and ε_s are the permittivity of free space and relative permittivity of semiconductor, respectively.

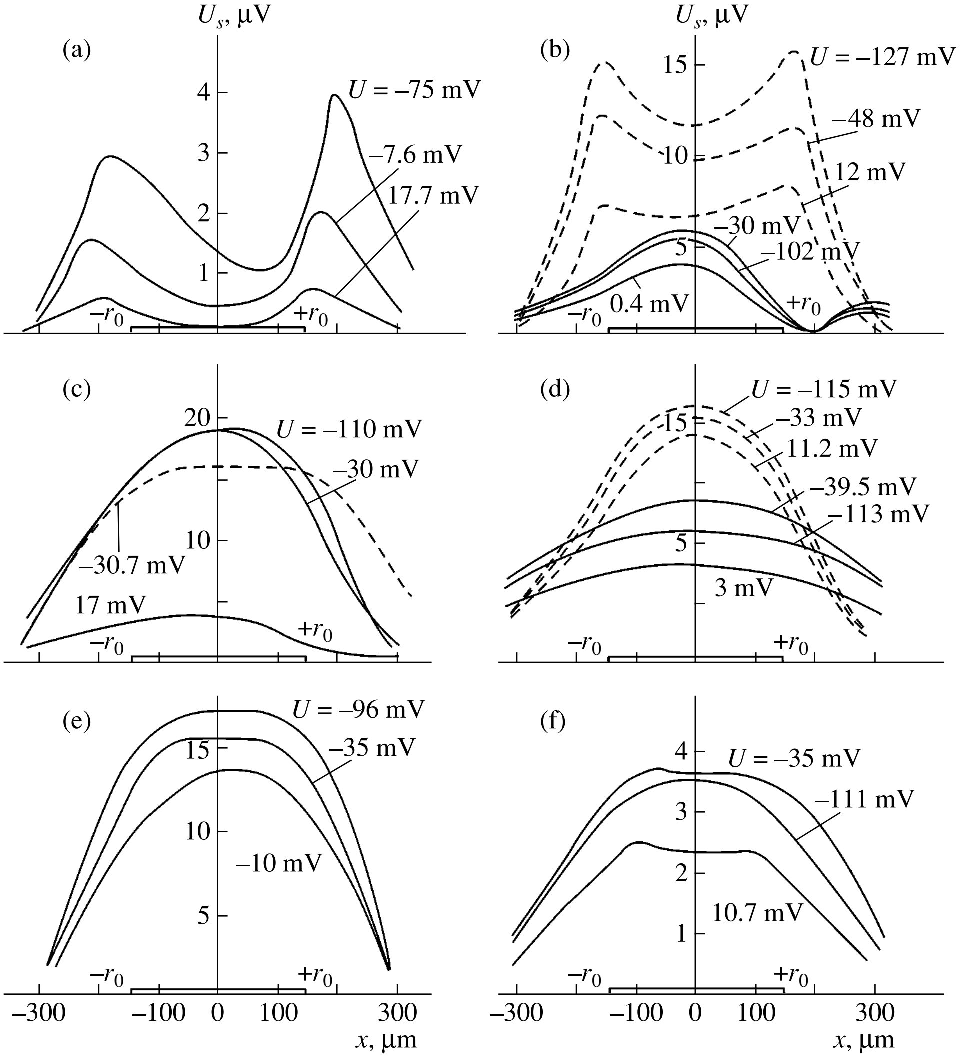

Fig. 4. Photoresponse U_s in relation to the coordinate x of CdHgTe-based n^+–p junctions for different bias voltages U. (a) Photodiode 2, $P = 0.05$ mW. (b) Dashed curves: photodiode 7, $P = 0.01$ mW; solid curves: photodiode 9, $P = 0.09$ mW. (c) Dashed curve: photodiode 8, $P = 0.01$ mW; solid curves: photodiode 20, $P = 0.08$ mW. (d) Dashed curves: photodiode 11, $P = 0.09$ mW; solid curves: photodiode 18, $P = 0.06$ mW. (e) Photodiode 12, $P = 0.05$ mW. (f) Photodiode 19, $P = 0.05$ mW.

Let us take the reduced electrostatic potential $Y_s = y = \varphi_s/kT$ at the ZnS/Cd$_x$Hg$_{1-x}$Te interface for $U = 0$ from capacitance–voltage characteristics of n^+–p junctions [12]. From these measurements, the hole concentration in the p-region p_p was also determined (see table). Let us estimate I_{gs} for the case when Y_s is positive and has the largest value $Y_s = +2.1$. In this case, the bands are bent downward and the surface is enriched with minority carriers (electrons), which form the reverse current of the junction (the leakage current).

We will assume that another component of the current exists, specifically, the surface generation–recombination current in the short surface channel [13]:

$$I_s = I_{s0}[\exp(-qU/kT) - 1], \quad I_{s0} = 2qn_iSA_\Sigma, \qquad (6)$$

where S is the rate of surface recombination (a variable parameter whose values are given in the figure captions) and $A_\Sigma = \pi(D_0 + 2L_n)^2/4 - A_0$, $A_0 = \pi D^2/4$. Here, A_0 and $D_0 = 2r_0$ are the surface area and diameter of the n^+–p junction over the photomask, A_Σ is the area of the ring with a width L_n, and L_n is the diffusion length of electrons in the p-region of the junction. Thus, we assume that recombination proceeds at the surface in the ring of area A_Σ.

Figures 1–3, along with the experimental I–U characteristics, show either calculated currents in the form of voltage dependences or the values of currents in the saturation mode if their effect is insignificant for plotting the I–U characteristics on the basis of these components. Note that, if we disregarded the I_{gs} current, we could not obtain a theoretical reverse portion of the I–U characteristic consistent with the experimental characteristic only for photodiode 2 (Fig. 1). The I–U characteristics shown in Figs. 1–3 are measured at two background temperatures, namely, at $T_b = 300$ K and the reduced background at $T_b = 240$ K (the PD "views" liq-

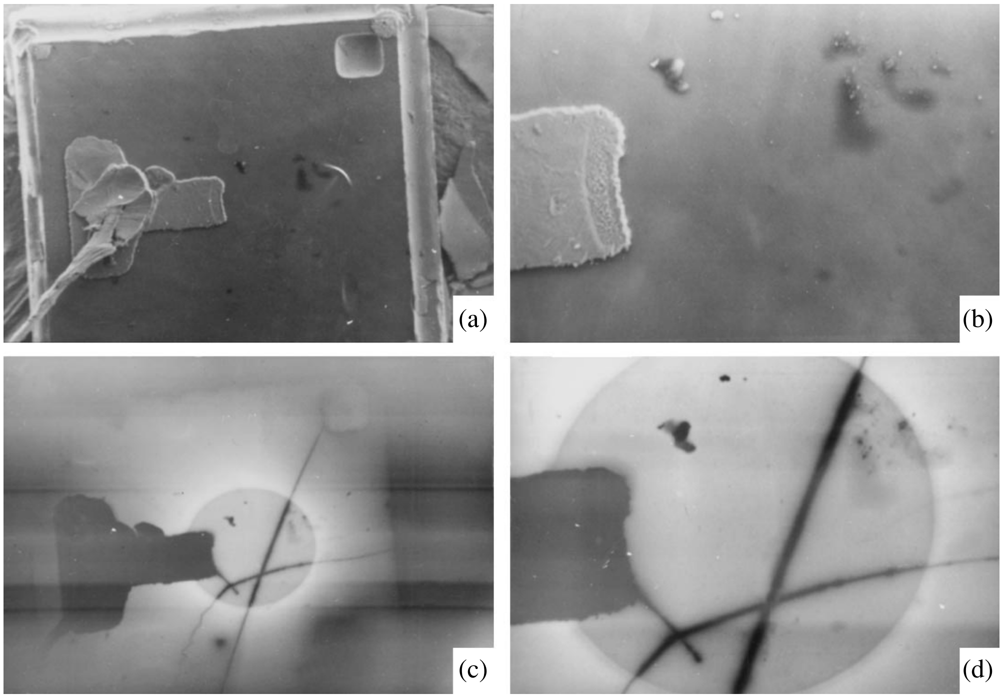

Fig. 5. Image of the crystal of CdTe-based photodiode 18 with the n^+–p junction (a, b) in the secondary electron mode and (c, d) in the EBIC mode. (a, c) Magnification ×100; (b, d) magnification ×300.

uid nitrogen; view angle $\theta \approx 45°$). The temperature T_b = 240 K is mentioned in the figure captions only for the currents that were measured at the reduced background.

For certain PDs, the effective diffusion lengths L_n of electrons in the p-type region of n^+–p junctions were measured by scanning a CO_2 laser beam (wavelength $\lambda = 10.6$ μm, beam diameter $d = 30$ μm) over the junction diameter (Fig. 4), whose values are given in the table (upper values). The measurements shown in Fig. 4 were performed for different biases U applied to the PDs in the small-signal mode. The values of emission power P of the laser are given in the caption to Fig. 4. The values of L_n were determined from the decrease in the signal from the peak value by a factor of e, i.e., at the level $U_s/U_s^{\max} = e^{-1} = 0.368$. In addition, the diffusion length $L_n = (D_n\tau_n)^{1/2}$ was estimated from τ_n and μ_n measured for starting samples of p-type conduction, which are also listed in the table (lower values). We may conclude from a comparison of these two values of L_n that the higher R_d is for the PDs, the closer these values are to each other, and that R_d is largely determined by the bulk properties of the starting substrate of p-type conduction rather than by the surface.

The cause of currents I_{ds} and I_s in certain PDs (Figs. 1–3) is local defects in the ZnS film that emerge during technological operations in the fabrication process of n^+–p junctions or the defects produced by the surface treatment of the material itself. Thus, we can see the residual traces of the polishing of wafers (PD 18) in Figs. 5c and 5d. These traces are hidden under ZnS and unobservable in the images obtained in the secondary-electron mode (Figs. 5a, 5b). However, the traces of polishing are apparent in the electron beam induced current (EBIC) mode in a scanning electron microscope (Figs. 5c, 5d) [14]. An analysis of the images allows us to separate bulk defects in the CdHgTe material itself from defects at the surface, in particular, defects at the outer surface of the ZnS film.

The decrease in the sensitivity of PD 18 in the short-wavelength spectral region with increasing reverse voltage U is characteristic of the effect of the surface (Fig. 6; see also Fig. 4). The width of the region of local photoconductivity induced by the electron beam in the scanning electron microscope (Figs. 5c, 5d) allows us to evaluate the diffusion length of photocarriers at the surface L_s.

The spread of the x and p values within the n^+–p junctions of diameter 300 μm, which is comparable with the wafer thickness, as well as the arbitrary uncontrollable orientation of the wafer relative to crystallographic planes (which is related to the history of fabrication of the $Cd_xHg_{1-x}Te$ wafers), can also cause I_{ds}. These causes lead to the distortion of the doping profile over the depth. In this case, the actual junction area differs considerably from the area defined by the photomask, and the SCR is a dissected region with a distorted electric field and excess currents. This conclusion is confirmed by studies of the sensitivity profile of the n^+–p junctions when the latter are scanned by the laser beam (Fig. 4, PDs 2 and 7). The shift of the photoconductivity peak to a value of r_0 larger than the nominal value with increasing U applied to the photodiode also indicates that the leakage current in PD 2 is related to

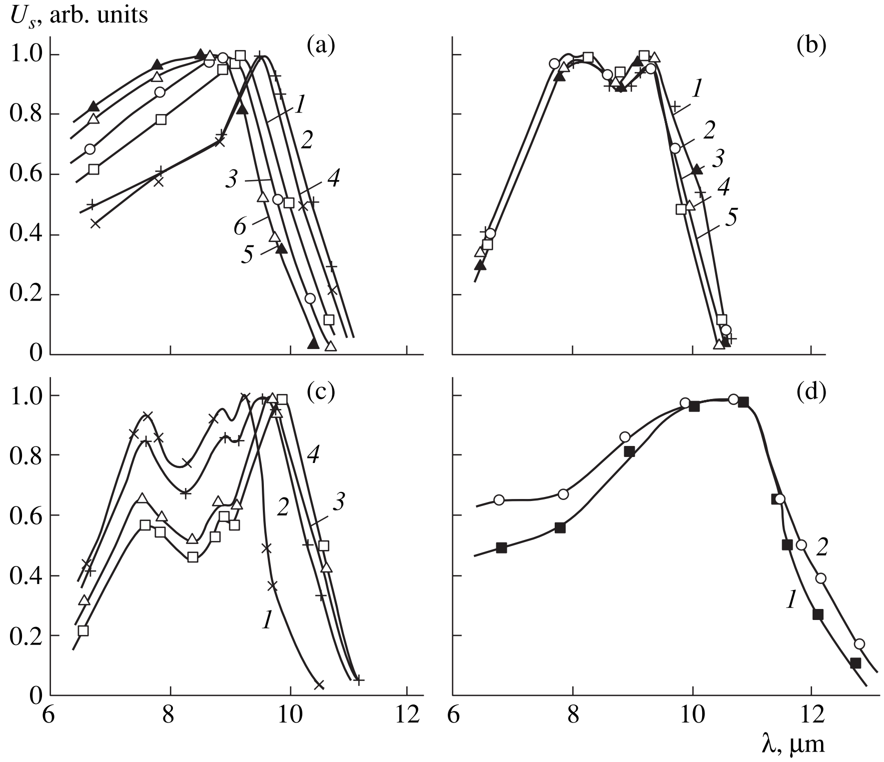

Fig. 6. Spectral characteristics of CdHgTe-based photodiodes at T = 78 K. (a) Photodiode 2, U = (*1*) –5, (*2*) –30, (*3*) –52, (*4*) –63, (*5*) –210, and (*6*) –770 mV. (b) Photodiode 12, U = (*1*) 0, (*2*) –15.5, (*3*) –50, (*4*) –200, and (*5*) –790 mV. (c) Photodiode 18, U = (*1*) +9.6, (*2*) 0, (*3*) –90, and (*4*) –243 mV. (d) (*1*) Photodiode 19, U = –43 mV, and (*2*) photodiode 20, U = –37 mV.

the surface (Fig. 4). For a positive bias and small negative U, the location of this peak coincides exactly with the r_0 boundary of the n^+–p junction defined by the photomask (diameter, 300 μm). With a further increase in negative U, the effective junction size, more precisely, the size of the SCR that emerges at the surface, increases. This reasoning is also confirmed by the shift of the spectral characteristics of PD 2 (Fig. 6) to shorter wavelengths as U increases, which is indicative of a spread of the junction SCR over the surface. As a result, the relative sensitivity at shorter wavelengths increases.

Thus, our studies showed that the shape of the I–U characteristics and low values of R_0A, which are sometimes observed in experimental PDs, are mainly caused by surface properties. Leakage currents over the surface are observed in all junctions, including those with high R_d. In the latter junctions, leakage currents distort the shape of the I–U characteristics, although these currents are not dominant. In all junctions biased by $-U \leq 0.01$ V, the background photocurrent is dominant (at angles of view $\theta \gtrsim 45°$). In contrast, when the background level is reduced, the I_s current is dominant. The U dependence of this current is similar to the dependence of I_d, which can often lead to an erroneous conclusion about the dominant current [15]. For $-U \geq 0.5$ V, the tunnel current I_t is dominant (Figs. 1–3), whereas for intermediate biases $U \approx (-0.01)$–(-0.4) V, the shape of experimental I–U characteristics depends on the surface leakage current.

REFERENCES

1. R. E. DeWames, G. M. Williams, J. G. Pasko, and A. H. B. Vanderwyck, J. Cryst. Growth **86**, 849 (1988).
2. A. I. Elizarov, V. I. Ivanov-Omskiĭ, A. A. Korniyash, and V. A. Petryakov, Fiz. Tekh. Poluprovodn. (Leningrad) **18**, 201 (1984) [Sov. Phys. Semicond. **18**, 125 (1984)].
3. M. C. Chen, Appl. Phys. Lett. **51**, 1836 (1987).
4. S. E. Schachm and E. Finkman, Opt. Eng. **29**, 795 (1990).
5. M. G. Andrukhiv, S. V. Belotelov, and I. S. Virt, Fiz. Tekh. Poluprovodn. (St. Petersburg) **27**, 1863 (1993) [Semiconductors **27**, 1026 (1993)].
6. W. Shockley, Bell Syst. Tech. J. **28**, 435 (1949).
7. S. T. Sah, R. N. Noyce, and W. Shockley, Proc. IRE **45**, 1228 (1957).
8. V. I. Turinov, Élektron. Tekh., Ser. 11: Lazer. Tekh. Optoélektron. **1**, 88 (1984).
9. J. C. Inkson, Solid-State Electron. **13**, 1167 (1970).
10. M. Cutler and H. M. Bath, Proc. IRE **45**, 39 (1957).
11. H. Statz, G. A. De Mars, H. Devis, and A. Adams, Phys. Rev. **101**, 1272 (1956).
12. V. I. Turinov, Élektron. Tekh., Ser. 1: Élektron. SVCh **2**, 14 (1992).
13. S. P. Tobin, S. Iwasa, and T. J. Tredwell, IEEE Trans. Electron Devices **27**, 43 (1980).
14. E. B. Yakimov, Izv. Ross. Akad. Nauk, Ser. Fiz. **56**, 31 (1992).
15. V. I. Turinov, Élektron. Tekh., Ser. 1: Élektron. SVCh **8**, 3 (1990).

Translated by N. Korovin